

State-to-state surface scattering of methane studied by bolometric infrared laser tagging detection

Présentée le 6 mai 2022

Faculté des sciences de base
Groupe SCI SB RB
Programme doctoral en chimie et génie chimique

pour l'obtention du grade de Docteur ès Sciences

par

Bo-Jung CHEN

Acceptée sur proposition du jury

Prof. C. Bostedt, président du jury
Prof. R. Beck, directeur de thèse
Prof. K. McKendrick, rapporteur
Dr T. Schäfer, rapporteur
Dr A. Osterwalder, rapporteur

Abstract

State-to-state molecule/surface scattering experiments prepare the incident molecules in a specific quantum state and measure the quantum state distribution of the scattered molecules. Such state-resolved scattering experiments provide highly detailed data on the molecule/surface interactions which can be compared directly to theories of molecule/surface scattering without the need for averaging many rotational and vibrational states. The comparison of state resolved experiments with theory can serve as stringent tests of the molecule/surface interaction potential and of the scattering dynamics. The overall motivation is to develop a predictive understanding of the molecule/surface interactions and reactions needed for the understanding and optimization of heterogeneous catalysis.

In this thesis, I describe the design, characterization, and first applications of a new apparatus, dedicated to performing state-to-state surface scattering using bolometric infrared laser tagging detection (BILT). An important advantage of the BILT detection method over other state-resolved detection techniques such as resonant multi-photon ionization (REMPI), is its applicability to any molecule with an infrared active vibrational mode and a rotationally resolved vibrational gas phase spectrum. For example, BILT detection can be used to detect important molecules such as methane and carbon dioxide for which REMPI detection is not possible.

Our new state-to-state scattering machine features a liquid helium-cooled bolometer detector installed on a rotatable lid allowing independent variation of the incident and the scattering angle. With this capability, one can study energy transfer such as the conversion of translational to rotational or vibrational energy as well as vibrational energy redistribution for molecules colliding with a well-defined single crystal surface at a wide variety of scattering geometries. By monitoring the laser tagging bolometer signal as a function of scattering angle, one can measure the state-resolved angular distribution of scattered products and study the quantum state-dependent spatial distribution of the scattered products. The design of the BILT machine also includes Doppler velocimetry which can serve to measure the velocity of scattered molecules in different quantum states.

To demonstrate the capabilities of the BILT machine, I studied the rotationally inelastic scattering of CH_4 from Ni(111). By properly choosing the incident angle and the seeded ratio of CH_4 in He gas mixtures, I vary the normal and the parallel component of incident velocity independently and study their effects on rotational excitation. The results show that rotational excitation depends not only on the kinetic energy along the surface normal but also on the parallel component although with lower efficiency. The extent of rotational excitation is found to increase with increasing surface temperature. The conversion efficiency appears to be higher for low-velocity component normal to the surface. The observations indicate a mechanism of rotational excitation by phonon annihilation with the probability related to the relative velocity of the incoming molecules and surface atoms. Using the experimentally determined formula which takes into account the conversion efficiency of the normal, the parallel component of the incident kinetic energy, the surface thermal energy, and the physisorption well to the rotational energy, the mechanism of rotational excitation of CH_4 scattering from Ni(111) is quantitatively unraveled.

Besides rotational inelastic scattering, I report very distinct behavior of vibrationally inelastic scattering of CH₄ from clean Ni(111) and graphene-covered Ni(111). Vibrational energy transfer to the surface dramatically changes when a clean Ni(111) surface is covered with a single layer of graphene. Theoretical calculations based upon reaction path Hamiltonian suggest that the probability of the vibrational energy transfer is related to the catalytic activity of the surface impact sites for CH₄ dissociation. Therefore, by monitoring the fate of the initially prepared vibrational energy, the state-to-state surface scattering technique can potentially serve as a probe of the catalytic activity of surfaces.

Keywords: State-resolved detection, molecular beam, methane, Ni(111), graphene, surface scattering, inelastic scattering, rotational excitation, vibrational energy redistribution, IR spectroscopy, surface corrugation.

Résumé

Les expériences de diffusion de molécules/surface d'état à état préparent les molécules incidentes dans un état quantique spécifique et mesurent la distribution d'état quantique des molécules diffusées. Ces expériences de diffusion à état résolu fournissent des données très détaillées sur les interactions molécule/surface qui peuvent être comparées directement aux théories de diffusion molécule/surface sans qu'il soit nécessaire de calculer la moyenne de nombreux états rotationnels et vibrationnels. La comparaison des expériences de résolution d'état avec la théorie peut servir de tests rigoureux du potentiel d'interaction molécule/surface et de la dynamique de diffusion. La motivation générale est de développer une compréhension prédictive des interactions molécule/surface et des réactions nécessaires à la compréhension et à l'optimisation de la catalyse hétérogène.

Dans cette thèse, je décris la conception, la caractérisation et les premières applications d'un nouvel appareil, dédié à la diffusion d'état à état de la surface en utilisant la détection par marquage laser infrarouge bolométrique (BILT). Un avantage important de la méthode de détection BILT par rapport à d'autres techniques de détection à résolution d'état telles que l'ionisation multiphotonique résonnante (REMPI), est son applicabilité à toute molécule ayant un mode vibrationnel actif dans l'infrarouge et un spectre vibrationnel en phase gazeuse à résolution rotationnelle. Par exemple, la détection BILT peut être utilisée pour détecter des molécules importantes comme le méthane et le dioxyde de carbone pour lesquelles la détection REMPI n'est pas possible.

Notre nouvelle machine de diffusion d'état à état comporte un détecteur bolomètre refroidi à l'hélium liquide installé sur un couvercle rotatif permettant une variation indépendante de l'angle d'incidence et de diffusion. Grâce à cette capacité, il est possible d'étudier le transfert d'énergie, comme la conversion de l'énergie de translation en énergie de rotation ou de vibration, ainsi que la redistribution de l'énergie de vibration pour les molécules qui entrent en collision avec une surface monocristalline bien définie dans une grande variété de géométries de diffusion. En contrôlant le signal du bolomètre de marquage laser en fonction de l'angle de diffusion, on peut mesurer la distribution angulaire des produits diffusés résolue par l'état et étudier la distribution spatiale des produits diffusés qui dépend de l'état quantique. La conception de la machine BILT inclut également la vélocimétrie Doppler qui peut servir à mesurer la vitesse des molécules diffusées dans différents états quantiques.

Pour démontrer les capacités de la machine BILT, j'ai étudié la diffusion inélastique rotationnelle de CH_4 à partir de Ni(111). En choisissant correctement l'angle d'incidence et le rapport d'ensemencement de CH_4 dans des mélanges de gaz He, je fais varier la composante normale et la composante parallèle de la vitesse incidente indépendamment et j'étudie leurs effets sur l'excitation rotationnelle. Les résultats montrent que l'excitation rotationnelle dépend non seulement de l'énergie cinétique le long de la normale à la surface, mais aussi de la composante parallèle, bien qu'avec une efficacité moindre. L'étendue de l'excitation rotationnelle augmente avec la température de la surface. L'efficacité de la conversion semble être plus élevée pour la composante à faible vitesse normale à la surface. Les observations indiquent un mécanisme d'excitation rotationnelle par annihilation de phonons dont la probabilité est liée à la vitesse relative des molécules entrantes et des atomes de surface. En utilisant la formule déterminée

expérimentalement qui prend en compte l'efficacité de conversion de la composante normale, de la composante parallèle de l'énergie cinétique incidente, de l'énergie thermique de surface et du puits de physisorption en énergie rotationnelle, le mécanisme d'excitation rotationnelle de la diffusion de CH₄ à partir de Ni(111) est quantitativement élucidé.

Outre la diffusion inélastique rotationnelle, je rapporte un comportement très distinct de la diffusion inélastique vibrationnelle de CH₄ à partir de Ni(111) propre et de Ni(111) recouvert de graphène. Le transfert d'énergie vibratoire à la surface change de façon spectaculaire lorsqu'une surface de Ni(111) propre est recouverte d'une seule couche de graphène. Les calculs théoriques basés sur le chemin de réaction Hamiltonien suggèrent que la probabilité du transfert d'énergie vibratoire est liée à l'activité catalytique des sites d'impact de surface pour la dissociation du CH₄. Par conséquent, en surveillant le sort de l'énergie vibratoire initialement préparée, la technique de diffusion d'état à état de la surface peut potentiellement servir de sonde de l'activité catalytique des surfaces.

Mots-clés : Détection résolue par état, faisceau moléculaire, méthane, Ni(111), graphène, diffusion en surface, diffusion inélastique, excitation rotationnelle, redistribution de l'énergie vibrationnelle, spectroscopie IR, ondulation de surface.

Contents

Abstract	i
Résumé.....	iii
Contents	v
List of abbreviations	viii
Chapter 1 Introduction	1
1.1 Motivation	1
1.2 Molecule-surface interactions and potential energy surfaces	3
1.3 Review of state-to-state surface scattering.....	6
1.4 State-to-state surface scattering of CH ₄ from Ni(111).....	10
1.5 Limitations of the previous setup.....	11
1.6 Design of a new state-to-state surface scattering apparatus.....	12
1.7 Outline of this thesis.....	12
Chapter 2 Experimental setup.....	14
2.1 Overview	14
2.2 Source chamber	17
2.2.1 Molecular beam source and nozzle source	18
2.2.2 Chopper motor and optocoupler	24
2.3 Time-of-Flight measurements and calibrations.....	26
2.3.1 Chopper delay	30
2.3.2 Ion flight-time	32
2.3.3 Neutral flight-time	34
2.3.4 Reliability of the calibrations.....	34
2.3.5 Generation of fast beams by hot nozzle.....	35
2.4 Scattering chamber	36
2.4.1 Top hub and the rotating platform	37
2.4.2 Chain drive mechanism.....	41
2.4.3 Vacuum condition.....	42
2.4.4 Molecular beam flux and dimensions	45
2.4.5 Pyroelectric detector	47

2.4.6	Sample mount and manipulator	50
2.4.7	Sample preparation and characterization	55
2.5	Cryogenic bolometer	59
2.5.1	Structural overview	59
2.5.2	Characterization and modification	62
2.5.3	Sensitivity of the bolometric detection	71
2.5.4	Angular distribution measurements	74
2.6	Laser setup.....	76
2.6.1	System overview of TOPO	76
2.6.2	Frequency tuning of TOPO.....	79
2.6.3	Frequency stabilization and scanning of TOPO	82
2.6.4	Argos OPO systems	86
2.6.5	Lamb-dip locking.....	86
2.6.6	Transfer cavity stabilization.....	88
Chapter 3 Bolometric infrared laser tagging.....		90
3.1	Introduction	90
3.2	Bolometric infrared laser tagging.....	90
3.3	Laser excitation by rapid adiabatic passage	93
3.4	The problem of RAP encountered in the BILT machine	97
3.5	Laser linewidth broadening.....	106
3.6	CH ₄ infrared spectroscopy	111
3.7	Nuclear spin isomers of CH ₄ and the allowed rovibrational levels	113
3.8	Coriolis coupling of the degenerate vibrational modes.....	116
3.9	Selection rules of IR transitions	116
Chapter 4 Rotationally inelastic scattering of CH ₄		118
4.1	Introduction	118
4.2	Experimental	121
4.3	Results	125
4.4	Discussion	136
4.5	Conclusion.....	139
Chapter 5 Vibrationally inelastic scattering.....		140
5.1	Introduction	140

5.2	Experimental	141
5.3	Vibrational relaxation of CH ₄ ($\nu_3, J = 1$) during scattering from Ni(111) and Gr-Ni(111) 142	
5.4	Rotational excitation of CH ₄ ($\nu_3, J = 1$) scattered from Ni(111) and Gr-Ni(111)	144
5.5	Theoretical predictions for state-to-state methane scattering.....	145
5.6	T_S -dependent $\nu_3 \rightarrow \nu_1$ redistribution.....	147
Chapter 6 Summary and outlook		150
6.1	Summary	150
6.2	Future experiments	154
References.....		156
List of Figures		162
List of Tables		172
Acknowledgments.....		174
Curriculum Vitae		177

List of abbreviations

AC	Alternating current
AES	Auger electron spectroscopy
BOA	Born-Oppenheimer approximation
BILT	Bolometric infrared laser tagging
CW	Continuous-wave
DC	Direct current
EHP	Electron-hole pairs
FPI	Fabry-Pérot interferometer
FSR	Free spectral range
FWHM	Full width at half maximum
HAS	Helium atom scattering
IR	Infrared
IVR	Intramolecular vibrational energy redistribution
LEED	Low energy electron diffraction
LIF	Laser-induced fluorescence
MCS	Multichannel scaler
OPO	Optical parametric oscillator
PES	Potential energy surface
PID	Proportional-integral-differential
PZT	Lead zirconate titanate (piezoelectric material)
QMS	Quadrupole mass spectrometer
RAP	Rapid adiabatic passage
REMPI	Resonantly enhanced multiphoton ionization
RMS	Root mean square
S/N	Signal-to-noise ratio
TOF	Time-of-flight
UHV	Ultra-high vacuum
VI	Virtual instrument

Chapter 1 Introduction

1.1 Motivation

In the research field of surface reaction dynamics, we seek to understand the interactions and reactions of gas-phase molecules on solid and liquid surfaces at a microscopic level. This knowledge is of crucial importance as these reactions play a key role in heterogeneous catalysis which is of utmost importance for the chemical industry. For example, the dissociative chemisorption of N_2 on iron-based catalysts is known as the rate-determining step of the Haber-Bosch process which synthesizes ammonia from nitrogen and hydrogen gas [1]. Much of the synthetic ammonia is used to produce fertilizers which are needed to feed a large fraction of today's world population [2]. Understanding the reaction mechanism is valuable as it can help to develop more efficient catalysts and improve the reaction conditions [3].

The energy transfer between a gas phase molecule and surface atoms is a decisive step to determine its sticking and reaction on a solid surface. Consider an incoming molecule with a certain amount of incident translational energy. During the collision with the surface, the molecule must lose sufficient energy in order to trap on the surface for a subsequent chemical reaction on the catalyst surface (by the Lindemann-Hinshelwood mechanism). An incident molecule can lose kinetic energy either by exciting phonons and/or electron-hole pairs in the solid or by converting translational energy to rotational and vibrational excitation. The molecules which trap and react on the surface are fully thermalized with the surface and will have lost their memory of the incident conditions. Whereas incident molecules that fail to trap but scatter back into the gas phase can reveal detailed information about the molecule/surface energy transfer process.

If we control not only the translational energy and incident angle of the molecular beam in a surface scattering experiment, but also prepare the incident molecules in a specific rovibrational quantum state and subsequently measure the quantum state distribution of the scattered molecules, we can obtain more detailed information about the energy transfer during the molecule/surface collision. This technique is called state-to-state surface scattering which represents a higher-level control of the molecule/surface collision. In a favorable case, we can even align or orient the incident molecules and study the stereodynamics of molecule/surface collision. The detailed dynamics of the molecule/surface collision are governed by the forces acting between the molecule and surface which are encoded in the potential energy (hyper) surface of the molecule/surface system. Gas/surface interaction potentials can be calculated by theoreticians who use them to perform accurate simulations and predictions of chemical reactions either by quasi-classical trajectory simulations (QCT) [4–6] or quantum dynamical wavepacket calculations [7]. Results obtained by the state-to-state scattering experiments can potentially serve as benchmarks to assess the accuracy of calculated potential energy surfaces. Furthermore, state-to-state scattering experiments allow us to prepare a system with highly controlled conditions and analyze the outcome of the scattering event in much detail. The resulting state-to-state scattering data is therefore valuable for testing theory because it can be compared to theoretical predictions without the need for extensive averaging.

State-to-state molecule/surface scattering experiments, although being conceptually simple, are challenging to realize experimentally. The surface scattering event disperses the collimated beam of state-prepared incident molecules into a distribution of scattering angles and rovibrational states resulting in a rather dilute molecular flux for each direction and quantum state. Hence, the detection method for state-to-state scattering needs to be not only state-selective but also highly sensitive. Resonantly enhanced multiphoton ionization (REMPI) is one widely used detection method that can satisfy both requirements [8]. A large number of molecule/surface systems have been studied with quantum state resolution by the REMPI technique. However, so far most of these studies are concerned with diatomic molecules [9–13]. The number of state-resolved scattering experiments for polyatomic molecules is still limited because of a lack of a feasible REMPI detection scheme that requires a sufficiently stable excited electronic state. Unfortunately, for some molecules such as CO_2 and CH_4 , which are important in many industrial and environmental aspects, there is no known REMPI scheme for their quantum state-resolved detection.

In our group, Van Reijzen and Werdecker developed an alternative state-resolved detection method that uses a cryogenic bolometer in combination with state-specific infrared laser tagging and which is more generally applicable than REMPI. Bolometer infrared laser tagging detection was initially reported by Wight and Miller [14,15] for the scattering of CH_4 and acetylene from an inert LiF surface. The results reported by Van Reijzen and Werdecker on CH_4 scattering from catalytically active Ni(111) have demonstrated the potential of the BILT technique as an alternative to REMPI detection but which is more widely applicable to any molecule with an infrared active vibration and a rotationally resolved infrared spectrum [16–18]. Unlike diatomic molecules, the multiple vibrational modes of polyatomic molecules increase the complexity of vibrational energy transfer at the gas/surface encounter and open the possibility for mode-specificity and bond-selectivity in gas/surface reactions. The mechanism of coupling between vibrational modes and intramolecular vibrational redistribution (IVR) due to molecule/surface interactions is still an unknown area for surface scientists. Fortunately, the BILT technique opens up a possibility to let us explore this field.

Although a number of interesting results have been observed using the BILT technique [16–18], its applications were limited in our initial experimental setup. Due to a fixed detector position, the apparatus did not allow for independent variation of the incident and the scattering angle. Also, due to the hydrocarbon outgassing from the first version of the bolometer, our scattering experiments had to be carried out at an elevated surface temperature (400 °C) in order to keep the surface clean. To eliminate these limitations, we decided to build an apparatus dedicated to state-to-state surface scattering experiments by BILT detection. The design and construction of the new apparatus is the main part of my thesis work which benefitted from significant contributions by Prof. Daniel Auerbach. Our newly designed state-to-state scattering machine is equipped with a redesigned bolometer detector mounted on a rotatory lid, allowing for independent variation of the incident and scattering angles. To demonstrate the capabilities of the new apparatus, I continued to study the rotational inelastic scattering of CH_4 from Ni(111). Using the ability to rotate the scattering surface and the detector independently, I studied the effects of the parallel and normal components of incident energy on the rotational energy transfer for the scattering of CH_4 from Ni(111). Better vacuum conditions now allow us to perform scattering experiments for a wider

range of surface temperature (T_s), which I used to explore the effect of T_s on the rotational excitation of the scattered methane. As I will show in this thesis, using the capabilities of the new apparatus, the mechanism of the rotational excitation of CH_4 from Ni(111) in a direct scattering process can be properly resolved.

1.2 Molecule-surface interactions and potential energy surfaces

Initiation of a molecule-surface reaction requires a collision between a molecule and a target surface. Consider a molecule incident on a solid surface, if the kinetic energy of the incoming molecule is low enough, the molecule will be trapped on the surface by van der Waals forces, as shown in the trajectory E_1 in Figure 1.1, a process which is referred to as *physisorption*. Since the physisorbed molecule is trapped only by weak van der Waals forces normal to the surface instead of forming a chemical bond, it may still be mobile in the 2 dimensions parallel to the surface. For physisorption to occur, the incident molecule must lose sufficient incident energy, such that the remaining kinetic energy normal to the surface is lower than the depth of the physisorption well V_P . The incident molecule can transfer its kinetic energy via excitation of surface phonons, conversion of translation to rotation (T \rightarrow R), or vibrational excitation (T \rightarrow V). If the trapped molecule subsequently acquires sufficient kinetic energy due to thermal energy transfer from the surface, it can desorb from the surface. This is referred to as *trapping-desorption*, a process during which the adsorbates spend sufficient time on the surface to thermalize with the surface and desorb with translational and internal energy reflecting the surface temperature T_s . For trapping-desorption, if the trapping probability does not vary significantly over the range of velocities present in a Boltzmann distribution at T_s , one expects that the angular distribution of the desorbing molecules is given by $\cos(\theta)$, where θ is the desorption angle measured from the surface normal.

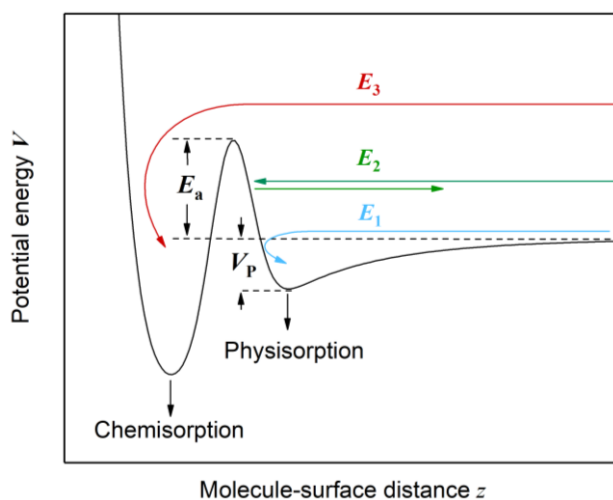


Figure 1.1 A plot of potential energy as a function of molecule-surface distance which illustrates the concepts of chemisorption and physisorption. The dashed line indicates the level of zero potential energy. See text for the concept.

If the incident molecule doesn't lose sufficient normal kinetic energy to be trapped on the surface, it will scatter back immediately into the gas phase via *direct scattering*, as shown in Figure 1.1, trajectory E_2 . Because the directly scattered molecules only interact with the surface very briefly (ps) and move away from the surface with a fraction of their incident energy, they can serve as a probe of the molecule/surface energy-transfer process if a suitable state-resolved detection method is available. In contrast to trapping desorption, directly scattered products typically show an angular distribution that is peaked near the specular angle.

Besides physisorption, a gas phase molecule can adsorb on the surface by forming a chemical bond with a specific surface site by a process which is referred to as *chemisorption*. Since a chemical bond is formed between the molecule and a surface atom, the product is mostly immobile except for H atoms. For CO chemisorption on Pt(111), the CO molecule is bound to the surface by its lone pair on the C-end [19]. In this case, no internal chemical bond is broken, thus the chemisorption of CO on Pt(111) occurs easily without overcoming a high activation barrier. On the other hand, *dissociative chemisorption* requires breaking an intramolecular chemical bond followed by bond formation between the resulting fragments and surface atoms. This type of chemisorption typically requires overcoming an activation barrier, as shown in Figure 1.1, trajectory E_3 . An example is CH_4 chemisorption on Ni(111) leading to $\text{CH}_3(\text{ads})$ and $\text{H}(\text{ads})$ with an activation barrier of ≈ 1 eV [20]. One distinguishes between a direct and a precursor mediated mechanism for chemisorption. For direct chemisorption, an incident molecule can dissociate immediately on impact if it possesses sufficient translational or vibrational energy to overcome the activation barrier. For the precursor mechanism, the reactant molecules first need to trap in a physisorbed state where they can diffuse in the plane of the surface. During their trapping time, the physisorbed molecules may dissociate if they encounter a low barrier reactive site such as a step or defect atom.

An important feature I haven't addressed so far is the "type" of incident energy needed for a molecule to overcome the activation barrier. Depending on the shape of the potential energy surface of a gas-surface system, the molecule may need translational, rotational, or vibrational energy to surpass the barrier. A potential energy surface (PES) describes the energy of a system as a function of parameters such as molecule-surface distance, bond length, bond angle, and molecular orientation. The number of degrees of freedom of a molecule-surface system exceeds 3 dimensions and therefore cannot be visualized on a 2-D surface. A way to simplify its complexity is by freezing some degrees of freedom and only plotting the energy as a function of a few selected parameters that are considered to influence the reaction of interest the most. An example that can be visualized is a reaction between an atom A and a diatomic molecule BC: $\text{A} + \text{BC} \rightarrow \text{AB} + \text{C}$. Assuming a collinear collision manner, the potential energy surface can be plotted as a function of the internuclear distance of A and BC r_{AB} and that of AB and C r_{BC} , as shown in Figure 1.2.

In the left two panels, the transition state of the reaction (corresponding to the saddle point of the PES) is located in the entrance valley, forming a so-called *early barrier*. The red lines in all panels indicate the trajectories of particles governed by the PES. Polanyi pointed out that in the case of an early barrier, the reagent AB can pass the barrier more efficiently with translational energy [21]. After passing the barrier, the initial translational energy will then be converted to

product vibration, as described by the red trajectory in the top-left panel. Whereas if the reagent enters the valley predominately with vibration, the vibrational energy won't be efficient to surpass the crest because the vibrational motion is perpendicular to the direction of the barrier, as shown in the bottom-left panel.

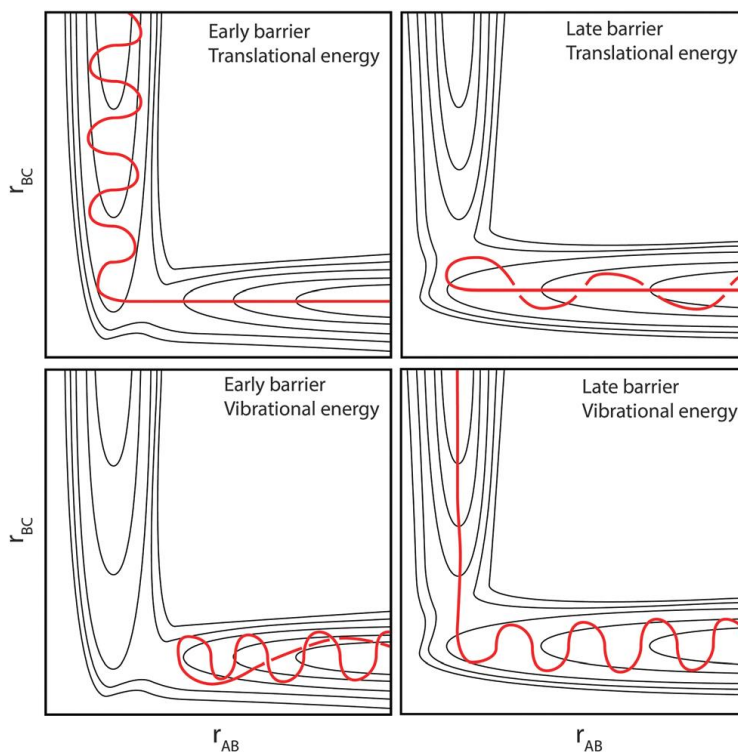


Figure 1.2 Potential energy surfaces of the reaction $A + BC \rightarrow AB + C$. Left panels show PES with an early barrier, i.e. the saddle point is located in the entrance valley, whereas the right panels present the late barrier type of PES. The top panels show the case of reagents entering the valley with only translational energy-yielding a vibrationally excited AB product. On the other hand, the bottom panels illustrate the cases where BC reagent is vibrationally excited leading to translation energy release. The red lines are the trajectories moving from right to left on the underlying PES. The figure is adapted from ref [20].

If the saddle point is located in the exit valley, the opposite dynamics will be observed. In the presence of a *late barrier*, the translational energy of the reactant AB does not allow to overcome the saddle point but simply be reflected back to the entrance valley by a potential well, as shown in the top-right panel. On the other hand, on the PES with a late barrier, vibrational energy couples the reagent to the product, as shown in the bottom right panel. In this case, the initial vibrational energy gives rise to product translational energy.

Although the simple 2-D model aims to describe binary collisions of diatomic molecules and atoms, the concept can be generalized to polyatomic molecules with more degrees of freedom. For the case of CH_4 chemisorption on Ni(111), it has been observed that the reaction can be promoted

by both incident translational and vibrational energy [22]. Further investigation shows that one quantum of the antisymmetric stretch mode of vibrational energy activates the CH₄ dissociation more efficiently than translational energy [23]. This reaction is therefore classified as possessing a late barrier. Different from diatomic molecules, the complexity of the system increases in the presence of vibrational modes in polyatomic molecules. Maroni and coworkers studied the mode-specific reactivity of CH₄ dissociation on Ni(100) and discovered that the reactivity of symmetric stretch mode ν_1 was about an order of magnitude higher than antisymmetric stretch mode ν_3 even though the energy of the two modes was almost identical ($\approx 3000 \text{ cm}^{-1}$) [24].

1.3 Review of state-to-state surface scattering

State-to-state surface scattering experiments prepare the incident molecules in a specific quantum state and resolve the final state distribution of the scattered molecules. The concept of this technique is to study gas/surface interactions in conditions with high degrees of control. With well-defined conditions such as kinetic and rovibrational energy of the incident molecules, crystalline structure, and surface temperature, the obtained results can be compared to theoretical models without the need for extensive averaging over initial and final quantum states. Furthermore, the effects of the above-mentioned parameters on scattering dynamics can be elucidated by monitoring the scattering patterns as a function of a certain scattering parameter. In practice, quantum-specific state preparation is done in a molecular beam due to the collision-free conditions. A molecular beam can be formed from a supersonic expansion of a gas from a high-pressure region into vacuum. The collisions in the expansion convert the random thermal energy of molecules into directed stream velocity with a narrow velocity distribution and will also cool the rotational degrees of freedom so that under optimal conditions only the lowest few rotational levels are populated. This property facilitates the excitation of a high portion of incident molecules to the desired quantum state by infrared laser pumping. Once excited by a narrow-band laser, the incident molecules remain in the stationary eigenstate until reaching the target surface. Without the collision-free conditions of the molecular beam, the state-prepared molecules would undergo rapid collision-induced relaxation. After the molecules scatter from the surface, a highly sensitive, state-selective detection method is needed to resolve the final state distribution. Popular techniques that satisfy these requirements are laser-induced fluorescence (LIF), resonantly enhanced multiphoton ionization (REMPI), and bolometric detection.

In 1981, Frenkel and coworkers studied the rotationally inelastic scattering of NO from Pt(111) using the LIF technique [25]. By analyzing the obtained LIF spectra, they found the rotational population follows a Boltzmann distribution with the rotational temperature $T_{\text{rot}} = 280 \text{ K}$, approaching $T_{\text{S}} = 290 \text{ K}$. The angular distribution of scattered NO displayed a cosine function. These two observations are the signature of scattering via trapping-desorption. Interestingly, the scattering patterns of NO on Pt(111) changed after covering the Pt(111) surface with an overlayer of graphite. Frenkel found that with the graphite layer, the scattered angular distribution became a lobular peak in the specular direction. Plus, the scattered rotational population did no longer follow a Boltzmann distribution. These two signatures suggested the scattering process from the graphite-covered surface was predominately direct. The graphite very likely reduced the depth of the

physisorption well to an extent that the incident NO molecules were no longer trapped in the well given the same amount of incident energy.

Again in 1981, Kleyn et. al. also used LIF to study the rotational inelastic scattering of NO, but from Ag(111) [26,27]. In their work, different scattering patterns were discovered. The angular distribution of scattered NO peaked near the specular direction. The measured final rotational distribution was separated into a low J part following Boltzmann distribution and a high J part showing a strong departure from Boltzmann behavior. It was found that the rotational excitations increased linearly as a function of the normal incident energy, but were insensitive to T_s . Taking into account these observations a direct scattering mechanism was concluded. The different scattering behavior of NO from Ag(111) than Pt(111) could be attributed to a relatively inert Ag(111) surface with a shallower physisorption well depth.

A few years later, Rettner and coworkers reinvestigated again scattering of NO from Ag(111) surface by REMPI [11]. This time they observed vibrational excitation ($v = 0 \rightarrow v = 1$) in a direct scattering process. The vibrational excitation probability was found to be strongly T_s dependent with an Arrhenius behavior of the observed activation, whereas the effect of incident kinetic energy on vibrational excitation was weak. The vibrational excitation appeared to be coupled to the deexcitation of thermal electron-hole pairs (EHPs) of the metal surface. Increasing kinetic energy then allowed the incident molecules to penetrate further into the electron cloud and facilitated the coupling between the molecular vibrations and the surface EHPs. The coupling of molecular vibration and EHPs can cause not only vibrational excitation but also relaxation. In 2000, Huang et. al. further investigated the coupling of NO vibrations and the EHPs on an Au(111) surface [12,28]. In this study, the incident NO molecules were state-prepared at a high vibrational level ($v = 15$). After scattered from the Au(111) surface, by detecting the final state distribution with REMPI, they found a significant vibrational relaxation from the initially prepared $v = 15$ down to $v = 5$, with the maximum population residing at $v = 7$. To confirm the relaxation was due to coupling to EHPs on the Au(111) surface, the second set of scattering experiments was performed on an insulating surface LiF. The incident NO molecules were state-prepared in $v = 12$. Different from the results measured on Au(111), after scattering from the LiF surface, the final vibrational distribution stayed mostly at the initially prepared $v = 12$. The comparison of NO scattering from metal and an insulating surface provided clear evidence that the molecular vibration could truly couple to EHPs. These electronically non-adiabatic behaviors questioned the validity of the Born-Oppenheimer approximation (BOA) in molecule/surface interactions and opened up a new field in surface reaction dynamics. Such vibrational excitations via an electronically non-adiabatic pathway were also observed in other molecule/surface scattering systems such as HCl and CO on Au(111) and N₂ on Pt(111) [29–32].

It is intuitive to consider that scattering patterns such as rotational population and angular distribution of molecules off surfaces can be sensitive to molecular structures. Scattering patterns were found to be strongly anisotropic for a heteroatomic molecule CO. In 1993, Hines et. al. used REMPI to study the scattering dynamics of CO from Ni(111) and observed scattered products via both direct scattering and trapping desorption pathways [33]. When a CO molecule is chemisorbed on a metal surface, it is known that CO bonds to the metal surface in a C-end down configuration

with the CO bond normal to the surface [19]. This preferential orientation is due to the electronic structure of CO where the reactive 5σ molecular orbital is essentially the lone pair localized on the C atom and the 2π molecular orbital is polarized toward the C-side. The 5σ and the 2π orbitals strongly interact with the metal d orbitals resulting in a strong CO-metal bond. At a near-surface normal position, the observed CO showed a Boltzmann distribution in the rotational population with the rotational temperature displaying a factor of 0.82 of the surface temperature and thus was considered as scattering via trapping-desorption. This trapping-desorption channel was interpreted as CO molecules collided the surface with the strongly attractive C-end. On the other hand, at the far superspecular position, the measured CO molecules showed non-Boltzmann behavior in their rotational distribution. The portions of high- J components increased with the incident kinetic energy and therefore was considered as molecules scattered via direct scattering. This channel was assigned as CO molecules that collided with the surface with the less attractive O-end. The energy of the highest observed J level was approximately the total incident kinetic energy but not just the normal kinetic energy, indicating the tangential force could also couple to the rotational excitation. It was thus suggested that the Ni(111) surface sampled by CO molecules must be corrugated.

State-to-state surface scattering experiments can also study stereodynamics at molecule/surface encounters by recording the REMPI signals as a function of laser polarization. Sitz et. al. studied the rotational inelastic scattering of N_2 from a clean Ag(111) surface by REMPI [34]. By measuring the rotational populations, the quadrupole, and the hexadecapole alignment moments of the scattered N_2 , they found that the scattered N_2 was highly aligned with its angular momentum parallel to the surface. Further investigation was carried out by studying the orientation of angular momentum (clockwise vs counterclockwise) of scattered N_2 from Ag(111) using an elliptically polarized laser [35]. Sitz et. al. found that the degree of orientation was strongly dependent on the rotational quantum number J and scattering angle. The presence of orientation in the scattering patterns indicated that there must have a tangential force involved during the scattering process. The observed rotational orientation could be qualitatively reproduced by a modified hard-cube model which took the tangential force into account. The source of the tangential force was then ascribed to the surface corrugation.

Thanks to the highly sensitive and state-selective detection of REMPI, a wide variety of surface scattering dynamics has been discovered as I have discussed above. However, it is obvious that most of the studies almost focus exclusively on diatomic molecules. State-resolved surface scattering studies of polyatomic molecules are still rare. Note that a state-resolved REMPI process requires a stable electronic excited state. Unfortunately, some of the polyatomic molecules such as CH_4 and CO_2 do not possess a stable lower-lying electronic state. Instead, they have a repulsive state which causes predissociation and therefore a short lifetime. As a consequence, only a broad absorption spectrum can be observed which is not state-resolved. Because of this reason, only ammonia, acetylene, and formaldehyde have been studied by REMPI [36–40].

Using REMPI detection, Kay et. al. studied the surface scattering of NH_3 on Au(111) and observed multi-quantum vibrational excitation of the ν_2 umbrella mode [40]. It was found that the vibrational excitations appeared when the normal component of incident kinetic energy E_{\perp} slightly exceeded the energy of the vibrational level being excited. The excitation probability was found

to be scaled linearly with E_{\perp} but independent of T_S , indicating a translational to vibrational energy conversion ($T \rightarrow V$). Taking into account all these observations, Kay and coworkers concluded that the vibrational excitation happened via an electronically adiabatic collisional mechanism. This excitation mechanism is fundamentally different than what was observed in the NO/Ag(111) system whose vibrational excitation mechanism is believed to be electronically non-adiabatic. Besides vibrational excitations, they found a propensity for rotational distribution populated in low K states. For a given J level, if one observed $K = J$, it means the molecule is spinning with the axis of rotation along its symmetric axis. For NH_3 , it corresponds to the 3-fold symmetric axis. However, the observed propensity of scattering into low K indicates that the NH_3 molecules preferentially spin in an end-over-end tumbling rotation.

Translation-to-vibration excitation was also observed in acetylene scattering from Au(111). In this system, Golibrzuch et. al. observed excitations of one and two quanta of the ν_4 trans-bending mode [39]. The excitation probability increased linearly as the incident translational energy. Similar to what has been observed in the $T \rightarrow V$ excitation of NH_3 on Au(111), the vibrational excitations appeared when the incident kinetic energy slightly exceeded the energy of the vibrational level. This slightly higher energy was considered as the amount of translational energy transferred to surface phonons and therefore not available to excite vibrations.

In 2017, Park et. al. used REMPI to study the surface scattering of formaldehyde from Au(111) which was the first report of state-resolved measurement of an asymmetric top molecule [37,41]. at the low incident kinetic energy of $E_i = 0.1$ eV, the scattering was dominated by trapping-desorption. The rotational distribution showed Boltzmann behavior with the rotational temperature similar to the surface temperature. As E_i increased to 0.3 – 1.2 eV, the scattered products came mostly from direct scattering. As an asymmetric top molecule, formaldehyde has 3 rotational axes corresponding to three distinct moments of inertia. After analyzing the REMPI spectra of the scattered formaldehyde molecules, they found the scattered formaldehyde preferentially spun along the a-axis (CO bond axis), corresponding to the twirling motion.

For some small polyatomic molecules such as CH_4 and CO_2 that can not be measured by REMPI with an internal-state resolution, a different technique was applied for state-resolved measurements. In 1998, Wight and Miller used a bolometer detector in combination with IR laser tagging of the scattered methane to detect the state distribution of CH_4 scattered from a LiF surface [14]. At the specular angle, the measured rotational population followed Boltzmann distribution with the rotational temperature $T_{\text{rot}} = 240$ K, slightly lower than the surface temperature $T_S = 300$ K. In the angular distribution of scattered CH_4 , they observed evidence for “rainbow scattering” which is referred as preferential final scattering angle of molecules caused by surface corrugation. The measured angular distribution showed a structured feature with two local maxima. These two maxima were interpreted as molecules colliding with the lowering and the rising parts of the corrugation, resulting in forward and backward scattering, respectively. Using the same setup, Wight and Miller also studied vibrational quenching of linear polyatomic molecule acetylene scattered from LiF(001) [15]. The incident acetylene molecules were prepared in one quantum of ν_3 antisymmetric stretch mode. By monitoring the scattering signals, they found no significant vibrational quenching on the directly scattered acetylene and even on trapping-desorbed products

at $T_S = 300 - 580$ K. Measurable quenching signature was observed for the trapping-desorbed products at a low surface temperature of 145 K.

State-resolved measurements of scattered CO_2 from a liquid surface were reported by Perkins et. al. using direct IR absorption spectroscopy [42]. Their scattering experiments were carried out on a series of perfluorinated, hydrocarbon, and hydrogen-bonded liquids. By analyzing the state populations and the absorption profiles of the Doppler velocimetry, Perkins was able to distinguish scattered products via direct scattering and trapping-desorption. The fraction of these two channels was found to be dependent on incident kinetic energy and type of liquids. The stereodynamics of this system was investigated by measuring the distribution of M_J states [43]. Practically, it was achieved by recording the difference of absorption signals measured by right and left circularly polarized light, namely the circular polarizance. Using this method, Perkins et. al. discovered that the scattered CO_2 from perfluoropolyether liquid surface showed a propensity of forwarding end-over-end spinning. This propensity increased strongly as a function of rotational quantum number J .

Although state-resolved measurements of scattered CH_4 and CO_2 are available, the scattering experiments are not carried out on catalytically active metal surfaces in both Miller's and Perkins' experiments. Because the vacuum conditions in their setups are not sufficient for maintaining a clean metal surface, their studies study scattering from inert surfaces. In Miller's works, most of the surface scatterings are measured on LiF and NaCl [44–46]. In Perkins's setup, to keep the liquid surface clean, a renewable liquid surface is formed by a rotating glass wheel which is partially submerged in a liquid reservoir. The choices of liquids are also limited to species with low vapor pressure to keep the vacuum conditions. The information gained from surface scattering experiments performed on inert surfaces is limited to energy transfer. Another important motivation for studying molecule/surface interactions is to study the reactions involved in heterogeneous catalysis for testing theoretical models and the development of improved catalysts. Therefore it is highly desirable to study surface scatterings on catalytically active metal surfaces.

1.4 State-to-state surface scattering of CH_4 from Ni(111)

As part of Van Reijzen and Werdecker's Ph.D. work, our group implemented the bolometric infrared laser tagging to study the state-to-state surface scattering of CH_4 following Miller's setup. In Miller's setup, the capabilities of the bolometric detection were limited not only by the vacuum conditions in their setup but also by the absence of a high-power mid-IR laser. For efficient optothermal detection, a high degree of saturation in excitations of scattered molecules is required. Unfortunately, a tunable and high-power IR laser was not available back in the 1990s. Due to the development of fiber amplifiers, high-power, tunable single-mode CW-IR OPOs have become available in 2010. The high-power, coherent and tunable IR radiation enables one to saturate the tagging transitions and prepare a large fraction of the incident and scattered molecules which greatly improves the sensitivity of the bolometric detection. Using this advantage, Van Reijzen and Werdecker implemented the bolometric detection technique with high power CW-IR OPOs to study state-to-state CH_4 scattering from Ni(111) and discovered unprecedented dynamics [16–18].

In our state-to-state study, the incident CH₄ was prepared with one quantum of ν_3 antisymmetric stretch mode and in the rotational state with $J = 1$. After scattering from a 673 K Ni(111) surface, we measured significant rotational excitation populating rotational levels up to $J = 8$. The rotational distribution was non-Boltzmann with the highest population in the initially prepared $J = 1$. Besides rotational excitations, we observed “surface-induced” vibrational energy redistribution where the initially prepared antisymmetric stretch mode (ν_3) of CH₄ redistributed to symmetric stretch mode (ν_1) in a direct scattered process. The branching ratio of the vibrational redistribution ν_1/ν_3 was measured to be ≈ 0.4 . This observation then brings up a question. “Is the surface-induced vibrational energy redistribution dependent on the type of surface atoms?” Further investigation confirmed that the vibrational energy redistribution is “surface dependent”. We found that by growing a layer of graphene on the clean Ni(111) surface, the $\nu_3 \rightarrow \nu_1$ redistribution was no longer observed [47]. Different than a clean Ni(111) surface, graphene-covered Ni(111) surface is considered as a catalytically inert surface. Our observation, therefore, indicates that the $\nu_3 \rightarrow \nu_1$ conversion efficiency reflects the catalytic activity of the surface which is supported by the quantum dynamics calculation of Bret Jackson on reaction path Hamiltonian PES. These results indicate that by observing the vibrational energy redistribution in the scattered molecules, the BILT technique can serve as a probe of surface catalytic activity. The exploration of the nature of the surface-induced vibrational energy redistribution remains an ongoing project in our group.

1.5 Limitations of the previous setup

So far I have shown some novel and interesting results on CH₄ scattering obtained by the BILT technique. However, as documented in Van Reijzen and Werdecker’s Ph.D. theses, the capabilities of the BILT technique were limited due to several reasons. The first reason was the fact that the sum of the incident and scattering was fixed at 135° relative to the incident molecular beam direction because the bolometer detector had to be attached to a fixed port on an existing UHV apparatus (our “old” machine). Due to this, angular distributions could be measured only by rotating the sample surface which changed the incident and the scattering angle simultaneously. Furthermore, due to the fixed detection angle of 135°, the scattering experiments were limited to a shallow incident angle of 65°, which limited the component of incident energy along the surface normal ($E_{\perp} = E_i \cdot \cos^2(65^\circ) = 0.178 \cdot E_i$). Since the probability for methane dissociation is known to scale with E_{\perp} , the state-to-state scattering experiments in this apparatus were limited to nonreactive conditions where E_{\perp} is much lower than the 1 eV barrier height for methane dissociation on Ni(111).

The second limitation was due to the lack of UHV compatibility of the bolometer detector produced by IRLabs. The first version of the bolometer detector produced hydrocarbon outgassing which was most likely coming from the non-UHV compatible adhesive used in the construction. This outgassing then reduced the cleanliness of the UHV chamber. To keep the Ni surface clean throughout the experimental time scale, we needed to heat the surface at 673 K such that carbon contaminants could be dissolved into the bulk crystal immediately. Therefore our surface scattering experiments were limited to high surface temperatures T_S . This limitation prevented us from studying scattering dynamics over a broad surface temperature range.

1.6 Design of a new state-to-state surface scattering apparatus

To overcome the aforementioned limitations of the first experimental setup, we designed a new apparatus dedicated to state-to-state surface scattering using the BILT technique. In the remainder of the thesis, I will refer to the new apparatus as the “BILT machine”. The design and the construction of the BILT machine were accomplished with invaluable help from Prof. Daniel Auerbach, who visited our lab repeatedly during the construction and testing of the BILT machine. A very useful feature of this new machine is the fact that the bolometer detector is installed on a differentially pumped rotatable lid, which allows us to move the bolometer detector while maintaining UHV conditions in the scattering chamber and in this way to record angular distributions of the scattering molecules for a fixed angle of incidence. Furthermore, the BILT machine contains a custom bolometer detector which was modified from the standard version offered by the manufacturer Infrared Laboratories and is manufactured from UHV compatible materials. With this, we expected to reduce the problem of hydrocarbon outgassing that we have encountered in the old setup. The third improvement is the much shorter sample-to-detector distance which was reduced from 360 mm to 81 mm. Assuming a $1/r^2$ dependence of the scattered molecule flux, we expect an increase in bolometer signal by a factor of 20 and thus much higher detection sensitivity. Finally, although it has not been realized during my Ph.D. work, the design of the BILT machine includes a Doppler velocimetry which will enable us to state-selectively measure the velocity of scattered molecules. In the next chapter, I will give a detailed description of the design of the BILT machine.

During my Ph.D. work, our group acquired a new tunable IR OPO (TOPO, Toptica) which provides a broader frequency tuning range (2200 – 4000 cm^{-1}) than offered by a single module of the Argos OPO that we had been using so far as tagging laser. In addition, the wavelength tuning of TOPO can be computer-controlled, which makes it possible to automate the state-resolved detection of scattered molecules by infrared laser tagging. The postdoctoral researcher Dr. Christopher Reilly developed a suite of python programs that enable the TOPO idler wavelength to find and probe a list of tagging transitions in an automated way which greatly reduces the time needed to measure the quantum state distributions of the scattered molecules.

1.7 Outline of this thesis

Since my Ph.D. project was centered on the design, construction, and application of the new BILT machine, a major part of this thesis is dedicated to its description and characterization. I will explain how we realize state-selective detection of scattered molecules using a bolometer in combination with infrared laser tagging. To demonstrate the capabilities of the BILT machine, I continue the work on methane/surface scattering initiated by Maarten Van Reijzen and Jörn Werdecker and report a detailed study of rotationally inelastic scattering of CH_4 from a Ni(111) surface. The remainder of this thesis is organized in the following way:

In chapter 2, I start by describing the design of the BILT machine. An overview first provides readers with a comprehensive understanding of the BILT machine. The different components of the machine will be discussed individually starting with the molecular beam source, the main scattering chamber, the rotary lid on which the bolometer is mounted, the differentially pump rotary seal of the lid, the surface sample mount on a 3-axis manipulator, the LEED and Auger spectrometers, and the bolometer detector. After introducing the design of the BILT machine, I present the vacuum conditions of the machine and the performance of the rotary seal. Later, I show the functions of surface preparations and characterizations. The working principle and the calibrations of time-of-flight measurements for characterizing molecule beams are also included in this chapter. A big portion of this chapter is dedicated to introducing and testing the new bolometer detector. Finally, I will describe the configuration of our laser setup. Since a new widely tunable OPO tagging laser was installed as a tagging laser during my Ph.D. work, I will explain the computer programmed frequency tuning algorithm and the new method of locking and scanning the tagging laser frequency.

In chapter 3, I start by describing the concept of the bolometric infrared laser tagging technique and how we convert the measured bolometer signals to the populations of the corresponding states. Then, I explain why the excitation method “rapid adiabatic passage” which has been implemented in the old setup is not applicable in the BILT machine and propose an alternative for efficient tagging of the scattered molecules. Finally, I provide an overview of CH₄ infrared spectroscopy relevant to our laser tagging.

To demonstrate the capabilities of the BILT machine, in chapter 4, I present the results of a state-to-state study of CH₄ rotational inelastic scattering from Ni(111). This topic is continued from the Ph.D. work of Werdecker. In my work, I extended our understanding of rotational excitation using the improved features of the machine. Using the variable scattering geometry of the BILT machine and the different seeded ratio of the incident beam, I study the effects of the parallel and the normal component of incident kinetic energy independently on the rotational excitation in a direct scattering process. The rotational distributions of scattered CH₄ were also measured over a broad T_s range to investigate the effects of surface thermal motions.

In chapter 5, I describe the results of the vibrational energy transfer during the direct scattering of methane from clean and graphene-covered Ni(111) and how the observed vibrational energy transfer depends on the catalytic activity of the scattering surface.

In the final chapter 6, I summarize the results presented throughout this thesis. Finally, I suggest several topics that can be potentially studied in the future by the BILT machine.

Chapter 2 Experimental setup

2.1 Overview

This chapter describes the setup of our bolometric detection method for scattered atoms/molecules, in particular, the design of the BILT machine as the development and construction of the apparatus is the main part of my Ph.D. work.

Figure 2.1 shows a schematic of our state-to-state gas/surface scattering experiments. A continuous supersonic jet expansion is generated by expanding gas from high pressure into a vacuum through a nozzle with a 60 μm diameter opening. The expansion is sampled by a 1 mm diameter skimmer producing a molecular beam with a narrow velocity distribution. Before the molecular beam collides with a Ni(111) surface, radiation from an infrared optical parametric oscillator (IR-OPO) prepares the molecules in a specific rovibrationally excited eigenstate. After scattering from the Ni(111) surface, the internal-state distribution of scattered molecules is interrogated by a second IR-OPO before arriving at the bolometer detector. Modulation of the tagging laser, either by amplitude or frequency combined with lock-in detection of the bolometer signal, allows for state-selective detection of the scattered molecules. To aid in the alignment, and for characterization of the internal states distribution of the incident molecular beam, a pyroelectric detector attaching to translational feedthrough is located in the third differential pumping stage. A chopper disk of 1% duty cycle spinning at 200 Hz can be used to modulate the molecular beam for time-of-flight measurements of the velocity distribution or molecular beam intensity-modulated scattering experiments.

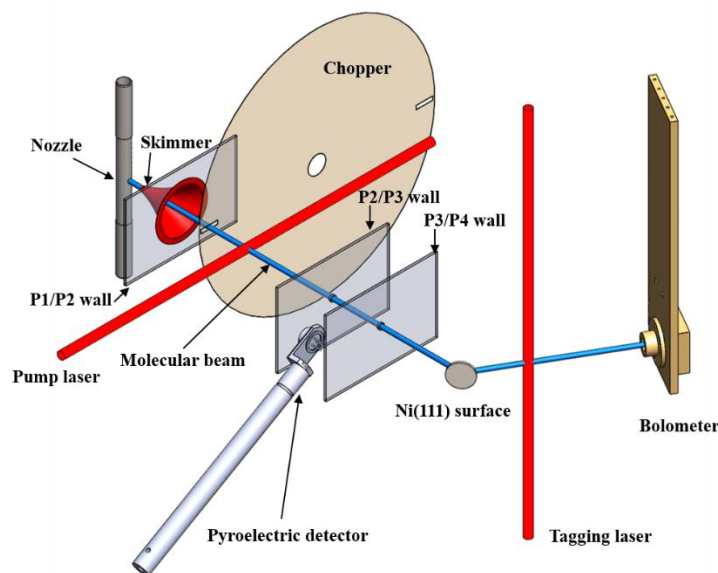


Figure 2.1 Schematic diagram of state-to-state gas/surface scattering experiments. The P1/P2, the P2/P3, and the P3/P4 walls separate the four differential pumping stages.

To unleash the power of the bolometric detection technique, I designed and assembled an apparatus dedicated to state-to-state surface scattering experiments with help from Prof. Auerbach. As shown in Figure 2.2, the machine consists of a source chamber (P1), 2 differentially pumped stages (P2 and P3), and a UHV chamber (P4) for surface preparations, characterizations, and scattering experiments. The core of the machine, the bolometer detector, is installed on a rotatory platform. The platform is mounted on ball bearings with 3 spring-loaded Teflon O-rings separating 2 differentially pumped stages which allow maintaining UHV conditions in P4 during rotation of the platform. The scattering target, in the present work a 10 mm diameter Ni(111) sample, is mounted on a rotatory sample mount which includes sample cooling by liquid nitrogen and e-beam heating by a W-filament located behind the sample. Separate rotation of the bolometer detector and the target surface allows for independent variation of the incident and the scattering angle. For target surface preparations, a sputter gun is used for Ar-ion sputtering. Following surface preparation by sputtering and annealing, the surface composition and the crystal structure can be characterized in-situ by Auger electron spectroscopy (AES) and low energy electron diffraction (LEED), respectively. To move the sample into different positions for scattering, AES, and LEED measurements, the sample mount is connected to a commercial X-Y-Z manipulator from Metallic Flex. Below, I define the x, y, and z axes of width, height, and length of the machine, respectively. I will follow this definition in the rest of the thesis.

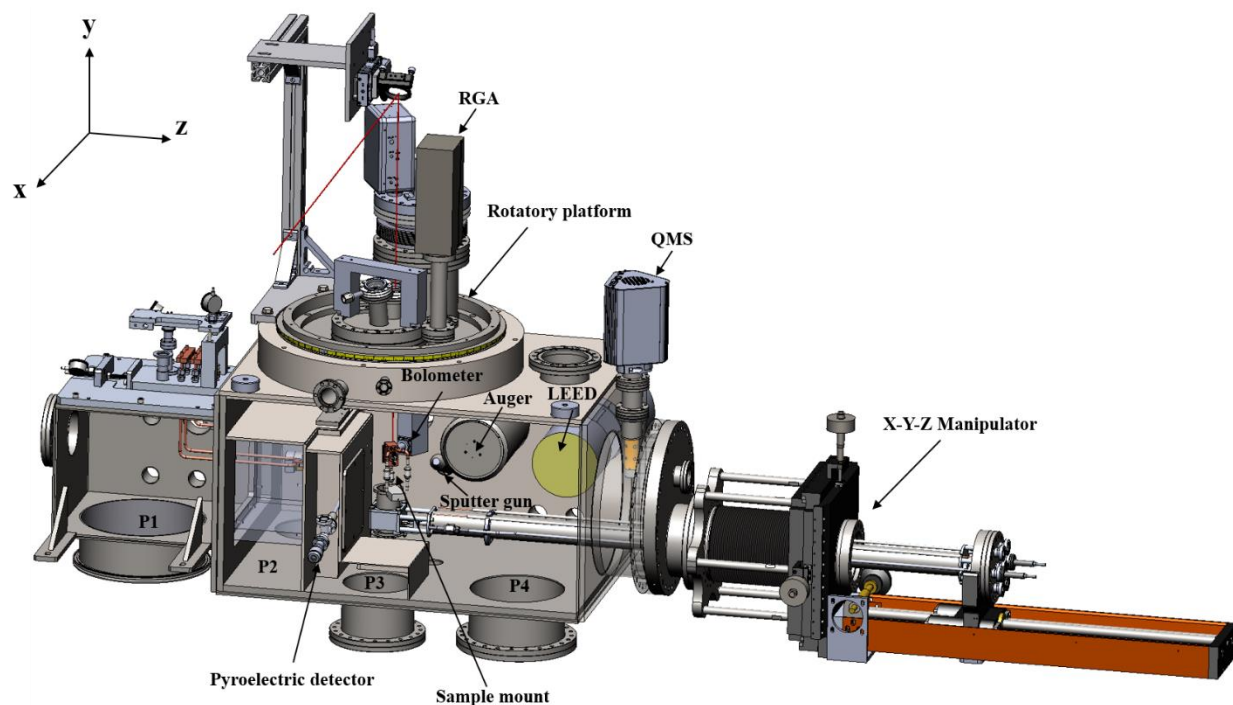


Figure 2.2 3D model of the BILT machine (Solidworks). The front wall of the model is transparent in order to show the internal components of the apparatus. See text for the functions of all the components. Pumps, cables, and pressure sensors are not shown in this model.

Two quadrupole mass spectrometers (QMS) are installed in the UHV chamber. The first, an SRS RGA 100, which is mounted on a CF40 port of the rotatory platform, is used for residual gas analysis and to monitor the molecular beam flux into the UHV chamber. The second QMS (Pfeiffer QMG 220) is mounted such that its crossbeam ionizer intercepts the molecular beam for TOF measurements of its velocity distribution.

In the remainder of this chapter, I will give a detailed description of the different components of the machine in the following order:

❖ **Source chamber**

Structure of the source chamber

Molecular beam source

Time-of-flight measurements and calibration

❖ **Main chamber**

Overview of the chamber

Vacuum conditions

Top hub and the rotatory platform

Pyroelectric detector

Sample mount and manipulator

Sample preparation and characterization

❖ **Cryogenic bolometer**

Overview

Characterization and modification

❖ **Laser setup**

2.2 Source chamber

The source chamber houses a heated nozzle source which is used to produce a supersonic expansion of either the pure sample gas (methane) or the same gas diluted in helium carrier gas. A 1 mm diameter skimmer (Model 2, Beam Dynamics) mounted on the back wall of the source chamber transmits a molecular beam of controlled kinetic energy into the second pumping state P2. As shown in Figure 2.3 the source chamber is a 360 mm x 320 mm x 280 mm stainless steel box made by the ISIC machine shop. On its front side, a CF100 viewport provides visual access to the nozzle source and a He-Ne laser that can be used as a tracer of molecular beam direction. The side walls each contain three CF40 and one CF63 port for pressure gauges and electrical feedthroughs. On the bottom, a 2000 L/s turbo molecular pump (Edward STP-iXR2206) is installed via a DN250 ISO-K connection. The source chamber attaches to the main chamber through an O-ring (Parker 2-463 Viton) sealed rectangular flange with two 12 mm diameter dowel pins defining its position on the main chamber. The source chamber is mounted on two rails with linear motion bearings and can be retracted from the rest of the apparatus for easy access to the skimmer and chopper motor in P1 and P2. The nozzle XYZ manipulator is installed on the top of the source chamber on a sliding aluminum plate which is sealed via an O-ring (Parker 2-457 Viton). A heated nozzle tube with a 60 μm diameter pinhole is clamped by two water-cooled copper blocks connecting to an L-shape arm of the source manipulator which allows for alignment of the nozzle relative to the fixed skimmer.

To minimize the source-to-sample distance, thus maximizing the molecular beam intensity at the sample, a rectangular aluminum extension (P1 extension) is added to the back of the source chamber. This extends the volume of the source chamber toward the main chamber and reduces the nozzle-to-target surface distance. At the end of the P1 extension, a stainless steel rectangular plate (skimmer mounting plate) covers the source chamber and defines the boundary between the first and the second pumping stages P1 and P2. The junctions between the source chamber/P1 extension and the P1 extension/skimmer mounting plate are again O-ring sealed (Parker 2-278 Viton). An electroformed commercial skimmer from Beam Dynamics is mounted on the cover plate to sample the central part of the supersonic jet expansion.

Since the size and the direction of the molecular beam are defined by the position of the skimmer and the apertures at the P2/P3 and the P3/P4 wall, precisely positioning the skimmer is crucial. To precisely define the relative position between the skimmer and the source chamber, there are 6 mm diameters dowel pins inserted into well-defined 6 mm diameters dowel holes at the skimmer mounting plate/P1 extension and the source chamber/P1 extension junction. Referring to the relative position between the source chamber and the main chamber, two 12 mm diameters dowel pins insert into the 12 mm dowel holes (with international tolerance grade H7) at the rectangular flange of the source chamber and the corresponding face of the main chamber align the source chamber assembly to a place. After assembling the entire source chamber and attaching it to the main chamber, the skimmer position is measured to be less than 0.1 mm away from the molecular beam axis defined by the alignment jigs mounting on the front and the backside of the main chamber.

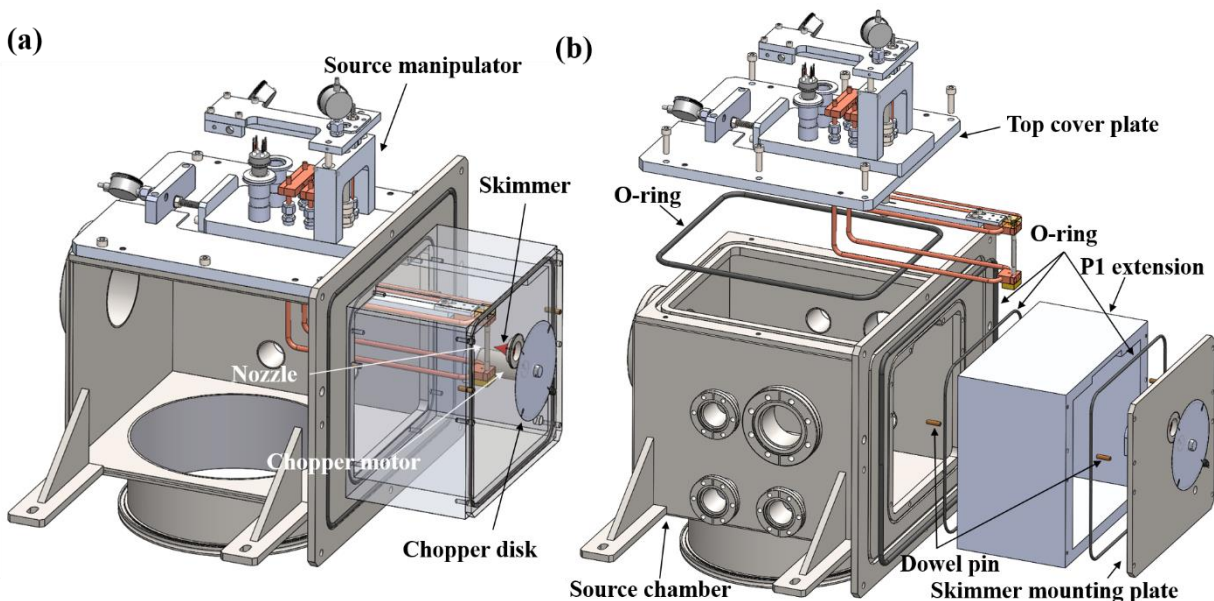


Figure 2.3 (a) 3D model of the source chamber. For visibility, some parts of the chamber are made transparent. (b) Exploded view of the source chamber assembly. The entire assembly consists of the source chamber, the top cover plate, the P1 extension, and the skimmer mounting plate. The junctions between these parts are sealed by Viton O-rings.

2.2.1 Molecular beam source and nozzle source

The expansion nozzle for the BILT machine differs from those used in the other two machines in the lab which are equipped with an axially mounted nozzle tube with a pinhole drilled at the end of the tube [48,49]. The nozzle design for the BILT machine is inspired by a high-temperature supersonic molecular beam source developed by Auerbach et. al. in 1991 [50]. The original molecular beam source allows for a tungsten nozzle to be heated to more than 2300 K. Since such high temperatures are not needed in our application, we simplified the original design. The advantage of the current design, compared to the nozzles used in the two other machines, is the fact that the nozzle tube is a simple straight metal tube with a laser-drilled hole in the center and which itself requires no welding. This allows the nozzle to be made from different materials in order to prevent degradation of the sample gas at high-temperature operation.

Figure 2.4 (a) shows a drawing of the nozzle tube with a 50 μm diameter of orifice. However, the actual laser-drilled orifice was measured to be 60 μm by an optical microscope. The wall thickness of the central part of the tube was reduced to localize the ohmic heating near its orifice as shown in Figure 2.4 (b). In addition, the thin wall provides optimal conditions for an isentropic supersonic expansion.

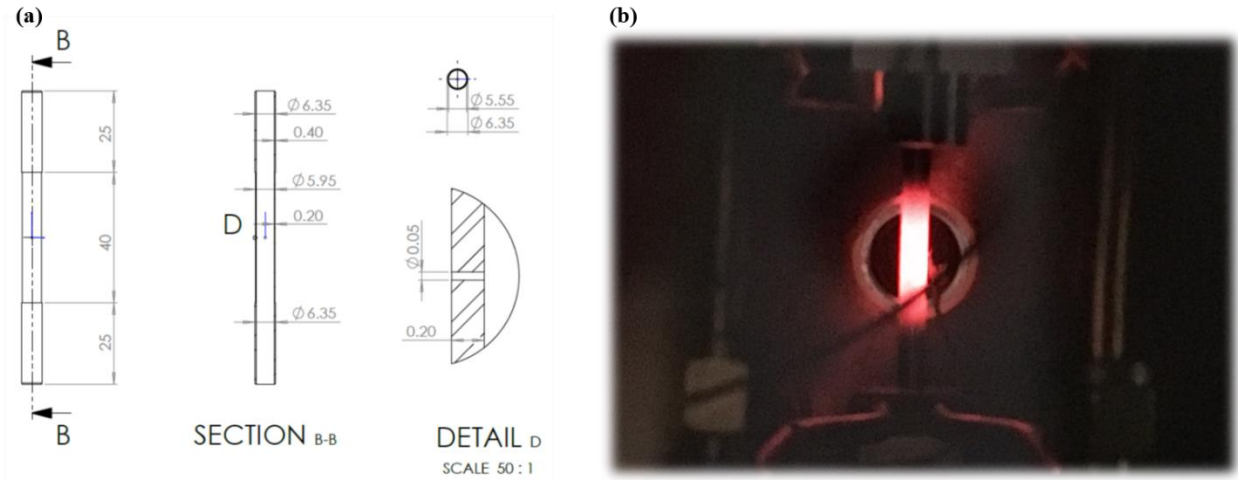


Figure 2.4 (a) Design of the expansion nozzle. Round tube with $\frac{1}{4}$ " OD and 0.4 mm wall thickness 0.4 mm which is reduced to 0.2 mm near the center. (b) Photo of the hot nozzle with $T_n=1200$ K. Only the central part with reduced thickness and thus higher resistance is glowing while the ends are clamped by water-cooled copper blocks.

The nozzle tube is mounted by clamping it between two copper blocks. As shown in Figure 2.5 (a) and (b), each copper block is water-cooled via two $\frac{1}{4}$ " copper tubes. To seal the openings on both sides of the nozzle tube, two brass blocks cover the ends with Viton O-rings seals. On the top brass block, a $\frac{1}{8}$ " copper tube acts as the gas inlet of the nozzle. For resistive heating of the nozzle tube, a DC current is applied via the copper cooling lines which are mounted through insulating $\frac{1}{4}$ " Swagelok fittings (Swagelok, NY-400-1-4 BT) on the base plate. The top copper is attached by an adjustable connecting bridge to the arm of the source manipulator. At the junction between the bridge and the copper block, we place four nylon washers as electrical insulators. Also, we use nylon screws to fix the copper block on the bridge. With this configuration, the heating circuit is properly insulated from the source manipulator.

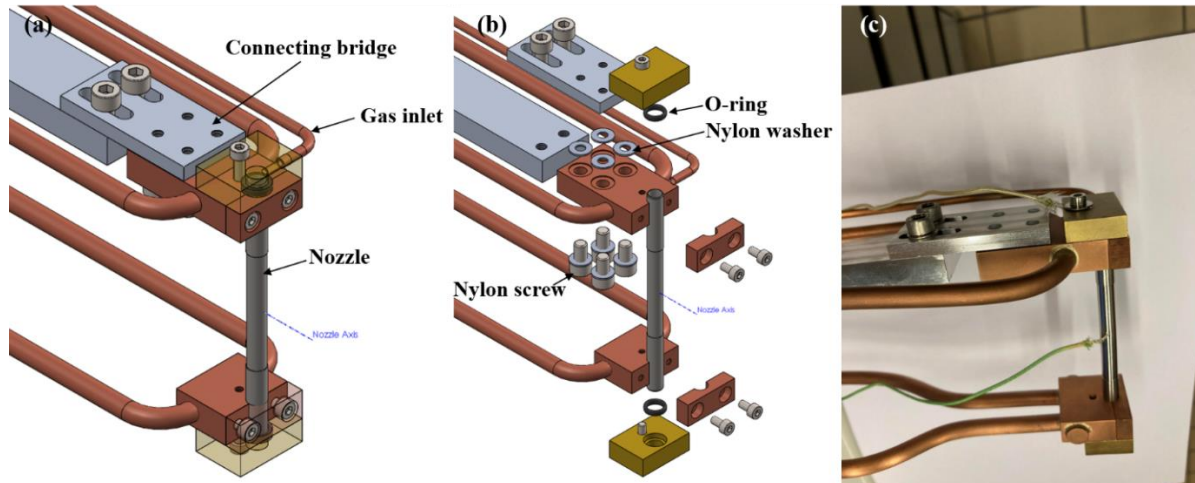


Figure 2.5 (a) 3D model of the nozzle and its holder. The top and the bottom brass blocks are made transparent to illustrate the O-ring sealed configuration inside. (b) Exploded view of the 3D model. Four nylon washers sit between the top copper block and the connecting bridge for electrical insulation. (c) the real object of the nozzle assembly. Two thermocouples are used, one is spot-welded to the side of the nozzle for measuring the nozzle temperature, and the other one attaches to the top brass block. Different than the 3D model, on the bottom copper block, the copper tubes are brazed from the back instead of from the side. We made this modification because the copper tubes interfered with the chopper motor in the original design.

In the center of the nozzle tube, a K-type thermocouple was spot welded for measuring the nozzle temperature, as shown in Figure 2.5 (c). A second K-type thermocouple attaches to the top brass block, in order to monitor the efficiency of the water cooling. With a cooling water flow of 200 liters/hour, the temperature of the brass block remains at room temperature while the central part of the nozzle is heating at 1200 K. The two thermocouples link to a CF16 2 pairs thermocouple feedthrough.

The nozzle heating current of up to 125 A is supplied by a DC current supply (Sorensen, DCS 8-125) which is regulated by a programmable temperature controller (Stanford Research Systems, PTC10). The SRS temperature controller reads the nozzle tube temperature via the attached thermocouple and uses PID control to generate a 0-10 V control voltage which results in a heating current of 0-125 A generated by the current supply. Figures 2.6 (a) and (b) show how the water cooling copper tubes are connected on the air side via two copper clamps to electrical cables of 6 mm diameter. Using the setup described the nozzle tube can be heated to 1200 K with 40 W of electrical power. Figure 2.7 shows the power needed to heat the nozzle from room temperature to 1200 K. We use 1/4" Teflon tubes to supply the cooling water manifold via brass Swagelok connectors. The two other existing machines use 1/8" tubes internally to deliver cooling water to the nozzle mount which limits the cooling water flow and provides a poor cooling efficiency. In this condition, cooling down the nozzle from 700 K to 300 K can take almost an hour. To improve the cooling efficiency, I chose to use 1/4" diameter copper tubes inside the BILT machine which reduces the nozzle cooling time from an hour to about 10 minutes.

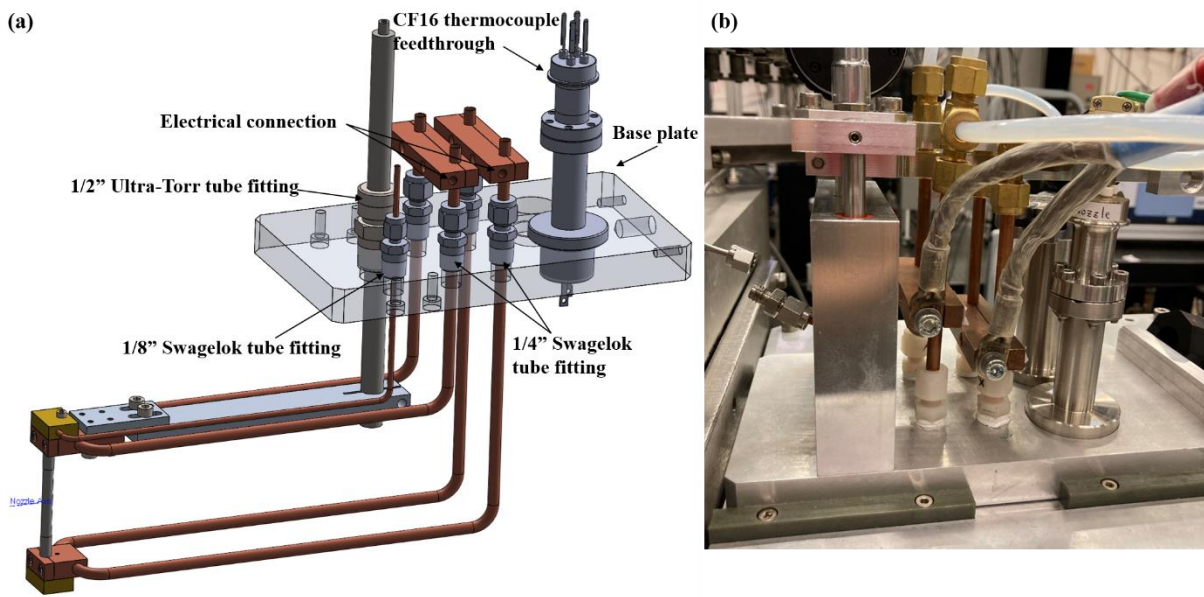


Figure 2.6 (a) 3D model of the nozzle tube mounting. For visibility, some parts of the source manipulator are removed in this model. On the base plate, there are four $\frac{1}{4}$ " Swagelok to $\frac{1}{4}$ " NPT nylon tube fittings (Swagelok, NY-400-1-4 BT) used as feedthoughts for the $\frac{1}{4}$ " copper water cooling tubes. A $\frac{1}{8}$ " Swagelok to $\frac{1}{4}$ " NPT nylon tube fitting is used for the $\frac{1}{8}$ " copper tube which delivers gas from a source manifold. (b) A photo of the fittings on the base plate.

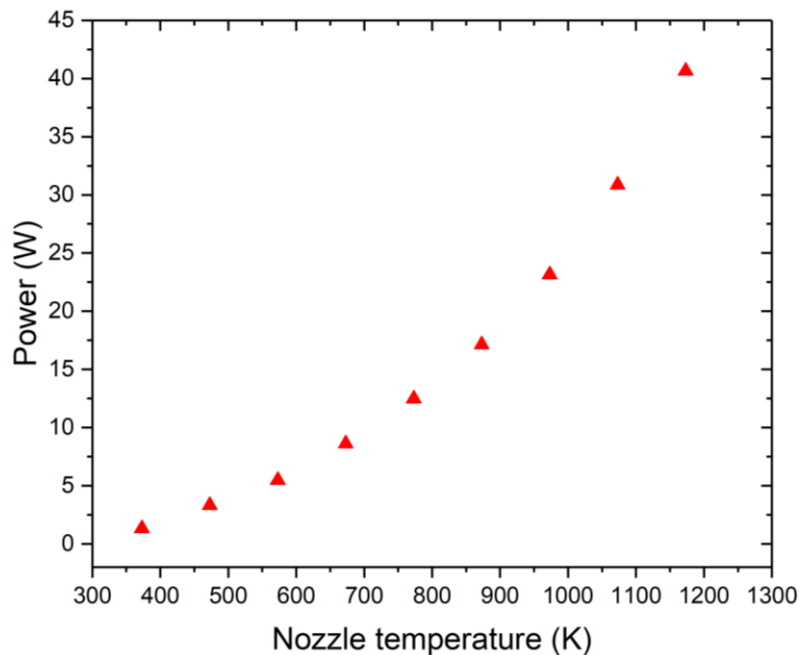


Figure 2.7 Heating power vs. nozzle temperatures from 300 to 1200 K. See text for the detail of the nozzle heating setup.

So far, I have explained the design of the nozzle, the structure of the mounting, and the heating and cooling setup. Next, I move on to describe the structure of the source manipulator which provides 3 axes motion to adjust the nozzle position. The z-motion, which is along the molecular beam axis, adjusts the nozzle-to-skimmer distance. The source manipulator is mounted on top of the cover plate of the source chamber on a Viton O-ring (Parker, 6-1390) seal, as shown in Figure 2.8 (a). The top cover plate is machined down in thickness at the contact area with the source manipulator. This area serves as a rail for a sliding motion in the Z-direction of the source manipulator. The cover plate is machined with a rectangular opening to accommodate the source and its tubings. Given the area of the opening 165.5 cm^2 , under 1 bar of pressure, this provides 1655 N of force exerting on the cover plate. A Z-drive mechanism allows the source manipulator to slide along the z-axis. Figure 2.8 (b) and (c) show the structure of the Z-drive mechanism consisting of an M8 threaded rod, a Z-drive block, and bearing housing. One end of the M8 threaded rod penetrates the bearing housing and is held by two nuts. Inside the bearing housing, we use thrust bearings to support the large axial force need to overcome the friction between the sliding plate and a cover plate when the Z-drive is moving the source manipulator. The other end of the threaded rod is connected to the Z-drive block which is attached to the base plate of the source manipulator. With the bearing housing fixed on the top cover plate, rotation of the threaded rod will translate the source manipulator along the Z-direction.

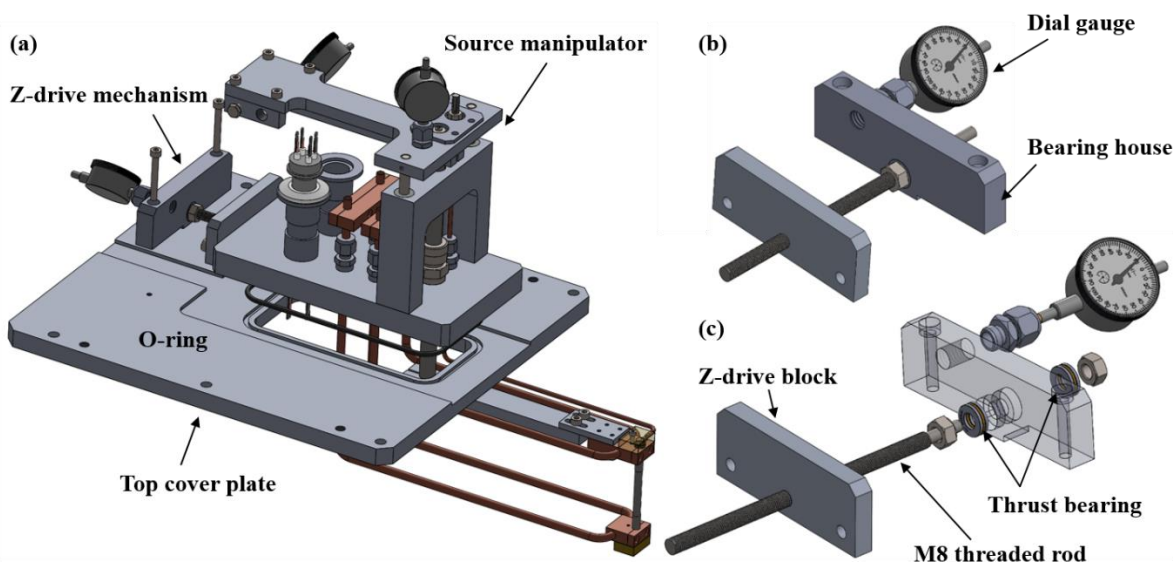


Figure 2.8 (a) 3D model of the source manipulator and the top cover plate of the source chamber in exploded view. (b) 3D model of the Z-drive mechanism. (c) Exploded view of the 3D model. the bearing housing attaches to the top cover plate and holds an M8 threaded rod by two nuts. Two thrust bearings (AST, F8-16M) located between the nut and the bearing house allow for rotation of the threaded rod which drives the Z-drive block and the source manipulator.

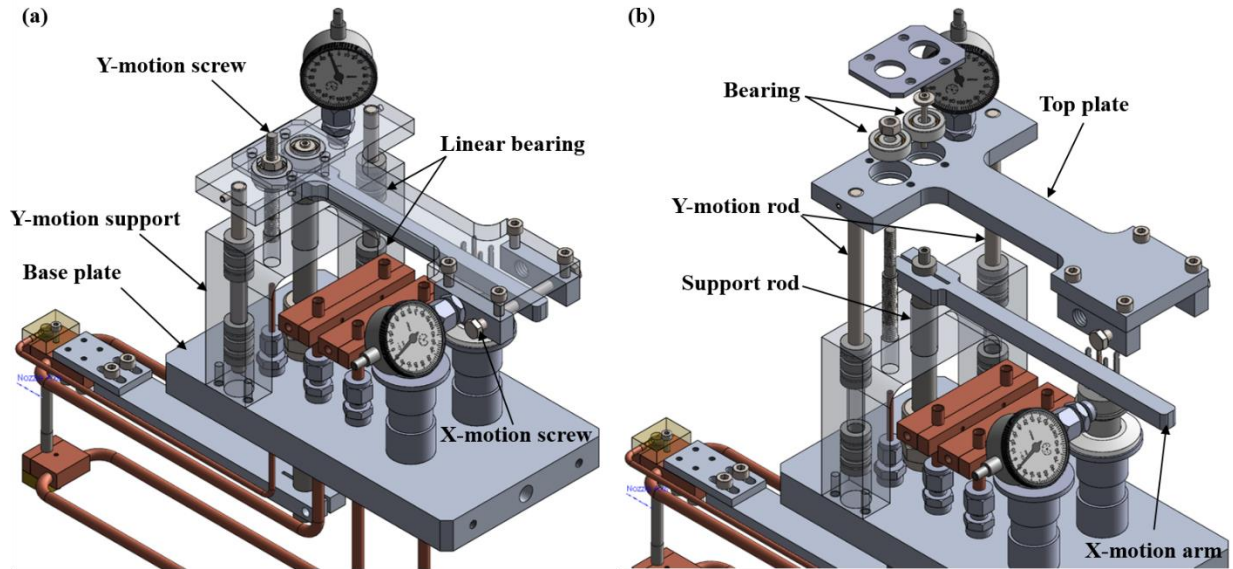


Figure 2.9 (a) 3D model of the source manipulator. To illustrate the detail near the bearings, some parts are made transparent. Two linear bearings are located in each leg of the Y-motion support. Two Y-motion rods from the top plate inserted into the bearings align the Y-motion. (b) Exploded view of the 3D model. The top plate accommodates two bearings (AST, 636H), one constrains the motion of the support rod, and the other constrains the Y-motion screw.

As shown in Figure 2.9 (a) and (b), the nozzle and copper block assembly attaches to an arm that clamps to a support rod. This rod is held on the base plate by a bored-through $\frac{1}{2}$ " Ultra-Torr tube fitting. O-ring seal in the Ultra-Torr fitting allows for rotation and translation of the rod which moves the nozzle in the X and Y direction, respectively. On the base plate, we design arch-like Y-motion support where we place linear bearings in its two legs. Above the support, a T-shape top plate connects to the support via two 8 mm diameters of Y-motion rods. These Y-motion rods insert into the linear bearings in the Y-motion support and align the Y-motion. On the upper end of the support rod, we reduce the diameter to 6 mm. This part with reduced diameter then inserts into a bearing accommodated in the top plate and is fixed by an M3 screw. Now the top plate has connected to the support rod, but to precisely control the motion, one more element is needed. Between the top plate and the Y-motion support, a Y-motion screw has the bottom end screwed into a tap hole on the Y-motion support, and the top end inserted into the second bearing on the top plate. When turning the Y-motion screw, we drive the top plate as well as the parts linking to the top plate: the support rod, the copper blocks, and the nozzle.

Referring to the X-motion, we achieve it by rotating the support rod. To do so, near the top end of the support tube, we attach an X-motion arm, as illustrated in Figure 2.9 (b). By turning an X-motion screw located at an attachment under the top plate, it pushes the X-motion arm and applies torque to the support rod. Please note that since we rotate the rod, actually we swing the nozzle in the horizontal plane (XZ plane) instead of a pure X-motion. With the 3-axes motions described above, we use them to optimize the nozzle position and maximize the beam flux arriving at the UHV stage.

2.2.2 Chopper motor and optocoupler

For experiments such as time-of-flight and scattering of a chopped molecular beam, the source chamber contains a 127 mm diameter chopper disk with a pair of 2 mm slits corresponding to a 1% duty cycle mounted on the back (P2) of the skimmer mounting plate, as shown in Figure 2.10 (a). This chopper disk is driven by a regulated brush-less DC motor (Maxon Motors, EC32) which has a position encoder (US Digital, E5 series) with 2048 steps of 360° rotation for precise control of the chopper position and speed.

The chopper disk is made by laser cutting a copper/beryllium foil (Cu98/Be2) with a thickness of 0.1 mm. As shown in Figure 2.10 (b), the chopper disk is mounted on a chopper hub and held by the outer nut. The chopper hub is a 24 mm diameter disk with an 8 mm diameter threaded tube extended from the middle. As shown in Figure 2.10 (c), for coupling to the motor shaft, the threaded tube at the inner side has four cutoff regions which reduce the rigidity of the tube. Plus, an inner nut has a tapered structure at the end of its tapered hole. When we fasten the inner nut, the tapered face presses the threaded tube on the hub inward and clamps the motor shaft tightly. If one simply uses a set screw to fix the chopper hub on the motor shaft, the unbalanced mass along the radial direction will cause strong vibrations when the chopper is spinning fast as we use up to 12000 rpm for TOF measurements. Any vibration in the machine is not desired as the bolometer can easily pick up microphonic noise.

For installation of the chopper disk assembly on the motor shaft, the clearance between the disk and the skimmer mounting plate is only 2 mm, too small for a normal wrench to be used to tighten the inner nut. Therefore we make a U-shape wrench with only 1 mm of thickness and customized matching-shaped nuts. As shown in Figure 2.10 (b), both the inner and the outer nuts are not simply rounded but have two flat faces machined. These two flat faces are actually where the U-shape wrench holds. One can also find the same feature on the chopper hub, as shown in Figure 2.10 (c).

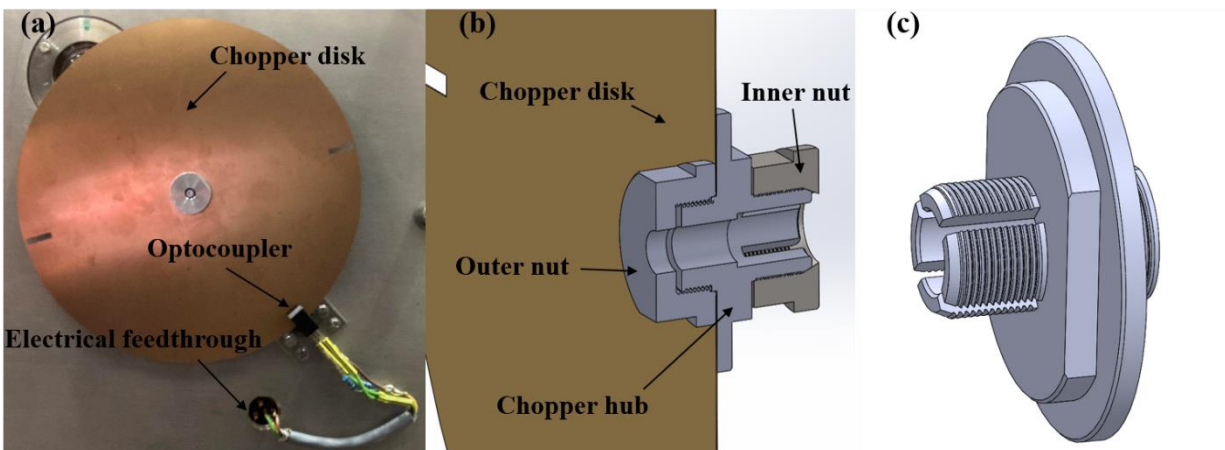


Figure 2.10 (a) Back of the skimmer mounting plate where the chopper disk and the optocoupler are located. The optocoupler is glued on a 25 x 20 mm rectangular plate which is bolted to the skimmer mounting plate. (b) Section view of the chopper disk and the hub assembly. The chopper hub has both sides threaded. On the outer side, the chopper disk is attached. The inner side connects to the motor shaft and the inner nut fixes the hub on the shaft. (c) 3D model of the chopper hub. Four slots are cut into the threaded tube for symmetric mounting of the hub with the chopper disk in order to prevent vibrations due to imbalance during fast rotation.

For modulation of the molecular beam for time-of-flight (TOF) measurements or molecular beam scattering, a reference signal is needed as a trigger for the multichannel scaler (MCS) used to measure the TOF or a reference frequency for lock-in detection of the bolometer signal. This so-called chopper reference is provided by an optocoupler (Fairchild H22LOI) mounted opposite to the skimmer opening which senses the passing of the chopper slits. With this configuration, when the first slit clears the skimmer opening, the optocoupler sees the second slit and produces a low-state signal for triggering the sampling device. To match the input requirements of the MCS, the circuit of the controller box inverts the optocoupler signal in order to provide a positive pulse as each slit moves into the open position.

To connect the electricity and the output signal of the optocoupler to a CF40 10 pin electrical feedthrough installed on the source chamber, we screw in a 5 pin electrical feedthrough on the front side of the skimmer mounting plate, as shown in Figure 2.10 (a). The leads of the optocoupler are then wired to the 5 pin feedthrough. On the feedthrough site, the wires are soldered on the cups, whereas on the optocoupler, wires are connected to the leads by crimp connectors in case disconnection is needed for maintenance. On the front side, a cable with corresponding plugs makes the connection between two feedthroughs. Referring to the connection of the chopper motor, the wires of the motor and the encoder are collected to a 25-pin vacuum type plug inserted into a CF63 25-pin subminiature D electrical feedthrough, as shown in Figure 2.11 (b).

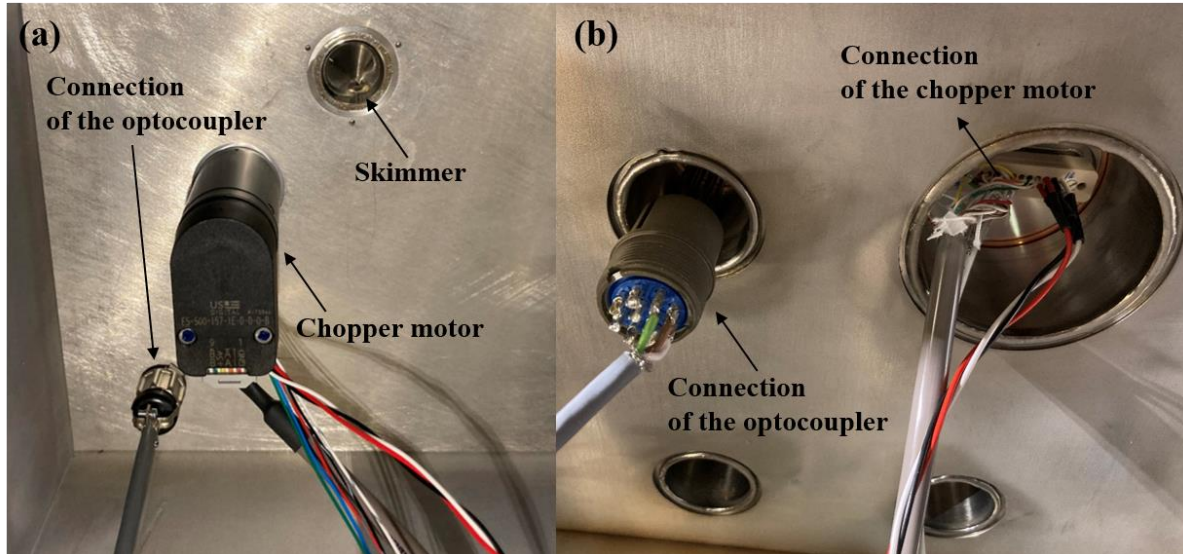


Figure 2.11 (a) Front side of the skimmer mounting plate where the chopper motor attaches and is fixed by four M3 screws coming from the other side. Near the corner, there is a 5-pin electrical feedthrough for delivery of power needed and signal output of the optocoupler. (b) Electrical connections of the optocoupler and the chopper motor on the vacuum side of the feedthroughs.

On the air side, a home build controller box consisting of a chopper motor controller (Maxon Motors, EPOS2), a 24V/9.2A DC power supply for the motor controller, and a 5V/3A DC power supply for the optocoupler collects the wires from the optocoupler and the chopper motor through a 3 pin LEMO connector and a 25 pin subminiature D connector, respectively. For the pinout of the optocoupler and the chopper motor, one can find a construction plan (made by the engineer P. Favre in the ISIC electronic workshop, EPFL) in the folder labeled “Maxon motor” in the lab CH GO 528. For operating the chopper motor, the chopper motor comes with a standalone software package (Maxon Motors, EPOS Studio) which includes three different operating modes for the motor: velocity mode at a set velocity in rpm, position mode where we move the chopper slit to any encoder position (2048 steps), and homing mode which takes the chopper to a predefined stored position.

2.3 Time-of-Flight measurements and calibrations

A supersonic jet is formed by the expansion of a gas from a high-pressure reservoir at a stagnation state (P_0 , T_0) into a low-pressure region (P_1) through a small orifice. A conical skimmer with a central orifice with very sharp edges can be used to sample the centerline of this jet expansion without significant perturbation due to scattering from the orifice edges to create a cold, collision-free molecular beam. The structure of a supersonic jet expansion is illustrated in Figure 2.12.

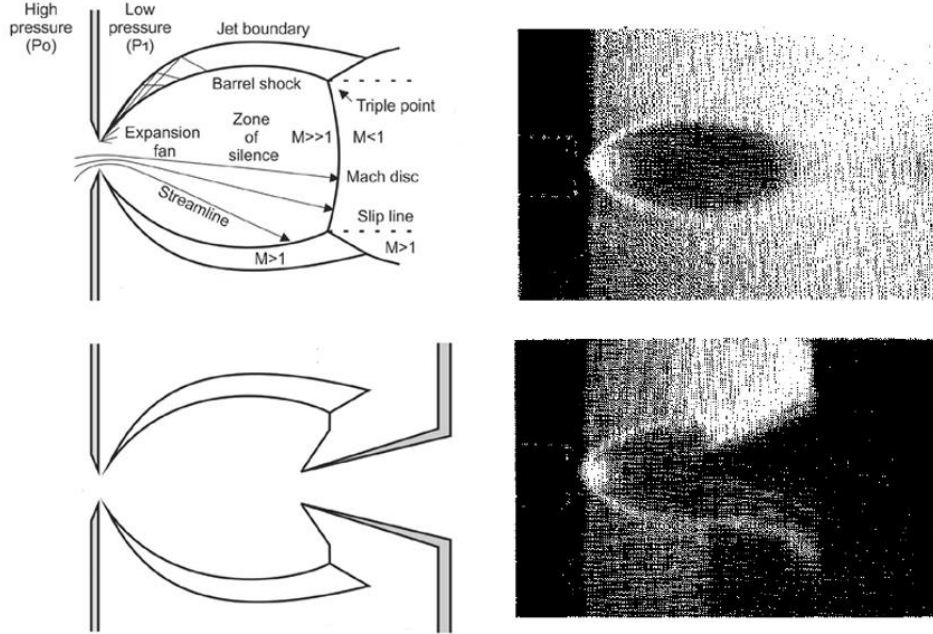


Figure 2.12 Left: structure of a supersonic jet expansion adapted from Ref [51]. M is the Mach number. Right: images of supersonic expansion of He obtained by electron beam induced fluorescence. Images are taken from Ref [52].

Assuming an ideal gas behavior of the flow, based on the first law of thermodynamics, the energy equation of the flow can be expressed as [53]

$$h + \frac{v^2}{2} = h_0 \quad (2.1)$$

where h_0 is the stagnation enthalpy per unit mass which is a constant along any streamline originating from the stagnation stage, h is the enthalpy per unit mass of the expanding gas, and v is the velocity of the expanding gas. During the expansion, the enthalpy decreases, and the velocity increases. Using the relation $dh = C_p dT$ for ideal gases, one can rewrite the equation as

$$v^2 = 2(h_0 - h) = 2 \int_T^{T_0} C_p dT \quad (2.2)$$

Since the gas cools down to only a few Kelvin during the expansion, $T_0 \gg T$, and we assume C_p stays constant in this temperature range. Using $C_p = \left(\frac{\gamma}{\gamma-1}\right) \frac{k_B}{m}$, one can derive the terminal velocity of the molecular beam:

$$v_\infty = \sqrt{\frac{2k_B}{m} \frac{\gamma}{\gamma-1} T_0} \quad (2.3)$$

where k_B is the Boltzmann constant, and γ is the heat capacities ratio C_P/C_V , m is the molecular mass. The velocity distribution of the molecular beam can be described by the flux-weighted Maxwell-Boltzmann distribution:

$$f(v) \propto v^3 \exp\left[-\frac{m}{2k_B T_{\parallel}}(v - v_0)^2\right] \quad (2.4)$$

where T_{\parallel} is the translational temperature along the molecular beam axis which quantifies the velocity spread of the molecular beam, and v_0 is the stream velocity.

Section 2.2 presented the design of our molecular beam source. The molecular beam source is used to generate a molecular beam with well-defined velocity and kinetic energy. To characterize the velocity distribution of our molecular beam, a tool for velocity measurements is needed. Here, we use the time-of-flight technique (TOF) which measures the flight time t of a molecule to travel a known distance D resulting in the velocity $v = D/t$.

Using the setup described in Section 2.2, a molecular beam is generated by supersonic jet expansion from the nozzle through the 1 mm skimmer. To produce a pulsed molecular beam, the chopper wheel having a pair of 2 mm slits with 1% duty cycle spins at 200 Hz and thus produces a molecular beam at a repetition rate of 400 Hz. When the first slit reaches the skimmer opening, the optocoupler mounted 180° opposite to the skimmer openings sees the second slit and produces a signal to trigger sampling of the multichannel scaler (Ortec, EASY-MCS). The molecular beam then travels from the chopper into the UHV chamber where it is sampled by the cross beam ionizer of the quadrupole mass spectrometer (Pfeiffer, QMG220) located after a neutral flight distance of 657 mm near the end of the UHV chamber. In the ionizer, a small fraction of the molecular beam is ionized by electron impact and the resulting cations are extracted in a direction perpendicular to the molecular beam by an electric field. The quadrupole mass filter then transmits the ions of the desired m/z to a secondary electron multiplier (SEM). Each ion arriving at the SEM creates a current pulse of a few ns pulse width which is amplified by a fast preamplifier (Ortec, VT-120 Fast Preamp). This amplified signal is connected to the input of a multichannel scaler (MCS) with a minimum dwell of 100 ns. The MCS has an adjustable threshold for the discriminator to distinguish ion signals from background noise. Once the MCS receives the start trigger from the optocoupler, it counts ion pulses and records the number of ions as a function of arrival time relative to the trigger.

An important observation I have to mention is that the measured TOF profile shows a tail feature as shown in Figure 2.13. This tail feature was also observed in other setups having a QMS mounting along the molecular beam axis [48,54]. In this geometry, the tail can be explained by the pump-out time needed for the molecules that reside in the QMS body. However, in the BILT machine, we are using a vertically mounted QMA with a cross-beam ionizer which allows one to extract ions perpendicular to the incident molecular beam. In this case, the molecules passing through the ionizer without being ionized will not be trapped inside the ionizer and should therefore not result in a pump-out time.

This tail feature can be attributed to the molecules scattered from the ionizer structure and therefore experiencing longer trajectories. This assumption is supported by the fact that the tail can be eliminated by placing a limiting aperture to reduce the incident beam size. By placing a 1 mm aperture 146 mm in front of the ionizer, one can remove the tail and the symmetric TOF profile is obtained, as shown in Figure 2.13 (a). According to this observation, I suspect that the molecules ionized at the corner of the ionizer follow a longer trajectory thus contributing to the tail on the TOF profile. To further confirm this assumption, I used different sizes of apertures to control the molecular beam size. When a 4 mm aperture was used, the tail showed up again, as shown in Figure 2.13 (b). This observation suggests that by limiting the molecular beam size at the center of the ionizer, one can remove the tail effectively.

For performing the TOF measurements with various molecular beam sizes, an aluminum plate with 1 mm, 2 mm, and 4 mm apertures was connected to a 3-axes manipulator installed on a CF100 on the top of the main chamber. With this setup, one can place the desired aperture in front of the ionizer. Now, this setup has been removed because it blocks the way of the sample mount Z-motion (along the molecular beam axis). Alternatively, an 1 mm aperture is machined on the Ta sample mounting plate on the sample mount which I will describe in the next few sections.

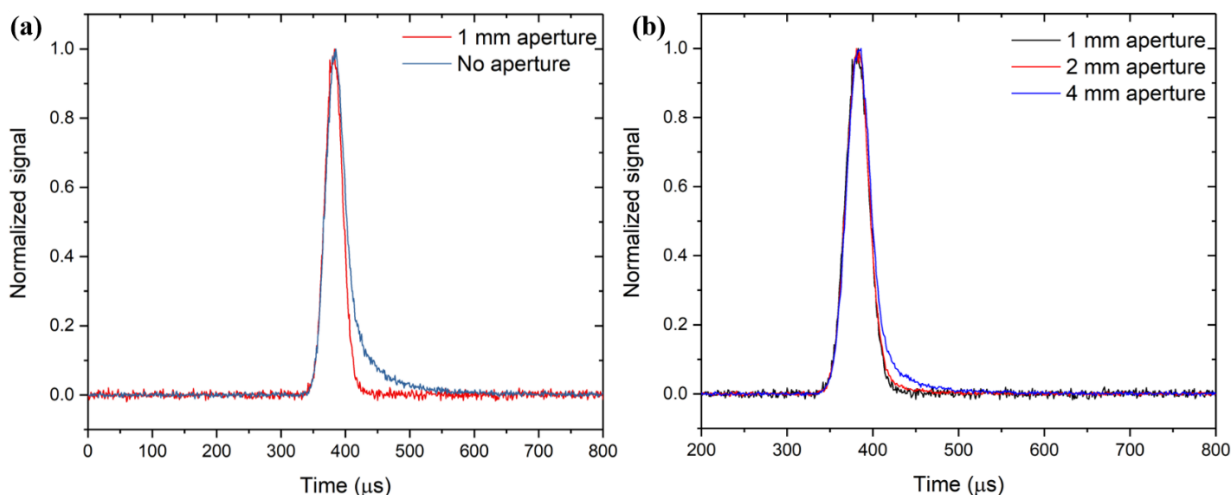


Figure 2.13 (a) TOF trace of CH_4 for a 3% CH_4 in He mixture and $T_n = 300$ K nozzle which corresponds to an average velocity of 1700 m/sec and average kinetic energy of 23 kJ/mol. The blue trace shows a weak tail since it was measured without an aperture limiting the molecular beam size. Placing a 1 mm aperture in front of the QMS ionizer removes the tail as shown in the red trace. (b) TOF measurements with the same gas mixture but with different limiting apertures.

The measured TOF profile $g'(t)$ is a convolution of the real TOF distribution of the molecular beam $g(t)$ and the chopper transmission function $S(t)$:

$$g'(t) \propto \int_0^{\infty} S(t - \tau)g(\tau) d\tau \quad (2.5)$$

This is because the chopper slit has a certain width, when it clears a continuous molecular beam, it transmits a different portion of the beam at different timing. The chopper transmission function

can be experimentally determined by measuring the transmitted intensity of a He-Ne laser using a photodiode. The He-Ne laser coming from the source simulates a molecular beam. After passing the chopper slit, the photodiode measures a transmission profile which can be approximated by a trapezoidal function. Here, I use a previously determined chopper transmission function with 24 μs plateau and 6 μs of rising and fall time since the same dimensions of skimmer and chopper are used.

Since we use the QMS with an electron bombardment ionizer, which is a density-sensitive detector, one must divide TOF distribution $g(t)$ by $v = D/t$ to get the detector response (flux = density $\times v$)

$$g_{den}(t) \sim \frac{1}{t} f\left(\frac{D}{t}\right) \quad (2.6)$$

The TOF measured by the setup described here includes not only the time needed for the molecules to travel from the slits to the ionizer but also a trigger delay from the optocoupler which we call chopper delay, and the time needed for ions to travel from the ionizer to the SEM. Thus, the total TOF can be represented by:

$$t_{total} = t_{chopper} + t_{neutral} + t_{ion} \quad (2.7)$$

where $t_{chopper}$ denotes the chopper delay, $t_{neutral}$ the neutral flight time, i.e. the time needed for a molecular to travel the distance between the slit and the ionizer, and t_{ion} the ion flight time. A precise determination of the molecular velocity needs proper calibrations taking these factors into account. In the rest of this section, I will present the deduction of these factors following a similar approach described in Chen's thesis where a similar configuration of TOF setup is used [48].

2.3.1 Chopper delay

Two factors contribute to chopper delay. The first factor is because the position of the optocoupler is not perfectly placed at 180° to the skimmer opening. The error of this contribution can be measured by spinning the chopper in a different direction. Given the misalignment of the optocoupler by an angle α from the ideal position, and the rotational frequency of the chopper f , the measured TOF will have a time error $\Delta t = \alpha/2\pi f$ involved. In a given spinning direction of the chopper, if the first slit reaches the optocoupler before the arrival of the second slit to the skimmer opening, the measured TOF presents a positive error Δt , i.e. a longer TOF. Whereas a negative error $-\Delta t$ presents in the opposite direction. Thus, the difference between the two TOFs measured in different spinning directions attributes to twice the time error of $2\Delta t$. In the TOF measurements of a He atom beam, I measured TOF of 399.2 μs when the chopper was spinning at +12000 rpm. Whereas 397.2 μs was measured in the opposite direction, -12000 rpm. Here, I use +/- to indicate different spinning directions. Given the distance between the optocoupler and the center of the chopper 60 mm, and the chopping frequency of 200 Hz, I calculate the misalignment of the optocoupler to be 0.08 mm.

The second factor comes from the fact that the optocoupler generates a trigger signal earlier than the arrival of the slit at the center of the skimmer opening. The optocoupler generates a trigger signal edge as the first slit arrives. However, in the meantime, the second slit is not yet centered at

the skimmer opening. This results in an early counting of the multichannel scaler and a corresponding time error in the measured TOF. In the ideal case, the optocoupler should generate a trigger signal when the center of the slit reaches it, whereas in the real case it is the edge of the slit. Based on this picture, the time error contributes to the time needed for half of the slit to clear the optocoupler at a given spinning frequency. In principle, this type of chopper delay will approach 0 if the chopper spins infinitely fast. Therefore, to derive an accurate TOF without the contribution from the chopper delay, I measured TOFs at different chopping frequencies, and by plotting the TOF versus frequency, one can extrapolate the TOF at an infinite chopping frequency where the chopper delay is 0.

Figure 2.14 presents the measured TOFs of a He atom beam at different chopping frequencies and directions. The linear fit provides an intercept which is the TOF without chopper delay. The difference between the TOF at a given frequency and the infinite speed is the chopper delay at this given frequency. At +200 Hz, I derived the chopper delay of 18.3 μs from He TOFs. In this work, I measured chopper delay using three different noble gases He, Ne, and Ar. I summarize these chopper delays when the chopper was spinning at +200 Hz in Table 1. In the end, I will use the average value of 18.2 μs over three gases in future calibrations.

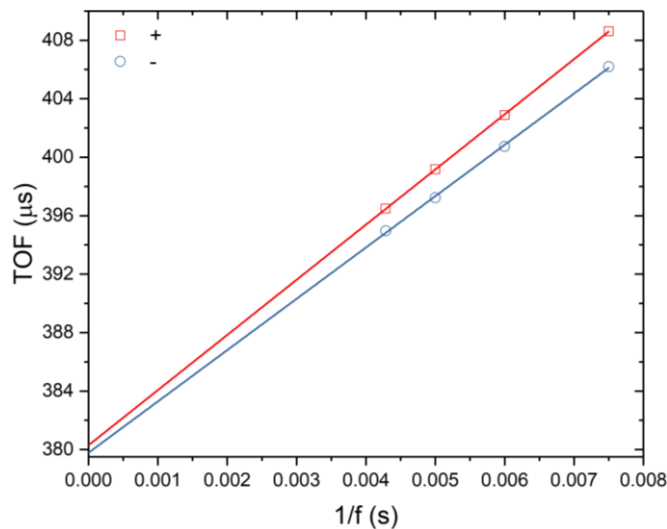


Figure 2.14 TOFs of a He atom beam measured at +8000, +10000, +12000, and +14000 rpm and the opposite direction. +/- denotes different spinning directions. Measurements were carried out using 2 bar of nozzle pressure and a room temperature nozzle.

Table 2.1 Measured chopper delay at +200 Hz for He, Ne, and Ar. The average value of 18.2 μs will be taken for calibrations.

Gas mixture	He	Ne	Ar
Chopper delay (μs)	18.9	17.6	18.2
Average chopper delay = 18.2 μs			

2.3.2 Ion flight-time

In a TOF measurement, the traveling molecules won't see the checkered flag at the reception of a molecular detector, especially when a QMS is used as the detector. With the QMS, selectively detecting molecules with the desired m/z is possible. This is of crucial importance in the case when a seeded beam is used. Once the molecules arrive at the ionizer (the reception), the ions formed at the ionizer are then extracted to the quadrupole mass filter (rod system) by appropriate ion optics. In a given voltage of the applied quadruple field, only ions with a specific m/z can pass the rod system otherwise are deflected. Finally, the m/z selected ions travel through the rod system and hit the SEM that generates ion signals. Thus, it takes a few more μs for the ions to finish this extra step. Assume the time needed for the ions to travel through the ion optics is negligibly small, so most of the ion flight-time contributes mainly to the travel time in the rod system. The kinetic energy of the ions traveling in the rod system is determined by the so-called field-axis voltage U which is defined as the potential difference between the ion formation area and the rod system:

$$\frac{1}{2}mv_{ion}^2 = eU \quad (2.8)$$

where e is the charge of the ions. The ion flight-time can be expressed as

$$t_{ion} = \frac{d}{v_{ion}} = \frac{d}{\sqrt{\frac{2eU}{m}}} \quad (2.9)$$

where d is the ion flight distance, which is essentially the slope if we plot t_{ion} versus $\sqrt{\frac{2eU}{m}}$. Again I use a He atom beam for this calibration. As shown in Figure 2.15 (a), the resulting TOFs show nonlinear responses to $\sqrt{\frac{2eU}{m}}$, which is not expected. I suspect the applied field axis voltage is not the same as what I set in the interfacing software, Quadera. The reason for this deviation is not clear. However, I found that one can resume the linearity by adding an offset to the field axis voltage.

$$U_{eff} = U - U_{corr} \quad (2.10)$$

where U_{eff} is the effective field axis voltage, and U_{corr} is the correction voltage. By replacing U by U_{eff} in equation (2.9), we have

$$t_{ion} = \frac{d}{v_{ion}} = \frac{d}{\sqrt{\frac{2eU_{eff}}{m}}} \quad (2.11)$$

Figure 2.15 (b) shows the resulting plot with $U_{corr} = 4.9 \text{ V}$, which gives the best linear fit. I derived U_{corr} by tuning it in a step of 0.1 V and maximizing the R^2 of the linear fit. With this correction, I calculated the ion flight distance to be 0.155 m.

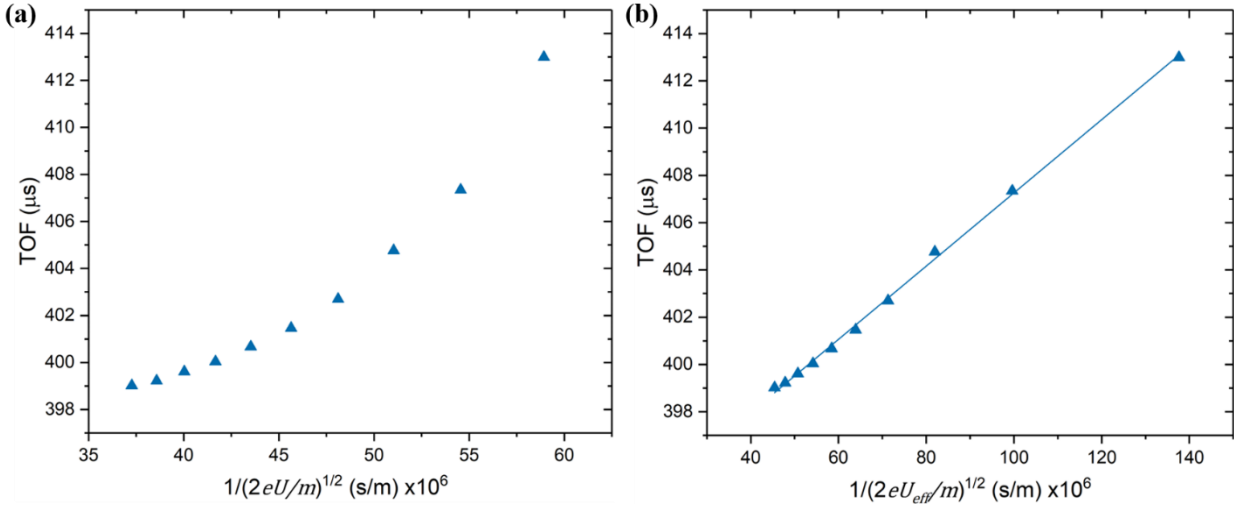


Figure 2.15 (a) TOF of a He atom beam measured at different field axis voltages ranging from 6 to 15 V. (b) Using the same set of data as (a), but replace the field axis voltage U by the effective voltage U_{eff} with 4.9 V of correction voltage U_{corr} . The slopes provides the ion flight distance of 0.155 m.

To further verify the validity of this assumption, I applied the same method for TOF measurements of different noble gases Ne, Ar^+ , and Ar^{2+} . No matter which gas I used, they all came with very similar U_{corr} which are around 5 V, as shown in Table 2.2. Since ion flight time depends on the m/z of the measured gas, what we have to pick up is the ion flight distance. Here, I will take the average ion flight distance of 0.143 m for the later calibrations.

Table 2.2 Correction voltage and the corresponding ion flight distance calculated from TOF data of He, Ne, Ar^+ , and Ar^{2+} .

Gas species	He	Ne	Ar^+	Ar^{2+}
Correction voltage U_{corr} (V)	4.9	5.0	5.1	5.0
The best R^2	0.99856	0.99939	0.99912	0.99839
Ion flight distance (m)	0.155	0.148	0.131	0.138
Average ion flight distance (m) 0.143				

2.3.3 Neutral flight-time

Based on our setup, neutral flight time is the time needed for a molecule to travel from the chopper slit to the ionizer of the QMS. It is the time we desire to obtain for characterizing the kinetic energy of the molecule. Once we have both the chopper delay $t_{chopper}$ and the ion flight time t_{ion} , then the neutral flight time is simply

$$t_{neutral} = t_{total} - t_{chopper} - t_{ion} \quad (2.12)$$

To obtain the molecular velocity, we need the final piece of the puzzle, the neutral flight distance D . Here, I define it as the distance from the chopper slit to the center of the ionizer which is 0.657 m measured by the 3D model in Solidworks.

2.3.4 Reliability of the calibrations

I performed TOF analysis using the MATLAB script developed by Maroni and it was further improved by Werdecker [54]. The script first deconvolutes the recorded TOF with the chopper transmission function, then subtract the arrival time by the chopper delay $t_{chopper}$ and the ion flight time t_{ion} . Finally, it converts the TOF spectrum to velocity distribution and performs the fitting with the flux-weighted Maxwell-Boltzmann distribution. To test the reliability of the calibrations described above, I characterized the velocity of various noble gas beams, He, Ne, and Ar, whose terminal velocity under supersonic jet expansion can be predicted accurately by eq (2.3). Table 2.3 summarizes the measured velocity of He, Ne, and Ar beams and the theoretical values. One can see the measured values agree very well with the theoretical ones, this suggests good reliability of the calibrations.

Table 2.3 Measured velocities of He, Ne, and Ar beams in comparison with the theoretical values. The experiments were carried out using a room temperature nozzle $T_n = 296$ K. The average energies show a very similar value because the theoretical energy is $\frac{5}{2}R \approx 6.1$ kJ/mol.

Gas species	Measured velocity (m/s)	Average energy (kJ/mol)	Translational temperature $T_{ }$ (K)	Theoretical velocity (m/s)
He	1754	6.2	2.5	1756
Ne	781	6.1	1.2	785
Ar	555	6.2	0.8	555

2.3.5 Generation of fast beams by hot nozzle

The kinetic energy of a molecular/atomic beam generated by supersonic jet expansion can be enhanced by increasing nozzle temperature T_n , as predicted by eq 2.3. Figure 2.16 presents the results of velocity measurements for helium atom beams with the T_n ranging from 289 to 1100 K and their corresponding theoretical velocities calculated by eq 2.3. As we can see in the plot, at the lowest temperature of 289 K, the measured velocity matches very well with the theoretical value. However, as T_n increases, the deviations between the measured and the theoretical values also increase. This observation indicates that the He gas in the stagnation stage is not yet thermalized with the nozzle. In future applications, to heat the nozzle for the desired kinetic energy, one can not simply calculate the target T_n by eq 2.3. Instead, velocity characterization by the TOF method is necessary. Table 2.4 summarizes the characteristics of hot helium atom beams with T_n from 289 to 1100 K.

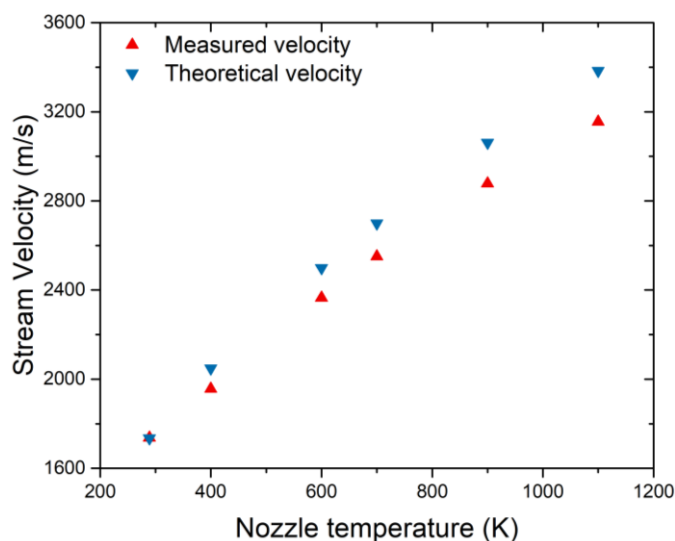


Figure 2.16 Measured velocities of helium atom beams as a function of nozzle temperature T_n and their corresponding theoretical velocities calculated by eq 2.3.

Table 2.4 Velocity characteristics of the He atom beam generated by 4 bar of nozzle pressure with nozzle temperatures ranging from 289 to 1100 K. The theoretical velocities are derived by eq 2.3.

Nozzle temperature (K)	Stream velocity (m/s)	Translational temperature (K)	Average energy (kJ/mol)	Theoretical velocity (m/s)
289	1737	1.3	6.1	1735
400	1957	2.1	7.7	2049
600	2366	5.3	11.3	2450
700	2551	7.9	13.2	2700
900	2878	15.2	16.9	3061
1100	3155	23.6	20.4	3384

2.4 Scattering chamber

The scattering chamber is a rectangular box with dimensions of 804 x 609 x 447 mm and contains the vacuum stages P2, P3, and P4. The UHV stage P4, where surface preparations, characterizations, and scattering experiments happen, occupies most of the volume of the chamber. Figure 2.17 (a) shows the 3D model of the scattering chamber. Its front side has a rectangular opening where the source chamber with the P1 extension attaches by an O-ring seal. The contact area with the source chamber is electropolished for a good O-ring seal. The top of the chamber contains a hub that supports a rotatable lid on a large 600 mm ball bearing. The junction between the hub and the lid is sealed by three layers of spring-loaded PTFE O-ring with two differentially pumped stages that maintain UHV condition during rotation of the lid. At the back of the chamber, a CF300 flange is used to connect a three-axis surface manipulator. Please note that CF300 is not covered by the international standard, different manufacturers could use different dimensions. Our scattering chamber was built by VACOM (VACOM Vakuum Komponenten & Messtechnik GmbH), thus, for purchasing accessories for the CF300 flange, such as gaskets, one should always order them from VACOM.

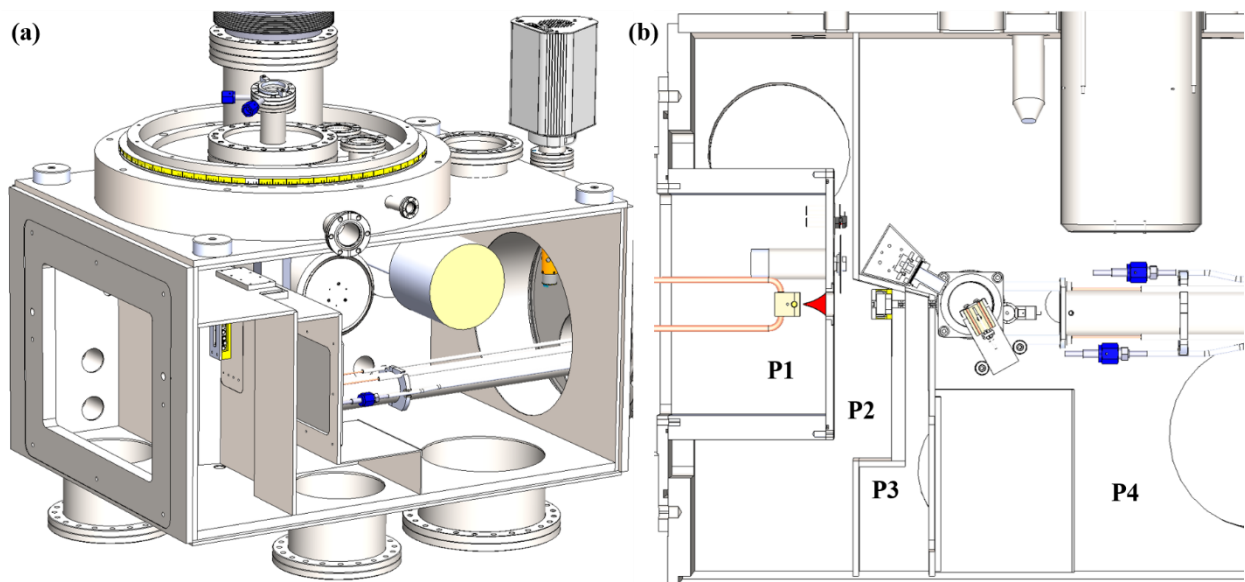


Figure 2.17 (a) 3D model of the scattering chamber without attached source chamber.

(b) Horizontal cross-section of the scattering chamber on the molecular beam axis showing the arrangement of four pumping stages. In the figure, the bolometer is located at the minimum detection angle of 30° from the MB axis. We design the recessed wall such that it matches the shape of the bolometer cold shield.

Figure 2.17 (b) shows the section view of the scattering chamber. The depth of the second stage is determined by the tube of 150 mm diameter connecting the CF160 flange to the P2 turbomolecular pump. In the middle of the P2 wall, the structure extrudes toward the P3 side, which creates extra space in P2. This extra space allows us to accommodate a separation valve but does not interfere with the front of the P1 extension. Thus, we insert the P1 extension further toward target surface in order to minimize the nozzle-to-sample distance. The P3 stage only occupies a small portion of the chamber as the main purpose is to provide differential pumping. The lower part of the P3 wall extends toward the P4 stage for connecting a turbo-molecular pump by a CF160 half nipple. The P2 and P3 walls are recessed on one side, which clears some space in P4. We design the geometry of this recessed wall to match the shape of the bolometer cold shield, such that we maximize the rotation angle range of the bolometer from 30° to 180° relative to the molecular beam axis.

For surface cleaning and analysis of the surface structure and chemical composition, the UHV stage contains an Ar⁺ sputter gun, a LEED spectrometer, and an Auger electron spectrometer (AES). These instruments are arranged horizontally along the Z-axis (MB axis) and a horizontally mounted surface manipulator with a Z-stroke of 45 cm is used to move the sample between the different positions used for surface cleaning, characterization, and scattering experiments.

2.4.1 Top hub and the rotating platform

One of the main improvements of the BILT machine compared to the initial testing setup is the ability to rotate both the bolometer detector and the target surface which allows for independent variation of the incident and the scattering angle. While being conceptually simple, it requires an appropriate rotary seal design to maintain UHV conditions during detector rotation. Furthermore, a large and precisely positioned bearing is needed which can support both the weight of the lid (60kg) as well as the atmospheric pressure (exerting about 24000N of force in total).

Figure 2.18 (a) and (b) illustrate the design of our rotary seals. In the top hub, three spring-loaded PTFE O-rings (Parker, FlexiSeal series NAA-M044500-05-001-1) and two differentially pumping stages constitute the structure of the rotary seal. To make the rotational motion smooth, a ball bearing (Kaydon Bearings, KD180XP0) is included between the load surfaces of the top hub and the rotating platform. The diameter of the rotating platform (at the inserting part) is 445 mm, but at the bottom, we design a tapered feature that can align the platform itself when inserting into the hub through three PTFE O-rings. The O-ring consists of a PTFE jacket and a metal spring as shown in Figure 2.19 (a) and (b). The width of the O-ring is wider than the space between the platform and the groove. So when one inserts the platform into the hub, the two sealing faces compress the O-ring. Then the compressed spring pushes the jacket outward by its restoring force and thus seals the two faces. The dimensions of the O-ring grooves follow the instruction from Parker for optimized sealability [55].

A 67 L/s turbomolecular pump (Pfeiffer, HiPace80) pumps the second differentially pumped stage that produces a background pressure at the order of 10⁻⁷ mbar. The first stage is pumped by a 1.7 L/s scroll pump (Edwards nXDS6) which also acts as a forepump for the turbomolecular pump. The base pressure in the first stage is 10⁻² mbar when the platform is static.

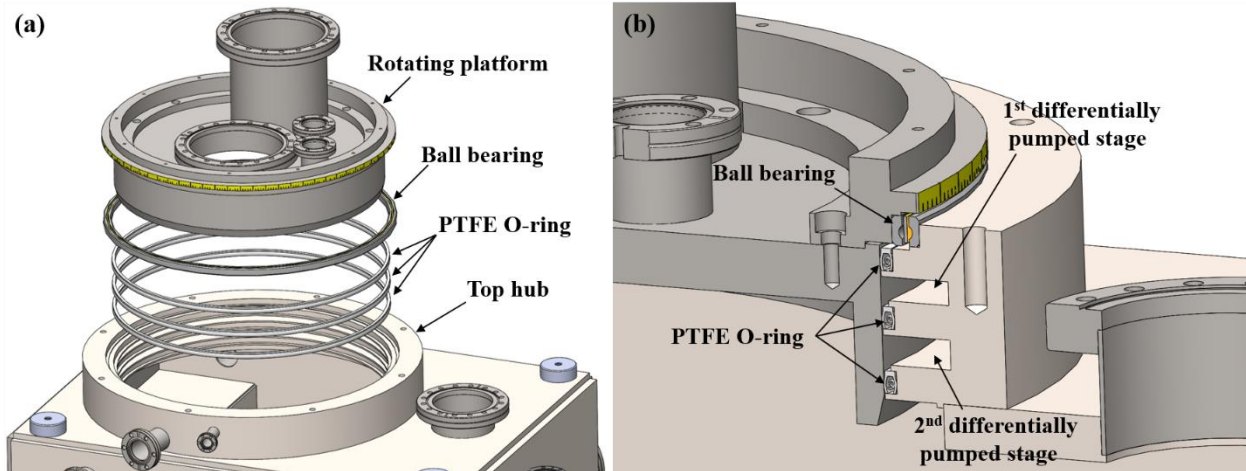


Figure 2.18 (a) Exploded view of the top hub and the rotating platform. Between them, three spring-loaded O-rings and two differentially pumped stages protect the UHV condition from leaking during the rotation of the platform. (b) Section view of the rotary seal. See text for the working principle.

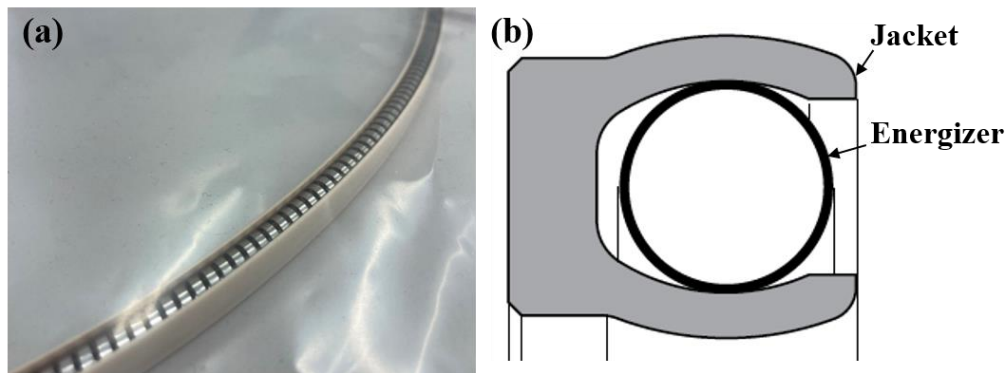


Figure 2.19 (a) Photo of the NAA type spring-loaded O-ring installed in the top hub. (b) Cross-section of the NAA type profile. The spring-loaded O-ring consists of a jacket and an energizer (spring), that are made out of PTFE and stainless steel, respectively.

The rotating platform is composed of a support ring and a base, as shown in Figure 2.20 (a). The support ring has the angle scale engraved with a step of 1° . It is the support ring that holds the entire rotating platform on the top hub and defines the vertical level. The bottom of the chamber includes two CF160 and two CF40 ports. The bolometer detector is mounted on a CF160 port through with a bellow (Kurt J. Lesker, MEW7506001C3, $100 \pm 16\text{mm}$) for precise vertical alignment of the bolometer detector to the scattering plane. When mounted on the main chamber, the distance from the long CF160 flange to the scattering plane is 413.7 mm. However, the flange-to-detector distance of the bolometer is 517.5 mm, as shown in Figure 2.20 (b). Thus the bellow with about 100 mm of length is needed to adapt the bolometer to a proper level.

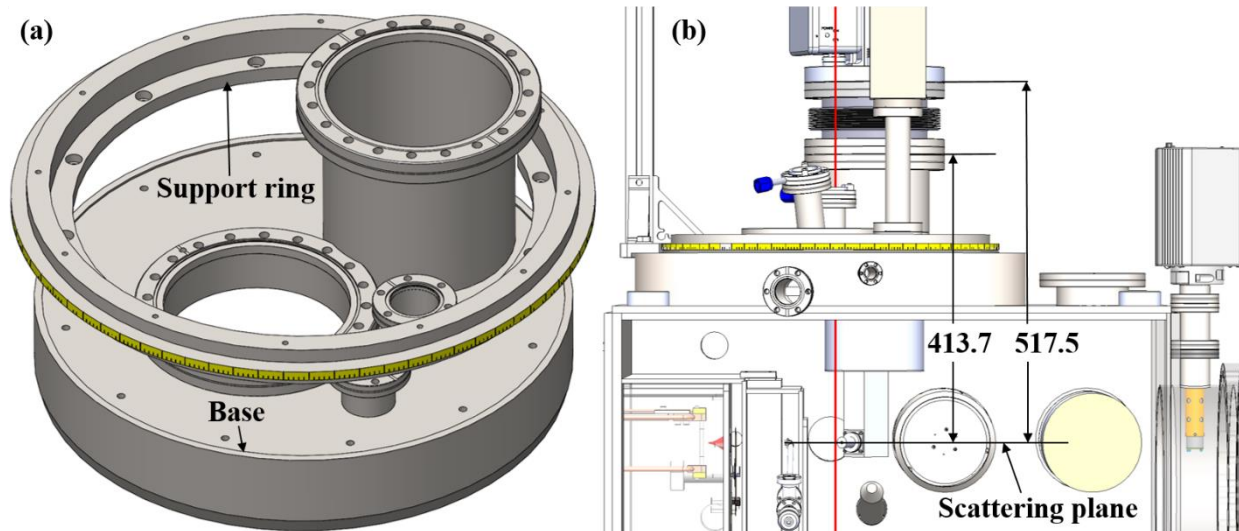


Figure 2.20 (a) Structure of the rotating platform which consists of a support ring and a base. The two pieces are bolted together by 11 M8 screws. (b) Section view of the chamber. The labels indicate the distance (in mm) from the CF160 flange to the scattering plane and from the CF160 flange of the bolometer to the bolometer detector.

On the short CF160 port, we install a so-called tagging and Doppler flange, as shown in Figure 2.21 (a). This flange contains two CF40 ports with differentially pumped CaF₂ windows for laser access. In future work, we plan to use a reflection of the tagging laser from a mirror mounted below the scattering plane to cross and excite the scattered molecules with a Doppler-shifted frequency. This leads to two peaks in the tagging spectrum, one sharp for the perpendicular crossing and one broadened by Doppler broadening which will be used to derive the velocity distribution of the scattered molecules. The output port for the reflected laser is mounted tilted by 12° about the incident port. This angle is determined by the Doppler velocimetry simulation done by Werdecker which shows promising velocity resolution. Interested readers are thus referred to his thesis [17]. In my Ph.D. work, the available time is not enough to finish the construction of the Doppler velocimetry. Therefore, the output port is currently not used.

We use a differentially pumped CaF₂ window to transmit the mid-infrared tagging laser beam into and out of the scattering chamber following the design by Chen [48], as shown in Figure 2.21 (b). The top window mount is a modified CF40 blank flange. A 50 mm diameter, 6 mm thick IR grade CaF₂ window (Crystran) is sealed by the first Viton O-ring. Since the mirror separates UHV from the air, its mechanical strength needs to handle the pressure difference. Given the thickness of the window 6 mm and the bore of the mount 38 mm in diameter, I calculated the safety factor to be more than 4 [56]. A second Viton O-ring is placed on the outside window edge to seal the junction between the window and the wall of the mount. Finally, a holder ring with a 45° tapered edge presses the O-ring against both the wall and the window. The dimensions of the groove follow the instruction from Parker for optimized sealability [57]. The space form between two O-rings is then pumped through a 4 mm diameter hole in the flange by the turbomolecular pump which also pumps the second stage of the rotary seal.

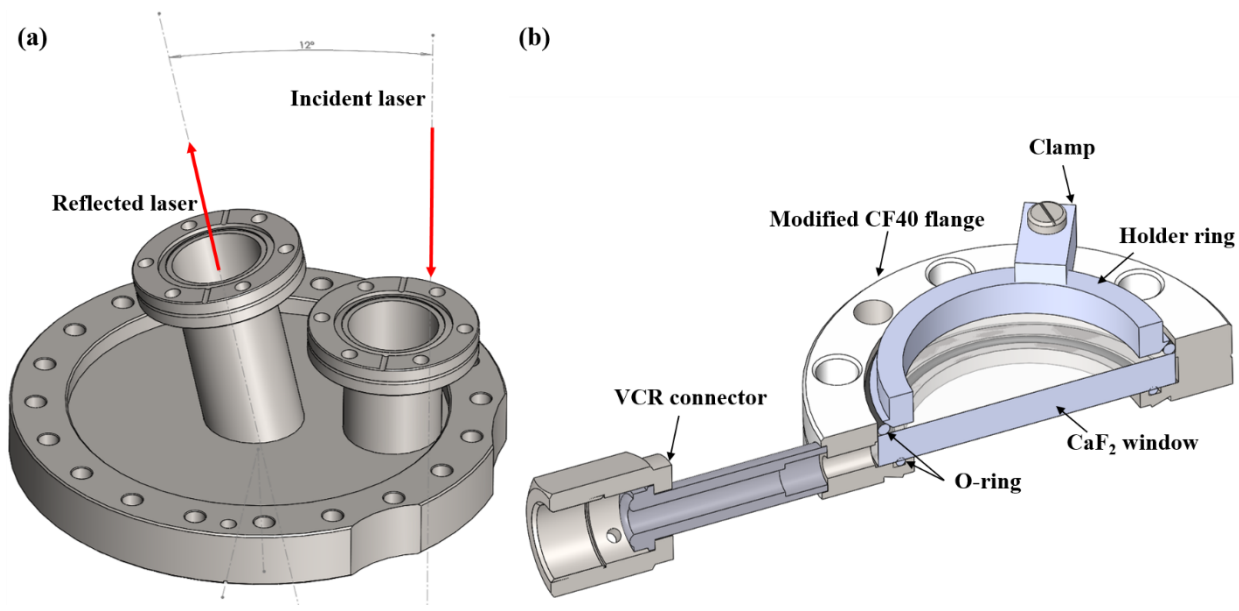


Figure 2.21 (a) 3D model of the tagging and Doppler flange. The red arrows highlight the path of the incident and the reflected laser beam. The port of the reflected laser tilts 12° about the incident port for the velocity resolution of the Doppler velocimetry. (b) Section view of the CF40 differentially pumped window as an access of the tagging laser. See the text for more detail.

On one of the CF40 ports, we install a residual gas analyzer (Stanford Research Systems, RGA100) for characterizing the vacuum condition of the UHV chamber. The final CF40 port is currently not used. We allocate this port for the possibility of introducing the tagging laser to the chamber via optical fibers. This idea is crucial if one performs CO₂ tagging experiments which bring up the problem of power loss due to the absorption of CO₂ in the air. This problem can be solved by purging the entire laser beam path with nitrogen gas, or by guiding the laser from the output to the vacuum chamber. The Argos OPO D-module provides the output frequency from 2170 to 2564 cm⁻¹. An indium fluoride fiber has above 95% of transmission at this range. However, so far, a polarization-preserved indium fluoride fiber is not yet developed. The other material, chalcogenide fiber, also provides good transmission in the range of interest. However, there are at least two problems. First, chalcogenide glasses normally have a high refractive index (2.4 for As₂S₃), this results in a high Fresnel loss at the interface when one needs to couple a laser from the air into the fiber. Second, chalcogenide fibers break down easily if a sudden change of laser power or temperature happens. Since chalcogenide fibers normally come at a very high price (more than 600 Euro per meter), regularly replacing the fiber is of course not desirable. Besides solving the problem by optics, one can simply use an isotopologue of CO₂ which has a low abundance in the air. Thus, there is currently no strong reason for using fiber optics.

2.4.2 Chain drive mechanism

The rotating platform is installed on the top hub with three PTFE O-rings sealing the junction. These spring-loaded O-rings introduce friction that makes rotating the platform difficult. In order to rotate the platform, a chain drive mechanism is used with two sprocket gears, as shown in Figure 2.22. The first sprocket gear with 76 teeth is bolted to the rotating platform. The second sprocket gear with 11 teeth is attached to a bearing housing installed on the scattering chamber. With this configuration, it reduces the torque needed to drive the platform by a factor of about 7. We measured 20 Nm of torque needed to drive the platform by a torque wrench.

The mount of the bearing housing consists of a base plate, a mobile plate, the bearing housing, and the shaft coupling to the 11 teeth sprocket gear, as shown in Figure 2.23. The base plate is bolted on the top hub and the site of a lifting lug. Plus, it serves as a rail for the mobile plate where the bearing house locates. The mount of the bearing housing can be moved to adjust the tension of the drive chain. For installation of the chain, two M8 screws on the mobile plate allow us to retract the mount and thereby loosen the tension on the chain. Once the chain is in place, we tighten the bolts and fasten the chain.

In order to automate the angular distribution measurements, we motorized the chain drive mechanism by adding a stepper motor (Trinamic, PD60-4-1160-TMCL) below the bearing housing. This stepper motor provides a maximum torque of 3.1 Nm, which is lower than the minimum torque needed. Thus, a 25x reduction gear is coupled to the motor, as shown in Figure 2.22. The motion control of the motor is now integrated into the bolometer signal acquisition VI that making automatically recording bolometer signals as a function of the scattering angle possible.

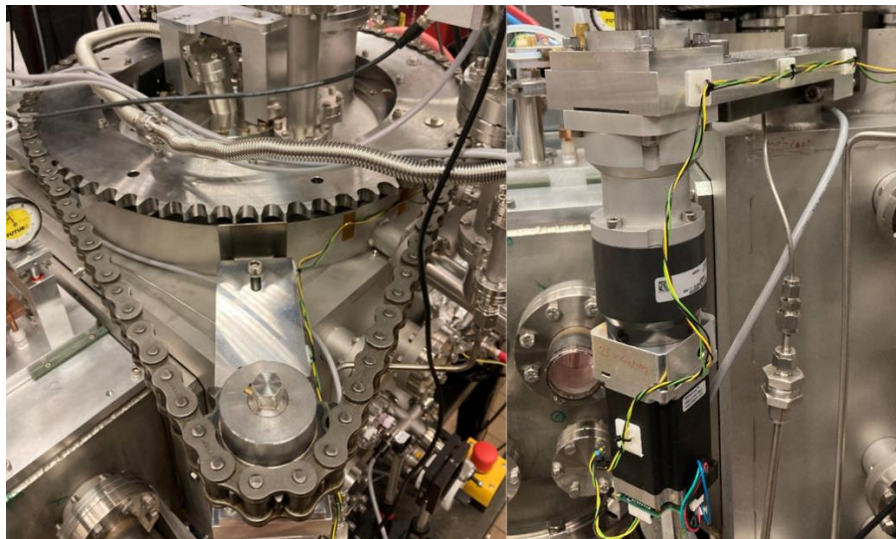


Figure 2.22 Left: Chain drive mechanism of the rotating platform. Right: Stepper motor and the 25x reduction gear installed below the bearing house. Between the bearing house and the reduction gear, there is a homemade adaptor flange.

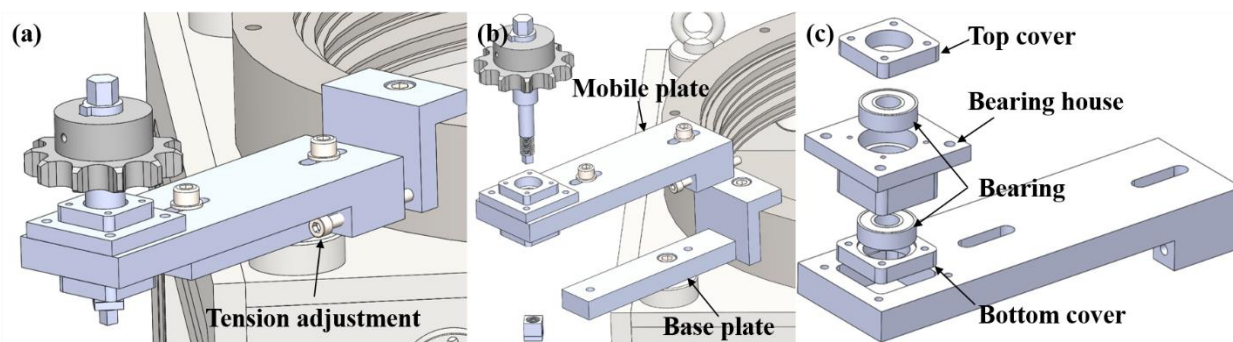


Figure 2.23 (a) 3D model of the bearing housing with the 11 teeth sprocket gear. Two M8 screws on the mobile plate allow for adjustment of the tension of the chain. (b) Exploded view of the bearing housing attachment which is composed of a base plate, a mobile plate assembly, and the sprocket gear. (c) Exploded view of the bearing house. It accommodates two bearings which constrain the motion of the gear shaft.

The big sprocket gear (76 teeth) has twelve M6 clearance holes which are used to attach the gear to the rotating platform. It also contains eight M10 clearance holes for lifting the rotating platform in case replacement of the PTFE O-rings is needed. For this, one needs long M10 threaded rods installed on the M10 tapped holes on the top hub with nuts placed between the hub and the gear. By turning the nuts equally on each threaded rod, one can lift the rotating platform. Here, the big sprocket gear acts as a support that holds the rotating platform on the nuts.

2.4.3 Vacuum condition

Table 2.5 summarizes the pump models, their specifications, and the typical base pressure in the four stages of the BILT machine. In the UHV stage, the background pressure is on the order of 10^{-9} mbar after one week of bakeout. The varnish adhesive used to glue the bolometer element to the diamond absorber (Fig 2.42) cannot be heated above 65°C . Therefore the temperature rise of the bolometer had to be limited during bakeout. Heating the UHV chamber and its content is accomplished by two 500W halogen IR lamps (Victory, 13169R Klar) installed inside the chamber. The infrared radiation heats mostly the sample holder which reaches a temperature of about 100°C as measured by a K-type thermocouple spot-welded on a Ni sample. However, the temperature of the chamber wall stays below 40° due to cooling by convection. During the baking, I applied a continuous flow of cold nitrogen gas from the liquid N_2 dewar to the LHe reservoir such that the bolometer temperature (monitored by a silicon diode) is controlled below 60°C . For a more efficient bakeout, we should either install heater elements to the chamber walls or build a bakeout box or tent similar to what is used for the other UHV chambers in the lab.

Table 2.5 Turbo-molecular pumps installed on different pumping stages, their specifications, and the typical background pressures at every stage. *The pressure at the UHV stage drops to $1 \cdot 10^{-10}$ mbar when the bolometer dewar is cold.

Stage	Pump model	S_p (L/s)	f_{rot} (Hz)	Pressure (mbar)
Source	Edward STP iXR2206	2200	609	$3 \cdot 10^{-7}$
2 nd differential	Pfeiffer TMU520	500	832	$7 \cdot 10^{-8}$
3 rd differential	Pfeiffer TMU521	510	832	$5 \cdot 10^{-9}$
UHV	Pfeiffer TMU1000	880	653	$1 \cdot 10^{-9}$ (* $1 \cdot 10^{-10}$)

After bakeout by the method described here, an RGA spectrum recorded with the bolometer dewars at 300K still shows a significant amount of water ($4.7 \cdot 10^{-9}$ mbar), as shown in Figure 2.24. A similar bakeout procedure was applied when the bolometer was not installed. In this case, we observed a much lower water signal at $m/z = 18$ by about a factor of 30. Baking the bolometer only at 55°C is inefficient especially since the bolometer dewar assembly is pumped only through the 4 mm aperture in the bolometer cold shield. Adding additional venting holes in the cold shield could be used to increase the pumping speed. However, since the bolometer will only be operated with the dewars filled with liquid N_2 and liquid He there should be no significant outgassing from the cold bolometer.

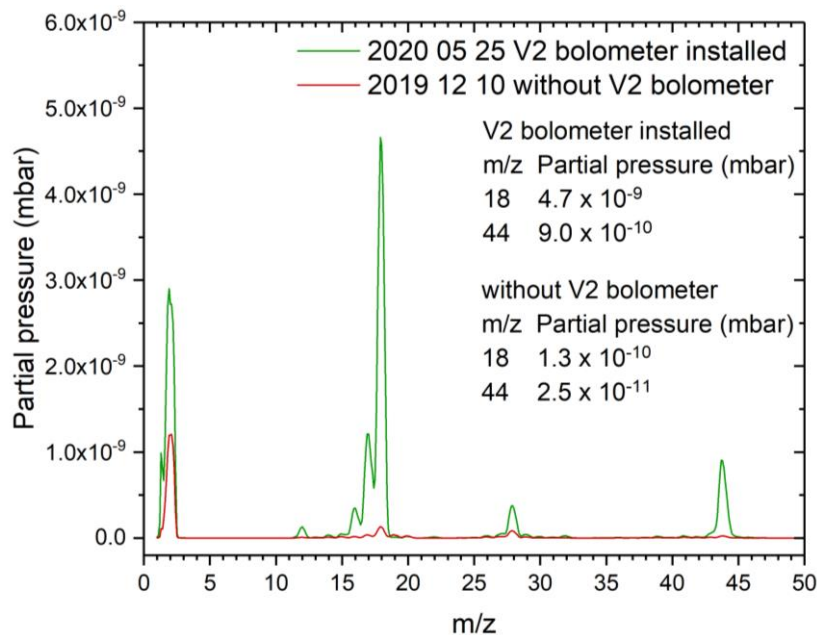


Figure 2.24 RGA spectra UHV chamber measured with and without the bolometer. Both spectra were measured after a week of bakeout. On the panel, I highlight the partial pressure of water ($m/z = 18$) and CO_2 ($m/z = 44$).

The other problem is that the bolometer is outgassing CO₂ according to the two RGA spectra measured with and without the bolometer installed, as shown in Figure 2.24. With the bolometer installed, the CO₂ partial pressure increased from $2.5 \cdot 10^{-11}$ to $9.0 \cdot 10^{-10}$ mbar. From a list of materials that constitute the bolometer, it is not clear which ingredient contributes to the outgassing. Fortunately, both the water and the CO₂ problem can be solved by cooling down the bolometer. As shown in Figure 2.25, the partial pressure of CO₂ reduces by more than a factor of 10 after cooling down both the LHe and LN₂ dewars. The RGA measurements show that when the bolometer is in its working condition, namely, the cold shield is cooled down to 77 K and the LHe dewar is filled with LHe, the partial pressures of both the water and CO₂ are negligible for our scattering experiments.

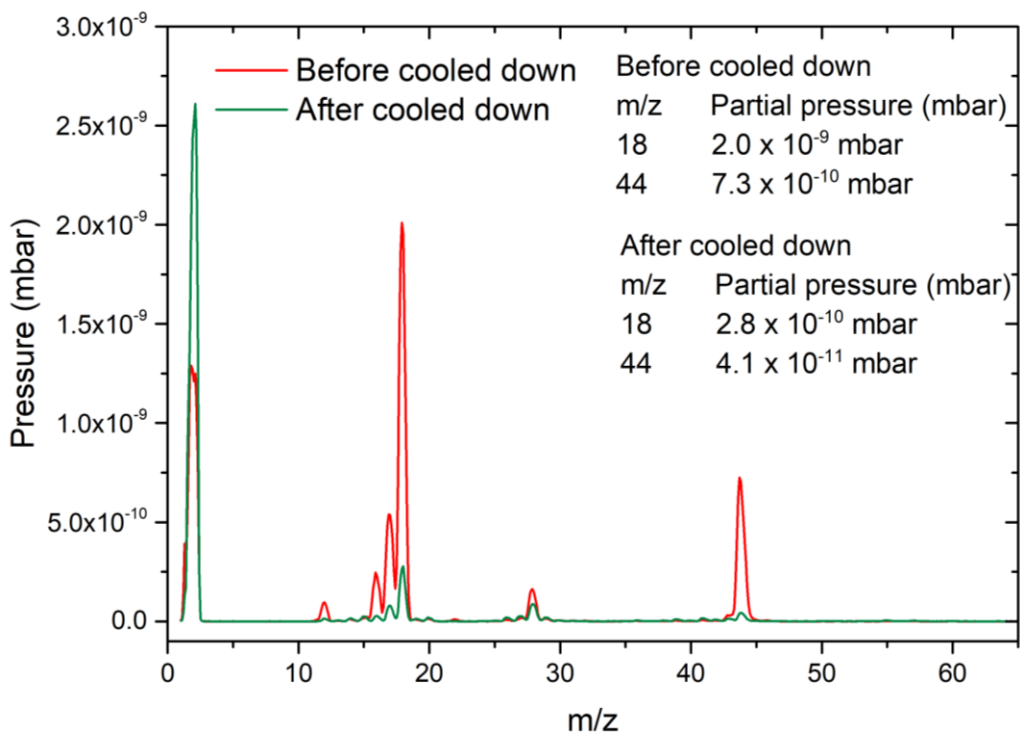


Figure 2.25 RGA spectra of the UHV chamber measured before and after cooling down the bolometer. The conditions “cooled down” mean the bolometer is at its operation conditions where the LN₂ dewar and LHe dewars are thermalized with LN₂ and LHe, respectively. After cooling down the bolometer, the partial pressure at $m/z = 44$ and the corresponding fragmentations at $m/z = 12, 16,$ and 28 reduced drastically.

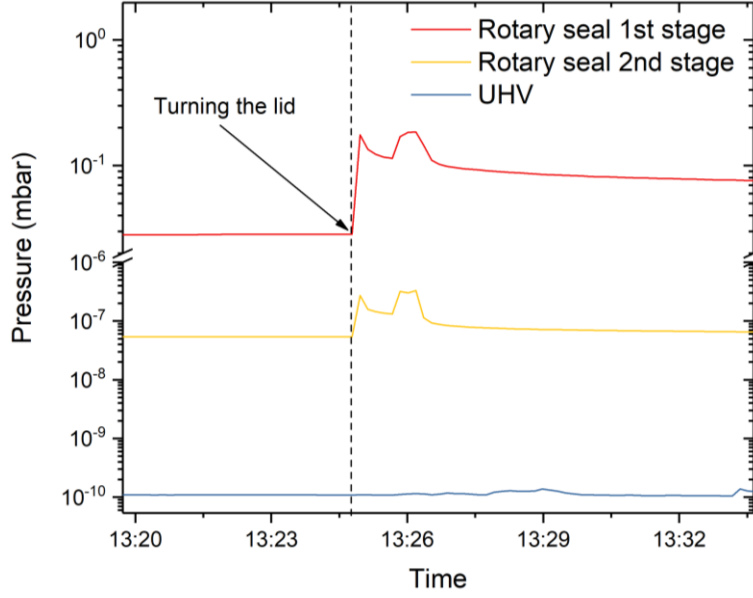


Figure 2.26 Pressure traces of the 1st, 2nd differentially pumped stages of the rotary seal, and the UHV stage. The dashed line highlights the timing (hh: mm) when the rotatory lid starts moving.

So far, I have presented the vacuum conditions of the BILT machine when the rotating platform is static. More importantly, we need the UHV stage still stay in good vacuum conditions when the platform is rotating. Figure 2.26 illustrates the pressure traces of the 1st, 2nd differentially pumped stages of the rotary seal, and the UHV stage. During bolometer rotation, the pressure in the 1st differential pumping stage increased from $3 \cdot 10^{-2}$ to $2 \cdot 10^{-1}$ mbar, in the second stage from $5 \cdot 10^{-8}$ to $3 \cdot 10^{-7}$ mbar and in the UHV chamber by less than $1 \cdot 10^{-10}$ mbar. This demonstrates the ability of the rotary seals for maintaining UHV conditions during bolometer rotation.

2.4.4 Molecular beam flux and dimensions

So far I have introduced the structure and the vacuum conditions of the scattering chamber, now I should continue to discuss the molecular beam flux and beam dimensions. The molecular beam cut from the supersonic jet expansion by the 1 mm skimmer in the source chamber passes two differential pumping stages before it enters the UHV stage. Figure 2.27 shows the dimensions between nozzle and skimmer and between two 1.75 mm diameters of collimators installed at the P2/P3 and the P3/P4 walls. Based on this geometry, the P3/P4 collimator is the limiting aperture that determines the beam size in the scattering, resulting in a beam divergence angle of 0.72° . When the molecular beam reaches the target surface located on the axis of detector rotation, the beam diameter expands to $d = 2.3$ mm (assuming free flight after the second aperture). With increasing angle of incidence, the beam shape projected on the target surface will change from circular to elliptical and the shape and area A depend on the angle of incidence on the surface θ :

$$A = \pi \times \frac{d}{2 \cos(\theta_i)} \times \frac{d}{2} \quad (2.13)$$

where A is the beam area projected on the surface at a given incident angle θ_i (measure from the surface normal), and d is the beam diameter at the axis of surface rotation. Table 2.6 lists the length of the long axis of the ellipse projected on the surface at several θ_i used often.

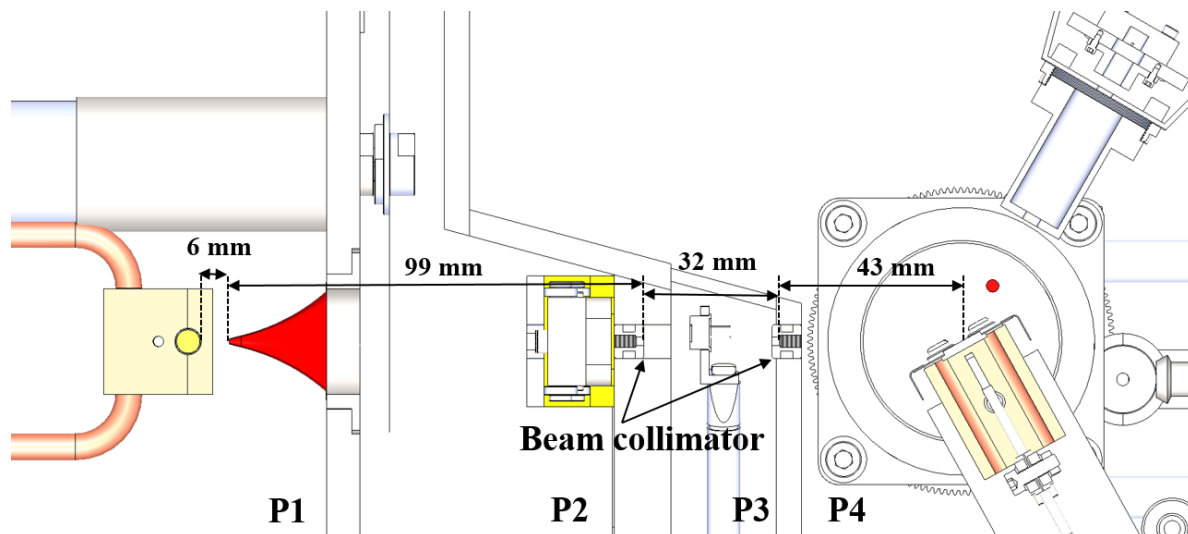


Figure 2.27 Section view of the BILT machine which highlights the nozzle-to-skimmer distance, the distance between collimators, and the collimator-to-rotational axis distance.

Table 2.6 Long axis length of the ellipse projected on the surface with θ_i used frequently.

Incident angle θ_i ($^\circ$)	Length of the long axis (mm)
31	2.7
36	2.8
45	3.3
54	3.9
59	4.5
65	5.4

The molecular beam flux incident on the target surface can be determined by a measurement of the partial pressure rise of methane measured by the QMS and the pumping speed of the turbo-molecular pump.

$$Flux = \Delta P \times S_p \quad (2.14)$$

First, we should calibrate the $m/z = 16$ signal of QMS with respect to the pressure rise caused by dosing pure CH_4 . This is particularly useful when a seeded sample gas is used. The mass-selected signals of QMS can directly measure the signal corresponding to the target species and filter out the contribution from the carrier gas. When using 3 bar of neat CH_4 in the nozzle at 298 K to generate a molecular beam shooting to the UHV chamber, the pressure rise measured by a cold cathode gauge is 7.8×10^{-8} mbar. Given the sensitivity factor of CH_4 to the cold cathode gauge 0.71, the effective pressure is thus 5.5×10^{-8} mbar. In the meanwhile, the $m/z = 16$ ion current measured by the QMS is 3.8×10^{-12} amps. Note that the ion current is measured simply by the Faraday cup of the QMS without the channeltron enabled. We then derived the calibration factor of QMS to CH_4 which is 1.4×10^4 mbar/amp. When using a 3 bar gas mixture of 3% methane in helium at a nozzle temperature of 298 K to generate a CH_4 beam, the QMS measures an ion current of 7.7×10^{-13} amps for $m/z = 16$, corresponding to a pressure rise of 1.1×10^{-8} mbar.

The nominal pumping speed of the UHV turbo-molecular pump for N_2 is 920 L/s. However, a 0.8 mm width of mesh is installed on the pump inlet to protect the blade from any falling objects, which reduces the pumping speed to 625 L/s (given the conductance of the mesh 1952 L/s). I assume the pumping speed of CH_4 takes a similar value as for N_2 . Using the relation $1 \text{ bar}\cdot\text{L} \cong 2.5 \cdot 10^{22}$ molecules, one can already calculate the flux of CH_4 by

$$\text{Flux} = \Delta P \times S_p \times 2.5 \times 10^{22} \quad (2.15)$$

which gives rise to $1.7 \cdot 10^{14}$ molecules/s. Consider scattering experiments with an incident angle of 65° , which gives rise to a beam size projected on the surface of 0.098 cm^2 . Then the number of molecules hitting the surface per cm^2 and sec is $1.8 \cdot 10^{15}$ molecules/ $(\text{cm}^2 \cdot \text{s})$. By knowing the sticking coefficient of a given gas-phase molecule and metal surface combination, one can calculate the number of monolayers build up within a given amount of time.

2.4.5 Pyroelectric detector

In a supersonic jet expansion, the different degrees of freedom of a molecule are cooled at different rates resulting in a non-equilibrium between translation, rotation, and vibration. Translational temperatures T_{trans} of a few K are measured by the TOF method described earlier in this chapter. Rotations take more collisions with the carrier gas and therefore the resulting rotational temperature $T_{\text{rot}} > T_{\text{trans}}$. The T_{rot} of the incident molecular beam can be determined by infrared pumping with an IR-OPO of the different rovibrational transitions and by measuring the rotational state populations using a pyroelectric detector inserted into the molecular beam. IR power modulation in combination with lock-in detection of the pyroelectric signal allows for state-selective detection of the methane molecule in the molecular beam.

The pyroelectric detector has a square sensor area with an edge length of 3.5 mm and is glued on an L-shape bracket with a circular opening, as shown in Figure 2.28. A 30 cm long aluminum rod connects the bracket and the front of a linear motion feedthrough which provides 1" of linear motion. The linear motion feedthrough together with a CF16 Tee is installed on a CF16 port tilting 12° from the horizontal plane. For alignment of the IR pump laser and characterization of the rotational state populations in the incident beam, we introduce the detector into the molecular beam by a linear motion feedthrough. The accompanying CF16 Tee provides access to a 9-pin subminiature type-C electrical feedthrough for electrical connections of the detector. The output signal is collected by a home-built, battery-powered amplifier which provides two different gain factors 10 and 100. Since the amplifier has a 4-pin LEMO input port, a cable that has a 9-pin subminiature plug at one end, and a 4-pin LEMO plug at the other end is needed. Figure 2.29 illustrates the pinout of the cable.

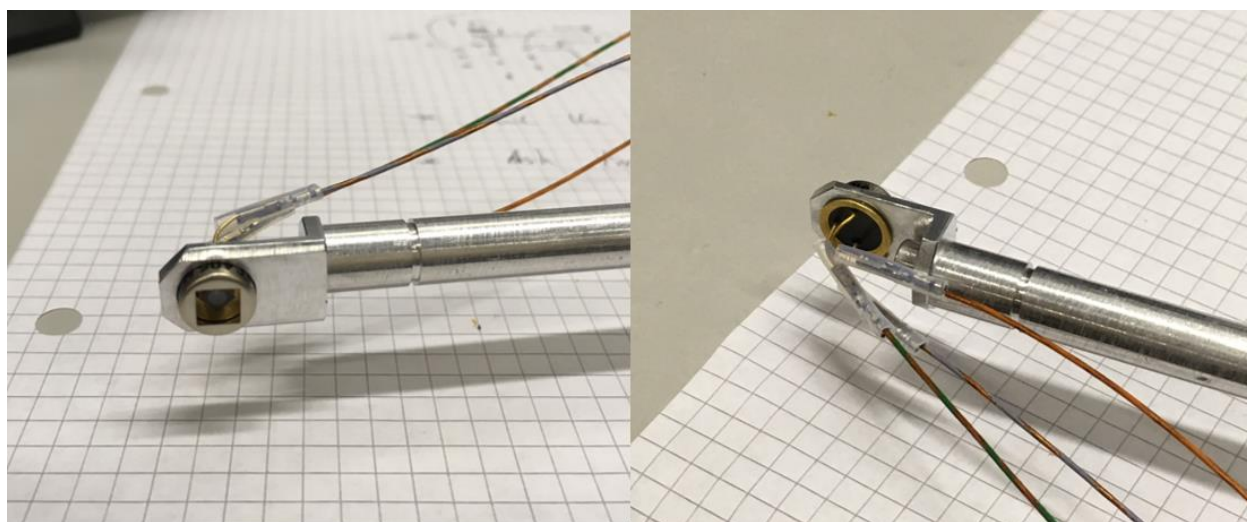


Figure 2.28 Left: front side of the pyroelectric detector. The detector has a square sensor area with an edge length of 3.5 mm. Right: Back of the detector. The leads of the detector connect to Kapton insulated wires via crimp connectors. The crimp connectors are covered by Teflon tubes to prevent a short circuit. In the end, a 9-pin subminiature type-C plug collects these three wires and connects to a CF16 9-pin subminiature type-C electrical feedthrough.

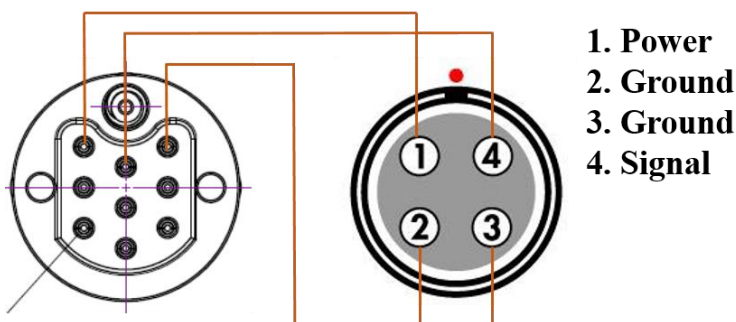


Figure 2.29 Pinout of the cable connecting the feedthrough of the pyroelectric detector to the home build amplifier. Left: 9-pin subminiature type-C female plug. Right: 4-pin LEMO male plug.

Using the pyroelectric detector together with IR laser pumping, one can characterize the state distributions of the incident beam and state preparation by the IR laser. Figure 2.30 illustrates an example of state-selective measurements of a CH₄ molecular beam. In these measurements, the pure CH₄ beam corresponding to $E_i = 100$ meV was shooting continuously, whereas the laser, which excited the $\nu = 0, J = 0$ of the CH₄ beam via R(0) ν_3 fundamental transition, was power modulated by a shutter (UniBlitz) at 2 Hz. To reach complete population inversion, the laser excitation was performed via the rapid adiabatic passage (RAP) [58]. The laser frequency was stabilized by the lamb-dip technique [49]. By lock-in detecting the pyroelectric signal after the amplifier, I recorded the signal corresponding to CH₄ molecules that were laser-excited, as shown in the left panel of Figure 2.30. Next, I adjusted the laser power by rotating a $\frac{1}{4}$ waveplate placed at the upstream of a polarization beam splitter and recorded the lock-in signal, i.e. recording a fluence curve, as shown in the right panel of Figure 2.30. There, we saw the asymptote was reached, indicating the population inversion was almost completed. In this case, the signal at the highest power was directly proportional to the population of the measured state. In terms of state-preparation of the incident beam, from the results of the fluence curve, we knew the molecules originally reside in $\nu = 0, J = 0$ were almost ($> 95\%$) excited to the desired state (here, in our case, $\nu_3, J = 1$).

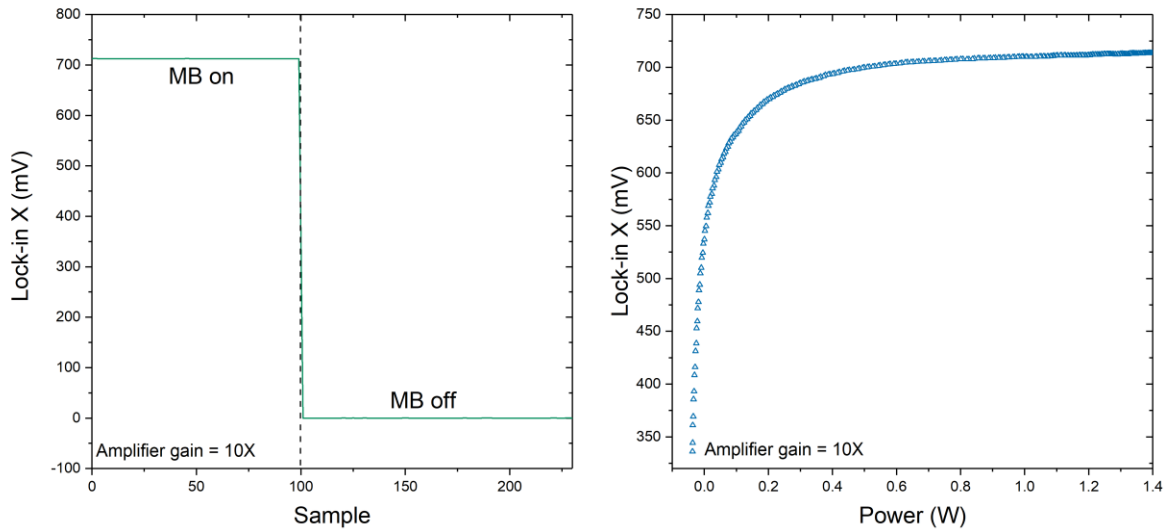


Figure 2.30 Left: Lock-in detected pyroelectric signal of the CH₄ R(0) ν_3 fundamental transition with $E_i = 100$ meV. The signals are recorded 100 samples for molecular beam on, and another 100 samples for beam off to subtract the background value. Right: Fluence curve of the R(0) ν_3 fundamental R(0) transition of the incident CH₄ beam with $E_i = 100$ meV. In both measurements, laser excitations are performed by Rapid adiabatic passage with a 25.4 cm cylindrical lens. The IR laser (Argos OPO I) was locked by the lamb-dip technique.

2.4.6 Sample mount and manipulator

A surface science apparatus needs tools for surface preparations and analysis such as an ion sputter gun, an Auger spectrometer (AES), and a low-energy electron diffraction spectrometer (LEED). A mechanism that provides for sample motion between different measurement positions within the vacuum chamber is also necessary. Furthermore, experiments of surface science normally require temperature control for the sample of interest as the reactivity can be different at different surface temperatures. Therefore, heating and cooling mechanisms also have to be included.

Figure 2.31 shows an overview of the sample mount as well as the manipulator. The sample of interest is mounted on a Ta plate which is attached to a copper block that provides for both sample heating and cooling. Below the sample mount, a sample rotation platform enables the rotational motion needed for controlling the incident angle of the molecular beam. This platform connects to a CF100 base flange via a 114 cm long stainless steel tube. On the base flange, we installed electrical feedthroughs for delivering electricity needed for surface heating, tube feedthroughs for transferring liquid nitrogen, and a rotary motion feedthrough for rotating the sample mount. The entire assembly is inserted into an X-Y-Z manipulator through a Z-motion travel flange. This manipulator (MetallicFlex) provides 45 cm of Z-motion (along the MB axis), enough to move the sample between LEED, Auger, sputter gun, and scattering position. On the X-Y table of the manipulator, it provides +/- 25 mm for both X and Y motions. With the X-motion (horizontal and normal to the MB axis), one can bring the sample to a proper working position of LEED and Auger measurements.

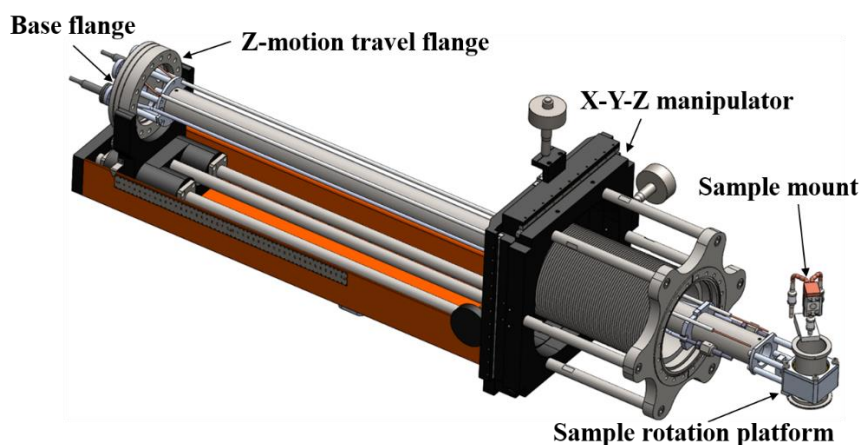


Figure 2.31 3D model of the sample mount as well as the manipulator. To illustrate the structure of the connections, the bellow of the manipulator is not shown.

Figure 2.32 illustrates the design of the sample mount which is based on a liquid N₂ cooled copper block that contains a filament for e-beam heating. At the front, a Ta plate holds a 12 mm diameter sample disk which with a top-hat shape. The sample is fixed to the Ta plate by two Ta wires spot-welded across the back of the sample disk. The Ta plate is electrically insulated from the copper block by two sapphire plates of 0.5 mm thickness that provide good thermal conductivity. The Ta plate is fixed on the copper block by four M3 screws which are insulated from the Ta plate with ceramic spacers (split bushes from Tectra GmbH) as shown in Figure 2. 32 (b).

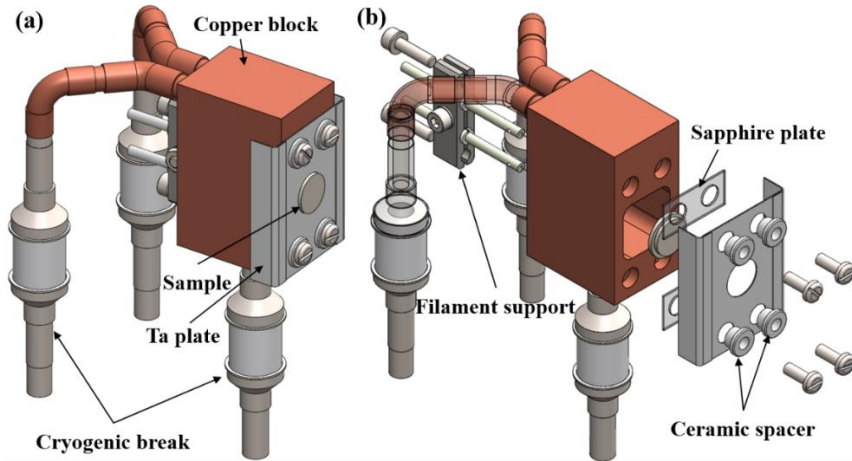


Figure 2.32 (a) 3D model of the sample mount. The copper block acts as a base where the rest of the parts attach. The block is mounted on a cryogenic break connecting to the sample rotation platform. Two other cryogenic breaks are brazed to the back of the block for liquid nitrogen cooling. (b) Exploded view of the sample mount. The copper block has a central opening to accommodate the heating filament. The sample is mounted on the front and centered at the opening.

A tungsten filament is installed inside the copper block. The filament is made of a 0.25 mm diameter tungsten wire in a rectangular coil shape, as shown in Figure 2.33 (b). This shape is formed by wrapping the tungsten wire on a 4 mm wide stainless steel plate with a thickness of 1 mm. The two ends of the filament are then inserted into 1 mm diameter holes at the end of the 2.5 mm diameter Ta rod. The filament is fixed on the Ta rod by M1.2 screws coming from the side of the rod. To put the filament in place, a pair of stainless steel clamps hold the two Ta rods with ceramic bushes as insulators. The configuration of the surface heating is shown in Figure 2.33 (a). To make the electron bombardment heating efficient, the filament is located only a few millimeters from the back of the sample. Also, the shape of the filament is chosen to expose a large surface area facing the sample.

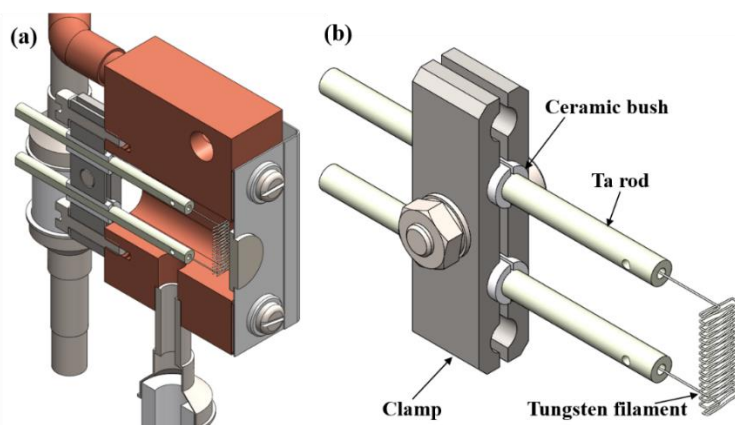


Figure 2.33 (a) Section view of the sample mount which shows the configuration of the surface heating. (b) 3D model of the filament and filament support assembly. The two ends of the filaments are fixed on the ends of the Ta rod by M1.2 screws. These two rods are then sandwiched by ceramic bushes and a pair of stainless steel clamps.

During surface heating, we would like to concentrate the heating power on the sample and keep the other parts of the sample mount cold to avoid outgassing and sample contamination. To achieve this, the copper block is cooled by flowing liquid nitrogen. The copper block has a channel for flowing liquid nitrogen supplied via copper tubes and cryogenic breaks connected to flexible stainless steel bellows to allow for surface rotation. The copper tubes, cryogenic breaks, and the bellows are brazed together using the brazing alloy Castolin 1020 consisting of 57% of silver, 22.5% of copper, 5% of tin, and 15.5% of zinc. Although zinc is normally not a UHV-compatible material, the brazing alloy has been used by other surface scientists who performed 120°C of bakeout and observed no measurable amount of zinc.

The sample mount is attached to a rotation platform providing support and rotary motion. As shown in Figure 2.34, the platform consists of a bearing housing, a Z-slide, and a gear assembly. The bearing housing is the main body of the platform which holds a rotating tube with two bearings (RBC, KA020CP0) giving smooth rotary motion. To make the bearings UHV compatible, the original grease lubricant in the bearing was removed by solvent and replaced by MoS₂ powder. A pair of bevel gears transmit the sample rotation and provide a gear ratio of 0.5 (36/72 teeth). At the other end of the vertical gear shaft, a 14 teeth spur gear is installed. This 14 teeth spur gear then drives a 144 teeth spur gear at the bottom of the rotating tube. The entire set of gears thus gives rise to a reduction ratio of 21. Finally, the rotary motion from the rotary feedthrough is transmitted to the horizontal bevel gear through a long (about 120 cm) 6 mm diameter stainless steel shaft with bellow connectors coupled with the three shafts together (rotary feedthrough-long shaft-gear shaft).

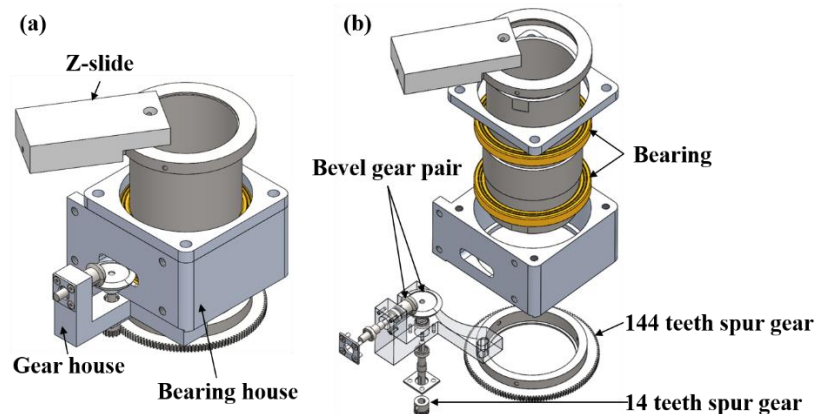


Figure 2.34 (a) 3D model of the sample rotation platform. The platform has a rectangular bearing housing as the main body. Inside, it holds a rotating tube with two bearings. On the top of the tube, a Z-slide, where the sample mount sits, is fixed on a collar. This Z-slide provides a translational motion for aligning the sample to the sample rotation axis. (b) Exploded view of the sample rotation platform. On the gear housing, there is a pair of bevel gears with a gear ratio of 0.5. Together with the pair of spur gears with the gear ratio of 14/144, the entire gear set provides a reduction ratio of 21.

The sample rotation platform is connected to the 114 cm long stainless steel tube via four spacer rods and a collar, as shown in Figure 2.35 (a). A similar structure is also used for installing the tube to the CF100 base flange. Since the base flange has to take over the torque introduced by the weight of the entire sample mount assembly on the other side of the lever arm, we design a wider collar and six spacer rods for high mechanical strength.

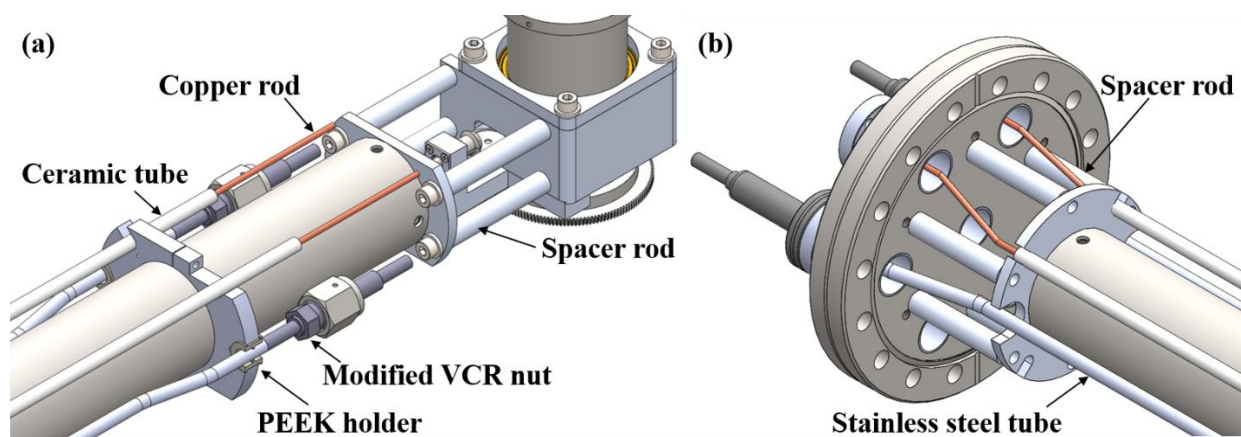


Figure 2.35 (a) Design of the connections between the sample rotation platform and the stainless steel tube. Please note that the bellows for transferring liquid nitrogen and the copper wires for delivering electricity are not shown in this model. (b) A 3D model which illustrates the connections between the stainless tube and the CF100 base flange.

The CF100 base flange includes seven CF16 half nipples which hold various feedthroughs. Figure 2.36 shows the arrangement of the seven half nipples. On the top two nipples, we install electrical feedthroughs that are specially designed for the power socket of the power supply (PREVAC, Heat3). On two of the nipples at the middle level, there are two 6 mm diameter cryogenic tube feedthroughs for transferring liquid nitrogen. In the center, the rotary motion feedthrough is mounted for driving the sample rotation. At the bottom, there is a two-pair, K-type thermocouple feedthrough. One is connecting to a K-type thermocouple spot-welded to the edge of the sample and the other is connecting to the Ta plate holding the sample. The final nipple has a 4-pin electrical feedthrough installed. Currently, only two of these pins are used. One is for applying a bias voltage to the copper block when performing E-beam heating, and the other is for grounding the sample such that the sample doesn't charge up.

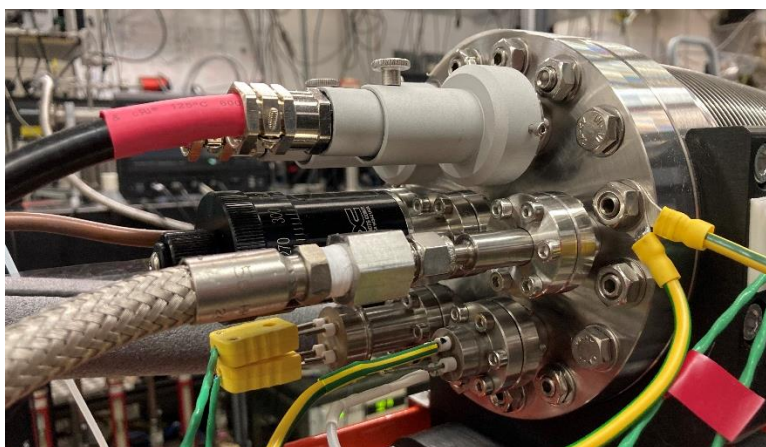


Figure 2.36 Arrangement of the feedthroughs installed on the CF100 base flange that couples the sample mount to the manipulator.

Between the electrical feedthroughs and the sample mount, we use 2.5 mm diameter of copper rods that run along the stainless steel tube to provide electrical connections. These rods are insulated by 6 mm ceramic tubes. One end of the copper rod couples to the electrical feedthrough by a barrel connector. The other couples to a flexible copper wire by a barrel connector. This electric wire is made by twisting three braided electrical wires together and is covered by ceramic beads for electrical insulation. Finally, the wire connects to the Ta filament support, again by a barrel connector, as shown in Figure 2.37.

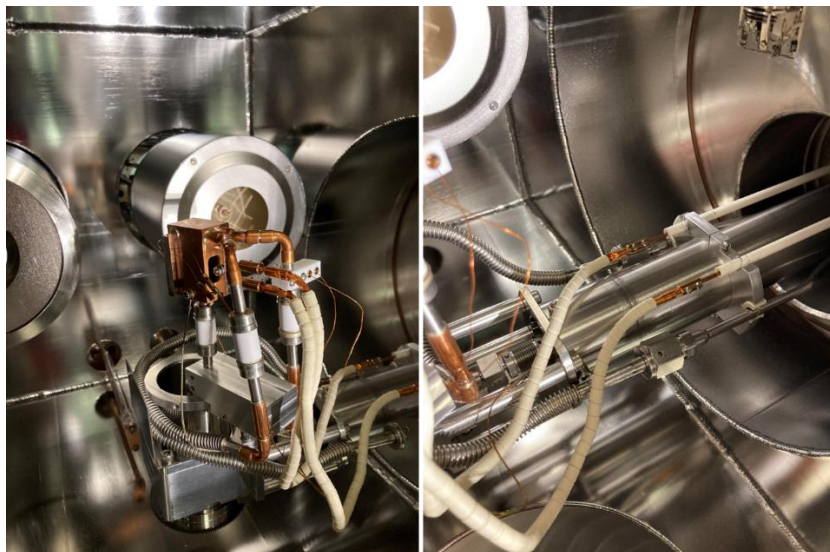


Figure 2.37 Left: Routing of the electrical wires and the liquid nitrogen bellows on the sample mount. Right: Connections from the flexible part to the stationary part.

The liquid nitrogen tubing, the cryogenic tube feedthrough, a 6 mm diameter stainless steel tube, and a VCR connector are welded together to form a single part. Here, we reduced the dimension of the male VCR nut such that it can insert into a CF16 port on the base flange. The VCR connector then links to the bellow of liquid nitrogen brazed on the sample mount. Note that the two liquid nitrogen tubes do not have the same length. This is because the sample mount has an asymmetric 90° of rotational motion and displaces the bellow more at a specific side. The tube at this side is thus designed shorter to compensate for the longer displacement. Near the sample mount, I designed an aluminum disk holder on the stainless steel tube. This disk has several cutout areas to accommodate the ceramic and liquid nitrogen tubes. Especially for the liquid nitrogen tube, instead of having direct contact with the disk, I placed a PEEK bush that has a low thermal conductivity as it is not necessary to cool down the disk.

2.4.7 Sample preparation and characterization

Studying surface reaction dynamics under well-defined conditions requires a clean sample surface as the contaminants can change the surface reactivity and can prevent a correct interpretation of the results. In the BILT machine, surface cleaning is done by Ar^+ ion sputtering. Following the sputter cleaning, an annealing process is needed to recover the single-crystal structure. The surface cleanliness is confirmed by an Auger electron spectroscopy (AES). In addition, the surface structure can be verified by low-energy electron diffraction (LEED). This section describes the surface preparation and characterization in detail.

Surface sample heating is carried out by the E-beam method which accelerates the electrons emitted from a hot tungsten filament by an electric field of 1000V. Using the setup described in Figure 2.33, for heating a Ni(111) sample at 673 K, we pass 4.8 A of current through the tungsten filament by a power supply (PREVAC, Heat3) with a bias voltage of 1000 V applied on the filament. In this condition, the emission current of the filament is measured to be 4 mA, corresponding to 4 W of power. The sample is grounded such that no charge is built up during the heating process. The copper block is biased at about -1300V to deflect electrons toward the surface and prevent heating of the copper block. To keep the surface temperature stable, the output power of the power supply is regulated by the Proportional-Integral-differential (PID) feedback loop of the power supply using the surface temperature as an input. A hot surface normally outgases and may contaminate the sample which is not ideal for studying surface science. To prevent the surrounding of the sample from heating up, during the surface heating process, liquid nitrogen is flowing to keep the sample mount cold. The cooling efficiency can be indicated by the Ta plate temperature. When the Ni(111) sample is heating at 673 K, the Ta plate is only at 153 K, whereas it is 113 K when the heater is off.

For removing contaminants on the surface, we perform Ar⁺ ion sputtering using a fine focus ion gun (Omicron, ISE100) which provides maximum beam energy of 5 keV. This ion gun is installed on a CF40 port tilted 20° down about the horizontal plane and 60 mm away from the scattering position. The ion gun provides an adjustable working distance of 23 to 150 mm (from the end cup to the sample). For surface cleaning, we position the sample away from the focusing point. In the current configuration, the working distance is 203 mm. Thus, we are using the diverging part of the ion beam for cleaning and the beam size is broad enough to cover the entire sample surface. Given the dosing pressure of Ar $1.2 \cdot 10^{-7}$ mbar, 4 mA of emission current, and 1600 eV of the beam energy, the Ni(111) sample received 1.6 μ A of ion current measured by a picoamp meter. At the beginning of every experimental day, the Ni(111) sample was cleaned using this condition at 323 K of surface temperature with 45° of incident angle for 20 minutes and followed by 10 minutes of annealing at 973 K.

After surface cleaning procedures, the surface contaminations are characterized by the Auger electron spectrometer (Staib Instruments, ESA150) with the Staib energy analyzer. This Staib energy analyzer is essentially an improved cylindrical mirror analyzer (CMA). Different from the classical CMA which has an entrance slit defining the energy resolution, the Staib CMA is equipped with a retarding optic in front of the cylinders. A negative voltage V_1 is applied to the retarding optic that decelerates electrons. Only the electrons with energy greater than eV_1 can pass the retarding field and enter the cylinders. There, the inner cylinder is also biased at V_1 , but a higher voltage V_2 is applied to the outer cylinder. The resulting CMA field determines the energy resolution of the system. This design allows a larger working distance (45 mm for the model ESA150) and less critical sample positioning. The energy resolution is electrically adjustable and thus there is no need to mechanically adjust the entrance slit. Furthermore, unlike the traditional CMA, increasing energy resolution doesn't reduce electron transmission.

Figure 2.38 shows the Auger spectra before and after the cleaning procedure. Before cleaning the Ni(111) surface, one can see a strong peak at 274 eV corresponding to the KLL transitions of carbon. Plus, at 513 eV, there we observed the KLL transitions of oxygen. After cleaning the surface, these two contaminants all vanish, and the three characteristic peaks of nickel LMM transitions above 650 eV increase.

As one may have noticed, the Auger spectra measured by the Staib ESA150 show a feature of higher response in the low-energy region. The reason causing this stronger background signal at low energy is not immediately clear. Here, I summarize the properties observed in the measurements. First, the low-energy background is sensitive to the lock-in phase angle. As shown in Figure 2.39, the low energy background is reduced if I change the phase angle from 167.3 to 153.0°. The phase angle of 167.3° is obtained by optimizing the elastic electron peak signal. This value also agrees with what is provided in the test report. Without sacrificing too much of the desired Auger electron signal, I found that using the phase angle 153.0 can reduce the low energy background significantly. The observation suggests that these unwanted low-energy electrons have a different arrival time to the SEM than the desired Auger electrons.

The second puzzle is related to the unreasonable peak height of the Ni characteristic peak at 61 eV. According to literature reported spectra [49,59], this low energy peak at 61 eV should display a similar peak height as the peak at 845 eV. However, in Figure 2.39, even with reduced low energy background, the peak height at 61 eV is about a factor of 10 stronger than that of 845 eV, suggesting that our Auger electron spectrometer has higher sensitivity in the lower energy region. In other words, the sensitivity shows an energy-dependent feature. This problem needs to be solved in the future for accurate quantitative measurements.

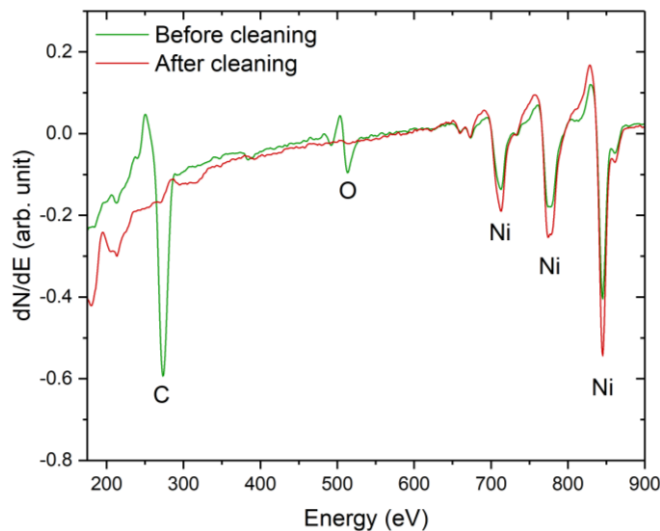


Figure 2.38 Auger spectra measured before and after surface cleaning. The spectra were measured with the following conditions. SEM gain: 1300 V, emission current: 4.5 μ A, step width: 1 V, modulation: 7 div, dE/E : 1 %, Lock-in sensitivity: 50 mV, and time constant: 300 ms.

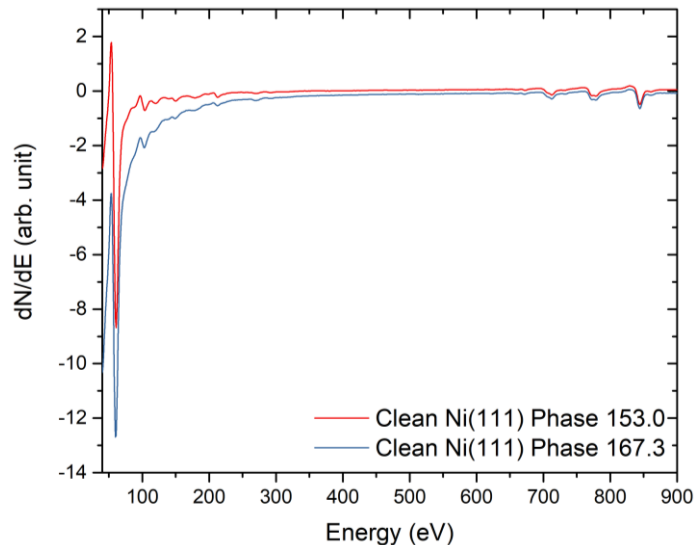


Figure 2.39 Auger spectra of a clean Ni(111) surface with two different phase angles. The experimental parameters are set the same as the spectra in Figure 2.38.

Surface cleaning by Ar ion sputtering can cause damage to the surface crystalline structure. Therefore an annealing process is needed to recover the surface structure. The surface crystalline structure can be characterized by the low-energy electron diffraction spectrometer (LEED). A low energy electron beam of 150 eV which corresponds to about 1 Å of de Broglie wavelength is suitable for diffraction experiments. Furthermore, this energy provides the minimum mean free path of electrons in solids, making these electrons optimum for probing surface structure. After surface annealing at 973 K for 10 minutes, a LEED pattern was measured by the LEED spectrometer (OCI Vacuum Microengineering, BDL800), as shown in Figure 2.40. There we observed sharp and bright hexagonal spots, indicating a well-ordered and clean (111) crystalline structure.

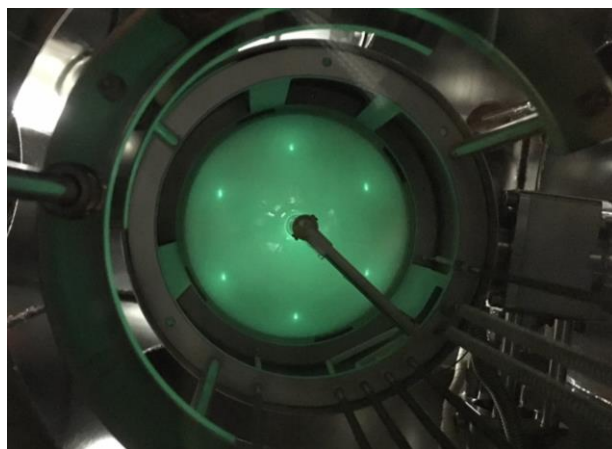


Figure 2.40 LEED pattern of the Ni(111) surface measured after the surface cleaning procedure. The pattern was measured with 150 eV of beam energy, 2.55 A of filament current, and 3.5 kV of screen voltage.

The LEED spectrometer is installed in a CF160 port which has a flange-to-MB axis distance of 346 mm. The LEED spectrometer has a retracted flange-to-sample distance of 273 mm and 100 mm of extension motion. For measuring a LEED pattern when the sample is sitting at the MB axis, 73 mm of extension is needed to bring the LEED optics to the working distance. The motion feedthrough provides 1.5875 mm of motion for one rotation, so 46 turns are needed to get the working distance.

2.5 Cryogenic bolometer

The bolometer is a thermal detector for radiation that measures a temperature rise caused by the heat dissipated into the bolometer element. It was first developed as an infrared detector and used in astronomy [60]. Back in the 1960s, Scoles and coworkers adapted a bolometer as a molecular beam detector [61]. Later, Miller et. al. expanded the usage of the bolometer to surface scattering experiments [14,15,46]. The bolometer detector used in the BILT machine is a doped silicon semiconductor (Infrared Laboratories, unit number: 3620) which acts as a very sensitive energy detector. The electrical resistance of the Si-element is very strongly temperature-dependent and by attaching the small bolometer element to a diamond adsorber disk it can be used as a highly sensitive molecular beam detector. When molecules collide with and adsorb on the cold adsorber they will transfer their internal and kinetic energy to the bolometer element, causing a change in electrical resistance. Using a bias current, this resistance change can be detected by the voltage drop across the bolometer which can be amplified and measured. Different than a metal, whose resistance increases linearly with temperature, the resistance of a semiconductor device reduces exponentially as the temperature increases. To improve the performance of the bolometer, one normally operates the bolometer at a cryogenic temperature. In this condition, the heat capacity reduces, and the responsivity increases.

2.5.1 Structural overview

Figure 2.41 (a) shows the structure of the bolometer detector which is mounted on a bracket attached to the cold plate of the LHe dewar. The dewar has a capacity of 2.29 L which is expected to provide about 20 hours of hold time. To reach this hold time, a liquid nitrogen cold shield is needed to protect the LHe dewar from room temperature IR radiation. The cold shield has direct contact with the liquid nitrogen dewar which has a capacity of 1.49 L. Between the LN₂ and the LHe dewar, three pieces of fiberglass supports provide thermal insulation. The entire assembly is integrated into a CF160 (8") flange where one finds an LHe and an LN₂ filling port, and a CF16 9 pin electrical feedthrough. There, again, fiberglass supports are used for thermal insulation between the flange and the LN₂ dewar. After transferring liquid helium and pumping through the lambda point, the bolometer temperature typically drops to about 1.7 K.

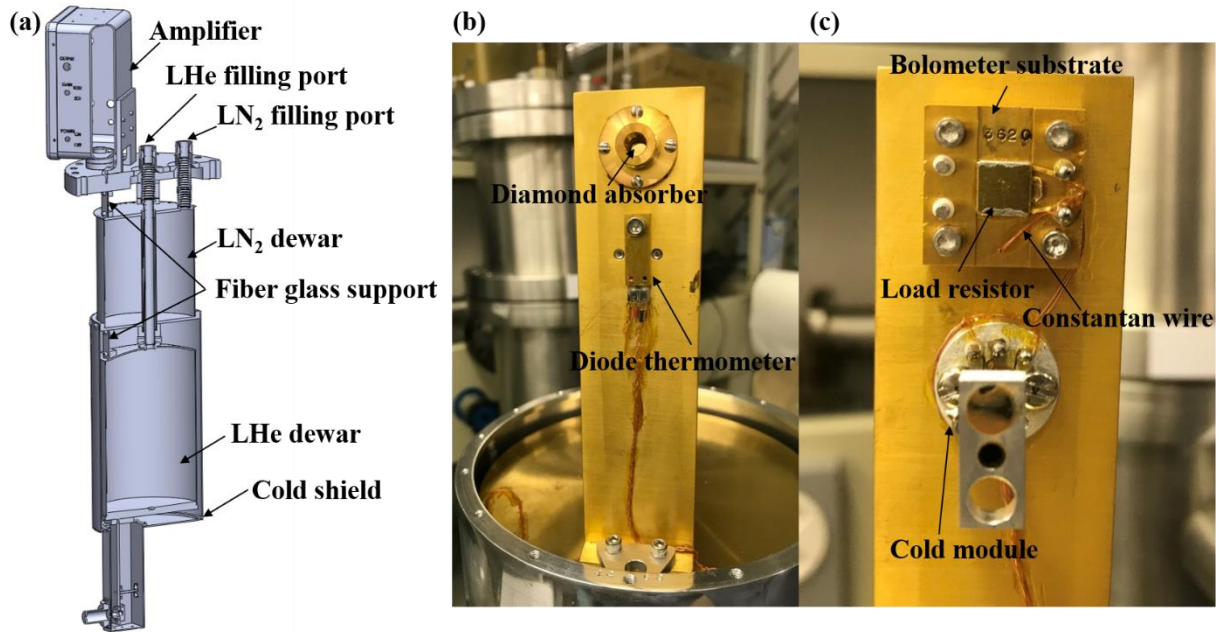


Figure 2.41 (a) 3D model of the bolometer detector in section view. (b) The front side of the bolometer pedestal. Inside the baffle, one can see the diamond absorber with Ag/Cr coating at the backside. Above the baffle, there is a doped silicone thermometer. (c) The backside of the pedestal. The bolometer element is installed inside the rectangular substrate. The cold module with the JFET is sitting near the bolometer substrate with a minimum wire length to prevent noise pick up.

Taking a closer look at the bolometer element, it is suspended by two copper leads on a rectangular substrate, as shown in Figure 2.42. These two leads are glued to the bolometer element with silver epoxy and provide thermal conductivity to the cryostat. To increase the detection area, a 4 mm round diamond absorber is glued to the bolometer element with GE varnish originally. However, in April 2021, the bolometer showed an unstable signal and reduced bandwidth. It was determined that the varnish used to glue the diamond absorber had deteriorated and showed a “gummy” texture reducing the thermal coupling of the bolometer to the cryostat. Therefore the bolometer was returned to IR labs for repair where the GE varnish adhesive was replaced by Stycast which is supposed to be more resistant to heating. The diamond absorber has a wedged geometry with 0.12 mm on the high side and 0.08 mm on the low side. On the backside of the diamond, it has a Cr/Ag coating that should reflect over 98% of light over a broad spectral range in order to reduce the bolometer response to stray light. One of the leads holding the bolometer element is grounded and glued on the copper substrate by GE Varnish. This Varnish was also replaced by Stycast during the repair. The second lead is electrically insulated but in thermal contact with the cryostat by passing it through a cap jewel to the backside of the substrate and connects to a Constantan wire whose resistance is independent of temperature. The cap jewel is a sapphire disk, providing a good thermal conductivity but electrical insulation.

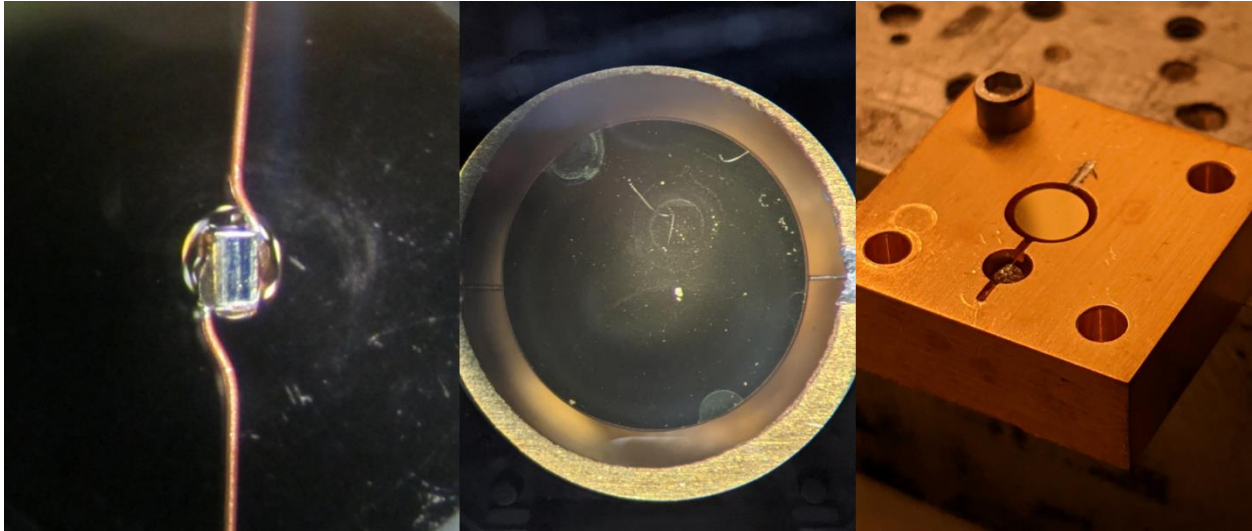


Figure 2.42 Left: The Si bolometer element bonded to the backside of the diamond absorber. Middle: Front side of the diamond absorber. The bolometer/diamond assembly is suspended by two copper wires on the copper substrate. Right: Front side of the bolometer substrate. One of the copper wires is glued to the substrate, and the other is held by a sapphire disk to prevent the signal short out but still provide a good thermal conductivity to the cryostat.

Besides the bolometer element, the circuit also contains a $20\text{ M}\Omega$ load resistor, and a bias battery, as shown in Figure 2.43. Typically the resistance of the load resistor is much greater than the bolometer resistance to prevent high current load which can damage the bolometer element. Plus, the bias current can be considered constant. The voltage drop across the bolometer is first amplified by a JFET (J230) in the source follower configuration. In this case, the JFET provides a voltage gain of unity but a large gain of current. In other words, it couples a signal source with very high impedance to an output circuit with low impedance and therefore serves as a buffer amplifier that protects the signal source from current load. Since the JFET electrical conductance diminishes at a temperature below 60 K, it is suspended by a fiberglass post on the base of the cold module to prevent direct contact with the cryostat. Furthermore, the cold module has a heater integrated. When the power is on, it heats the JFET to about 77 K. After the JFET, the second stage of the preamp amplifies the voltage by the available gain factors of 10, 100, 200, and 1000. This amplifier is AC-coupled, hence only a time-varying signal can be measured. A constant power such as the background IR load from the room temperature chamber will be filtered out.

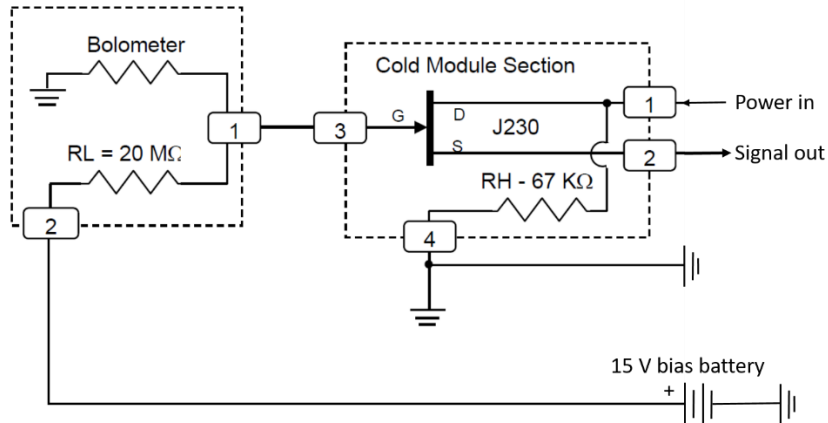


Figure 2.43 Circuit diagram of the bolometer as well as the JFET. The figure is provided by Infrared Laboratories.

2.5.2 Characterization and modification

The performance of the bolometer (#3620) was first tested in the old surface science apparatus to compare the signal with the old bolometer (#3518). In this case, the experiments are carried out in the same scattering geometry, molecular beam flux, and lock-in setting, therefore the difference in the signal contributes mainly to the sensitivity of the bolometer. In the remainder of the thesis, I will use the term “V2” and “V1” referring to the new bolometer with the unit number 3620, and the old one (3518), respectively.

For the first test, we compared the sensitivity of the V2 bolometer with the V1 bolometer used previously on the old machine. For this test, we performed He atom scattering from a 673 K Ni(111) surface with a modulation frequency of 142 Hz. For the V2 bolometer, we observed a signal of only 0.53 mV at the specular position using a gain of 10. This signal, taking into account the different gain factors, was a factor 13 weaker than what was observed previously with the V1 bolometer (137 meV with a gain factor of 200). For methane scattering, no signal could be observed above the noise background. Obviously, there was a serious sensitivity problem with our new V2 bolometer which was specially designed by IR-labs for our BILT machine!

The responsivity of a bolometer can be characterized by measuring the voltage drop across its resistance for a given bias voltage V_{bias} and a corresponding heating power applied to the bolometer. Variation of V_{bias} and measurement of the voltage drop across the bolometer V_{bolo} , one obtains a load curve for characterizing the bolometer DC characteristics. Instead of the 15 V bias battery, we used an external power supply to apply the bias voltage from 0 to 40 V. following the circuit diagram in Figure 2.43, the current through the bolometer and load resistor is given by

$$I_{Bolo} = \frac{V_{bias} - V_{bolo}}{R_L} \quad (2.16)$$

where R_L is the resistance of the load resistor which is $20\text{ M}\Omega$. The resulting load curves are shown in Figure 2.44. Curve a is the first load curve we measured to diagnose the problem of the bolometer with a weak sensitivity. It looks very different from the factory data provided by IRLabs shown in curve d. in Figure 2.44. Our measurement shows a very weak voltage drop compared to the one from IRLabs corresponding to a low bolometer resistance. This indicates that in addition to the power applied by the bias voltage via Joule heating, the bolometer receives too much infrared radiation from its surroundings which raises the bolometer temperature enough to strongly reduce its sensitivity.

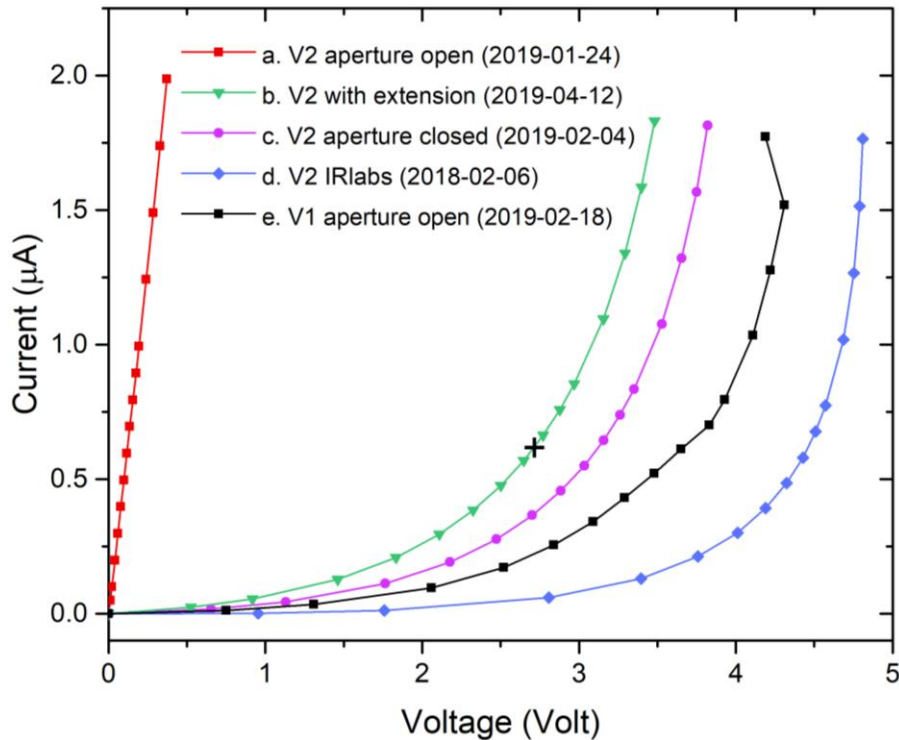


Figure 2.44 DC load curves of different conditions measured by reading the voltage drop across the bolometer from the JFET when applying a bias voltage from 0-40 V to the bolometer circuit. (a) Original V2 bolometer without any modification on the cold shield (b) V2 bolometer with a 30 mm extension aperture attached to the cold shield. The “+” highlights the working point of the bolometer when using a 15 V bias battery. (c) Original V2 bolometer but with the 4 mm aperture blocked by aluminum tape. (d) Factory data of the V2 bolometer provided by IRLabs. Data was measured when the aperture was closed. (e) Original V1 bolometer with the aperture open. The measurement date is recorded in the bracket with the format (year-month-day).

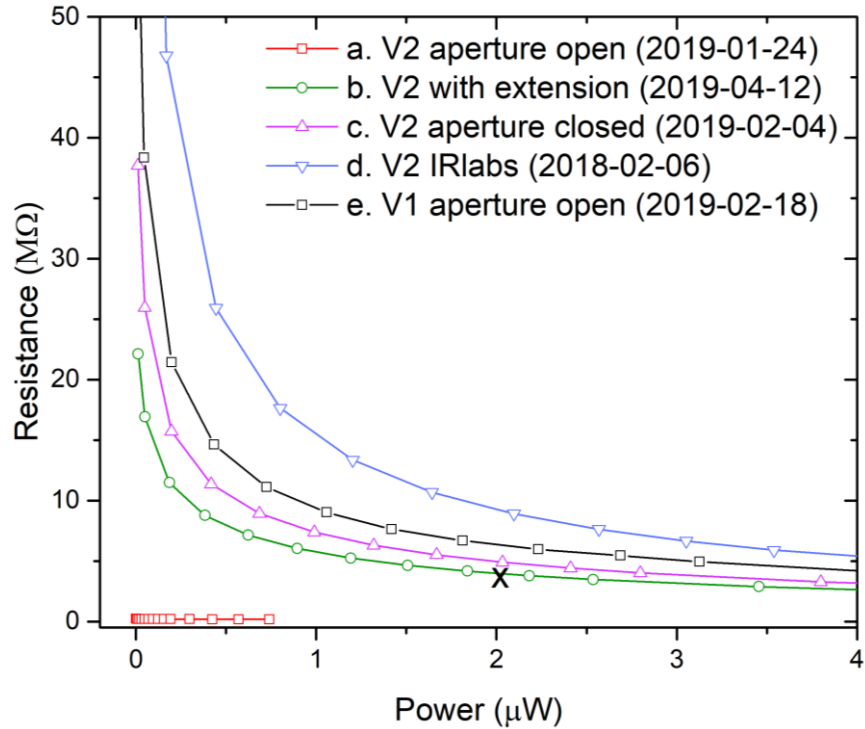


Figure 2.45 Load curves of the same set of data from Figure 2.44, but plotted in bolometer resistance versus power applied by the external power supply.

A more intuitive way to present the load curves is to plot them in a resistance-power (RP) plot instead of a current-voltage (IV) plot, as shown in Figure 2.45. Since the resistance of the bolometer is a very sensitive function of the bolometer temperature, the resistance strongly depends on the heat load received by the bolometer. If we compare Curve a and Curve d in Figure 2.45, we see that at a given amount of power provided by the applied bias voltage, Curve a shows a very low resistance. Note that for semiconductors, their resistance reduces as the temperature increases. Thus our measurement indicated the bolometer was hotter than what it was when IRLabs was performing the measurement. We suspected that the reason for the hotter condition is due to a higher background IR load.

To verify our assumption, we closed the 4 mm aperture on the bolometer cold shield with aluminum tape to prevent background IR radiation from reaching the bolometer. In this case, we observed a load curve similar to the factory data with a proper voltage drop, as shown in Figure 2.44, Curve c. This observation clearly indicates the problem of the background IR load that reduces the bolometer sensitivity.

On the other hand, the load curve measured for our V1 bolometer used in the old machine with the aperture opened (Curve e in Figure 2.44) showed a proper voltage drop similar to what we measured for the V2 bolometer with its aperture closed. The different load curves for the V1 and the V2 bolometer can be explained by the difference in IR shielding for the two bolometer systems resulting in a different field of view for the bolometer in the two cases. The distance between the aperture on the cold shield to the bolometer element is about 31 mm for the V1 bolometer, whereas it is only 13 mm for the original V2 bolometer. Given the diameter of the bolometer absorber and the aperture of 4 mm, the acceptance angles are 14.7° and 34.2° for the V1 and the V2 bolometer. This makes the V2 bolometer receive 5 times more infrared power from the background. Moreover, in the V1 bolometer, besides the LN₂ cold shield, there is an additional cold shield directly attached to the LHe dewar that may make the bolometer element even colder, as shown in Figure 2.46. More characterizations are needed to verify this consideration in the future.

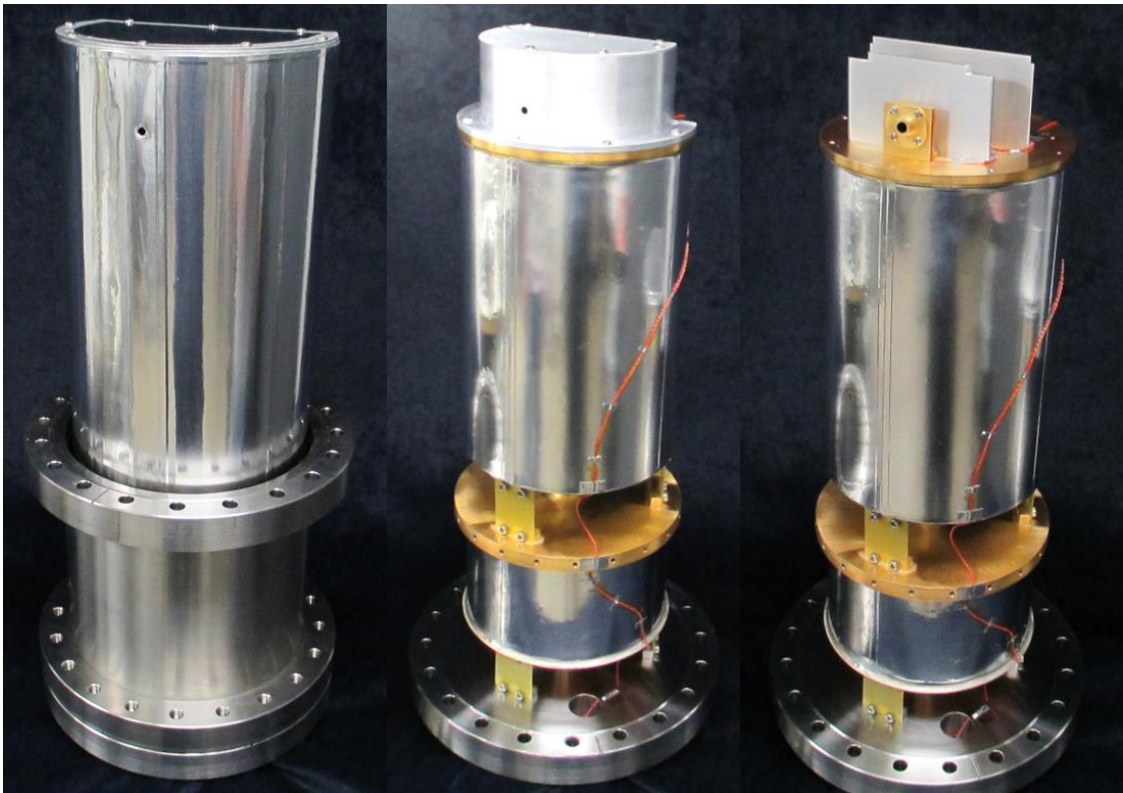


Figure 2.46 Photos of the V1 bolometer system. Left: Complete assembly of the bolometer system with the LN₂ cold shield. Middle: Bolometer system with the LN₂ cold shield removed. Right: Bolometer system with both the LN₂ and LHe cold shields removed.

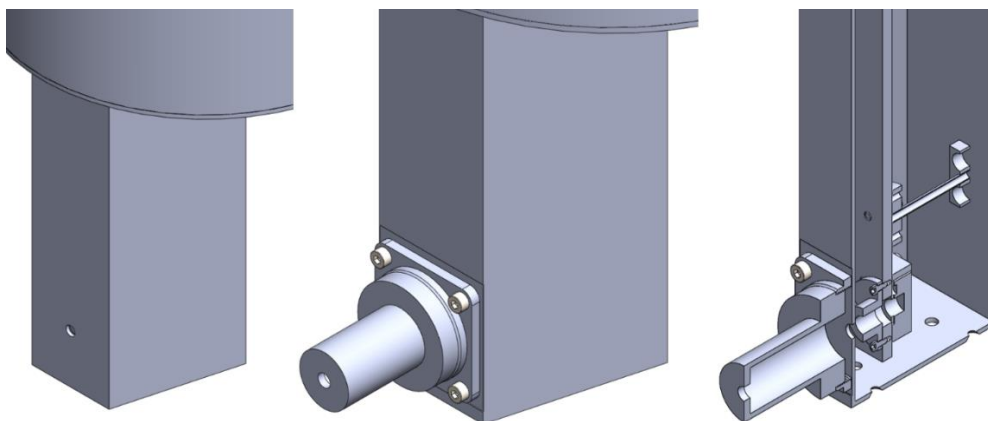


Figure 2.47 Left: original structure of the LN₂ cold shield on the V2 bolometer. Middle: Modified cold shield with an adaptor flange and a 30 mm long extension aperture of 4 mm diameter. Right: section view of the modified cold shield.

To reduce the IR load of the V2 bolometer, we added a 30 mm long extension aperture on the cold shield, as shown in Figure 2.47. This extension reduces the field of view angle to 9.4° which effectively lowers the background load by a factor of about 13. With this extension, the measured load curve shows a much higher voltage drop than without the extension, as shown in Figure 2.44, Curve a and b.

With the modified cold shield, I measured 52 mV of HAS signal using a gain factor of 100, which is 10-fold higher than that of an unmodified cold shield, as shown in Figure 2.48. In the experiments, signals are recorded for 400 samples when the molecular beam was on and then another 400 samples when the beam is off with a dwell time of 300 ms. The lock-in time constant was set to 300 ms. Even with the reduced IR loading, the methane scattering signal was still not observable over the noise until we changed the lock-in input setting from “ground” to “float”. Figure 2.49 shows a comparison of the lock-in signals for CH₄ scattering measured by the input setting “float” and “ground”. There, we clearly see that with the input setting “ground”, the noise level is an order of magnitude higher than “float”. This indicates that the noise was likely due to a ground loop and a different grounding condition between the V1 and the V2 bolometer. With the reduced noise, we were able to measure a CH₄ scattering signal of 0.149 mV. Signals of methane scattering and HAS and their corresponding noise level are summarized in Table 2.7.

After reducing the IR heat loading and the ground loop problems, the bolometer is now sufficiently sensitive to detect scattered methane signals. However, if we compare the scattered methane signals of the V1 and the V2 bolometer measured in the old machine under the same experimental conditions (scattering geometry, surface temperature, gain factor, and molecular beam flux.), the V2 bolometer is still about a factor of 5 less sensitive than the V1 bolometer. After adding the extension piece, in principle the V2 bolometer should see less IR load from the room temperature chamber, however, it is still less sensitive. The exact reason is not immediately clear. More characterizations are needed to improve the sensitivity of the V2 bolometer for higher performance.

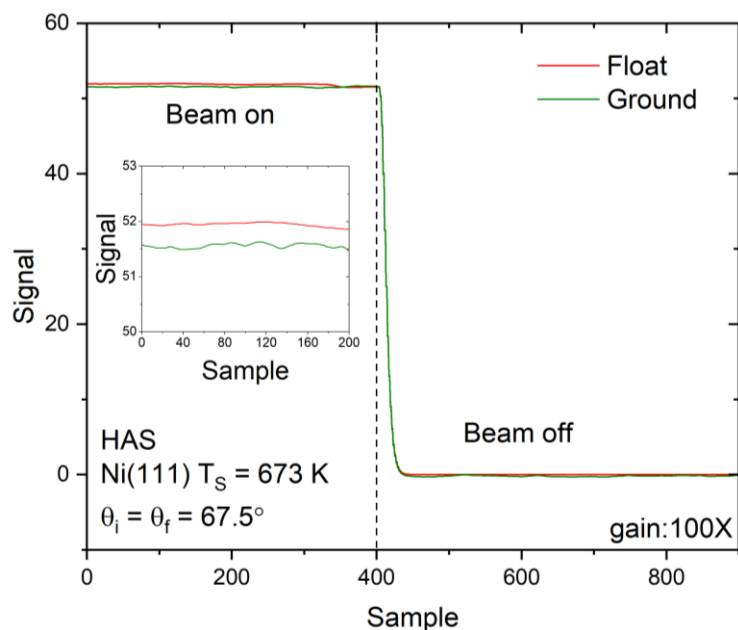


Figure 2.48 Lock-in signals of HAS experiments measured by the V2 bolometer in the old machine using different input settings “float” and “ground” in the lock-in amplifier. Experiments are performed with an RT helium atom beam with a nozzle pressure of 2 bar, then scattered from a 673 K Ni(111) surface at the geometry $\theta_i = \theta_f = 67.5^\circ$.

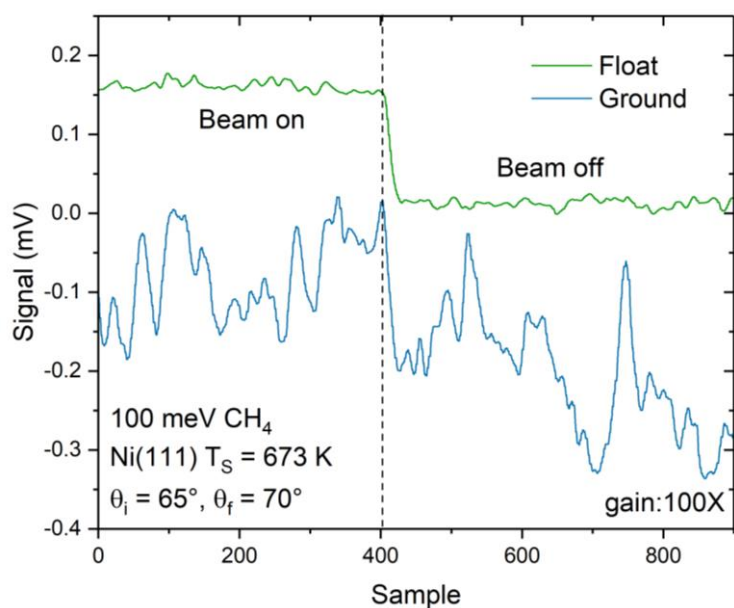


Figure 2.49 Lock-in signals for methane scattering measured by the V2 bolometer in the old machine using different input settings “float” and “ground” of the lock-in amplifier. Experiments are performed with a pure CH₄ beam and RT nozzle using a nozzle pressure of 3 bar, then scattered from a 673 K Ni(111) surface at the geometry $\theta_i = 65^\circ$, $\theta_f = 70^\circ$. The signal of “Ground” (blue) is shifted down by 0.05 mV for better visibility.

Table 2.7 Lock-in signals of CH₄ and helium atom scatterings with different lock-in input setting and their corresponding noise levels and signal-to-noise ratios.

Experiments, input setting	Average signal (mV)	RMS noise (mV)	S/N
HAS, float	51.850	0.008	6481
HAS, ground	51.74	0.07	739
CH ₄ scattering, float	0.149	0.005	30
CH ₄ scattering, ground	-	0.08	-

Going back to the load curve of the bolometer, the working point of the bolometer is determined by the bias voltage V_{bias} . In our case, it is 15 V provided by a bias battery. The working point is highlighted by “+” in Figure 2.44, Curve b. The inverse value of the slope corresponds to the bolometer resistance, which determines the sensitivity (V/Watt) of the bolometer. In this case, one would expect that a lower V_{bias} will reduce the bolometer temperature and thereby increase its resistance leading to higher sensitivity. However, the bolometer signal (in mV) is proportional to the applied V_{bias} . Hence, lowering V_{bias} also sacrifices the output signal. Figure 2.50 shows the measured HAS signal as a function of V_{bias} , ranging from 1 to 20 V. There, we observe a plateau of the HAS signal between 15 and 20 V of V_{bias} . And clearly, reducing the V_{bias} below 10 V makes drastic attenuation of the bolometer signal. According to this observation, we decide to use the 15 V bias battery for the rest of our measurements.

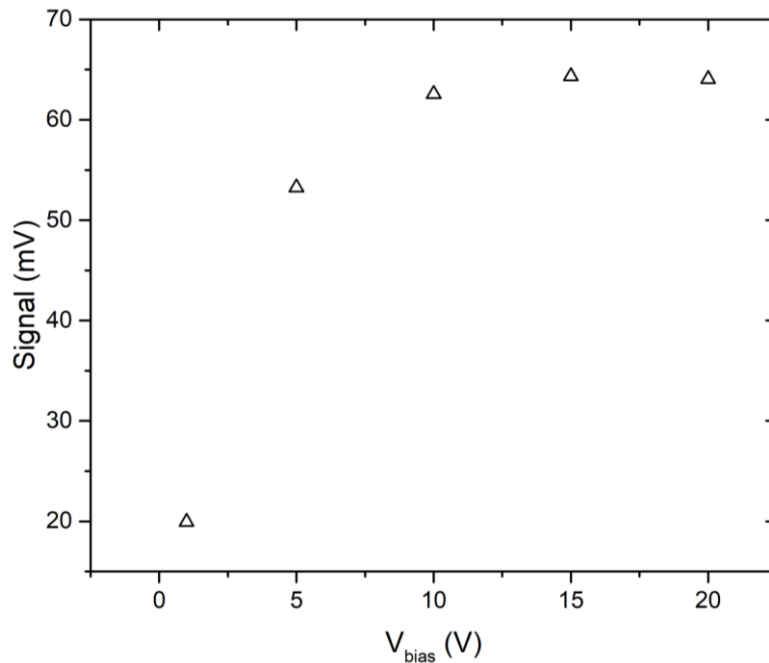


Figure 2.50 HAS signals recorded at a range of V_{bias} from 1 to 20 V. The V_{bias} is provided by an external power supply. HAS was performed in the old machine with the scattering geometry $\theta_i = \theta_f = 67.5^\circ$, a room temperature nozzle, 2 bar of nozzle pressure, and 673 K of Ni(111) surface.

For improved signal-to-noise ratio the bolometer signal is measured using either a modulated molecular beam or tagging laser in combination with phase-sensitive detection using a lock-in amplifier. Selecting the optimal modulation frequency is not trivial where one needs to take into account the bolometer frequency bandwidth and noise spectrum. The bolometer bandwidth is quoted as 1 kHz, meaning the responsivity reduces by half at this frequency. The characteristic time constant of the bolometer is determined by its heat capacity C and the thermal conductivity G , given by

$$\tau = \frac{C}{G}. \quad (2.17)$$

In other words, the bolometer needs a moment to dissipate the heat it receives from the cryostat due to its limited thermal conductivity. Once the heat accumulates faster than the dissipation rate, then the received power heats the bolometer and reduces the responsivity. In terms of getting a higher responsivity of the bolometer, operating the bolometer at a lower modulation frequency is favorable. However, in the low-frequency region, $1/f$ noise is stronger. Moreover, due to its high sensitivity, the bolometer is vulnerable to microphonic that contributes to noise in the low-frequency region. Figure 2.51 illustrates a comparison of the noise spectra of the V1 and the V2 bolometer. In both cases, we observe noise peaks that happen at 50 Hz and the multiples, corresponding to the oscillation from the surface heater. The main difference we can see is a more noisy feature below 180 Hz for the V2 bolometer. Because of this feature, the modulation frequency of 142 Hz which we normally used for the V1 bolometer is not adequate for the V2 bolometer.

Selecting a proper modulation frequency is a compromise between the noise level and the sensitivity. Both the $1/f$ noise and the sensitivity decrease with increasing modulation frequency. In addition, we find that there are noise spikes at certain frequencies that should be avoided. To find a proper modulation frequency, I measured the HAS signal as a function of the modulation frequency of a chopped helium beam, from 60 to 320 Hz. The results are summarized in Table 2.8. According to these results, I found the measurements with modulation frequencies between 180 and 320 Hz show promising S/N at about 8000. Below 180 Hz, the noise increase is dramatic. This agrees with the measurements of the noise spectrum in Figure 2.51, where we observed an increase in noise below 180 Hz. The measurement with a modulation frequency of 100 Hz shows a noise spike due to the light from neon lamps in the lab. In the present work, most of the chopped molecular beam experiments, unless mentioned, were performed with a modulation frequency of 280 Hz. Some of the laser tagging experiments were measured at other frequencies for minimizing noise.

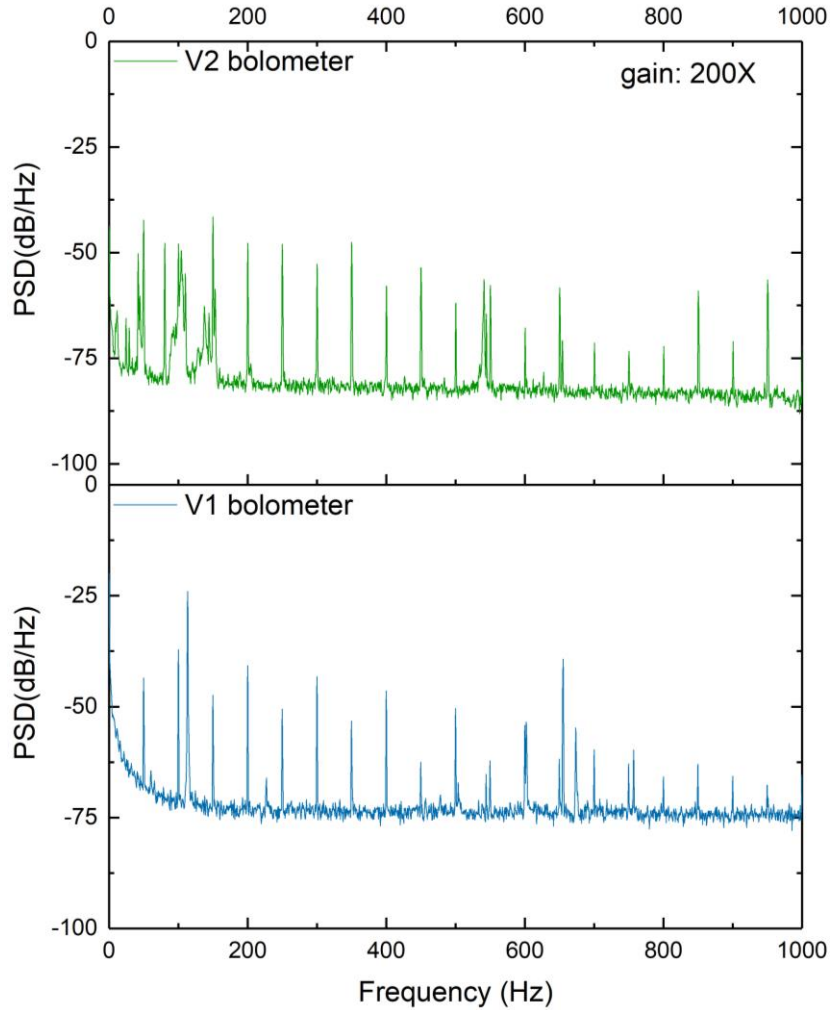


Figure 2.51 Noise spectra of the V1 and the V2 bolometer measured by a 14-bit 48 kHz DAQ card (NI USB-6009) The waveforms are first filtered by a low-pass filter at a frequency cutoff of 2 kHz. Then the waveforms are converted to the frequency spectra by the fast Fourier transform and the power spectral density (PSD) is calculated by the build-in routine in LabVIEW.

Table 2.8 Frequency response of the V2 bolometer deduced by HAS experiments measured at different modulation frequencies. The signals are derived by averaging 200 samples with a dwell time of 300 ms and a time constant of 300 ms.

Modulation frequency (Hz)	Average signal (mV)	RMS noise (mV)	SNR
60	60.05	0.02	3003
100	58.7	0.4	147
160	57.15	0.02	2858
180	56.168	0.007	8024
220	54.372	0.007	7767
280	52.130	0.006	8688
320	50.217	0.006	8370

2.5.3 Sensitivity of the bolometric detection

After testing the V2 bolometer in the old machine, the bolometer was installed in the BILT machine where it is located much closer to the target surface. The current design allowed for a reduction of the surface to bolometer distance from 360 to 81 mm for the old and BILT machines, respectively. With this reduced distance, we predict a 20-fold increase in the scattering signal. Comparing the scattering signal for CH₄ with incident energy 100 meV and identical scattering geometry ($\theta_i = 65^\circ$, $\theta_f = 70^\circ$) from a 673 K Ni(111) surface, I measured 3.8 mV of lock-in signal with a gain factor of 100 on the bolometer amplifier which compares to 0.149 mV measured by the same bolometer and the same gain factor in the old machine resulting in a 25 fold increase in bolometer signal. The fact that the improvement is higher than 20 can be attributed to a stronger molecular beam flux coming from the source.

To calculate the sensitivity of the bolometer, we must first figure out how many molecules the bolometer captures at a given scattering condition. The flux received by the bolometer can be described by

$$F_{out} = f_{out}(\theta) \times \Delta\Omega \quad (2.18)$$

where $f_{out}(\theta)$ is the angular distribution of the scattered molecules, and $\Delta\Omega$ is the solid angle of the bolometer. Normally, the angular distribution can be described by a $\cos^n(\theta)$ function with the power n indicating the width of the distribution. With this, the distribution function can be decomposed into

$$f_{out}(\theta) = f_{out}^0 \times \cos^n(\theta) \quad (2.19)$$

where f_{out}^0 is a constant scaling up to the incident beam flux. If we integrate the distribution function over an entire solid angle Ω , we get the flux of the incident beam F_{in} .

$$F_{in} = \iint f_{out}^0 \cos^n(\theta) d\Omega \quad (2.20)$$

Using $d\Omega = \sin\theta d\theta d\varphi$, eq 2.20 becomes

$$F_{in} = f_{out}^0 \int_0^{2\pi} \int_0^\pi \cos^n(\theta) \sin(\theta) d\theta d\varphi = f_{out}^0 \times \frac{2\pi}{n+1} \quad (2.21)$$

Now the scaling factor is simply

$$f_{out}^0 = F_{in} \times \frac{n+1}{2\pi} \quad (2.22)$$

Then the flux received by the bolometer can be represented as

$$F_{out} = \Delta\Omega \times F_{in} \times \frac{n+1}{2\pi} \times \cos^n(\theta) \quad (2.23)$$

and

$$\Delta\Omega = \frac{\Delta A}{r^2} \quad (2.24)$$

Where ΔA is the detector area, and r is the sample-to-detector distance. So finally we have

$$F_{out} = \frac{\Delta A}{r^2} \times F_{in} \times \frac{n+1}{2\pi} \times \cos^n(\theta) \quad (2.25)$$

To derive the incident molecular beam flux F_{in} , we use the approach described in section 2.4.4. From the partial pressure rise of methane in the P4 stage and the pumping speed of the P4 turbo molecular pump, we calculate the molecular beam flux of the incident beam of 100 meV methane as 8.2×10^{14} molecules/s for 3 bar of nozzle pressure. Next, we need to know the angular distribution of the scattered CH_4 which was measured by rotating the bolometer detector. Figure 2.52 illustrates the angular distribution of CH_4 scattering for $E_i = 100$ meV and $\theta_i = 65^\circ$. The experimental data is fit by $\cos^n(\theta_f - \theta_M)$, where θ_M is the angle at the maximum of the distribution. The fit yields the fitting parameters $n = 12.8$ and $\theta_M = 55.1^\circ$. At $\theta_M = 55^\circ$ I measured the maximum signal of 13.0 mV with the amplifier gain of 200X. The fact that we measured θ_M lower than the specular angle is due to phonon annihilation which happens preferentially when a slow (relative to the surface normal) incident beam is scattered from a hot surface [62,63]. Given the diameter of the diamond absorber of 4 mm, corresponding to an area of 12.6 mm^2 , and the surface-to-detector distance of 81 mm, we can now calculate the beam flux captured by the bolometer which is 3.5×10^{12} molecules/s for a continuous molecular. In the chopped MB experiments, we have to take into account the 1% duty cycle which reduces the flux on the bolometer to 3.5×10^{10} molecules/s.

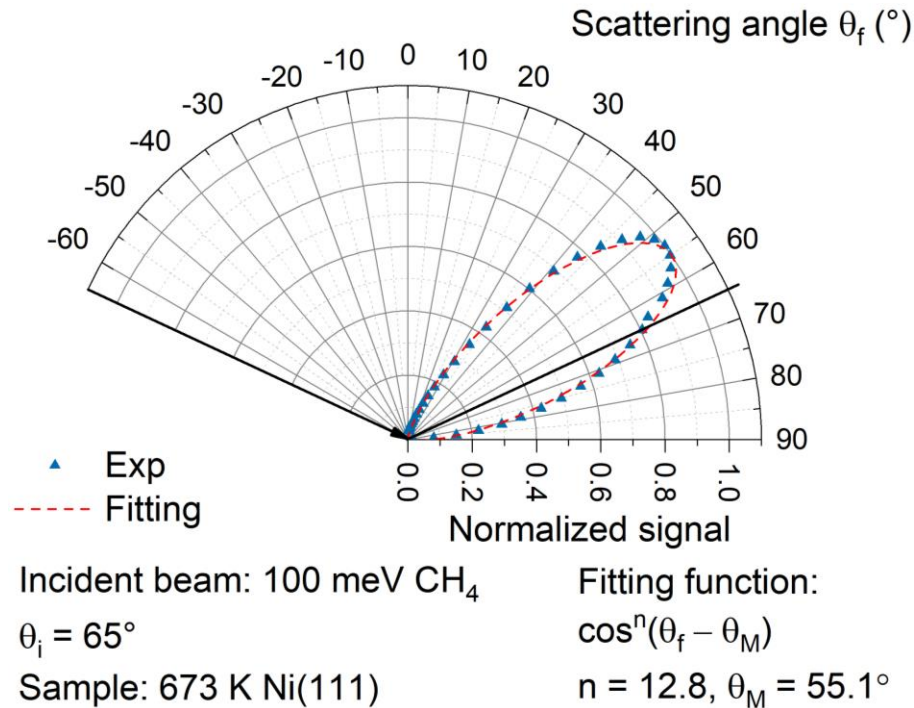


Figure 2.52 Angular distribution of scattered CH_4 from a 673 K Ni(111) surface. The incident beam is pure methane at $P_0 = 3$ bar, $\theta_i = 65^\circ$. The bolometer detector was rotated to detect scattering angles θ_f from 5° to 95° . The red dash line is a fit of the $\cos^n(\theta_f - \theta_M)$ function to the data.

With the known incident flux of molecules on the bolometer, we need to estimate how much energy is dissipated. Assuming elastic scattering, the kinetic energy of the scattered molecules is equal to $E_i=100$ meV. After being scattered from a 673 K Ni(111) surface in the scattering geometry $\theta_i = 65^\circ$, $\theta_f = 70^\circ$, we knew the average rotational energy of the scattered molecules is 13.4 meV [17]. When the methane molecules hit the diamond absorber which is at about 1.7 K, they freeze on the surface and produce some magnitudes of adsorption energy. Here, I take the enthalpy of sublimation of methane which is reported to be 100 meV [64]. Assuming the sticking coefficient of methane on 1.7 K of diamond is 1, all the methane molecules hitting the absorber all stay on the surface. Under our scattering conditions, the incident energy is low enough such that vibrations are not likely to be excited. Hence I assume no contribution from vibrational energy. After taking into account the beam flux, kinetic, rotational, and adsorption energy, I estimate the power received by the bolometer is about 1.2 nW. With this power, the bolometer produces 13 mV of signal with the gain set to 200. So the sensitivity is

$$Sensitivity = \frac{S_{bolo}}{P_{in}} = \frac{6.5 \times 10^{-5} V}{1.2 \times 10^{-9} W} = 5.4 \times 10^4 \frac{V}{W} \quad (2.26)$$

Note that the signal I report here is the DC signal generated by the lock-in amplifier, it is not the same magnitude as the peak height of the raw bolometer signal. The lock-in amplifier (Stanford Research System, SR830) multiplies the input signal with a pure sine wave and measures the single Fourier component of the signal at the modulation frequency. If the input signal is a sine wave, the output signal generated by the lock-in amplifier will be the RMS of the sine wave amplitude ($1/\sqrt{2} \times amplitude$). If the input signal is not a sine wave, the reducing factor can be more. As an example, a 2 V peak-to-peak square wave of input is applied to the lock-in amplifier. It can be expressed as

$$S(t) = 1.273 \sin(\omega t) + 0.4244 \sin(3\omega t) + 0.2546 \sin(5\omega t) + \dots \quad (2.27)$$

where $\omega = 2\pi f$. Now if the lock-in amplifier is working with a modulation frequency of f , it singles out the first component $1.273 \sin(\omega t)$. The measured and displayed value is $\frac{1}{\sqrt{2}} \times 1.273 = 0.9 V$. Our input signal of the chopped molecular beam cannot be described as a simple function, thus the reducing factor is not immediately clear. Due to this reason, I decide to report the bolometer sensitivity when it is working with the lock-in amplifier. Furthermore, most of our measurements are performed in lock-in detection mode for a better signal-to-noise ratio.

One can also report the bolometer sensitivity in terms of the number of molecules it can measure with an acceptable S/N. When the bolometer was measuring 3.5×10^{10} molecules/s, we measured 13.0 mV of lock-in signal. In this measurement, the lock-in parameters were set to [time constant = 300 ms, sensitivity = 50 mV, and dynamic reserve = low noise], producing an RMS noise of 0.006 mV. I then derive $S/N = 2167$. To measure a signal with S/N above 2, we need at least 3.5×10^7 molecules/s, assuming each molecule provides similar energy to the bolometer as the CH_4 molecule in a 100 meV molecular beam.

Since now the exact angular distribution function of CH₄ scattering from Ni(111) has been determined, I recalculate the sensitivity of the V1 bolometer in the old machine. As documented in Van Reijzen's Ph.D. thesis, the molecular beam flux of a 100 meV CH₄ beam was measured to be 9×10^{14} molecules/s [16]. At the scattering geometry ($\theta_i = 65^\circ$, $\theta_f = 70^\circ$), the molecule flux measured by the V1 bolometer is calculated to be 1.2×10^{11} molecules/s using eq 2.24 with the surface-to-detector distance 360 mm. Using the approach described earlier in this section, the energy measured by the bolometer is estimated to be 0.04 nW with a 1% duty cycle. At this condition, the V1 bolometer measured 1.3 mV with a gain factor of 200X. Therefore the sensitivity with the lock-in amplifier is 1.6×10^5 V/W, about 3 times higher than the V2 bolometer. This is close to what we observed if we compared the chopped scattered CH₄ signals of the V1 and the V2 bolometer both in the old machine, where we found the V1 bolometer was about 5-fold more sensitive than the V2 bolometer.

2.5.4 Angular distribution measurements

The main improvement of the BILT machine is the independent variation of the incident and the scattering angle. Different from the old setup where we can only rotate the sample mount, in the BILT machine, measurements of angular distribution now are performed by recording bolometer signals as a function of bolometer angle at a fixed incident angle. To demonstrate this capability, I present here the angular distributions of helium atom scattering experiments at three different incident angles. The He atom beam was modulated at 280 Hz by a 1% duty cycle chopper. At fixed incident angles, I recorded lock-in signals of scattered He measured by the bolometer detector as a function of scattering angle. Figure 2.53 shows the resulting angular distributions of the three incident conditions. In all cases, we observed sharp peaks positioned at specular angles.

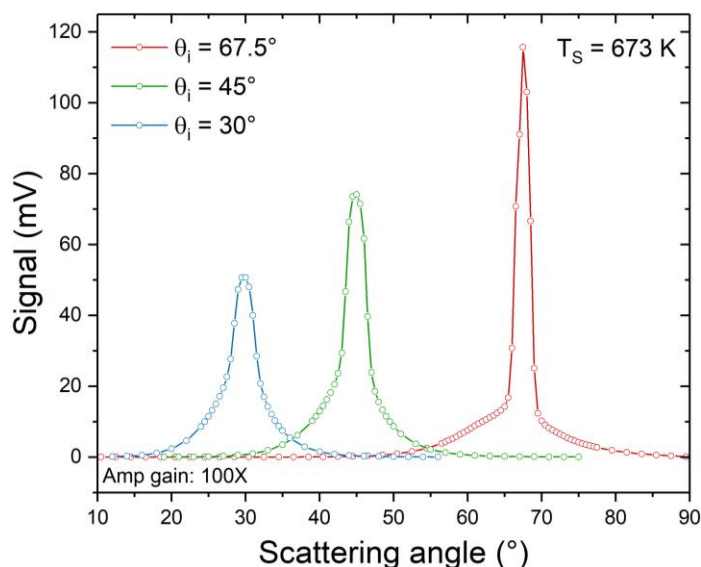


Figure 2.53 Angular distributions of helium atom scattering in three different incident angles ($\theta_i = 30, 45, \text{ and } 67.5^\circ$). The He beam is generated by 2 bar of nozzle pressure at room temperature. The Ni(111) sample was heated at 673 K. The bolometer preamplifier was set to gain 100X.

The de Broglie wavelengths of the He atoms are of the order of a few Å. The He atom scattering can be considered as a diffraction process. The strong specular peak is then corresponding to zeroth-order diffraction. Since He atom does not possess rovibrational degrees of freedom, the measured bolometer signals of scattered He corresponds only to the kinetic energy of He atoms dissipated on the bolometer. In Figure 2.53, we see as the incident angle reduces, the peak height also decreases accordingly. This is because the Debye-Waller factor is proportional to the normal component of the incident energy E_{\perp} [65]. A strong Debye-Waller factor indicates a stronger attenuation of the specular peak due to the surface thermal motions.

Due to the absence of the rovibrational degree of freedom and the light mass of He atoms, the scattering process of He is predominantly elastic. We can then assume the width of the He specular peak reflects the divergence of the incident He atom beam. Taking this assumption, the width of the scattered He atom beam that reaches the bolometer is expected to be 3.3 mm, slightly smaller than the size of the diamond absorber (4 mm). In this case, the measured width of HAS angular distribution can be considered as the instrumental angular resolution. Given 4 mm of the diameter of the bolometer diamond absorber and the surface-to-bolometer distance of 81 mm, the angular resolution is expected to be 3° , which is in good agreement with the measurements shown in Figure 2.53. The comparison of angular distributions for scattered He and CH_4 are shown in Figure 2.54. The broader angular distribution of scattered CH_4 is very likely caused by firstly, the higher mass of CH_4 molecule that facilitates momentum transfer to Ni atoms, and secondly, the existence of the rovibrational degrees of freedom that opens up more pathways of energy transfer such as translational to rotational energy conversion. Helium atom scattering is extremely sensitive to surface conditions. Besides Auger electron spectroscopy, the surface cleanliness can also be verified by monitoring the intensity of specular Helium atom scattering. Even a small coverage of adsorbates will strongly reduce the specular He scattering signal.

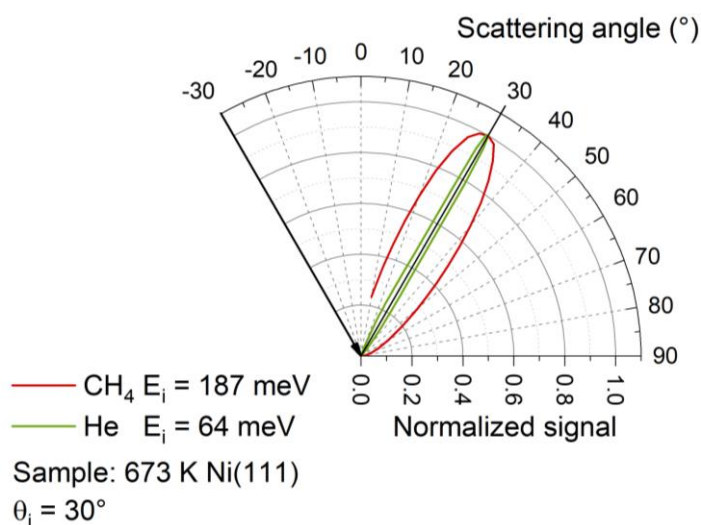


Figure 2.54 Normalized angular distributions for scattered CH_4 and He from a Ni(111) surface at $T_s = 673$ K. The arrow indicates the incident angle of 30° . The methane beam was generated by 3 bar of nozzle pressure at $T_n = 600$ K. For the He beam, I used a nozzle pressure of 2 bar and $T_n = 300$ K.

2.6 Laser setup

State-to-state molecule/surface scattering experiments require two lasers, one for state preparation of the incident beam and another for state interrogation of the scattered molecules. In our lab, there are three Argos CW-IR-OPO systems. Two of them are equipped with C-module cavities which provide an idler output frequency from 2564 to 3125 cm^{-1} with $> 1\text{W}$ of output power. The spectral range of the C-module is suitable for exciting C-H stretching mode at about 3000 cm^{-1} of frequency and thus serves as an adequate light source for exciting the ν_3 fundamental transitions of CH_4 . Here, I labeled the two Argos systems as OPOI and OPOII according to their purchase order.

The linewidth of the Argos OPO is about 1 MHz, but its frequency can drift several MHz within an hour. The transitions of the ν_3 fundamental in incident CH_4 can be as narrow as 2.5 MHz. Hence, an active stabilization mechanism is needed for the Argos OPOs. In the present setup, the OPOI is frequency stabilized by the lamb-dip technique. As I will introduce later, this technique only allows one to lock the laser frequency at the transitions whose initial levels are significantly populated at the available temperature range of the gas cell. Furthermore, this technique does not allow scanning the laser frequency. Due to these limitations, OPOI usually acts as the pump laser which excites the incident molecules to a specific rovibrational eigenstate.

For OPOII, we implement transfer cavity stabilization. The original setup was built by Dr. Bradford Perkins during his visit to EPFL. Later, this setup was improved by Jörn Werdecker by developing a locking and scanning algorithm in the LabVIEW program. With this technique, OPOII can not only be frequency stabilized at any available frequency needed for interrogating a large range of J -levels of scattered CH_4 , but also scan across transitions.

During the work of the thesis, our group acquired a new tunable CW-IR OPO system from Toptica called TOPO (Tunable Optical Parametric Oscillator). Similar to our existing 3 Argos systems, TOPO also consists of a seed laser, a fiber amplifier, and the OPO head. But different from the Argos system, without changing the OPO head, TOPO can provide a tuning range from 2500 to 5050 cm^{-1} . Furthermore, the frequency tuning of the laser is completely controlled by a Digital Laser Controller DLC pro, and no manual adjustments are needed. With this, a computer-controlled scan through all the transitions of interest is possible. This feature makes the TOPO system useful as a tagging laser. As most of the state-resolved experiments are now done using the TOPO system, I will discuss in more detail the laser system and our tuning process in the next subsection.

2.6.1 System overview of TOPO

The TOPO laser system consists of a distributed feedback diode laser (DFB pro BFY, Toptica) as the seed laser which is amplified in a fiber amplifier (IPG photonics) to provide 10 W at 1064 nm of pump power to the OPO in the TOPO head, and a digital laser controller (DLC pro, Toptica), as shown in Figure 2.55

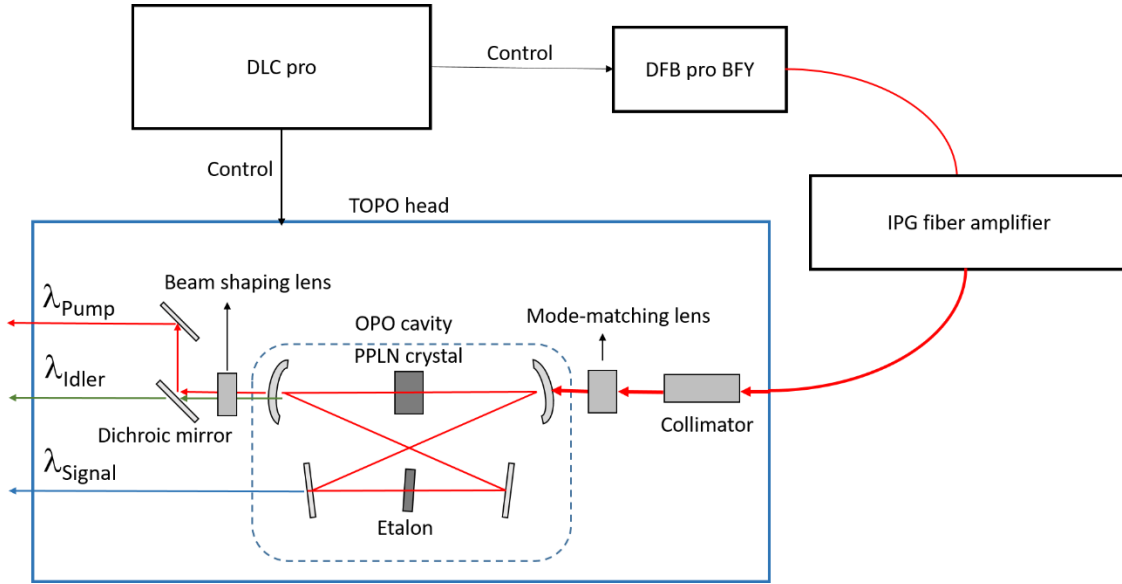


Figure 2.55 Scheme of the TOPO laser system. See the text for more detail.

Distributed feedback diode laser (DFB) is a type of semiconductor laser whose resonator contains a periodic structure (diffraction grating) on the active layer (gain medium). This structure acts as a Bragg reflector that singles out the laser longitudinal mode of interest and ensures high coherence and single-frequency operation. The laser frequency is then determined by the dimension and the refractive index of the grating pitch. The refractive index changes as the temperature and the current density vary. Hence the laser frequency can be tuned by programming the diode temperature and the working current. The DFB pro BFY provides laser wavelength centered at 1064 nm and output power of 30 mW. At 1064 nm, the thermal tuning coefficient is about 20 GHz/K. Temperature tuning can provide a mode hop-free tuning range of 700 GHz at a tuning rate of 100 GHz/s. On the other hand, current tuning provides a smaller tuning range (29 MHz), but a higher bandwidth up to MHz. When modulating the laser frequency at a higher rate, normally current tuning mode is more adequate.

The laser output coming from the DFB is amplified to up to 10 W by a diode-pumped ytterbium fiber amplifier (IPG Photonics), then sent through a fiber bundle to the OPO cavity inside the TOPO head. The generation of high-power Mid-IR radiation is done by an optical parametric oscillator (OPO). Instead of utilizing stimulated emission of a gain medium inside the laser cavity, OPO uses parametric amplification which converts the photons of the pump laser into two photons with lower frequencies, called Signal and Idler for higher and lower frequency photons, respectively. The three interacting waves obey the conservation of energy and momentum.

$$\frac{1}{\lambda_{pump}} = \frac{1}{\lambda_{signal}} + \frac{1}{\lambda_{idler}} \quad (2.28)$$

Parametric amplification occurs in nonlinear media which possess nonvanishing second-order susceptibility $\chi^{(2)}$, allowing interaction of three waves. For efficient conversion of a nonlinear process, the phase-matching condition needs to be fulfilled

$$k_3 = k_2 + k_1 \quad (2.29)$$

Where k_i is the wave vector of the i th wave. For the complete mathematical treatment of phase-matching, readers are referred to reference [66]. Under the phase-matching condition, when the pump laser propagates through a nonlinear crystal, frequency conversion happens and the energy flows from the pump laser to the signal and the idler. However, if the condition is not satisfied, i.e. a phase mismatch exists, the direction of energy transfer changes periodically, resulting in low conversion efficiency. Phase matching can be achieved for example in a birefringent nonlinear crystal where the refractive index depends on the directions and polarizations of the interacting waves. By properly choosing the polarization of the incoming beam and the orientation of the crystal, one can cancel phase-mismatch and thus high conversion efficiency is obtained.

Another approach to obtaining high conversion efficiency is to use the so-called quasi-phase-matching. This technique uses a periodically poled nonlinear crystal which has the advantage that no angle tuning is needed for phase matching which allows the pump, signal, and idler wave to propagate parallel over a long distance and achieve high gain. In the periodically poled material, the sign of the nonlinearity changes periodically. It reverses the nonlinear interaction when a wrong direction of energy conversion takes place, such that we obtain a positive net energy flow from the pump to signal and idler. The frequencies of the signal and the idler waves then depend on the periodicity of the poled structure. Using the quasi-phase-matching technique, even though a real phase matching does not occur, the high conversion efficiency is still guaranteed. Furthermore, with quasi-phase-matching, all the interacting waves can have the same polarization and orientation, which allows one to use a stronger element in the nonlinear tensor. As a result, the conversion efficiency can be higher than the real phase matching.

For our applications in the mid-IR spectrum, a fan-out periodically poled lithium niobate (MgO:PPLN) is used in the OPO cavity. Fan-out structure means the periodicity changes across the crystal, making a wide range of tunability possible with just one crystal. The crystal is mounted on a translational motor stage with a resolution of 40 nm. By translating the crystal, one adjusts the domain periodicity and thus the phase-matched frequency band. The crystal temperature is controlled by a heating element mounted on the crystal and the translational stage as an integrated assembly, such that good thermal stability is guaranteed during the translational motion. The tuning range of the TOPO is $2500 - 4570 \text{ cm}^{-1}$ and $4830 - 5050 \text{ cm}^{-1}$ for idler and signal output, respectively. The laser spectral range and specifications are summarized in Table 2.9.

Table 2.9 Specifications of the TOPO laser output

	Signal	Idler
Coarse tuning range	$4830 - 5050 \text{ cm}^{-1}$	$2500 - 4570 \text{ cm}^{-1}$
Output power	2 W	1 W
Linewidth	< 2 MHz	2 MHz
Mode hop free tuning range	500 MHz	up to 300 MHz

2.6.2 Frequency tuning of TOPO

There are five tuning elements available for tuning the idler frequency of the OPO:

- (1) Translation of the PPLN crystal perpendicular to the beam axis allows us to use a different domain of periodicity that favors specific signal and idler frequencies.
- (2)(3) Changing the diode temperature and current vary the output frequency of the DFB laser. Since the OPO cavity is designed to be singly-resonant only with the signal wave, tuning the pump frequency in this way changes the idler frequency but leaves the signal frequency unchanged.
- (4) Inside the cavity, a thin etalon is installed on a servo motor, providing spectral narrowing and frequency fine-tuning.
- (5) Tuning the intracavity piezo voltage changes the length of the cavity and thus the resonant frequency of the signal.

The tunable ranges of the above-mentioned parameters are summarized in Table 2.10. Given a target laser frequency, a recommended procedure by Toptica is first by adjusting the crystal position until significant laser power is observed when the measured laser frequency is close to the target frequency. Then adjust the etalon angle until the difference between the measured frequency and the target frequency is smaller than 30 GHz. Finally, for the fine-tuning, referring to the idler, one can reach the target frequency by tuning the diode temperature of the DFB. Whereas for the signal output, the target frequency can be accomplished by tuning the intracavity piezo voltage. The exact tuning procedure has been modified to reduce the probability of mode hops, as I will introduce shortly. In the present work, I study the population of scattered methane molecules by exciting the C-H stretch mode which has a vibrational frequency of about 3000 cm^{-1} , in the spectrum of the idler output. Hence in the remainder of this section, I will focus on the frequency tuning of the idler output.

Table 2.10 Tuning range and resolution of frequency tuning parameters.

Tuning method	Output affected	Range	Resolution
Crystal (motor) position	Signal, Idler	Full system range	1.3 THz
Diode current	Pump, Idler	29 GHz	1.5 GHz/mA
Diode temperature	Pump, Idler	30-300 GHz	20 MHz/mK
Intracavity etalon angle	Signal, Idler	400 GHz	30 GHz
Intracavity Piezo voltage	Signal, Idler	500 MHz	50 kHz/mV

For good single-mode tuning performance, one can create a so-called Look-Up Table (LUT) which consists of a range of laser frequency, their corresponding crystal position, and etalon angle that provide maximized power. In the interfacing software of the DLC pro, the crystal position is more often called “motor position” as the crystal motion is driven by a motor. So in the remainder of this section, I use the term “motor position” referring to the crystal position. With the LUT, given the desired laser frequency, the DLC pro can immediately pick up a pair of motor-etalon values which provides an output frequency closest to the target frequency. Following fine-tuning using the diode temperature, one can reach the target frequency efficiently.

To generate a LUT, using the strategy suggested by Toptica, we scan the etalon angle E from the minimum E_{\min} (5000) to the maximum servo step E_{\max} (6500) in the step of $\Delta E = 10$. At every servo step, we scan the motor position M from the minimum M_{\min} to the maximum position M_{\max} . At every Etalon-motor step (E, M) , the laser power, and the frequency of the idler output are recorded. Figure 2.56 illustrates a LUT of idler power as a function of etalon- motor position. The orange-green fringes indicate the positions (E, M) where significant idler power is measured, meaning allowed modes are resonating in the OPO cavity. The distances between adjacent fringes are determined by the free spectral range of the etalon. These Etalon-motor positions where high output power is measured are the desired reference points to let a tuning algorithm begin with laser frequency tuning. The Etalon-motor positions with high power output are shown in Figure 2.57

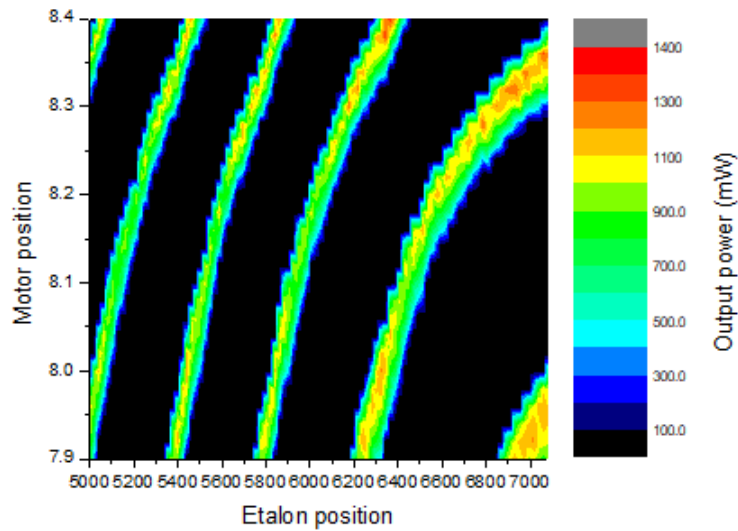


Figure 2.56 Results of a measured LUT, plotted as Idler power as a function of etalon-motor position.

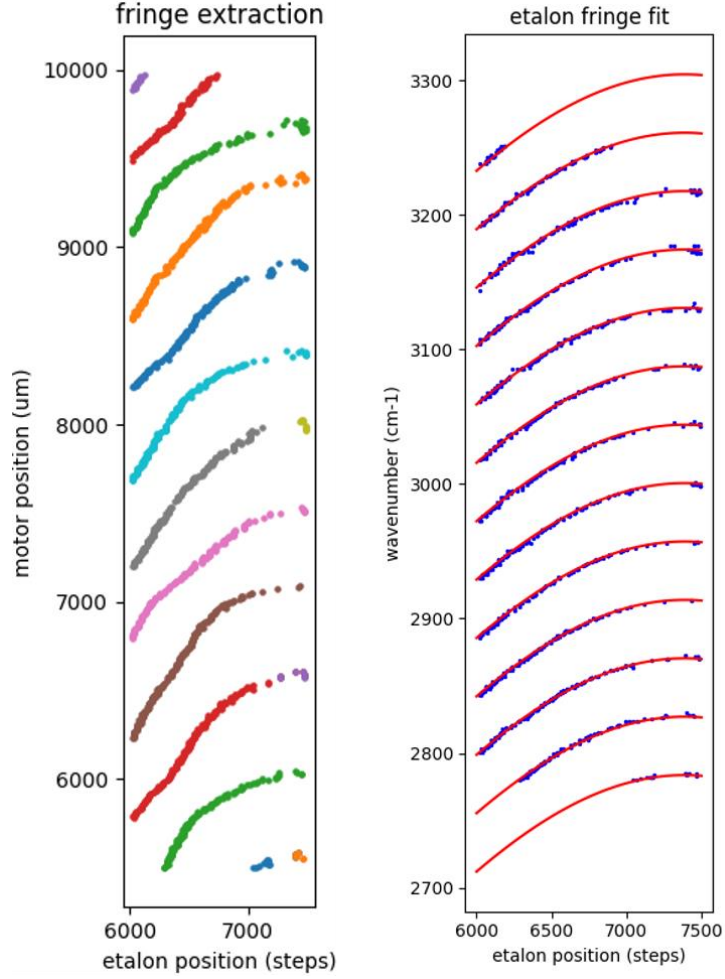


Figure 2.57 Left: extracted fringes from Figure 2.56. Right: LUT data plotted as Idler frequency as a function of etalon angle. The red curves are fitting with cubic spline functions.

The current frequency tuning algorithm was originally provided by Toptica but further improved by our Postdoctoral researcher Christopher Reilly to reduce the occurrence of mode hops. Given a target idler frequency ω_{target} , the algorithm first searches the LUT for a pair of motor-etalon values (E, M) that provide the closest frequency to ω_{target} . Next, it scans the motor position to maximize the Idler power. At the new etalon-motor position (E, M') , if the difference between the measured frequency ω_{measured} and ω_{target} is lower than a threshold value of 0.55 cm^{-1} .

$$|\omega_{\text{measured}} - \omega_{\text{target}}| < 0.55 \text{ cm}^{-1}, \quad (2.30)$$

then we bring the laser frequency to ω_{target} by tuning the diode temperature. This threshold value is determined by the resolution of etalon tuning. However, if the condition eq 2.30 is not satisfied, then we adjust the etalon angle to a new position E' such that ω_{target} is approached. After moving the etalon angle, the output power is again optimized by adjusting the motor position. With this process, normally the threshold condition eq 2.30 is satisfied. Then the tuning algorithm will continue to bring the frequency to the target value by temperature tuning. Once the target frequency is reached, the transition line of interest is measured by scanning the laser over a range of about 150 MHz by current tuning. This method is then repeated for all the lines needed to measure. As an example, measuring a set of R-branch transitions of methane v_3 fundamental up to $J = 10$ (totally 11 lines) by this method takes only less than 30 minutes.

To date, the latest algorithm saves the new etalon-motor values if they satisfy the threshold condition eq 2.30 and no mode-hop occurred throughout the tuning process. For the next frequency tuning of the same target frequency, the tuning algorithm will call the latest saved etalon-motor values. This efficiently reduces the time needed to reach the target frequency. Simply taking the etalon-motor value from the original LUT can provide a good starting point for tuning. However, very often mode hops happen and the algorithm needs more etalon tuning trials to search for new (E, M) values.

2.6.3 Frequency stabilization and scanning of TOPO

Different from our Argos systems, which use either transfer cavity or Lamb dip technique for frequency stabilization, for the TOPO laser, we developed a different laser locking method by using a Fabry-Pérot interferometer (FPI). The FPI (Thorlabs, SA200-30C) is a confocal cavity with a free spectral range (FSR) of 1.5 GHz and a minimum finesse of 200. One of the cavity mirrors is mounted on a piezoelectric transducer (PZT). When scanning the PZT which changes the cavity length, transmission fringes can be observed when the conditions of constructive interference are satisfied. The condition is given by

$$4nL = m\lambda \quad (2.31)$$

where L is the length of the cavity, n is the refractive index of the intra-cavity medium, and m is a positive integer that takes the values 1, 2, 3... From eq 2.31, we know the distance between two adjacent peaks is $\lambda/4$. Given a certain scanning range or PZT voltage, one observes more fringes for a higher frequency ray than the lower one. In other words, for a higher frequency ray, it needs a shorter displacement of the cavity mirror to see the next fringe. Hence the position of the fringe reflects the frequency of the light ray. This property can be exploited to stabilize and scan the laser frequency.

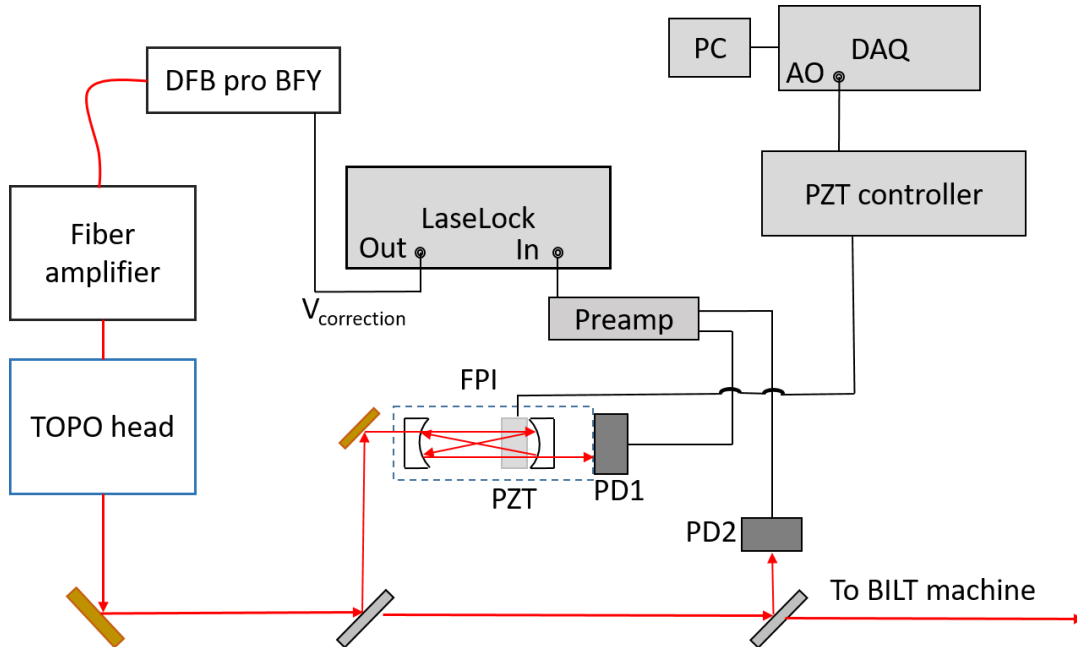


Figure 2.58 System setup of the laser stabilization and scanning mechanism by the Fabry-Pérot interferometer (FPI) and the LaseLock electronics.

The laser frequency stabilization is accomplished by the LaseLock electronics (TEM, LaseLock digital). The system setup is shown in Figure 2.58. First, a CaF_2 pickoff reflects a small amount of laser power into the FPI cavity. The piezoelectric transducer is driven by the PZT controller (Thorlabs). At the output of the FPI, the first photodiode PD1 (Thorlabs, PD) measures the transmitted power of the IR laser. At a later stage of the main laser beam path, a second CaF_2 window reflects a small portion of the laser to the second photodiode PD2 for monitoring the laser power. The output signals of the two photodiodes are collected by the LaseLock electronics via a preamplifier.

With the LaseLock electronics, we perform so-called side-of-the-fringe locking. The LaseLock measures transmission fringes coming out from the FPI that characterize the laser frequency. Then we specify a setpoint of locking which is equal to half of the height of the transmission peak, located at the side of the fringe. This point is selected as it has the highest slope, i.e. the transmitted power is most sensitive to fluctuations of the laser frequency. To lock the laser at the target frequency ω , we first adjust the piezo voltage V_{PZT} to find the signal that is equal to half of the height of the transmission peak at the set point S_{set} . Note that the height of the transmission peak is proportional to the laser power. To eliminate the disturbance from the fluctuation of the laser power, the input signal to the LaseLock is configured as the ratio of the two photodiode signals $S_{\text{PD1}}/S_{\text{PD2}}$. Now, if the laser frequency drifts from the target value ω to a random value ω' , the position of the fringe also changes, resulting in different transmitted power and the corresponding signal S_{measured} , as shown in the left panel of Figure 2.59. Once we enable the locking loop, the PID regulator minimizes the error signal $S_{\text{error}} = S_{\text{measured}} - S_{\text{set}}$ by sending a correction voltage to the DFB and adjusting the laser frequency back to ω through current tuning.

The DFB features two BNC jacks for diode current tuning mode via external voltage signals. The specifications of the two ports (AC and DC couple) are summarized in Table 2.11. For frequency stabilization, we use the DC-coupled port as it provides a smaller scaling factor that is suitable for small frequency drift. We use the AC port for adding noise to broaden the linewidth of the laser, which I will discuss in detail in the next chapter.

Table 2.11 Specifications of the AC and DC ports on the DFB laser head for controlling current tuning mode.

	Sensitivity	Impedance	Max. rated voltage
AC coupled	2.2 mA/V	50 Ω	± 1.8 V
DC coupled	0.73 mA/V	150 Ω	± 5 V

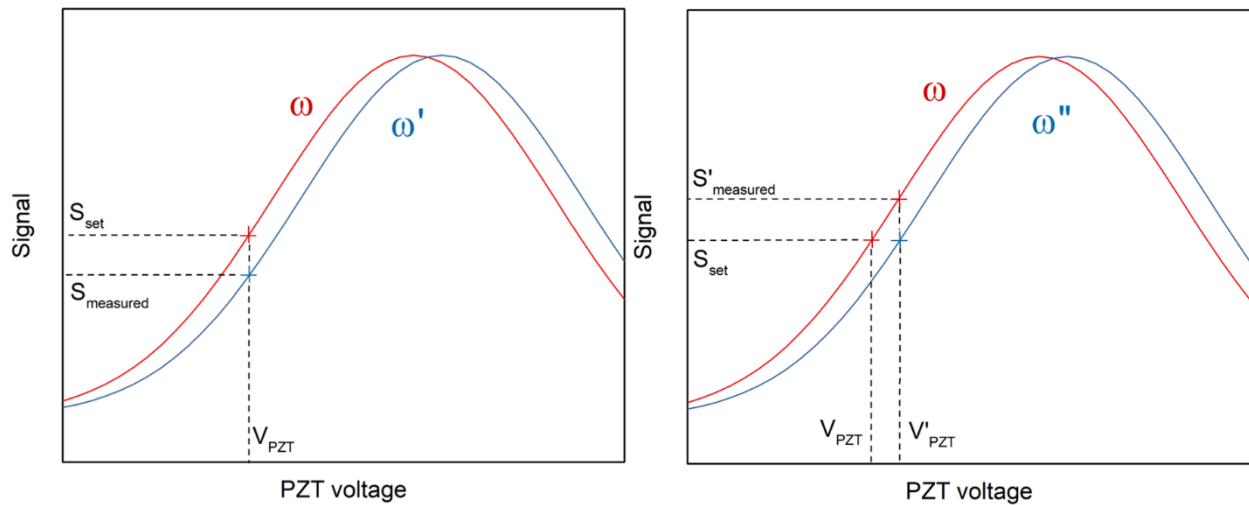


Figure 2.59 Illustration of the side-of-the fringe locking method for laser frequency stabilization (Left) and laser frequency scanning (Right). See text for the working principle.

When the laser frequency is stabilized by the side-of-the fringe locking, one can scan the laser frequency by adjusting the PZT voltage. Following the illustration in the right panel of Figure 2.59, once we increase the PZT voltage from the initial value V_{PZT} to a new value V'_{PZT} , the transmitted power increases, and the measured signal changes from S_{set} to $S'_{measured}$. To bring the signal back down to S_{set} , the PID regulator then sends a correction voltage to the DFB for altering the laser frequency. When the frequency reduces from the initial value ω to a new value ω'' , the fringe position also changes accordingly, such that the setpoint S_{set} is reestablished. A frequency scanning process is accomplished by continuously tuning the PZT voltage.

The performance of the FPI locking is illustrated in Figure 2.60. There, I compare the R(0) A1 transition of the ν_3 fundamental of CH₄ measured with and without applying the FPI locking, after scattering from a 673 K Ni(111) surface. The scattering experiments were performed at the geometry of $\theta_i = 36^\circ$, $\theta_f = 41^\circ$ with an incident beam energy of 185 meV. On the left panel of Figure 2.60, the absorption profile shows spiky features which are due to frequency instability. After applying the FPI locking, the spiky features are gone and a smooth profile is observed, as shown in the right panel of the same Figure. By adopting the FPI stabilization, the spectral quality is improved and the occurrence of failure scans is also reduced.

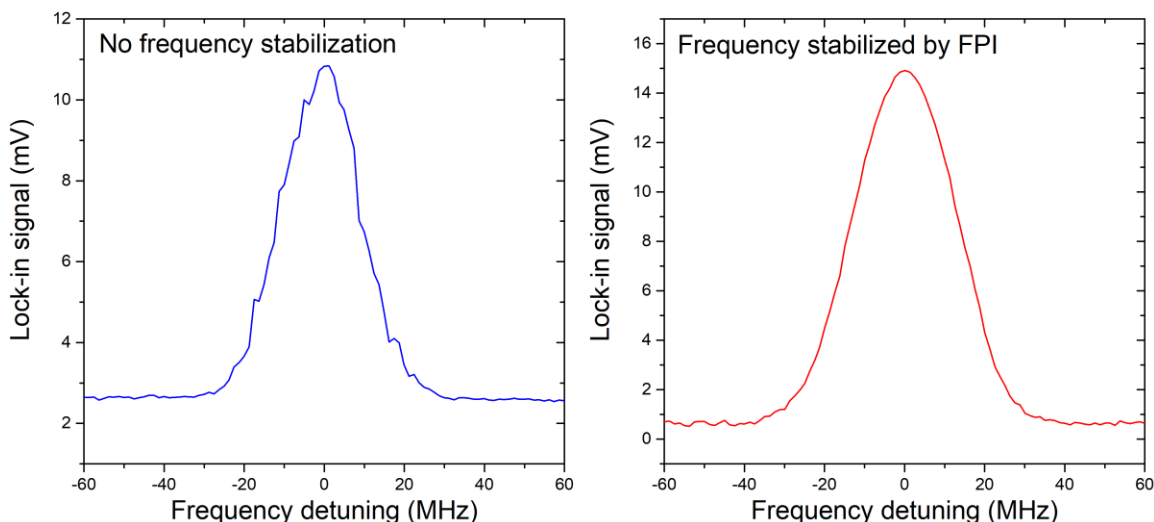


Figure 2.60 Absorption profiles of the R(0) A1 transition of the ν_3 fundamental of scattered CH₄ from a 673 K Ni(111) surface. The incident methane beam is generated by a 20% mixture in He at room temperature nozzle, providing 185 meV of kinetic energy. Scattering geometry is $\theta_i = 36^\circ$, $\theta_f = 41^\circ$. Bolometer amplifier gain is set to 1000.

Note that the frequency stabilization method described here was developed in the later stage of my Ph.D. work. Hence only part of the measurements in this thesis was performed in this way. For the rest of the results carried out without the stabilization method, they followed the scanning strategy described in 2.6.2. Although some of the spectra were measured without the FPI stabilization, the accuracy is still guaranteed by applying fitting functions to the absorption profiles. In the next chapter, I will discuss how I interrogate the state population of scattered methane molecules.

2.6.4 Argos OPO systems

The working principle of the Argos OPOs is very similar to TOPO described in section 2.6.1. The main difference is the seed laser. The Argos system uses a Yb-doped fiber laser (Koheras Adjustik, NKT Photonics) as its seed laser. It delivers about 14 mW of output power centered at 1064 nm with its linewidth < 100 kHz. Frequency tuning of the seed laser is achieved by applying strain to the fiber by the built-in Piezoelectric element (PZT) that changes the refractive index and thus the allowed resonance frequency inside the cavity. The tuning range of the seed laser is about 100 GHz, corresponding to the PZT voltage of 0-150 V. Besides the seed laser, the Argos systems have a narrower tuning range due to the available tuning range of the PPLN crystal adopted in the Argos OPO cavity. Finally, frequency tuning to the target value requires manual tuning of the crystal position, then power optimizing by tuning the etalon angle, and finally the frequency fine-tuning by the seed PZT. When the Argos OPO was still used as the tagging laser, the time needed for manual frequency tuning over a list of transitions can occupy a least a third of the measurement time.

To date, the fiber amplifier of the OPO-I system had been replaced at the end of 2019. The old fiber amplifier broke down due to the failure of the cooling system. Plus, the output power was reduced drastically compared to its original status as it has been used for more than 10 years. To compensate for this reduced power, the output coupler in the OPO cavity was replaced by a mirror with higher reflectivity (100%) to reduce the lasing threshold. With this modification, we sacrificed the signal output which is acceptable because we do not use the signal output in our applications. However, the modification still introduced the problem of multimoding. Now, with the new fiber amplifier, we can go up to 20W of power. The output coupler in the C-module OPO cavity is restored back to the original mirror with lower reflectivity (98%), hence the problem of multimoding is eliminated. Although the fiber amplifier of OPO-I can provide a maximum power of 20 W, corresponding to an idler output of 3.8 W at 3038 cm^{-1} , it is not recommended to work at the highest power as the lifetime of the laser will be shorter. Typically I use OPO-I for preparing the incident CH_4 beam in a quantum of ν_3 vibrational mode. In this case, it is enough to just use 12 W of pump power which results in about 1.4 W of idler output at 3038 cm^{-1} . Whereas for OPOII, typically 20 W of pump power is used which provides about 2 W of idler power for exciting scattered molecules residing in a broad range of rotational levels.

2.6.5 Lamb-dip locking

A Lamb dip is a saturation hole-burning of a Doppler-broadened absorption profile. Consider an intense laser passing through a gas cell with a gas species of interest. Molecules inside the gas cell are traveling in random directions. When one scans the laser frequency across the transition of the gas species, the molecules absorb the laser at a Doppler-shifted frequency

$$\omega_D = \omega_0 + \Delta\omega \quad (2.32)$$

where ω_0 is the center frequency of the transition, $\Delta\omega$ is the Doppler shift $\frac{\omega_0}{c}v_z$, c is the speed of light, and v_z is the molecular velocity component along the laser propagation axis. Now, if we add a mirror at the exit port of the gas cell and reflect the laser beam following its original path, the class of molecules which absorb the incident laser at $\omega_0 + \Delta\omega$ will absorb the retroreflected beam at the reversed Doppler shift $\omega_0 - \Delta\omega$ and are thus off-resonant from the retroreflected laser. Only the class of molecules with no Doppler shift, i.e. traveling normal to the laser propagation axis, are resonant with both the incident and the retroreflected laser. When the laser frequency is tuned to the center frequency, it depletes the transition and thus “burns a hole” in the absorption profile, as shown in Figure 2.61. This dip can act as an accurate reference for laser locking at the center frequency of the transition.

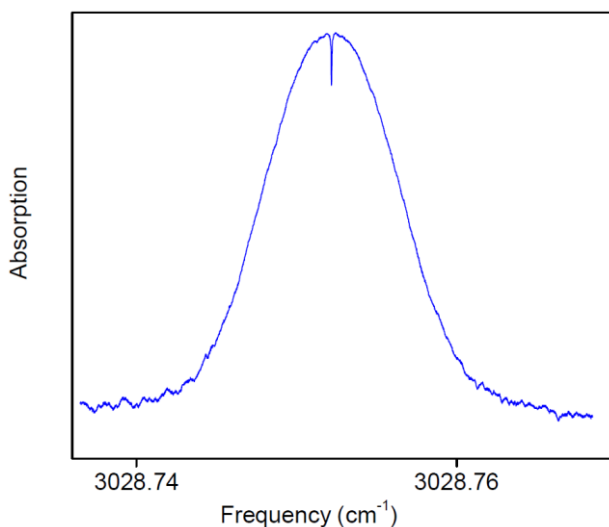


Figure 2.61 Doppler-broadened absorption profile with Lamb dip observed for the CH₄ R(0) ν_3 fundamental transition. Spectrum is taken from Ref [49].

Laser frequency stabilization is accomplished by the Laselock electronics which is the integration of a lock-in amplifier, a PID regulator, and a voltmeter. The complete working principle and detail of tuning the Laselock parameters can be found in Bruce Yoder’s thesis [49]. Here, I only introduce the essential concepts. First, a sine wave voltage signal is sent from the Laselock to the seed Piezoelectric element which creates dithered signal in the absorption profile measured by an LN₂-cooled photodiode. The signal is then fed into the input of the lock-in amplifier which produces time-derivative of the input signal. The Lamb dip waveform will then be converted to a derivative peak shape with the dip appearing at the zero-crossing point. The PID regulator is set to top-of-fringe stabilization with the setpoint = 0. Any frequency detuning from the center frequency will result in a non-zero lock-in signal. The difference between the measured lock-in signal and the setpoint serves as the error signal of the PID circuit. Once the PID regulator is enabled, it sends a correction voltage to the seed PZT for frequency tuning to minimize the error signal. By this method, the laser frequency can stay at the center frequency of the transition.

2.6.6 Transfer cavity stabilization

Although the Lamb dip technique provides an accurate and robust way of stabilizing laser frequency on the target transition, it is not applicable for our tagging laser due to several restrictions. Using Lamb dip locking, one can only lock the laser frequency at the transition whose initial level is significantly populated at room temperature. In principle, one can heat the gas cell to make the molecules populate at higher energy levels. However, due to the relatively high rotational constant of CH₄, populating at higher rovibrational levels by heating the gas cell is not feasible. Besides this limitation, Lamb dip locking also doesn't allow laser frequency scanning. This will limit us from recording the lineshape of the transitions, where we can extract information on velocity distributions of scattered molecules. Due to the above-mentioned limitations, this technique is only used to lock the laser for state preparation of the incident beam.

To overcome these limitations, for the tagging laser, the transfer cavity technique is implemented. The main element of the transfer cavity is essentially a Fabry-Pérot interferometer (PFI) as I have discussed in Section 2.6.3. But instead of just the IR laser, a HeNe laser is also aligned into the cavity. This HeNe laser acts as the reference for IR laser stabilization because of its good frequency stability. The term “transfer cavity” means it transfers the frequency stability of the HeNe laser to the target IR laser.

When scanning the PFI, we observed both the IR and the HeNe transmission fringes which satisfy the following conditions

$$4n(\lambda_{IR})l_m = m\lambda_{IR} \quad (2.33)$$

$$4n(\lambda_{HeNe})l_k = k\lambda_{HeNe} \quad (2.34)$$

where $\lambda_{IR/HeNe}$ is the wavelength of the IR/HeNe laser, l_m and l_k are the cavity lengths when m th and k th cavity modes are excited by the IR and the HeNe laser, respectively. Figure 2.62 illustrates the IR and the HeNe fringes. For frequency stabilizing the IR laser, we first introduce a physical quantity ΔL_{mk} defined as the difference between l_m and l_k . ΔL_{mk} then acts as the setpoint of a PID regulator. If the frequency of the IR laser drifts, the measured ΔL_{mk} changes accordingly. Then the PID regulator generates a correction voltage to the seed PZT of the OPOII for maintaining ΔL_{mk} constant. For scanning the IR laser frequency, it is accomplished by ramping the setpoint value ΔL_{mk} in the PID. Although the concept is simple, special handling is required in the event where the initially selected fringe drifts out of the cavity Piezo range during the scanning process. The LabVIEW VI for transfer cavity stabilization and scanning is developed by the former Ph.D. student Jörn Werdecker. For more detail on this VI and its working principle, interested readers are thus referred to his thesis [17].

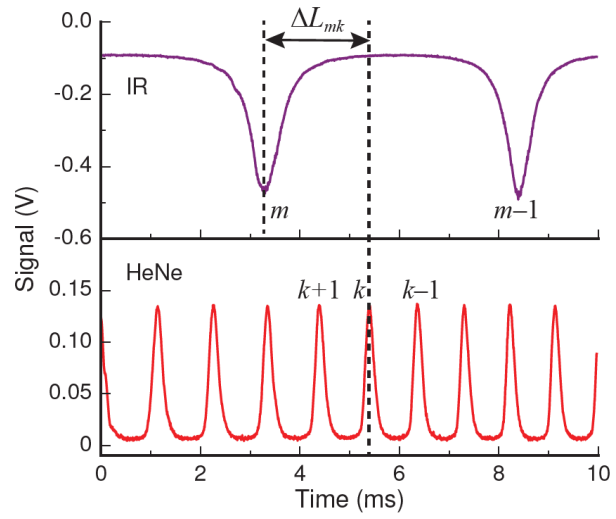


Figure 2.62 Transmission fringes of the IR and HeNe laser produced by our transfer cavity. The figure is adapted from Ref [17].

Chapter 3 Bolometric infrared laser tagging

3.1 Introduction

As I have shown in chapter 2, the bolometer detector measures all types of energy from molecules it captures including translational and internal energy. The bolometer itself is therefore not a state-selective detector. State-selective bolometric detection depends on the use of a narrowband infrared laser which can state-selectively excite molecules from a specific initial rovibrational state. In this chapter, I introduce the bolometric infrared laser tagging (BILT) technique which allows for state-selective detection of scattered molecules. Then, I will briefly discuss the method of coherent excitation by the rapid adiabatic passage (RAP) which allows for the complete population inversion of a two-level system. Using RAP excitation of a rovibrational transition, the resulting bolometer signal is directly proportional to the population of the lower state. By tuning the laser frequency over several transitions corresponding to the rovibrational levels of interest and recording their bolometer signals, one can measure the populations of the internal states for the scattered molecules.

This method has been implemented by Van Reijzen and Werdecker in the previous testing apparatus [16,17]. However, as I will explain in detail in this chapter, this method does not apply to the BILT machine due to geometric constraints. To overcome this problem, instead of using RAP, we frequency-broaden the linewidth of the TOPO laser such that all the Doppler velocity classes of scattered molecules can be excited. With this method, we observed the asymptotes of the fluence curves. Later in this chapter, I will explain the configuration of the new method and present some measured results.

3.2 Bolometric infrared laser tagging

The angular distribution of scattered He and CH₄ shown in chapter 2 was recorded by detecting the scattered atoms or molecules by the liquid He-cooled bolometer which is mounted on the rotatable lid. The signal/noise ratio of the measurement is optimized by modulating the molecular beam with a fast chopper wheel in combination with phase-sensitive detection using a lock-in amplifier. In this case, the bolometer signal corresponds to the total energy deposited into the bolometer element by the scattered particles which includes translational, rotational, and vibrational energy. This type of bolometric detection is therefore not state-selective. Furthermore, if a seeded molecular beam is used, distinguishing the seed molecules (CH₄) from the carrier gas (He) species is not possible by the above-mentioned method.

To make the bolometric detection state-selective, we add an IR “tagging” laser which is tuned to excite scattered molecules from a specific initial rovibrational quantum state and adds the photon energy $h\nu$ (≈ 36 kJ/mol for a C-H stretch mode) to the internal energy of the scattered molecules. If we now modulate either the amplitude or the frequency of the tagging laser, instead of chopping the incident molecular beam, we can use phase-sensitive detection to selectively detect the bolometer signal generated only by the “tagged” scattered molecules which absorbed an

infrared photon. Figure 3.1 illustrates the principle of the state-selective tagging measurements. The high state of the signal is caused by the excess rovibrational energy added by the laser. The translational energy of the scattered molecules is constant and therefore is filtered out by the bolometer preamplifier as it is set as AC-coupled. Now, if we lock-in detect the modulated signal, the lock-in amplifier will demodulate this signal and produce a DC signal. This DC signal corresponds to only scattered molecules in the quantum state excited by the IR laser. Hence, state-selective detection is achieved. Since the excess energy added by the IR laser serves as a “tag” for labeling the scattered molecules residing in the rovibrational state of interest, we call this method BILT detection for *Bolometric Infrared Laser Tagging*.

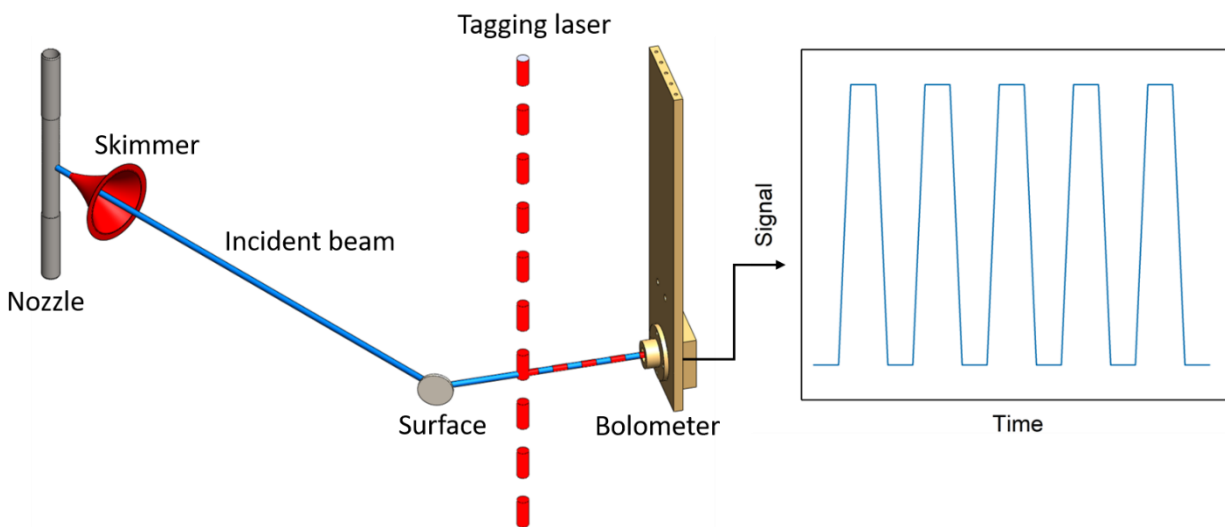


Figure 3.1 Schematic of state-selective bolometric detection i.e. tagging experiments. See text for the working principle.

As an example, Figure 3.2 shows a typical tagging signal of the CH_4 ν_3 fundamental R(0) transition. The incident CH_4 beam is generated by expanding pure methane gas from 3 bar pressure through a nozzle at room temperature into a vacuum resulting in a methane translational energy of 100 meV. The surface scattering was performed at the geometry $\theta_i = 65^\circ$, $\theta_f = 70^\circ$. Note that for amplitude modulation of the tagging laser, scattered infrared light is also modulated at the reference frequency of the lock-in detection and will be detected as a frequency-independent background signal by the bolometer. To derive the tagging signal S_{tag} corresponding to the rovibrationally excited molecules, it is necessary to subtract the scattered light contribution S_{SL} from the total signal S . The scattered light signal S_{SL} is measured by blocking the molecular beam using a beam flag in the UHV stage driven by a stepper motor. The bolometer signal measured when the molecular beam is closed is simply the contribution from the scattered light. In Figure 3.2, the gap observed right after closing the molecular beam is due to the sudden change of the bolometer signal that saturates the bolometer preamplifier.

If the tagging experiments are performed by frequency modulation mode (FM), scattered laser light is not included in the lock-in detected bolometer signal because the laser power is constant. Frequency modulation is particularly useful when recording a broad range spectrum. As mentioned in Werdecker's Ph.D. thesis, recording an IR spectrum with power modulation mode can take more than 4 hours even just scanning one wavenumber of the spectral range [17]. The slow scanning speed (about 2 MHz/s) is necessary because of the slow response time of the bolometer detector. Furthermore, the laser power is not constant throughout the scanning range, giving rise to a fluctuated spectral background. These two problems can be solved by applying tagging experiments with frequency modulation mode. With this method, the laser power variation is not presented in the FM spectra. Plus, since the laser linewidth is broadened by the applied modulated voltage signal, the scanning rate can be improved to above 10 MHz/s without causing attenuation of the bolometer signal. For more detail about the concept of frequency modulation and the configuration of the setup, readers can find it in Werdecker's Ph.D. thesis [17].

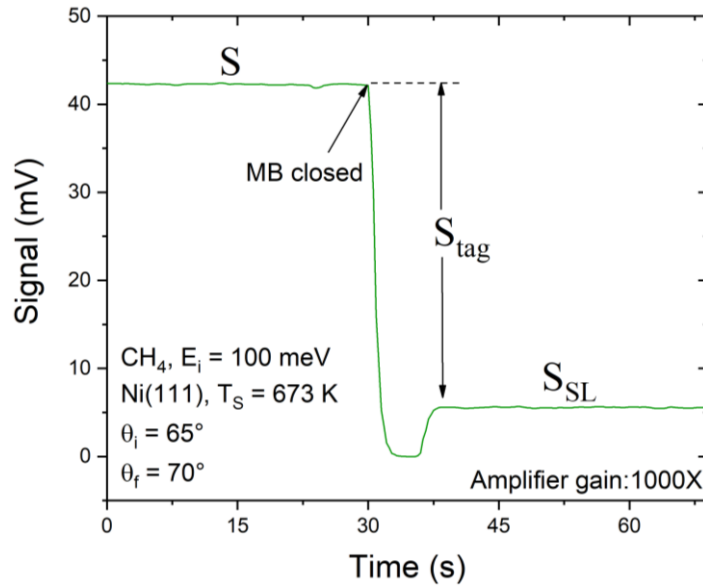


Figure 3.2 Tagging signal of the CH_4 ν_3 fundamental $R(0)$ transition. Both the lock-in time constant and the dwell time were set to 300 ms. After 100 samples, the molecular beam was blocked by a beam flag to record the scattered light signal.

The background-subtracted tagging signal can be converted to the tagged quantum state population. The tagging signal S_{tag} is proportional to the flux of molecules excited to the upper state $|2\rangle$ and the energy difference between the upper and the lower state $\hbar\omega_{12}$

$$S_{\text{tag}} \propto \Delta N_2 \cdot \hbar\omega_{12} \quad (3.1)$$

where ΔN_2 is the net population of molecules that are excited to the upper state. In our case, we excite scattered CH_4 molecules by adding a quantum of ν_3 vibrational mode which is about 3000 cm^{-1} (372 meV) of energy. The highest kinetic energy used in this work (241 meV) is lower than

the vibrational energy. Thus, we can conclude the initial population of the upper state in the scattered CH₄ is zero. If the upper state is populated in the beginning, the tagging laser will cause stimulate emission resulting in a negative tagging signal. The goal of the tagging experiments is to interrogate the population of the lower state. Thus, we express eq 3.1 in the form of the lower state population N_1

$$S_{tag} \propto N_1 \cdot f_{tag} \cdot \hbar\omega_{12} \quad (3.2)$$

where f_{tag} is the excitation probability. According to this expression, the population of the lower state N_1 can be extracted from the tagging signal S_{tag} if the excitation probability is known or if it is the same for all the scattered molecules. The excitation probabilities are different for scattered molecules traveling in different velocities which will introduce difficulty in extracting state populations from tagging signals. This problem can be eliminated using a high-power laser that saturates the absorption, such that the tagging signals are velocity-independent.

3.3 Laser excitation by rapid adiabatic passage

According to eq 3.2, it is obvious that the tagging signal is proportional to the excitation probability of the transition. A high degree of excitation probability needs powerful laser pumping. The Argos OPO systems available in the lab can provide laser beams with high brightness, narrow linewidth, and high coherence that are adequate for our applications. With high-power laser pumping, the saturation of a transition can be reached corresponding to 50% of population inversion. However, due to the high coherence of our IR laser, this limitation can be overcome by the technique called rapid adiabatic passage (RAP). RAP has been implemented in our lab since the Ph.D. work of Bruce Yoder [49]. Using this technique, a nearly complete population inversion can be achieved.

Here, I describe the theory of RAP using the approach reported by Kroon et. al. [67]. Consider a two-level system, the state $|\psi(t)\rangle$ of the system is the superposition of the lower state $|1\rangle$ with energy $\hbar\omega_1$ and the upper state $|2\rangle$ with energy $\hbar\omega_2$

$$|\psi(t)\rangle = c_1(t)|1\rangle e^{-i\omega_1 t} + c_2(t)|2\rangle e^{-i\omega_2 t} \quad (3.3)$$

The state $|\psi\rangle$ satisfies the time-dependent Schrödinger equation with the Hamiltonian $H = H_0 + H_1$, where H_0 is the original Hamiltonian without an optical field, and H_1 is the perturbation term due to the presence of an optical field. If a linear polarized laser beam with angular frequency ω and electric field amplitude E is introduced into the system, inserting eq 3.3 into the time-dependent Schrödinger equation yields the following differential equations

$$\frac{dc_1(t)}{dt} = \frac{i}{2} R_{12} e^{-i\Delta\omega t} c_2(t) \quad (3.4)$$

$$\frac{dc_2(t)}{dt} = \frac{i}{2} R_{21} e^{+i\Delta\omega t} c_1(t) \quad (3.5)$$

Where $|R_{12}| = \left| -\frac{\langle 1|\mu_z|2\rangle E}{\hbar} \right| = |R_{21}| = R$ the Rabi frequency, μ_z is the transition dipole moment along the laser polarization direction, and $\Delta\omega = \omega_2 - \omega_1 - \omega$ the difference between the laser frequency and the transition frequency. The solution of eq 3.4 and 3.5 is given by

$$|c_2(t)|^2 = \left(\frac{R}{\Omega}\right)^2 \sin^2\left(\frac{\Omega t}{2}\right) \quad (3.6)$$

$$\Omega = [R^2 + (\Delta\omega)^2]^{\frac{1}{2}} \quad (3.7)$$

When the laser is resonant with the transition, i.e. $\Delta\omega = 0$, $\Omega = R$, and eq 3.6 becomes

$$|c_2(t)|^2 = \sin^2\left(\frac{Rt}{2}\right) \quad (3.8)$$

In this case, the population of the upper state $|c_2(t)|^2$ oscillates at the Rabi frequency R as time evolves.

So far, we have discussed the case of introducing a fixed frequency laser field that is tuned to be resonant with the transition. Now, consider a case when the laser frequency is time-dependent. The phase factor of the electromagnetic field, in this case, is given by $\exp[i \int_{-\infty}^t \omega(t') dt']$. Substituting it into eq 3.4 and 3.5 yields

$$\frac{dc_1(t)}{dt} = \frac{i}{2} R_{12} c_2(t) \exp\left[-i \int_{-\infty}^t \Delta\omega(t') dt'\right] \quad (3.9)$$

$$\frac{dc_2(t)}{dt} = \frac{i}{2} R_{21} c_1(t) \exp\left[+i \int_{-\infty}^t \Delta\omega(t') dt'\right] \quad (3.10)$$

where $\Delta\omega(t') = \omega_b - \omega_a - \omega(t')$. With the assumption that the frequency sweep is a linear function of time, the analytical solution for eq 3.9 and 3.10 had been worked out by Zener [68]. Assume all the population resides in the lower state at the beginning, resulting in the boundary conditions $c_1(-\infty) = 1$ and $c_2(-\infty) = 0$. The asymptotic behavior at $t \rightarrow \infty$ is expressed as

$$|c_1(\infty)|^2 = \exp\left[\frac{-\pi R(0)^2}{2\Delta\dot{\omega}(0)}\right] \quad (3.11)$$

$$|c_2(\infty)|^2 = 1 - |c_1(\infty)|^2 \quad (3.12)$$

where $\Delta\dot{\omega}(0)$ is the frequency sweep rate. Given a condition where the sweep rate is much slower than the square of the Rabi frequency, e.g. $\Delta\dot{\omega}(0) \ll R(0)^2$, then the population of the lower state will be converted almost completely to the upper state. In this case, the system follows the adiabatic curve and is said to undergo adiabatic following. It means the given perturbation, which is the laser field, is changing slowly such that the quantum mechanical system can adapt its configuration. This concept can be qualitatively understood by considering the picture of the dressed molecule, as depicted in Figure 3.3. Consider a molecule travels through curved laser wavefronts, the molecule experiences a frequency chirp due to Doppler frequency shift. Let the initial population

of the molecules all reside in the ground state. As the molecule experiences the frequency chirp, it is first dressed by the blue-shifted photos, forming a state with energy $E_1 + \hbar\omega(t)$ which is higher than E_2 . The frequency detuning then reduces as the molecule traverses through the waveform, and the detuning turns negative as the molecule passes the middle of the waveform where the two states meet. The frequency chirp which the molecule experiences is reflected by the finite slope of the diabatic curve connecting the “dressed” ground states, as labeled by $E_1 + \hbar\omega(t)$ in Figure 3.3. If the frequency sweep rate is slower than the square of the Rabi frequency, that is

$$\Delta\dot{\omega}(0) \ll R(0)^2 \quad (3.13)$$

Then the system will follow the adiabatic curve when the molecule traverses the frequency sweep, as indicated by the red curve in Figure 3.3. This pathway leads the initial population in lower state $|1\rangle$ all the way to the upper state $|2\rangle$, such that complete population inversion is achieved. Eq 3.13 is known as the *adiabatic condition*.

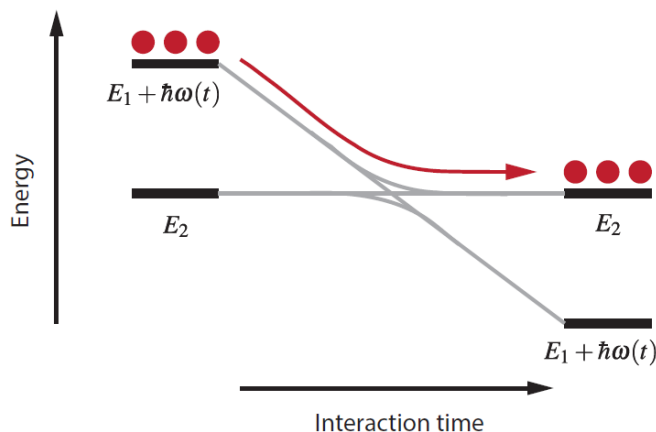


Figure 3.3 Diagram that illustrates the concept of rapid adiabatic passage. See text for the concept. The figure is adapted from Ref [49]

It is clear that to perform RAP for population inversion, the molecules need to experience a time-dependent frequency detuning. An appropriate frequency chirp can be realized by focusing a laser beam with a lens which creates curved wavefronts of the electromagnetic field. The molecule which moves through the curved wavefronts will experience a time-dependent laser frequency (chirp) due to the Doppler effect. When a molecule traverses the curved wavefronts, as indicated by the black arrow in Figure 3.4 (a), it first feels a blue-shifted laser due to the positive Doppler shift, once it crosses the middle of the wavefronts, where the detuning is zero, the detuning turns negative caused by the negative Doppler shift, as presented in Figure 3.4 (b). The effects of the focusing conditions on the RAP efficiency are very well reported by Chadwick [69]. To demonstrate the performance of RAP, Figure 3.5 presents the measured fluence curves of the $R(0) v_3$ fundamental transition for an $E_i = 241$ meV incident CH_4 beam with and without an $f = 254$ mm cylindrical lens. The experiments were performed with a continuous CH_4 beam by the laser beam

was chopped at 2 Hz by a mechanical shutter. The pyroelectric signals were lock-in detected at the modulation frequency referenced by the shutter. The cylindrical lens was placed about 37 cm away from the molecular beam axis. In Figure 3.5, we see when the cylindrical lens is used, the resulting fluence curve reaches the asymptote at lower power. The signal at the highest power is about twice higher than without the lens. This can be explained by the nearly complete population inversion via RAP, whereas without RAP, one excites on average only 50% of the molecules due to Rabi cycling. Note that if the velocity spread along the laser propagation axis is broader than the laser linewidth, the enhancement in the signal can be more than a factor of 2 when RAP is applied.

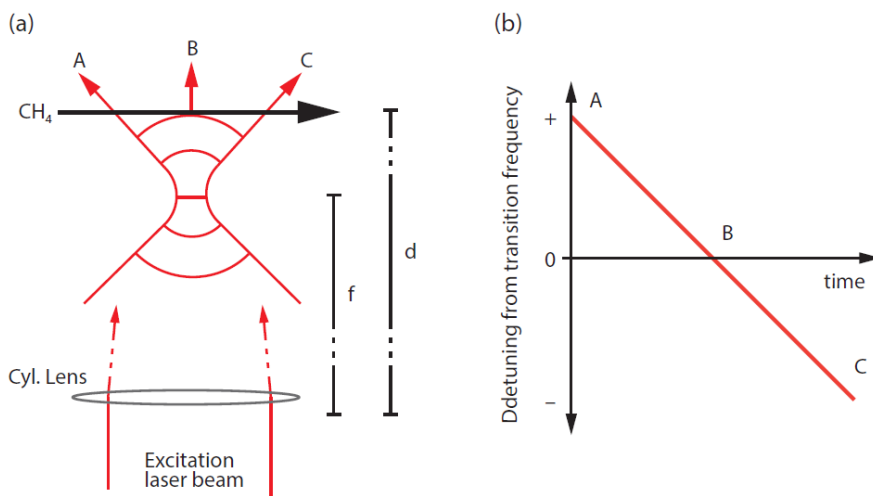


Figure 3.4 (a) schematic diagram of the curved waveform created by a cylindrical lens. The black arrow indicates the propagation direction of the CH₄ molecule. (b) Frequency detuning from the transition the molecule experiences as it travels from A to C. Figures are adapted from ref [17]

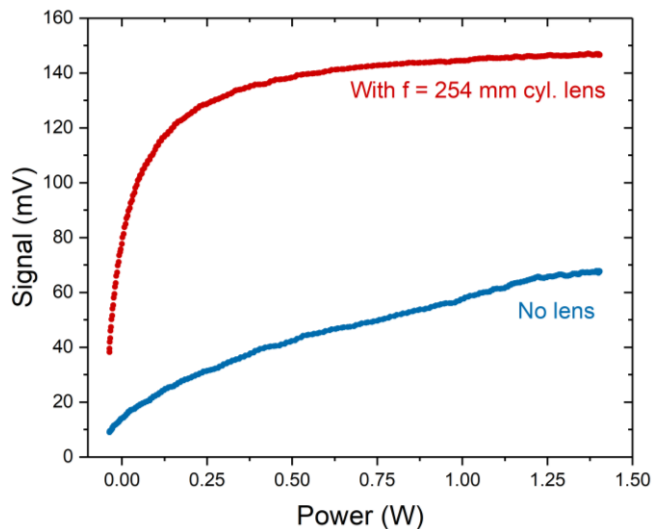


Figure 3.5 Fluence curves of the v_3 R(0) fundamental transition for a 241 meV incident CH_4 beam measured with/without a cylindrical lens. The amplifier gain of the pyroelectric detector was set to 10X. The incident beam was generated by expanding a 3% CH_4 mixture in He at 3 bar of nozzle pressure and room temperature nozzle.

The RAP technique enables us to prepare a molecular beam in a specific quantum state with a maximum excited fraction. This not only improves the performance for studying molecular reactivity on surfaces but also for molecule/surface scattering experiments. A larger influx of state-prepared molecules will result in more scattered molecules which will maximize the sensitivity of the BILT detection.

3.4 The problem of RAP encountered in the BILT machine

In our lab, the RAP technique has been implemented not only for state-preparation of incident molecular beams but also for exciting the scattered molecules in tagging experiments initially reported in the Ph.D. work of Van Reijzen [16]. This technique was tested in the BILT machine for the tagging experiments but a problem was encountered due to a broader residual Doppler shift in the scattered molecules. One of the main differences between the BILT and the old machine is the shorter surface-to-bolometer distance of 81 vs 360 mm, respectively. With the reduced distance, we expect the molecular flux measured by the bolometer to be increased by a factor of 20 leading to much-improved sensitivity. As I have shown in Chapter 2, for the chopped methane beam scattering experiments, we do observe a more than 20-fold increase in bolometer signal. However, in the laser tagging experiments, the improvement in the bolometer signal is only two-fold* if I compare the v_3 R(0) transition. (*Note that the tagging signal of the old machine was measured by the V1 bolometer. As I have discussed in Chapter 2, the V2 bolometer is about a factor 5 less sensitive than the V1, this factor is not taken into account when comparing the tagging signals between the two machines). The reason for the lack of tagging signal increase is the larger acceptance angle of the bolometer in the BILT machine as illustrated in Figure 3.6 (a). Reducing the sample to bolometer distance from 360 to 81 mm increases the acceptance angle of the

bolometer by a factor of 5. A larger acceptance angle results in a larger residual Doppler width of the tagging transitions given by:

$$\omega_D = \omega_0 \times \frac{v \times \sin\alpha}{c} \quad (3.14)$$

Where ω_0 is the center frequency of a transition, v is the velocity of the scattered molecule, c is the speed of light, and α is half of the bolometer acceptance angle, as shown in Figure 3.6 (b). Due to the larger residual Doppler width in the BILT machine, using our current focusing conditions for RAP, the resulting total frequency sweep cannot cover the entire residual Doppler width of the scattered molecules. Therefore, only a fraction of the scattered molecules can be excited by the tagging laser. As a result, the improvement of the tagging signal is not as strong as initially hoped for. Furthermore, the asymptotes of the fluence curves for most of the v_3 fundamental transitions are more difficult to reach, which makes the determination of state-population more difficult. To demonstrate this problem, first I will provide the equations for calculating the frequency sweep rate and the total frequency sweep for excitation by rapid adiabatic passage. Then, I will compare the scattering geometries of the two machines and their corresponding total frequency sweep. Finally, these calculations will be compared to experimental lineshape measurements of scattered CH_4 .

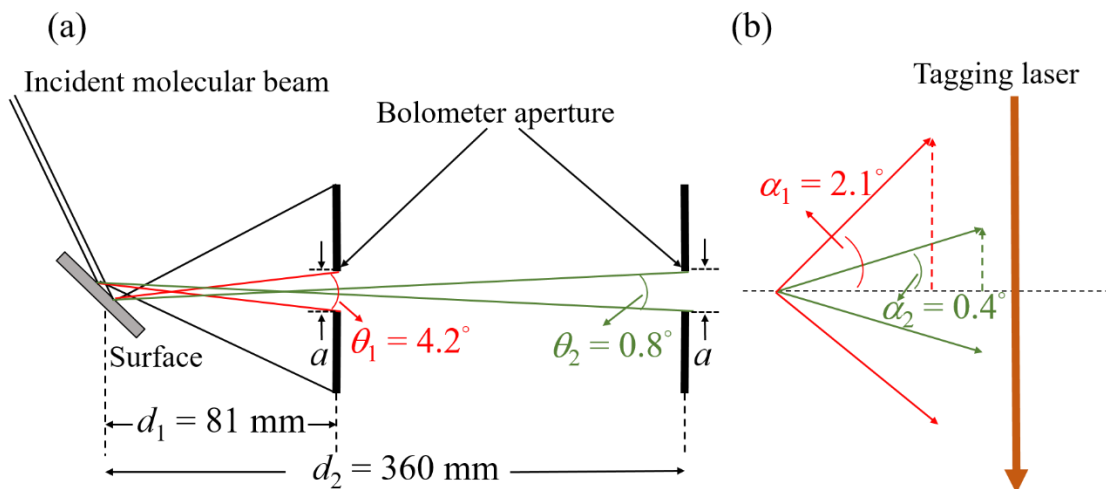


Figure 3.6 (a) Schematic of the correlation between the acceptance angle and the sample-to-bolometer distance. The acceptance angles θ_1 and θ_2 are calculated with the scattering geometry of $\theta_i = 65^\circ$, and $\theta_f = 70^\circ$ for the BILT and the old machine, respectively. (b) A diagram that shows the concept of broader residual Doppler shift for a wider acceptance angle. The solid arrows indicate the velocity vectors of scattered molecules with the largest angles α_1 and α_2 about the surface-to-bolometer axis that can be captured by the bolometers of the BILT and the old machine, respectively. Here, α is half of the acceptance angle. The dashed arrows are the velocity components projected on the laser propagation axis.

For deriving the total frequency sweep in a certain focusing condition, I adopt the approach reported by Chadwick [69]. Consider a molecule with velocity v_x passing perpendicular through a focusing laser at a position z away from the focal point, as shown in Figure 3.4 (a). The frequency sweep rate is given by

$$\frac{d\omega}{dt} = \frac{v_x^2 \omega_0}{R(z)c} \quad (3.15)$$

where $R(z)$ is the radius of curvature of the wavefronts at position z defined by the distance between the beam waist and the molecule. $R(z)$ can be calculated by

$$R(z) = z + \frac{z_R^2}{z} \quad (3.16)$$

Thus the wavefront radius $R(z)$ reaches a minimum at $z = z_R$

Here z_R is the Rayleigh range, given by

$$z_R = \frac{\pi \omega_x(0)^2}{\lambda} \quad (3.17)$$

where $\omega_x(0)$ is the beam waist at the focal point ($z = 0$), and λ is the laser wavelength. Assuming a Gaussian beam, the beam waist can be derived by

$$\omega_x(0) = \frac{f\lambda}{r\pi} \quad (3.18)$$

where f is the focal length of the lens and r is the radius of the unfocused laser beam. The total frequency sweep experienced by a molecule is simply given the sweep rate multiplied by the time taken for the molecule to cross the laser beam, as given by

$$\frac{d\omega}{dt} T_{trans} = \frac{v_x^2 \omega_0}{R(z)c} T_{trans} \quad (3.19)$$

The transit time T_{trans} can be calculated by knowing the beam waist at a distance z from the focal point and the velocity of the molecule

$$T_{trans} = \frac{2\omega_x(z)}{v_x} \quad (3.20)$$

The beam waist at position z can be derived by

$$\omega_x(z) = \omega_x(0) \sqrt{1 + \frac{z^2}{z_R^2}} \quad (3.21)$$

Consider the scattering of CH_4 from a Ni(111) surface with an incident kinetic energy $E_i = 100$ meV, corresponding to the molecular velocity of about 1000 m/s. Assume the scattered CH_4 still

maintains the incident velocity of 1000 m/s. The distance between the $f = 254$ mm cylindrical lens on the top tagging window and the scattering plane is about 380 mm, corresponding to $z = 126$ mm. Given the laser beam radius of 2 mm and the laser wavelength of $3.3 \mu\text{m}$ for the $\text{CH}_4 \nu_3 \text{R}(0)$ fundamental transition, the total frequency sweep is calculated to be 4.7 MHz. However, the residual Doppler broadening in the BILT machine with the aforementioned scattering conditions is calculated to be 23 MHz by eq 3.14. Because of this reason, the scattered molecules captured by the bolometer were not fully resonant with the tagging laser therefore only a portion of molecules are excited.

Now we should quantitatively compare the scattering geometries between the old and the BILT machine. The surface-to-bolometer distances for the BILT and the old machine are 81 mm and 360 mm, respectively. If we assume the beam spot projected on the surface is a point source, simply by linking the point with the two sides of the detector, the full acceptance angle is calculated to be 2.83 and 0.65° for the BILT and the old machine, respectively. If the molecular beam size projected on the surface is much smaller than the bolometer aperture, the acceptance angle is simply determined by the size of the bolometer aperture and the sample-to-detector distance. However, in reality, the molecular beam size projected on the surface is finite and cannot be treated as a point. In this case, determining the acceptance angle needs to take into account the dimensions of the molecular beam size on the surface and also the incident angle, as illustrated in Figure 3.6.

To figure out the size of the molecular beam size projected on the surface, first, we need to estimate the size of the molecular beam, which is given by the size of the beam shaping aperture in the P3/P4 wall and the divergence of the molecular beam. The divergence of the molecular beam is determined by the nozzle-to-aperture (P4) distance and the diameter of the aperture. For the BILT machine, the dimensions can be found in Figure 2.27. Given the distance = 137 mm and the diameter of the aperture = 1.75 mm, the divergence of the molecular beam is estimated to be 0.73° . The molecular beam size on the surface sample is expected to be 2.3 mm. For off-normal incidence, the projection of the molecular beam on the surface will be an ellipse. The dimension which determines the acceptance angle is the long axis of the ellipse. If the incident angle is 65° , the length of the long axis can be calculated to be 5.4 mm. The acceptance angle of the bolometer at 70° of scattering angle is estimated to be 4.2° for the BILT machine, as shown in Figure 3.7. Using the same approach, the acceptance angle of the old machine is estimated to be 0.8° at the scattering geometry of $\theta_i = 65^\circ$, $\theta_f = 70^\circ$. The dimensions needed to deduce the acceptance angles for the two machines are summarized in Table 3.1

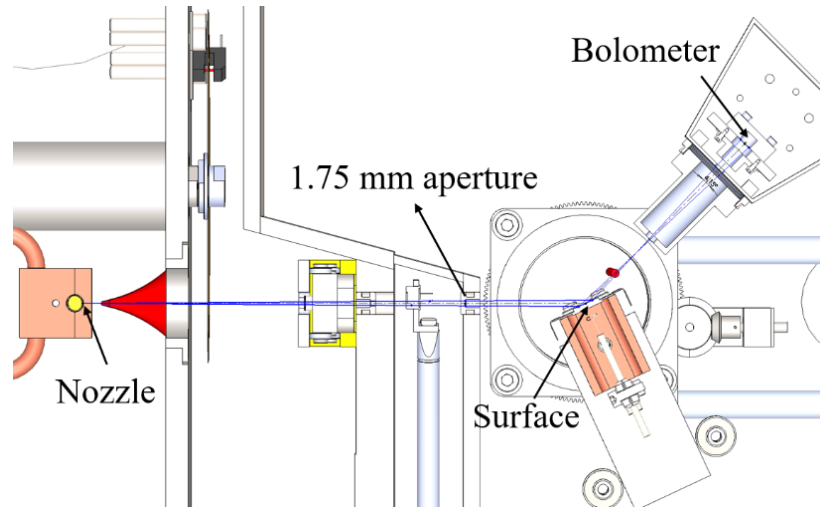


Figure 3.7 Illustration for the scattering geometry of the BILT machine that shows the divergence of the incident molecular beam and its projection on the surface and the resulting acceptance angle of the bolometer. Scattering geometry in this figure is set to $\theta_i = 65^\circ$, $\theta_f = 70^\circ$.

Table 3.1 The collection of parameters needed to estimate the bolometer acceptance angles for the two machines. The dimensions of the old machine are derived by the value recorded in the Ph.D. thesis of Van Reijzen and Werdecker [16,17]. *The nozzle-to-aperture distance of the old machine is estimated from a Solidworks 3D model built by Van Reijzen. Note that in this model, the nozzle-to-skimmer distance is not included therefore I assume a value of 5 mm.

	BILT machine	Old machine
Sample-to-detector distance (mm)	81	360
Size of the aperture (P4) (mm)	1.75	1
Nozzle-to-aperture distance (mm)	137	254*
Aperture to surface distance (mm)	44	97
Beam size on the surface at $\theta_i = 0^\circ$ (mm)	2.3	1.4
Beam size on the surface at $\theta_i \neq 0^\circ$ (mm)	5.4 ($\theta_i = 65^\circ$) 3.3 ($\theta_i = 45^\circ$)	3.3 ($\theta_i = 65^\circ$)
Acceptance angle ($^\circ$)	4.2 ($\theta_i = 65^\circ$, $\theta_f = 70^\circ$) 4.5 ($\theta_i = \theta_f = 45^\circ$)	0.8 ($\theta_i = 65^\circ$, $\theta_f = 70^\circ$)

With the acceptance angle derived above, one can calculate the residual Doppler broadening for the two machines at the same incident and scattering angles using eq 3.14. This results in 22.0 and 4.2 MHz for the BILT and the old machine, respectively. Assuming the velocity of the scattered CH_4 is about 1000 m/s, the total frequency sweep produced by an $f = 254$ mm cylindrical lens is calculated to be 4.7 MHz and 4.6 MHz for the BILT and the old machine, respectively, by eq 3.19. Note that the slightly different value of the total frequency sweep is due to the fact that the cylindrical lens for the BILT machine is placed slightly farther from the scattering molecules (BILT: 380 mm, Old: 350 mm), corresponding to a larger z value (BILT: 126 mm, Old: 96 mm). The calculation clearly shows that the residual Doppler broadening of the BILT machine is much

larger than the total frequency sweep, explaining why the tagging signals measured by the BILT machine are not as high as expected. Whereas in the old machine, the narrower residual Doppler broadening can be fully covered by the total frequency sweep.

The calculations discussed above are supported by the tagging linewidth measurements. For these measurements, the cylindrical lens was removed such that linewidth broadening produced by the RAP lens was not included. The linewidth of the R(0) ν_3 fundamental transition was measured by scanning the tagging laser frequency (OPO-II) locked to the transfer cavity in the power-modulation mode and lock-in recording the bolometer signals. The resulting linewidths measured by the BILT and the old machine are shown in Figure 3.8. In both cases, the incident CH₄ beam was generated by 3 bar of pure methane gas and $T_n = 300$ K, resulting in 100 meV of kinetic energy whose velocity is about 1000 m/s. The scattering experiments were performed at the geometry of $\theta_i = 65^\circ$, $\theta_f = 70^\circ$ for the old machine, whereas the scattering geometry for the BILT machine was set to $\theta_i = \theta_f = 45^\circ$ for convenience in the first few tests. Although the incident and the scattering angles of the BILT machine were not set to be the same as the old machine in these measurements, the change of the residual Doppler broadening caused by this difference is expected to be less than 10%, as I have calculated in Table 3.2. The measured full width at half maximum for the BILT machine is approximately 5.5 times broader than the one of the old machine. This factor agrees very well with the ratio of the residual Doppler broadening of the two machines $\frac{\sin 2.25^\circ}{\sin 0.4^\circ} = 5.6$ (eq 3.14). The experimental results unambiguously show the wider residual Doppler broadening of the BILT machine and are consistent with the calculations. The calculated residual Doppler broadening and the experimentally measured linewidths for the two machines are summarized in Table 3.2

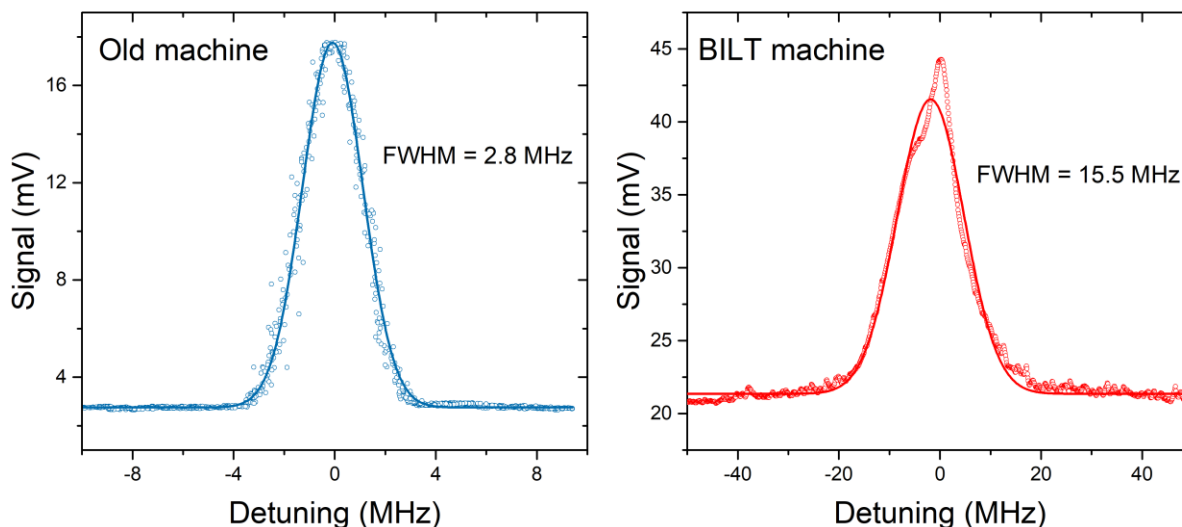


Figure 3.8 Lineshape measurements of the $R(0) \nu_3$ fundamental transition for the BILT and the old machine with incident CH_4 beam at $E_i = 100$ meV. The preamplifier gain was set to 1000. The scattering geometry of the old machine measurement was set to $\theta_i = 65^\circ$, $\theta_f = 70^\circ$. Whereas for the BILT machine is was $\theta_i = \theta_f = 45^\circ$. Note that the lineshape measurements were performed without the cylindrical lens. The solid curves are fittings using the Gaussian function.

Table 3.2 Calculated total frequency sweep, residual Doppler broadening, and measured FWHM of the $R(0) \nu_3$ fundamental transition for the BILT and the old machine. For the total frequency sweep, I assume the velocity of the scattered CH_4 is 1000 m/s. The distances z between the $f = 254$ mm cylindrical lens and the surface-to-detector axis are taken into account for the calculations.

	BILT	Old
Total frequency sweep (MHz)	4.7 (at $z = 126$ mm)	4.6 (at $z = 96$ mm)
Residual Doppler broadening (MHz)	22.0 ($\theta_i = 65^\circ$, $\theta_f = 70^\circ$) 23.5 ($\theta_i = \theta_f = 45^\circ$)	4.2 ($\theta_i = 65^\circ$, $\theta_f = 70^\circ$)
Measured FWHM (MHz)	15.5	2.8

It is now clear that due to the wider residual Doppler broadening, the frequency sweep produced by the $f = 254$ mm cylindrical lens can excite only a fraction of the scattered molecules. As a result, the improvement of laser tagging signals is not as high as expected. In terms of the $\nu_3 R(0)$ fundamental transition, the signal measured by the BILT machine is only twice as large as for the old machine at the same incident and scattering angle. For other ν_3 fundamental transitions which have lower Hönl-London factors, the improvement can be lower. Furthermore, the asymptotes of fluence curves measured by the BILT machine for most of the ν_3 fundamental transitions were not reached with the available tagging laser power. For example, Figure 3.9 shows the fluence curves for the $\nu_3 Q(3) A_2$ fundamental transition measured by the two machines. Note that “A2” here denotes the symmetry of the lower state rotational wave function. We can see the fluence curve

measured by the BILT machine is less saturated than the one by the old machine. If the asymptote of a fluence curve is not reached but close, the asymptotic value can still be deduced by fitting the curve with the Landau-Zener type formula,

$$S_{tag}(P) = A[1 - \exp(-cP)] \quad (3.22)$$

where A and c are adjustable parameters corresponding to the asymptotic value and the transition dipole moment, respectively, and P is the laser power. However, the fluence curve measured by the BILT machine is too far from the asymptote, such that the accurate asymptotic value cannot be derived by the fitting function. As a consequence, the state population cannot be extracted from the tagging signal.

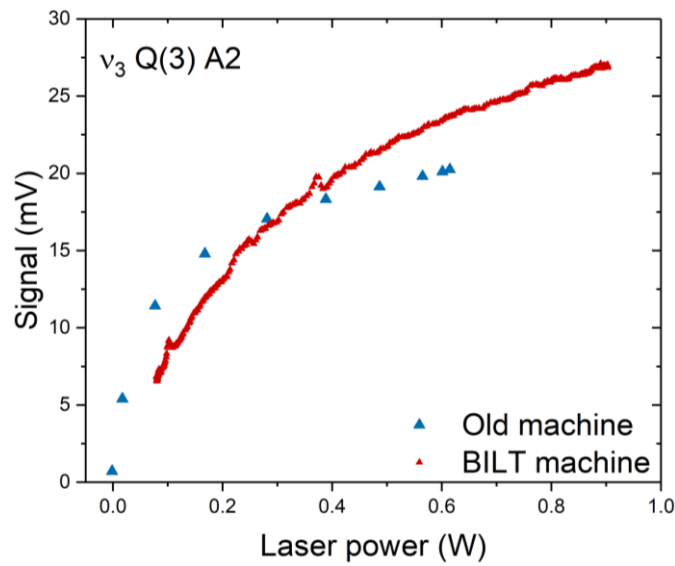


Figure 3.9 Fluence curves of the v_3 Q(3) A2 fundamental transition measured by the BILT and the old machine using the same scattering geometry of $\theta_i = 65^\circ$, $\theta_f = 70^\circ$ and the incident beam energy of 100 meV.

To solve the problems caused by the broader residual Doppler broadening, one may first consider using a different focusing condition that provides a higher total frequency sweep. Using eq 3.19, to cover 23 MHz of the residual Doppler shift, one would need a cylindrical lens with a focal length shorter than 5 cm. A shorter focal length will result in a smaller radius of curvature of the laser wavefronts. As a result, this increases the frequency sweep rate and reduces the Rabi frequency which is not favorable for fulfilling the adiabatic condition (eq 3.13). To verify this concern, I calculated the frequency sweep rate and the Rabi frequency with several focusing conditions. The Rabi frequency is given by

$$R = \frac{\mu \cdot E}{\hbar} \quad (3.23)$$

where μ is the transition dipole moment and E is the electric field of the laser beam. Here, I consider the case of the ν_3 R(0) fundamental transition with an Einstein A coefficient of 25.36 s^{-1} according to the HITRAN database, resulting in a transition dipole moment of $1.8 \times 10^{-31} \text{ Cm}$ [70]. Given the laser power of 1 W, the tagging laser beam diameter of 4 mm, and the bolometer acceptance angle of 4.2° , the results are shown in Figure 3.10 for two different velocities of scattered molecules, 1000 and 1700 m/s. In both cases, as the focal length is decreased, the ratio $\frac{R^2}{d\omega/dt}$ also decreases. For the excitation to undergo adiabatic following, one needs to fulfill the adiabatic condition, namely $\frac{d\omega}{dt} \ll R^2$. For the case of slow scattered molecules with 1000 m/s, the square of Rabi frequency is less than 2-fold higher than the sweep rate when an $f = 5 \text{ cm}$ cylindrical lens is used. In this case, the excitation won't proceed via the adiabatic following and therefore nearly complete population inversion won't be achieved. For scattered molecules faster than 1700 m/s (corresponding to the velocity generated by the 3% CH_4 in He mixture with 300 K nozzle), the calculated squared Rabi frequency is smaller than the sweep rate for an $f = 5 \text{ cm}$ cylindrical lens. In this case, laser excitation via RAP is not expected to succeed. To increase the Rabi frequency, a higher laser fluence would be needed. This can be achieved by using a higher power laser or reducing the laser beam size down to 1 mm diameter with the current laser power. However, such a small laser beam size cannot spatially cover all the scattered molecules captured by the bolometer.

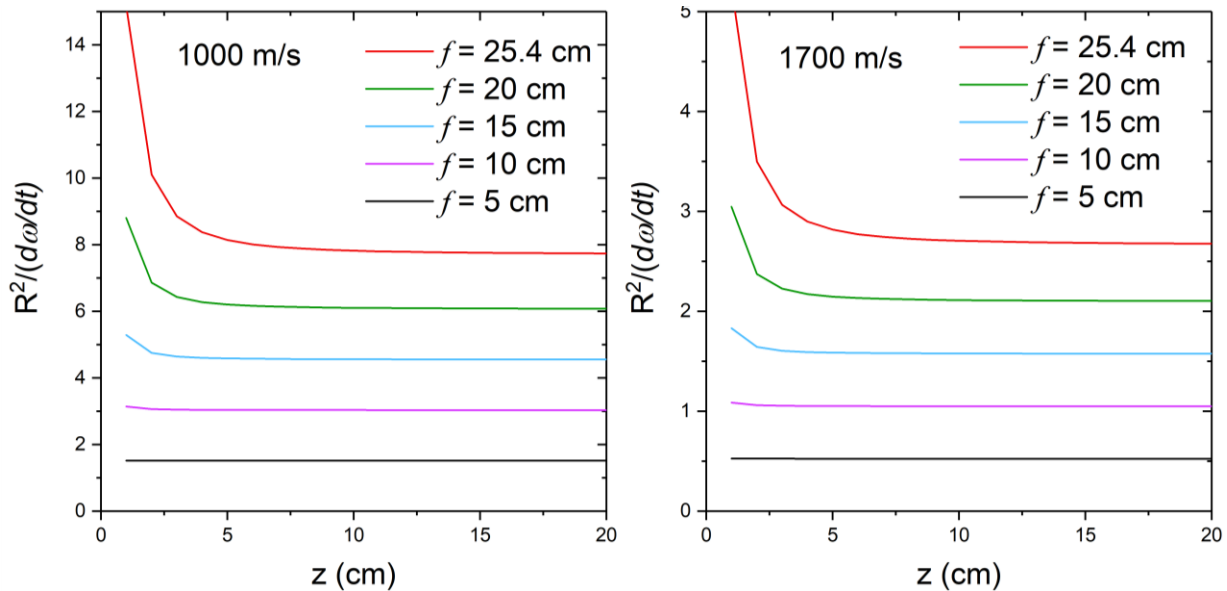


Figure 3.10 Ratio of calculated squared Rabi frequency and frequency sweep rate for different focal lengths used for RAP excitation of the ν_3 R(0) fundamental transition with frequency 3028 cm^{-1} and transition dipole moment $= 1.8 \cdot 10^{-31} \text{ Cm}$. The laser power is set to 1 W with 4 mm of the beam diameter. The velocities of the scattered molecules are set to 1000 m/s (left) and 1700 m/s (right).

3.5 Laser linewidth broadening

It is clear from the above discussion that complete population inversion by RAP can't be achieved with the available laser power in our current setup. As an alternative to excitation by RAP, we decided to broaden tagging laser linewidth in order to match the residual Doppler width of scattered molecules. For the TOPO system, this can be realized by adding white noise to the external frequency modulation input of the DFB seed laser. One of the advantages of the TOPO system is the fact that its DFB seed laser can be frequency modulated up to a GHz. For such a strongly broadened tagging laser, RAP is no longer applicable because the fast variation in laser frequency cannot provide a required smooth frequency sweep. As a result, instead of reaching unity of the excitation probability, we expect an exciting fraction of 50% due to saturation of the tagging transitions. As I will show below, the available laser power of the TOPO laser is sufficient to saturate all the R-branch transitions of the ν_3 fundamental up to $J = 10$. By this method, we expect to reach an excitation probability of 50% of the scattered molecules impinging on the bolometer.

The noise applied to the seed laser is generated by the oscilloscope (Teledyne Leroy, Wavesurfer 3024) which has a built-in function generator. The function generator can provide white noise signals with 0-60 MHz bandwidth and an RMS amplitude of 150 mV. The bandwidth of the laser diode current modulation is about 1000 MHz. The DFB laser is equipped with an AC and a DC input for current modulation. The linear response range for the AC coupled input is lower (± 1.8 V) but more sensitive with a sensitivity of 2.2 mA/V. Whereas the DC input has a higher linear range of ± 5 V but a lower sensitivity of 0.73 mA/V. To test the performance of the laser excitation with the frequency broadened laser, we measured absorption profiles of the ν_3 R(0) fundamental transitions for the scattered CH_4 as a function of noise amplitude. The profiles were measured by recording the bolometer signal while scanning the TOPO laser frequency across the transition. The scattering experiments were carried out at the scattering geometry of $\theta_i = 65^\circ$, $\theta_f = 70^\circ$ with the incident beam energy of 241 meV (3% CH_4 in He).

Figure 3.11 presents the resulting absorption profiles with noise amplitudes in the range of 0-150 mV applied to the AC-coupled input of the DFB seed laser. There we see as the noise amplitude increases, the peak height first increases until 80 mV of noise amplitude (RMS), above 80 mV, absorption peak height decreases with increasing linewidth. The behavior can be understood in the following way. As the noise amplitude increases, the laser frequency is broadened accordingly, which allows the laser to excite a larger fraction of the Doppler width of the scattered molecules. However, if the laser linewidth is broadened more than the residual Doppler width, the excitation efficiency decreases, resulting in a lower peak height. Although the peak height decreases at noise amplitude > 80 mV, the peak area which is proportional to the number of molecules detected by the bolometer keeps increasing with increasing modulation amplitude > 80 mV and reaches an asymptote at 120 mV, as shown in Figure 3.12.

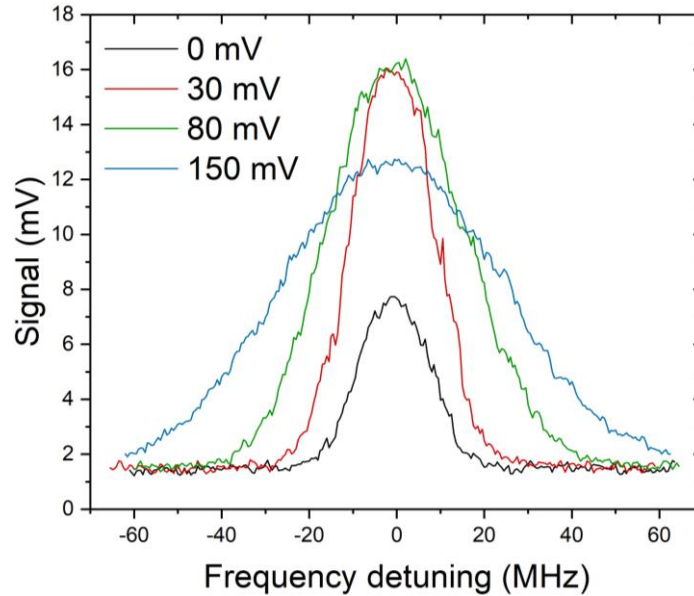


Figure 3.11 Absorption profiles for the ν_3 R(0) fundamental transition for CH₄ scattered from a 673 K Ni(111) surface for tagging laser frequency modulation amplitude ranging from 0 to 150 mV applied to the AC-coupled input of the DFB seed laser. Experiments are performed with the scattering geometry of $\theta_i = 65^\circ$, $\theta_f = 70^\circ$ and $E_i = 241$ meV.

The peak height, peak area, and the FWHM of the absorption profiles measured at different noise amplitudes are summarized in Figure 3.12. The peak height and FWHM are derived by fitting the experimental data points with Gaussian functions and extracting the height and the width parameters. At a low modulation amplitude of 0-30 mV, the FWHM of the absorption profiles are identical, about 20 MHz, and are determined mainly by the residual Doppler broadening. As the noise amplitude increases to 150 mV, the absorption linewidth reaches 60 MHz, determined by the convolution of the residual Doppler broadening and the laser frequency linewidth. The laser linewidth is then estimated to be about 40 MHz at 150 mV of noise amplitude. However, this is much lower than expected if we consider the quoted transfer function of the DFB seed laser. Given the electric coefficient of the DFB laser 1.5 GHz/mA and the sensitivity of the AC-coupled input of 2.2 mA/V, when applying 150 mV of noise, we expect to have the laser frequency linewidth of 500 MHz, which is much higher than the measured value. The reason which causes the discrepancy is not immediately clear. We suspect some elements in the laser have lower bandwidth than the applied noise such that the applied noise signal cannot be fully transferred to the variation of the laser frequency.

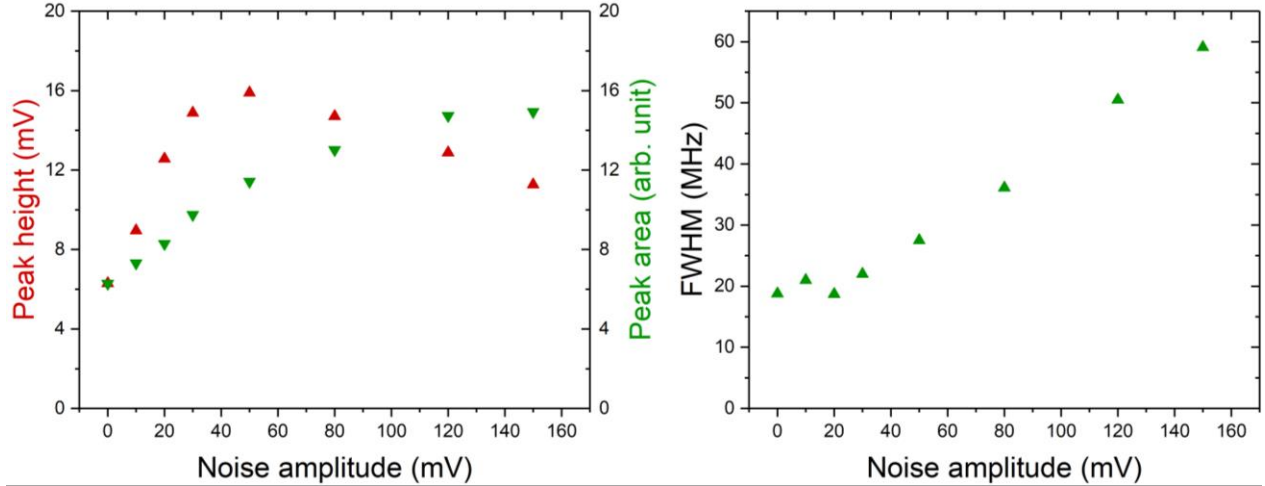


Figure 3.12 Characteristics extracted from the absorption profiles shown in Figure 3.11. Left: peak height (red data points) and peak area (green data points) of the absorption. Right: FWHM of the absorption profiles. All values are derived by fitting the experimental spectra with Gaussian functions and then extracting the corresponding fitting parameters.

Using the frequency-broadened tagging laser, we expect to be able to saturate the tagging transitions of the scattered molecules and achieve equal population in the excited and ground-state creating an excited fraction of 50%. Saturation can ensure that the tagging signals are independent of the velocities of the scattered molecules. At saturation, the measured tagging signal is proportional to the population of the lower level of the tagging transition which facilitates the determination of the rotational state populations for the scattered molecules. In practice, the saturation of a transition can be verified by measuring a fluence curve which gives the tagging signal as a function of laser power. The fluence curve can be described by the modified Landau-Zener formula [17], given by

$$S_{tag}(P) = \frac{A}{g_1} \sum_{M=-J_1}^{J_1} [1 - \exp(-a \langle J_1 M_1, 10 | J_2 M_2 \rangle^2 P)] \quad (3.24)$$

where A is the asymptotic value, g_1 is the degeneracy of the lower state, a is an adjustable parameter that is proportional to the Einstein coefficient A_{21} , P is the laser power, and $\langle J_1 M_1, 10 | J_2 M_2 \rangle$ is the Clebsch-Gordan coefficient for a transition between two rotational levels with the rotational quantum number (J_1, M_1) and (J_2, M_2) . Note that when a linear polarized laser is used for excitations, the transition dipole moments are not identical for different M levels of a given J . This is due to the different spatial orientations of the molecules with respect to the direction of the laser polarization. The strength of the coupling between two rotational levels (J_1, M_1) and (J_2, M_2) induced by a linear polarized light is governed by the Clebsch-Gordan coefficients. The selection rule for linear polarized light states $\Delta M = 0$, but the transition between two $M = 0$ levels is forbidden for Q branch. The product of the Einstein coefficient and the square of the

Clebsch-Gordan coefficient (Hönl-London factor) determines the initial slopes of the fluence curve. This product is essentially the square of the transition dipole moment

$$\mu_{12} = \langle J_1 M_1, 10 | J_2 M_2 \rangle \sqrt{\frac{3\varepsilon_0 \hbar c^3}{2\omega_{12}^3}} A_{21} \quad (3.25)$$

Therefore a stronger transition comes with a steeper initial slope and thus the asymptote is reached at lower laser power. The analytical expressions for the Hönl-London factors are summarized in Table 3.3. The calculated values for the R and the Q branch using these expressions are plotted in Figure 3.16. As one can see in Figure 3.16, for the R branch transitions of a given J , the Hönl-London factors are lower for higher M levels, whereas the opposite trend is observed for Q branch transitions. It is worth noting that the Q branch transitions show a greater range of Hönl-London factors between M levels of a certain J . Considering the case of $J = 4$, for R branch transitions, the Hönl-London factor of $M = 0$ is 0.56, and the lowest value is given by 0.20 from $M = 4$ which is about 3 fold lower than $M = 0$. For Q branch transitions of $J = 4$, the strongest Hönl-London factor of 0.8 occurs for $M = 4$, but for $M = 0$ it is only 0.05, more than 10 times lower than $M = 4$. Because of this feature, tagging via Q branch transition makes the lower M levels harder to saturate. For this reason, for tagging a specific J level, the R branch transitions are preferable if the three branches all have similar Einstein coefficients.

Table 3.3 Analytical expressions of Hönl-London factors for different branches of transitions using a linear polarized light.

Branch	Expression
R	$ \langle JM, 10 (J+1)M \rangle ^2 = \frac{(J-M+1)(J+M+1)}{(2J+1)(J+1)}$
Q	$ \langle JM, 10 JM \rangle ^2 = \frac{M^2}{J(J+1)}$
P	$ \langle JM, 10 (J-1)M \rangle ^2 = \frac{(J-M)(J+M)}{J(2J+1)}$

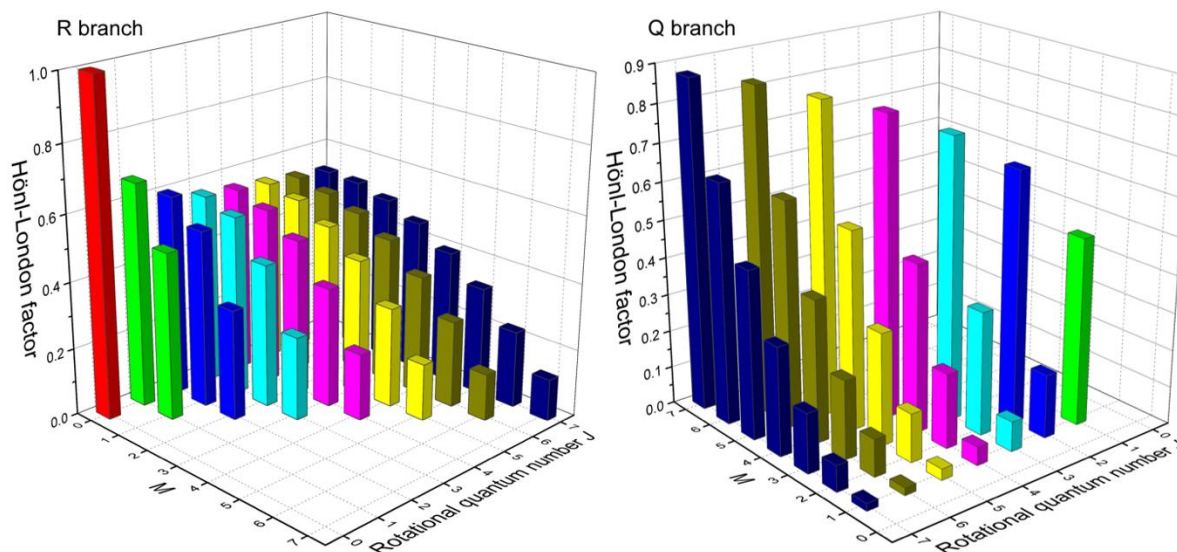


Figure 3.13 Hönl-London factors calculated by the expressions in Table 3.3 for R branch (left) and Q branch (right) transitions.

To confirm that saturation can be reached with the frequency-broadened tagging laser, we measured fluence curves for several $\nu_3 \leftarrow \nu = 0$ rotational transitions. Figure 3.14 shows the fluence curves of the R(6) A2 and R(9) A2 transitions of scattered CH_4 with 100 mV of white noise applied to the DC input of the DFB seed laser. In both cases, we observed the asymptote of the fluence curve with 1 W of laser power. Except for the R(0) transition, the transition dipole moments for the ν_3 R branch fundamental transitions up to $J = 10$ are similar. Their Einstein coefficients are in the range of $25\text{-}30 \text{ s}^{-1}$. For the R(0) transition, the transition dipole moment is twice as large due to its strong Hönl-London factor (as shown in the left panel of Figure 3.13). Therefore we conclude that with the available output power of the TOPO laser, we can saturate all the R branch transitions of the ν_3 fundamental up to $J = 10$. In this case, the tagging signal measured at the highest laser power is a measure of the rotational state population in the vibrational ground state $\nu = 0$.

The fluence curves shown in Figure 3.14 were measured for a fast incident CH_4 beam with $E_i = 241 \text{ meV}$. Assuming a direct scattering process, a fast incident molecule beam will also result in fast scattered molecules. Faster molecules are harder to saturate because the molecules spend less time in the laser field. If the saturation can be observed for the tagging experiments with fast molecules, tagging experiments with slower molecules will also be saturated by the same laser power. The incident beam with $E_i = 241 \text{ meV}$ is the fastest gas mixture I used in this thesis work so it follows that the tagging detection at lower incident energy will also be saturated. In the next chapter, I will use this method to study the rotational inelastic scattering of $\text{CH}_4(\nu = 0)$ from Ni(111).

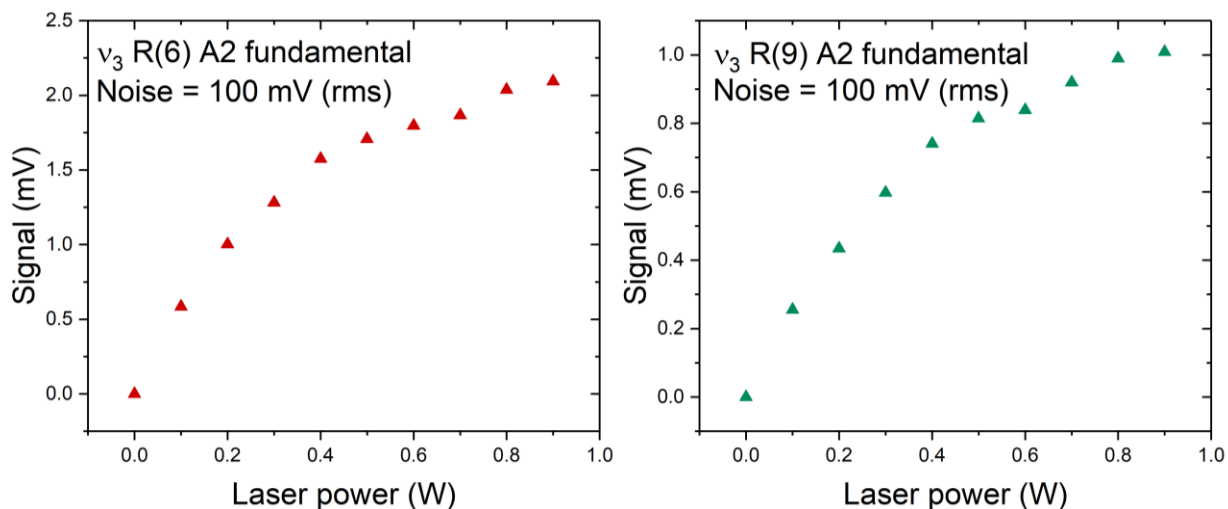


Figure 3.14 Fluence curves of the ν_3 R(6) A2 and the R(9) A2 transitions of scattered CH_4 measured the frequency-broadened laser. The frequency broadening was performed by adding 100 mV (RMS) of white noise to the DC-coupled input of the DFB seed laser. The scattering experiments were carried out at the geometry of $\theta_i = 65^\circ$, $\theta_f = 70^\circ$ with 241 meV of incident beam energy.

3.6 CH_4 infrared spectroscopy

State-resolved CH_4 /surface scattering experiments using BILT detection require a suitable infrared laser for the tagging excitation of the scattered CH_4 . The TOPO system from Toptica and the 2 Argos OPO systems from Aculight with C-modules allow for excitation of the antisymmetric C-H stretch normal mode ν_3 of CH_4 near 3000 cm^{-1} . Understanding the IR spectroscopy of methane is important for the state-specific preparation of the incident molecules as well as for the state-resolved detection of the scattered molecules. While CH_4 possesses a simple molecular structure, its IR spectroscopy is complicated due to several anharmonic couplings and the nuclear spin of the four hydrogen atoms. In this section, I will explain the structure of the rovibrational levels for different nuclear spin isotopes of CH_4 as it is indispensable for understanding the results of my thesis work. This requires some basic concepts of group theory, readers not familiar with group theory are referred to the literature [71,72].

A CH_4 molecule consists of a carbon atom at the center with 4 hydrogen atoms attached, forming a tetrahedral structure belonging to the T_d point group. The H-C-H bond angle is 109.5° at its equilibrium geometry. The CH_4 molecule with 5 atoms then possesses $3n - 6 = 9$ normal modes, but only 4 distinct vibrational frequencies due to the degeneracies of the normal modes. There is a nondegenerate symmetric stretch mode, a doubly degenerate bending mode, a triply degenerate antisymmetric stretch mode, and a triply degenerate bending mode. The motions of the normal modes, their corresponding symmetry, and the vibrational frequencies are shown in Figure 3.15. These normal mode frequencies follow roughly the relation

$$\nu_1 \approx 2\nu_2 \approx \nu_3 \approx 2\nu_4 \approx 3000\text{ cm}^{-1} \quad (3.26)$$

Because of these resonances and anharmonic coupling, vibrational levels cluster every 1500 cm^{-1} in energy forming so-called polyads, as shown in Figure 3.16.

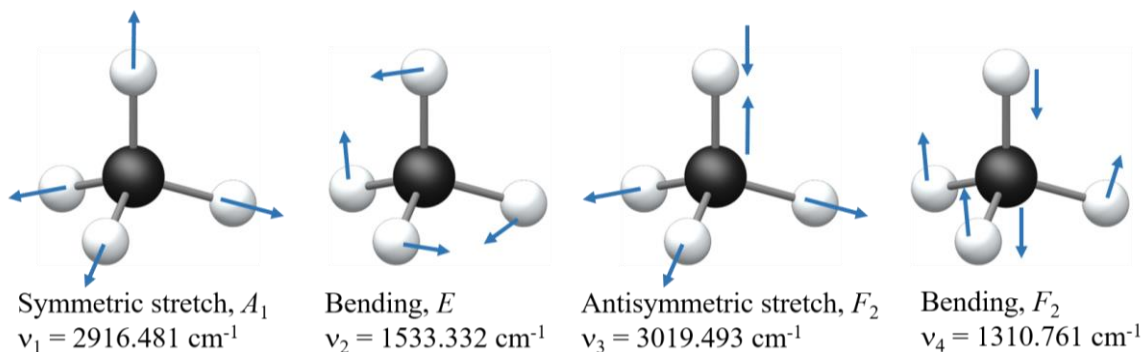


Figure 3.15 Normal vibrational modes of CH_4 , their corresponding symmetry, and the vibrational frequencies. The vibrational frequencies are adapted from ref [73].

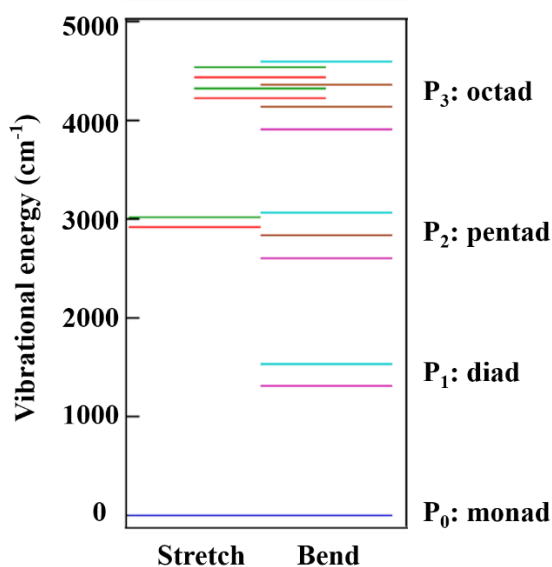


Figure 3.16 Energy levels of the first four polyads of CH_4 , adapted from ref [16].

The polyad number P_n is defined as

$$n = 2V_1 + V_2 + 2V_3 + V_4 \quad (3.27)$$

where V_i is the number of quanta of the ν_i vibrational mode. For example, the $n = 2$ pentad is composed of the zero-order levels ν_1 , $2\nu_2$, ν_3 , and $2\nu_4$. Because of the proximity of the levels within a polyad, the vibrational eigenstates are mixtures of the normal modes, overtones, and combination bands, which results in the polyad structure of the vibrational spectrum [74]. In addition, due to the degeneracy of all the normal modes except ν_1 , the levels within each polyad split into several

sublevels which increase dramatically with polyad number. For example, there are 5 vibrational levels of pentads, these levels then interact and form a total of 9 sublevels. For octad, there are already 24 sublevels. Fortunately, for the scattering of methane at relatively low energy < 200 meV, only the $n = 0, 1,$ and 2 polyads (monad, diad, and pentad) are energetically accessible for the scattered molecules). Therefore dealing with the complexity of higher polyads is not necessary here.

The excitation frequencies of most of the fundamental transitions and their Einstein coefficients are documented in the HITRAN database [70,75,76]. A list of hot band transitions originating from states ν_1 and ν_3 was kindly provided by Prof. Vincent Boudon from the University of Bourgogne in Dijon. These data are now available also on the Calculated Spectroscopic Database of the VAMDC portal [77]. Besides the theoretically calculated data for hot band transitions, more precise data of CH₄ hot band transitions based on experimentally measured IR spectra are available since 2018 [78], due to the development of a high-enthalpy source that allows to heat gases up to 2000 K [79].

3.7 Nuclear spin isomers of CH₄ and the allowed rovibrational levels

The CH₄ molecule contains four indistinguishable H atoms. Hydrogen atoms with nuclear spin $1/2$ are fermions that are described by a total wave function that must be antisymmetric with respect to the interchange of indistinguishable H-atoms. Four particles with the spin $I = 1/2$ with $m_s = \pm 1/2$ give rise to a total of $2^4 = 16$ possible total nuclear spin wavefunctions. The symmetries of these nuclear spin wavefunctions have been characterized by Wilson to be $A, F,$ and E for $I = 2, 1,$ and $0,$ respectively [80]. The nuclear spin symmetries $A, F,$ and E corresponds to the T point group which contains only the rotational symmetry elements of the T_d point group. The relative occurrences of the three nuclear spin wavefunctions with symmetry $A, F,$ and E have been determined to be 5, 3, and 1, respectively.

Because the interconversion of nuclear spin is extremely slow, CH₄ molecules with different total nuclear spin can be considered as three different nuclear spin isomers of CH₄. These are classified as *meta*, *ortho*, and *para*-CH₄ for the total nuclear spin 2, 1, and 0, respectively. As I will show, due to Pauli-allowed symmetry restrictions, the 3 different nuclear spin isomers have uniquely allowed rovibrational levels. This property is important when searching for an excitation scheme in the tagging experiments and understanding the CH₄ line list data from the HITRAN database [70].

The total wavefunction of a molecule can be decomposed into the electronic ψ_{el} and the nuclear wavefunction ψ_{nuc} within the Born-Oppenheimer approximation. The nuclear motion part can be further decomposed into a product of the vibrational, rotational, and nuclear spin wavefunctions. The total wavefunction can then be expressed in the form

$$\psi_{tot} = \psi_{el} \psi_{vib} \psi_{rot} \psi_{ns} \quad (3.28)$$

Due to the fermionic features of the four hydrogen atoms, the total wavefunction needs to be anti-symmetric when exchanging two hydrogen atoms, governed by the generalized Pauli principle. In our work of CH₄-surface scattering experiments, no matter the incident or the scattered CH₄, we concern only with the electronic ground state, whose wavefunction is symmetric. Hence, we only have to consider the symmetry properties of the nuclear part. To obey the Pauli principle, the product of the symmetry representations for the vibrational, rotational, and nuclear spin must contain Pauli-allowed symmetry species that are A_1 and A_2 in the case of CH₄, corresponding to A in the T subgroup [73], that is

$$\Gamma^{vib} \otimes \Gamma^{rot} \otimes \Gamma^{ns} \supseteq A \quad (3.29)$$

The symmetries of the three nuclear spin states, as mentioned above, are A , F , and E for *meta*, *ortho*, and *para*-CH₄, respectively. To fulfill the condition of eq 3.29, not all the rovibrational states can exist for a certain nuclear spin isomer. According to the multiplication properties of irreducible representations, only the rovibrational states having the same corresponding symmetry as the nuclear spin wavefunctions can exist [74]. The A_1 and A_2 rovibrational symmetries in the T_d point group correspond to A nuclear spin symmetry in the T subgroup. Also, the F_1 and F_2 rovibrational symmetries map to the F nuclear spin symmetry. The products of different symmetry representations do not contain A symmetry and therefore not Pauli-allowed, such as $A \times E = E$ and $A \times F = F$. Whereas the products of the same symmetry representations contain A symmetry, given by $A \times A = A$, $E \times E = 2A + E$, and $F \times F = A + E + 2F$. As a consequence, each nuclear spin isomer of CH₄ possesses its uniquely allowed rovibrational levels. In other words, for a given nuclear spin isomer, not all the rovibrational states can exist due to the symmetry restriction. The Pauli-allowed rovibrational levels for CH₄ with vibrational states of symmetries A_1 and F_2 for CH₄ have been worked out by Wilson [80], and are shown in Figure 3.17.

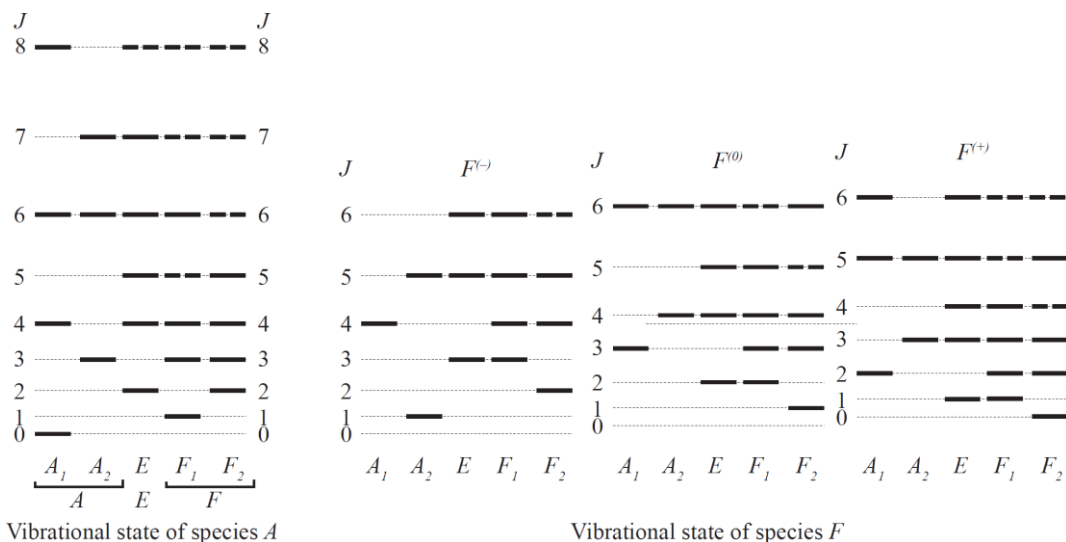


Figure 3.17 Allowed rotational levels of vibrational states with symmetry A_1 (left) and F_2 (right). Note that the F_2 vibrational state splits into three Coriolis stacks. The figure is adapted from ref [17].

Note that for a given nuclear spin isomer and a rotational quantum number J , more than one sublevel can exist. The number of sublevels for a given J is equal to $2K + 1$ if we take into account the degeneracies of sublevels and sum up all the nuclear spin isomers. Here, K is the projection of rotational angular momentum J on a reference axis in the molecular fixed frame. In principle, since CH_4 is a spherical top molecule, the moments of inertia are equivalent no matter which reference axis is chosen, making the $2K + 1$ sublevels degenerate. However, due to anharmonicity and centrifugal distortion, this degeneracy is partially lifted such that the sublevels are split by 300-3000 MHz. The vibrational ground state $\nu = 0$ and the ν_1 state (symmetric C-H stretch mode) both have A_1 vibrational symmetry. Their Pauli-allowed rotational levels are in the left diagram in Figure 3.17. For the triply degenerate ν_3 vibrational state (anti-symmetric stretch mode), the existing rotational levels are shown in the right panel of Figure 3.17. The structure is further complicated by the Coriolis interaction.

As I have mentioned earlier, the three different nuclear spin isomers of CH_4 can be treated as different species due to the slow rate of interconversion between spin states. Furthermore, although the energy difference of sublevels for a certain J is only a few tenths of a wavenumber, they can be distinguished and selectively excited by our single-mode IR lasers. In our surface scattering experiments, it is thus possible to selectively excite and detect a specific nuclear spin isomer. It is therefore important to estimate the statistical weight of a certain rovibrational sublevel belonging to a specific symmetry. This can be deduced by counting the number of total symmetric species in the resulting product of $\Gamma^{rovib} \otimes \Gamma^{ns}$. For rovibrational states with A , E , and F symmetries, their products with the nuclear spin states of the same symmetries are $A \times A = A$, $E \times E = 2A + E$, and $F \times F = A + E + 2F$, and therefore produce 1, 2, and 1 totally symmetric species A , respectively. Recall that there are 5, 1, and 3 nuclear spin wavefunctions with A , E , and F symmetry, respectively, that can produce the above products, giving rise to the statistical weight of 5, 2, and 3 for

rovibrational levels with A , E , and F symmetry, respectively. At higher J levels, the relative number of rovibrational sublevels with A , E , and F symmetry for a certain J converges to 1, 1, and 3. After multiplying these values with the statistical weight of the rovibrational wavefunctions, we find the relative abundance of three nuclear spin isomers, given by 5/16, 2/16, and 9/16 for the *meta*, *para*, and *ortho*-CH₄, respectively.

3.8 Coriolis coupling of the degenerate vibrational modes

Besides the effects of the nuclear spin symmetry, the structure of rovibrational levels is further complicated by the Coriolis coupling in the F_2 antisymmetric stretch vibrational states. Coriolis coupling is caused by rovibrational interactions. At the macroscopic scale, due to the rotation of the earth, the resulting Coriolis force causes the counterclockwise rotation of tornados in the northern hemisphere. At the molecular level, Coriolis forces play an important role in degenerate vibrational states. Consider a molecule with a doubly degenerate vibrational mode V , the difference between the two vibrational states V_1 and V_2 is essentially the relative directions of their vibrational motions of atoms. Assuming the molecule is originally vibrating in the V_1 state, when the molecule is rotating, the Coriolis force can veer the vectors of the vibrating atoms. The veered motions are essentially the motions of the V_2 mode. As a consequence, the Coriolis force acting on the V_1 state leads to excitation of the V_2 state of the degenerate vibrational mode. If the two modes are not in phase, the coupled motions of the two modes give rise to circular motions of the atoms and therefore angular momentum. Since this type of angular momentum is generated by vibrational motions, it is called vibrational angular momentum l . This vibrational angular momentum can then be coupled to the rotational angular momentum depending on the relative directions. The presence of Coriolis coupling can be predicted by Jahn's rule. It states that Coriolis coupling of two vibrations happens only when the product of the symmetry species of the two vibrations contains the symmetry species of rotation [81]. According to this rule, the Coriolis coupling does not occur for the doubly degenerate bending mode of CH₄ which possesses E symmetry, as $E \times E = A_1 + A_2 + E$, without F_1 (rotation in T_d point group). Whereas the triply degenerate antisymmetric stretch mode (ν_3) which has F_2 experiences first-order Coriolis coupling, which is verified by Jahn's rule, as $F_2 \times F_2 = A_1 + E + F_1 + F_2$, containing the symmetry species of rotations F_1 . This coupling then splits the F_2 vibrational states into three Coriolis stacks with the labels $F^{(-)}$, $F^{(0)}$, and $F^{(+)}$, as shown in the right panel of Figure 3.17.

3.9 Selection rules of IR transitions

For a transition between two vibrational states to happen via optical excitation, it requires a non-zero transition dipole moment, that is

$$\mu = \int \psi_v^* \hat{\mu} \psi_{v'} dr \neq 0 \quad (3.30)$$

Without working out the integral, the allowed vibrational transitions can be predicted by group theory. An allowed vibrational transition requires a total symmetry species A_1 included in the

product of the symmetry species of the initial vibrational state, the dipole moment, and the final vibrational state, given by

$$A_1 \in \Gamma^{v'} \otimes \Gamma^\mu \otimes \Gamma^{v''} \quad (3.31)$$

As a consequence, for CH₄, only the ν_3 and the ν_4 vibrational modes are infrared-active. For rovibrational transitions, the selection rules of IR transitions read $\Delta J = +1, 0, -1$, resulting in R branch, Q branch, and P branch transitions, respectively. It is worth noting that an additional selection rule $\Delta R = 0$ exists for excitation from the ground vibrational state to the ν_3 vibrational states within $F^{(-)}$, $F^{(0)}$, and $F^{(+)}$ Coriolis stacks [82]. Here, R is the sum of the rotational angular momentum J and the vibrational angular momentum l . For the ν_3 fundamental mode, l takes the value $+1, 0, -1$, corresponding to $F^{(-)}$, $F^{(0)}$, and $F^{(+)}$ Coriolis stacks, respectively. Taking into account the selection rules $\Delta J = +1, 0, -1$ and $\Delta R = 0$, one finds that for the ν_3 fundamental transitions ($A_1 \rightarrow F_2$), R branch transitions can only excite the vibrational ground state to $F^{(-)}$ Coriolis stack, Q branch to $F^{(0)}$, and P branch to $F^{(+)}$.

In the present work, since our vibrational excitations are carried out by linearly polarized lasers, selection rules regarding M levels also need to be considered. When linearly polarized light is used for the excitation, the oscillating electric field creates a reference plane. Molecules having different spatial orientations with respect to the reference plane then present various coupling strengths to the laser electric field. As a result, the transition dipole moments of a given J are M level-dependent, as described by eq 3.25. Also, an excitation via linear polarized light does not allow for a change of the M value. The M level selection rules stipulate $\Delta M = 0$, and $M = 0$ to $M = 0$ is not allowed for Q branch transitions

Chapter 4 Rotationally inelastic scattering of CH₄

4.1 Introduction

Molecular beam-surface scattering can serve as a probe of the interaction potentials between the incident particles and the surface. For the scattering of atomic species, the angular distributions and the diffraction patterns convey information on surface structure, such as corrugation [83–86]. Time-of-flight measurements of scattered atoms enable one to study the coupling of incident kinetic energy and momentum into surface degrees of freedom such as surface phonons [83]. Whereas for molecules, more information can be extracted due to the presence of their internal degrees of freedom. Besides excitation of surface phonons, other pathways for energy transfer exist such as translational to rotational energy conversion (T → R) or vibrational excitation (T → V). The state-to-state surface scattering technique enables us to study molecule-surface interaction with a high degree of control, making it a powerful tool to probe energy transfer during the gas-surface encounter in detail. By interrogating the quantum state of molecules directly scattered from a surface, we expect to extract information about the underlying potential energy surface (PES) the molecules experience. The experimentally obtained data can be used for assessing the accuracy of theoretically constructed PES. An accurate PES is one of the most important building blocks for theoreticians to perform accurate predictions for chemical reactions [4,5,87].

Rotational excitation is ubiquitous in gas/surface scattering and occurs when torque is exerted by the molecule/surface interaction during the collision event. Due to its orientation-dependent nature, studying rotational excitation can serve as a probe of the anisotropy on the PES with respect to the spatial orientation of the incoming molecule. A large anisotropy can make a strong coupling between molecular rotation and other degrees of freedom. Monitoring the scattered rotational energy can in principle help us understand more details on the PES. Consider an American football bouncing from a flat surface with an initial orientation θ , defined by the angle between the long axis of the football and the surface normal. If the football hits the surface end-on ($\theta = 0$ or 180°) or side-on ($\theta = 90^\circ$), then no torque is exerted on the football and it will scatter elastically without rotational excitation. If the football hits the surface at any other angle, the football experiences an amount of torque covered by the incident momentum and leaves the surface with a changed angular momentum. At the molecular level, in direct scattering processes, often a so-called "rotational rainbow" is observed [33,86] when there is a singularity in the differential scattering cross-section. The optical rainbow is due to the wavelength-dependent scattering of light by falling rain droplets. Here, the rotational rainbow means the incoming molecules with a range of initial orientations preferentially scatter into a specific rotational level J_{Max} after colliding with a surface. Instead of observing a narrow distribution at J_{Max} , we normally observe a broad distribution peaking around J_{Max} . Since the final angular momentum is determined by the incident conditions and the dynamics at the gas/surface encounter, the scattered rotational distribution is normally non-Boltzmann. For a fast direct scattering process, where the incident molecule typically interacts with the surface for

less than a picosecond, its internal energy does not thermalize with the surface and thus provides valuable information on energy transfer in the gas/surface interaction dynamics.

Rotational excitation in surface scattering has been studied for several decades both theoretically and experimentally [26,27,33,37,40,41,88–90]. Kleyn et. al. studied the rotational inelastic scattering of NO from Ag(111) using laser-induced fluorescence. In the scattered rotational distribution, they observed a low- J portion ($J < 20$) showing Boltzmann distribution and a high- J portion that was interpreted as the rotational rainbow [26,27]. Using resonantly enhanced multi-photon ionization (REMPI) in combination with the molecular beam technique, Lykke et. al. studied the rotational inelastic scattering of N₂ from Au(111) [90]. There, the scattered rotational distribution was found to be non-Boltzmann and showed pronounced maxima at large angular momentum transfer depending on the incident kinetic energy. These maxima were assigned as indications of the rotational rainbow. Again with the REMPI technique, Lykke et. al. investigated the scattering of HCl from Au(111) [91]. The rotational distribution showed also rainbow features. The scattered rotational energy displayed a bilinear dependence on both the normal incident energy E_{\perp} and also surface temperature T_s .

Hines et. al. used the REMPI technique to study rotational state distributions of CO scattered from Ni(111) [33]. In this study, both direct scattering and trapping-desorption products were observed. For the direct scattering channel, non-Boltzmann rotational distributions were observed and interpreted as the interaction of the weakly attractive O-end of the CO molecule with the Ni(111) surface. Whereas for the trapping-desorption channel, the rotational distributions could be fit well by Boltzmann distributions and T_{rot} reflecting 0.82 of T_s . This channel was assigned as the interaction of the strongly attractive C-end of the CO molecule with the surface. This system shows strong orientation-dependent scattering dynamics. The feature is also observed in the scattering of NO from Au(111). Vibrational excitations and relaxations of NO colliding with a metal surface are known as couplings of molecular vibrations and surface electron hole-pairs (EHPs) [92]. Bartels and coworkers oriented the incident NO by selectively exciting Λ -doublet states and observed a higher vibrational relaxation probability with the NO molecule hitting the surface with its N-end [93]. In the vibrationally elastic channel where the scattered NO stayed in the initially prepared $v = 3$, a hotter rotational distribution was observed when NO hit the surface with O-end. Whereas in the vibrationally inelastic channel where the vibrational energy of NO relaxed from $v = 3$ to $v = 2$, rotational distributions were almost identical no matter the initial orientation. These observations are interpreted in terms of a strong angular-dependent electron transfer-mediated nonadiabatic gas-surface interaction. The angular-dependent vibrational relaxation acts as a filter to select NO molecules hitting the surface with N-end and therefore gives rise to identical rotational distribution independent of the initial prepared orientation.

Most of the existing work on rotationally inelastic scattering concerns diatomic molecules, while only a little work has been reported for polyatomic molecules such as acetylene, methane, formaldehyde, and ammonia [14,36,37,39,46]. Using bolometric detection in combination with direct IR laser pumping, Miller et. al. studied CH₄ scattering from LiF(100) [14]. They observed rainbow scattering in the scattered angular distribution due to the surface corrugation. Note that the term “rainbow scattering” is different from the “rotational rainbow” described above. The

“rainbow scattering” is referred to the propensity of final scattering direction caused by surface corrugation. There, one would observe two local maxima in the angular distribution due to forward and backward scatterings. Forward and backward scatterings correspond to the incoming molecule hitting the falling and the rising parts of the corrugation, respectively. The observed distribution of rotational energy of the scattered CH₄ showed no departure from Boltzmann distribution even though a direct scattering process was proposed. Although rotational state-resolved measurements of CH₄ were possible at that time, the vacuum conditions in Miller’s setup did not allow for scattering from clean metal surfaces, especially catalytically active metal surfaces. Therefore their studies were limited only to inert samples such as LiF and NaCl. Using the same technique, Miller and coworkers studied the rotational inelastic scattering of C₂H₂ from LiF(100) surface [46]. They observed an increase of E_{rot} as a function of E_{\perp} at low energies ($23 < E_{\perp} < 65$ meV). However, when $E_{\perp} > 65$ meV, E_{rot} was essentially independent of E_{\perp} . This energy cutoff was close to the vibrational frequencies of the C₂H₂ bending modes. This observation was therefore interpreted as vibrational excitation via T → V conversion. In 2015, the T → V conversion of acetylene was studied again but on an Au(111) surface using the REMPI technique by Wodtke et. al [39]. In this work, they found E_i -dependent vibrational excitation of the ν_4 trans-bending mode as well as rotational excitation, suggesting a direct scattering mechanism. The excitation probabilities were orientation-dependent. When the acetylene molecule hit the surface side-on, the change of angular momentum was weak but more likely to excite the bending mode. Whereas if the molecule hit the surface with any other angle, rotational excitations were favorable. Besides spectroscopic methods, rotational inelastic scattering experiments can also be achieved by a non-optical approach. Al Taleb et. al. used the high-resolution time-of-flight setup to study the angular distribution of CH₄ scattered from Ni(111) and Ir(111) [94,95]. In both works, they observed several rotational inelastic diffraction peaks (RID) that could be assigned as excitations of different J levels. However, in these studies, quantitative determinations of scattered rotational energies were not presented.

Referring to axis-specific rotation in the scattered products, Kay et. al. investigated rotational inelastic scattering of NH₃ from Au(111) using REMPI [36]. They observed the NH₃ molecules tended to scatter into lower K states, corresponding to the tumbling motion. With the REMPI technique, Park et. al. reported the scattering dynamics of formaldehyde from Au(111) [37]. The scattered formaldehyde molecules showed a high propensity for spinning along the a-axis. It is then intuitive to assume that the scattering patterns can be strongly dependent on the molecular structure. However, so far, there are only a few studies of rotational inelastic scattering of polyatomic molecules from well-defined metal surfaces. More studies of polyatomic molecules with different structures are desirable for further understanding of gas/surface interactions.

Quantum-state resolved molecule/surface scattering of CH₄ has been studied in our group by M. Van Reijzen and J. Werdecker [16,17]. As documented in the Ph.D. thesis of J. Werdecker [17], he observed a surprisingly strong rotational excitation of the scattered CH₄ from a Ni(111) surface at a surface temperature of 400°C. A molecular beam with incident kinetic energy $E_i = 100$ meV and $\theta_i = 65^\circ$ results in a normal kinetic energy $E_{\perp} = 17.8$ meV ($E_{\perp} = E_i \cdot \cos^2(\theta_i)$). The average rotational energy of the scattered methane was measured as 13.4 meV. Assuming that only E_{\perp} contributes to rotational excitation, this observation suggests a very high efficiency of 75% for T

→ R conversion. For rotational states with $J > 4$, the energy transferred to rotation even exceeds E_{\perp} . However, by increasing E_{\perp} by a factor of 5, we only observed an increase in average rotational energy of 3 meV in the scattered CH_4 . This suggests a weak dependence on incident energy and there must have been other pathways contributing to the rotational energy. Werdecker proposed three possible explanations: First, the observation indicates that the surface corrugation of the Ni(111) surface cannot be neglected. Surface corrugation will introduce a coupling between the parallel and the normal kinetic energy. Second, the incident molecules are accelerated in the normal direction by falling into the physisorption well which adds up to 120 meV to E_{\perp} [96]. Third, the surface thermal motion could excite the rotational motion of the incoming molecules, especially the experiments were carried out at an elevated surface temperature of 400°C, corresponding to 58 meV of thermal energy.

Due to the fixed detector position in our “old” machine, we were not able to change the incident and scattering angles independently which prevented a detailed study of the role of normal and parallel incident energy. Furthermore, the first version of the bolometer was not UHV compatible and hydrocarbon outgassing from the adhesives on the bolometer heat shields created carbon contamination on the timescale of the experiments. This required a surface temperature of at least 400°C in order to maintain a clean surface by dissolving any carbon contamination quickly into the bulk Ni crystal which prevented a study of the T_s -dependent of the rotational energy transfer.

Since both these limitations were eliminated in the design of the new BILT machine, we decided to further investigate the dependence of the rotational energy transfer on the kinetic energy and angle of the incident methane molecules. In this study, I varied both incident energy E_i and incident angle θ_i to change the normal and the parallel components of the kinetic energy. This allowed me to study the effect of normal and parallel kinetic energy on the rotational energy of the scattered CH_4 . Furthermore, the BILT machine has a lower base pressure and cleaner vacuum conditions, which enable us to keep the sample surface clean at a lower surface temperature. This makes it possible to perform scattering experiments over a wider surface temperature range. At $T_s = 200^\circ\text{C}$ and 10^{-10} mbar, the Ni(111) sample stayed clean for more than 3 hours as observed by AES which is enough time to perform about 5 runs of R-branch tagging scans in order to measure the rotational state distribution of the scattered methane. With this improvement, we can now test the influence of the surface temperature on rotational energy transfer. If the surface thermal motion or thermally induced corrugation are important for the rotational excitation, we expect to observe an increase in the average rotational energy of the scattered methane.

4.2 Experimental

To study the contributions of the parallel and the normal kinetic energy to the rotational excitation of the scattered CH_4 , I performed two sets of experiments. Parallel and normal incident energies were changed independently by choosing a suitable CH_4/He seed ratio and scattering geometry, as shown in Figure 4.1. I used three different CH_4/He mixtures and scattering geometries for each set of experiments. The details of the gas mixtures, their corresponding kinetic energies, and the scattering geometries for both sets of experiments are summarized in Tables 4.1 and 4.2 for varying

E_{\perp} and E_{\parallel} , respectively. Note that the detection angle is always shifted by 5° from the specular position to prevent the bolometer from seeing the strong flux of scattered He which tends to saturate the bolometer signal. The average translational energy E_i of the incident methane is characterized by TOF measurements and by the fitting of a flux-weighted Maxwell Boltzmann distribution to the TOF data. The characteristics of the beam kinetic energy are summarized in Table 4.3. E_i was varied by changes in CH_4/He seed ratio at constant nozzle temperature in order to prevent the molecules from populating high J levels in the incident beam. Since the goal is to study rotational excitation during scattering, the ideal condition is to have most of the incident molecules in $J = 0$.

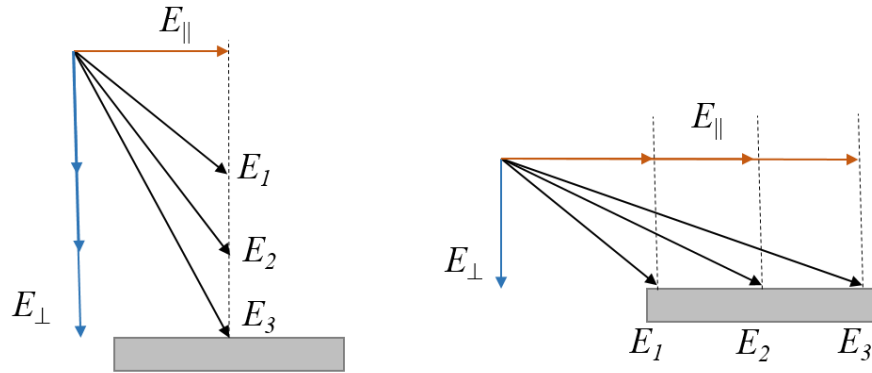


Figure 4.1 Schematic of the two sets of experiments. Left: changing E_{\perp} at constant E_{\parallel} . Right: changing E_{\parallel} at constant E_{\perp} .

Table 4.1 Incident kinetic energies and the corresponding scattering geometries for the experiments of varying E_{\perp} .

Gas mixture	50% CH_4 in He	20% CH_4 in He	3% CH_4 in He
Kinetic energy E_i (meV)	130	185	241
Incident angle θ_i ($^{\circ}$)	45	36	31
Scattering angle θ_f ($^{\circ}$)	50	41	36
E_{\perp} (meV)	65	121	177
E_{\parallel} (meV)	65	64	64

Table 4.2 Beam energies and the corresponding scattering geometries for the experiments of varying E_{\parallel} .

Gas mixture	50% CH_4 in He	20% CH_4 in He	3% CH_4 in He
Kinetic energy E_i (meV)	130	185	241
Incident angle θ_i ($^{\circ}$)	45	54	59
Scattering angle θ_f ($^{\circ}$)	50	59	64
E_{\perp} (meV)	65	64	64
E_{\parallel} (meV)	65	121	177

Table 4.3 Molecular beam energy characteristics of three different mixtures.

Gas mixture	50% CH ₄ in He	20% CH ₄ in He	3% CH ₄ in He
Nozzle temperature (K)	297	297	297
Nozzle pressure (bar)	3	3	3
Stream velocity (m/s)	1250	1490	1700
Translational temperature (K)	5.5	3.8	3.7
Average kinetic energy E_i (meV)	130	185	241
FWHM of E_i (meV)	26	26	29

The rotational state populations of the incident molecular beam were characterized using the pyroelectric detector which can be translated into the molecular beam in P2. It is used to selectively detect the vibrationally excited methane molecules by the Argos CW-IR OPO stabilized by the transfer cavity. The measurements were carried out using lock-in detection and chopping the excitation laser beam with a modulation frequency of 2 Hz using the UniBlitz shutter. For all the measurable J -levels, fluence curves are recorded and the rotational populations are derived from the asymptotic pyroelectric detector signals, shown in Figure 4.2. The populations for the three seed ratios and their corresponding rotational energies $\langle E_{\text{rot}} \rangle_0$ are compiled in Table 4.4. We find that more than 95% of the population of *meta*-CH₄ cools to $J = 0$ for each of the three different seed ratios used. The populations in rotational states above $J = 4$ are negligibly small and below our detection limit. For *meta*-CH₄, the $J = 1$ and 2 levels cannot be populated for symmetry reasons which makes $J = 3$ the next allowed J -level above $J = 0$. This relatively large rotational energy gap helps concentrate the population in $J = 0$ by rotational cooling in the supersonic expansion. Using this property, one can prepare a *meta*-CH₄ beam in $v = 0$ with an almost pure $J = 0$ rotational state. Assume that the nuclear spin does not change in the scattering process, we can treat the three nuclear spin modifications of CH₄ as separate species which can each be identified by their unique rovibrational spectra.

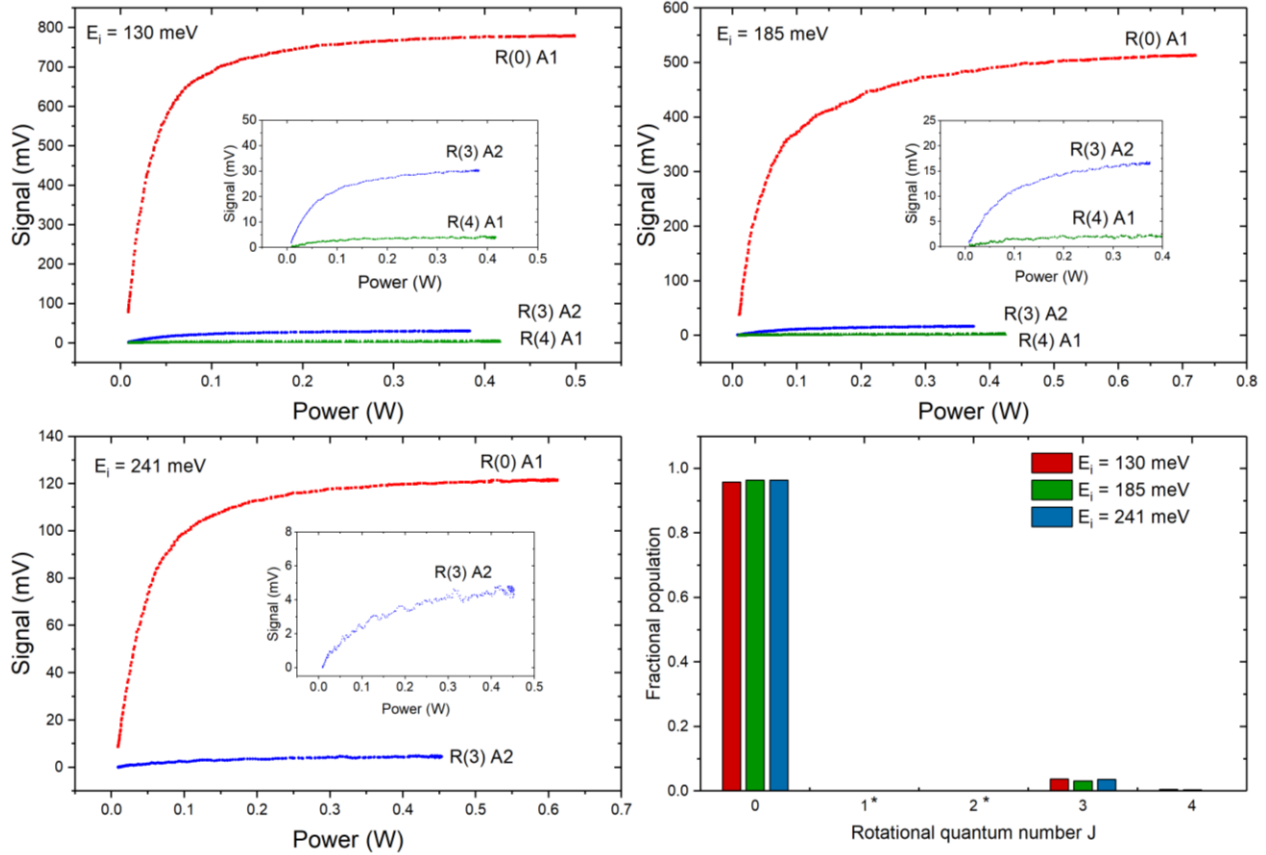


Figure 4.2 Fluence curve measurements for interrogating the populations of the three incident molecular beams. The preamplifier of the pyroelectric detector was set to gain 10X. The insets show signals for R(3) A2 and R(4) A1 transitions on a smaller scale for visibility. Populations of the three beams are summarized in the bottom-right bar graph. The asterisk * labels non-existing J -levels due to Pauli-allowed symmetry restriction.

Table 4.4 Rotational state populations of the 3 incident beams and their corresponding rotational energies.

Beam energy E_i (meV)	130	185	241
J	Population		
0	0.958	0.964	0.964
3	0.037	0.032	0.036
4	0.005	0.004	-
$\langle E_{\text{rot}} \rangle_0$ (meV)	0.35	0.30	0.28
$\langle E_{\text{rot}} \rangle_0$ (cm^{-1})	2.84	2.42	2.28

4.3 Results

The rotational state distributions of scattered *meta*-CH₄ for different scattering geometries and beam energies were measured by scanning the TOPO line-by-line through R-branch transitions for $J = 0$ up to $J = 10$ using the tuning strategy described in Chapter 2. Beyond $J = 10$, signals are usually lower than the detection limit of our current setup. For example, Figure 4.3 shows the R-branch tagging spectra for the measurement with $E_{\perp} = 121$ meV, $E_{\parallel} = 64$ meV. By applying noise to broaden the linewidth of the TOPO laser, allowing us to excite all the Doppler velocity classes, we expect to reach the asymptotes of the fluence curves for these R-branch transitions with up to 1 W of laser power. Thus, the tagging signals at the highest laser power are directly proportional to the population of the corresponding state. To increase the accuracy, especially for some scans that were measured when the Fabry-Pérot (FPI) stabilization was not implemented yet, I fit the tagging spectra by Gaussian functions and extract the peak height. For the working principle of the FPI laser frequency stabilization, readers are referred to Chapter 2. The population is derived by dividing the signal of all the individual peaks by the total signal. Note that for the R(10) A2 transition, with 150 MHz of the scanning range, I observed an additional peak located about 40 MHz higher than the R(10) A2 line. Based on the spectroscopic data in the HITRAN database [70,75,76], this line is assigned to the R(10) F2 transition which belongs to *ortho*-CH₄. Since the two lines are partially overlapped, I performed a fitting with two different Gaussian functions and in this way extract the peak height of the R(10) A2 line.

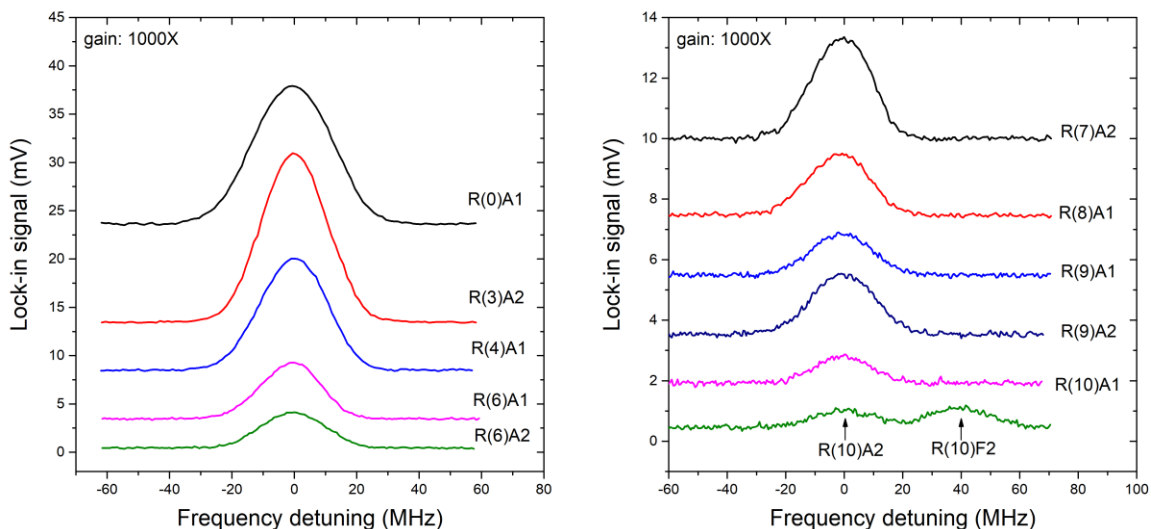


Figure 4.3 Tagging signals of an R-branch scan for scattering of CH₄ from a 673 K Ni(111), with $E_i = 185$ meV at $\theta_i = 36^\circ$, and $\theta_f = 41^\circ$, corresponding to $E_{\perp} = 121$ meV and $E_{\parallel} = 64$ meV.

Effects of E_{\perp} and E_{\parallel} on E_{rot}

Figures 4.4 and 4.5 present the results of the methane scattering experiments from a $T_S = 673$ K Ni(111) surface of varying E_{\perp} at a constant E_{\parallel} of 65 meV, and varying E_{\parallel} at a constant E_{\perp} of 65 meV, respectively. The tagging signals are recorded by scanning the TOPO through all the existing J levels of *meta*-CH₄ up to $J = 10$. The J levels labeled by an asterisk do not exist for *meta*-CH₄ due to symmetry restrictions. Finishing the R-branch scans of CH₄ scattering with several mixtures and incident conditions takes at least a day. Deducing reliable uncertainties by a standard normal distribution method that needs a high amount of samples costs a long time and is thus not feasible in our case. Here, instead of using the normal distribution, I adapt the student's t-distribution, which is suitable for a small number of samples, to estimate the uncertainty. The results presented in Figures 4.4 and 4.5 are repeated at least 3 times. The error bars are calculated by

$$\bar{x} \pm t \times \frac{s}{\sqrt{n}} \quad (4.1)$$

where \bar{x} is the average value, t is the t-value that can be found from the t-distribution table with a given number of samples and confident interval. s is the standard deviation of the samples, and n is the number of samples. Here, I use the t-value corresponding to an 80% confidence interval. As one can see from eq 4.1, as the number of samples increases, the statistical error decreases. Plus, a higher number of samples corresponds to a smaller t-value. No attempt was made to include the error propagation of systematic errors in the reported results.

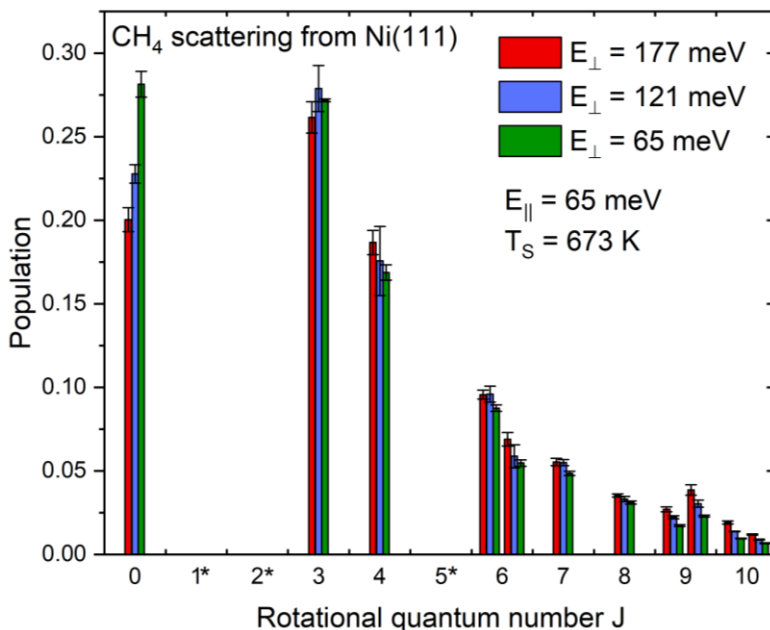


Figure 4.4 Rotational populations of scattered *meta*-CH₄ from a 673 K Ni(111) surface with $E_{\perp} = 65, 121,$ and 177 meV at a constant E_{\parallel} of 65 meV. Error bars indicated an 80% confidence interval for repeated measurements based on student's t statistics.

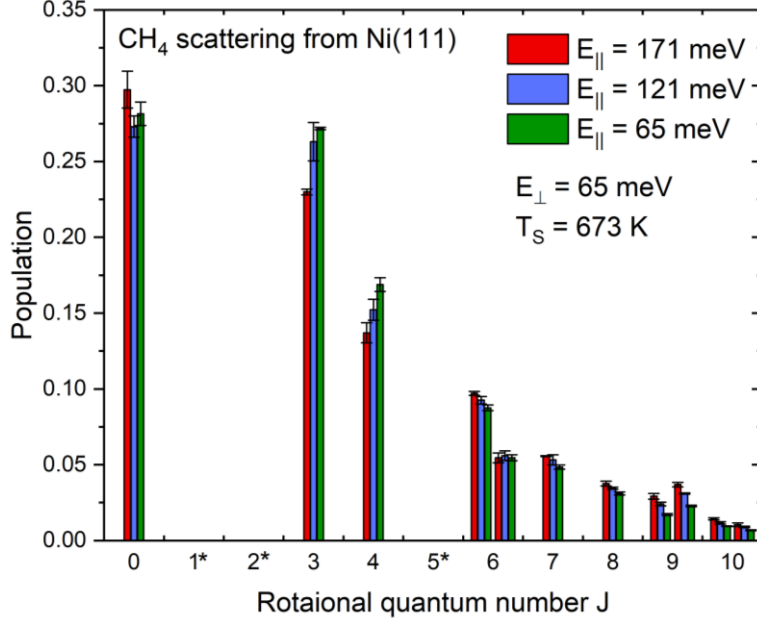


Figure 4.5 Rotational populations of scattered *meta*-CH₄ from a 673 K Ni(111) surface with $E_{\parallel} = 65, 121, \text{ and } 177$ meV at a constant E_{\perp} of 65 meV. Error bars indicated an 80% confidence interval for repeated measurements based on student's t statistics.

For both sets of experiments, we see slightly hotter rotational distributions for both increasing E_{\perp} and E_{\parallel} . This indicates that both normal and parallel components of the incident kinetic energy contribute to the rotational energy of the scattered methane. The scattered state populations are non-Boltzmann for a direct scattering process. In order to quantify the rotational energy transfer, I calculate the average rotational energy of the scattered methane, defined as the sum of rotational energies weighted by the population.

$$\langle E_{rot} \rangle = \frac{1}{S_{total}} \sum_{J=0}^{10} \sum_{n \in J} S_{J,n} E_{J,n} \quad (4.2)$$

where S_{total} is the total signal, $S_{J,n}$ is the signal corresponding to the rotational level J and n th sublevel, and $E_{J,n}$ is the energy of the n th sublevel of the rotational level J . Next, we need to subtract the initial rotational energy $\langle E_{rot} \rangle_0$ in the incident beam from the average rotational energy to get the effective rotational energy transfer

$$\langle E_{rot} \rangle_{eff} = \langle E_{rot} \rangle - \langle E_{rot} \rangle_0 \quad (4.3)$$

This effective rotational energy is the energy transferred to the scattered molecules during the collision process, excluding the small amount of rotational energy (< 0.4 meV) contained in the incident molecular beam. Figure 4.6 shows the plot of effective rotational energy as a function of incident normal (red triangles) and parallel (blue triangles) kinetic energy. Note that the data point of $E_{\perp} = 65$ meV is recorded by the same experiment as $E_{\parallel} = 65$ meV ($E_i = 130$ meV at $\theta_i = 45^\circ$). When increasing E_{\perp} , we observe that $\langle E_{rot} \rangle_{eff}$ increases from 14.5 meV to 18.3 meV as E_{\perp} rises

from 65 meV to 177 meV. When changing E_{\parallel} by the same amount, $\langle E_{\text{rot}} \rangle_{\text{eff}}$ increases from 14.5 meV to 16.8 meV. These observations show that both E_{\perp} and E_{\parallel} contribute to the rotational excitation of the scattered methane with a slightly stronger effect due to E_{\perp} . Assuming a linear response, I performed linear fit to both sets of data and found the T \rightarrow R conversion efficiencies $d\langle E_{\text{rot}} \rangle_{\text{eff}}/dE_{\perp} = 0.034$ and $d\langle E_{\text{rot}} \rangle_{\text{eff}}/dE_{\parallel} = 0.021$. Our observation unambiguously proves that, for the scattering of a spherical top molecule CH₄ from Ni(111), E_{\parallel} can be converted to $\langle E_{\text{rot}} \rangle$. Although the conversion efficiency is weak, it is not negligible. This implies the Ni(111) surface is more corrugated than we expect since a corrugated potential is needed to facilitate the conversion of E_{\parallel} to E_{rot} . For more evidence of the corrugated features on (111) metal surfaces and their effects on scattering patterns, I will come back to discuss them shortly in the next section.

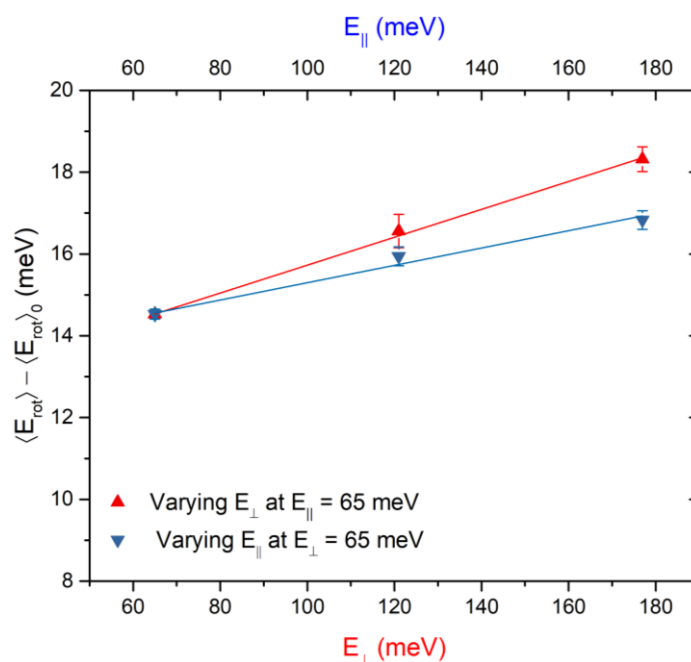


Figure 4.6 Effective rotational energy as a function of E_{\perp} (red) and E_{\parallel} (blue). Data points are derived from the results presented in Figures 4.4 and 4.5.

Momentum transfer between gas molecules and surface atoms

Before I move on to discuss the effects of T_S on E_{rot} , I should discuss the tendency of momentum transfer between a gas molecule and surface atoms at a gas-surface encounter. When a gas molecule collides with a surface, it can not only lose a portion of translational energy by exciting surface phonons but also receive a magnitude of energy by phonon annihilations. Logan and others reported a classical hard-cube model to predict the tendency of momentum transfer taking into account the velocity of the incoming molecule normal to the surface u_{n0} , the velocity of the surface atom v_0 , and their masses [63,97,98]. The model can qualitatively describe the angular distributions of scattered He, Ne, and Ar atoms from Pt [97]. The model is based on two assumptions. Firstly,

the potential between the gas molecule and the surface is simply repulsive. Namely, both the gas phase molecule and the surface atoms are considered rigid elastic particles. Secondly, the surface potential is uniform in the plane of the surface, and no corrugation is presented. Therefore, tangential forces do not play a role in this model. The motions of surface atoms are limited only to the vertical direction with respect to the surface plane. In this case, the momentum exchange between the gas molecule and surface atoms only affects the momentum component normal to the surface.

Based on this model, we now consider a picture of two particles collision in one dimension as depicted in Figure 4.7. The particle S is oscillating with a velocity magnitude v_0 back and forth horizontally in the box defined by the dashed lines, resembling a surface atom having a certain vibrational amplitude and velocity normal to the surface. On the right side, a particle G is propagating toward particle S with velocity u_{n0} . Particle G is allowed to penetrate into the box such that it can collide with particle S. According to this picture, if the velocity magnitude of particle S v_0 is faster than particle G, the collisions of the two particles will happen very likely on the right-hand side of the box. In this case, particle G hits particle S while S is moving toward G. It is more likely for particle S to transfer momentum to particle G in this condition. On the other hand, if the $u_{n0} \gg v_0$, then particle G can hit particle S at any position in the length D without preference. In this case, the collision probability of particle S moving toward G is similar to S moving away from G. This concept can be applied to practical gas-surface collisions. A gas molecule with very low speed cannot penetrate far into a surface because it will quickly be kicked out by the faster-moving surface atoms. In contrast, a very fast gas molecule can then collide with the surface atoms at any instantaneous amplitude with a similar probability.

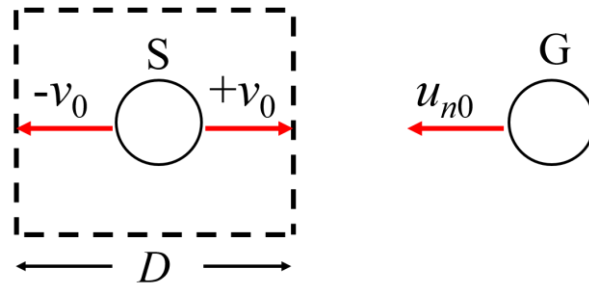


Figure 4.7 A picture of two particles collision reported by Goodman [98]. See text for the principle.

According to this picture, the ratio of the probabilities for collisions that occur when the surface atom is moving upward over downward is given by [97]

$$\frac{P_{upward}}{P_{downward}} = \frac{u_{n0} + v_0}{u_{n0} - v_0} \quad (4.4)$$

If a gas molecule receives a magnitude of momentum added up by surface phonons (i.e. phonon annihilations) during a collision process, the molecule will bounce back to the gas phase with a higher momentum component normal to the surface. The resulting angular distribution of scattered products will peak at a position smaller than the specular angle. This feature is observed in our system, CH₄ scattering from Ni(111) when a slow incident CH₄ beam is scattered from a hot Ni(111) surface.

In the BILT machine, the surface and detector can be rotated separately, which enables independent variation of the incident and scattering angles. By modulating a CH₄ beam, and lock-in detecting the bolometer signal for a wide range of scattering angles at a fixed incident angle, we measured the angular distribution of scattered methane. Figure 4.8 shows angular distributions of scattered CH₄ with 100 meV of incident kinetic energy from a clean Ni(111) surface at $T_S = 473$ and 673 K. The scattering experiments were carried out at a grazing incidence of $\theta_i = 65^\circ$. There, we observe the angular distributions peak at angles smaller than the specular angle. This shift in the distribution can be caused by a momentum transfer from the surface atoms to the incoming molecules which adds an amount of momentum to the scattered molecules, as predicted by the hard cube model described above. Energy transfer from the surface atoms to the scattered molecules, which corresponds to the annihilation of the surface phonons, is more probable when a slow molecule/atom is scattered from a hot surface where the surface atoms possess higher velocities. As the T_S increases from 473 to 673 K, the angular distribution is shifted further away from the specular, indicating more normal momentum is added up to the scattered CH₄ by surface atoms. The opposite trend can be found when faster incident CH₄ is scattered from a colder Ni(111) surface. I recorded the angular distribution of CH₄ as a function of incident energy E_i at $T_S = 373$ K and $\theta_i = 45^\circ$ as shown in Figure 4.9. There, we see the peaks of the distributions shift from 43° to 47° as E_i increases from 100 meV to 269 meV, indicating conversion of E_\perp to surface phonons or E_{rot} .

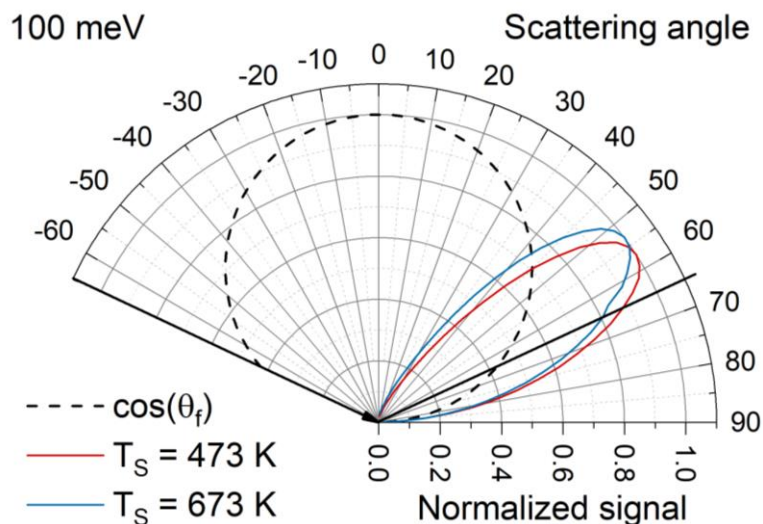


Figure 4.8 Angular distributions of CH₄ scattering from Ni(111) with a surface temperature of 473 K (blue curve) and 673 K (red curve). The black dashed curve shows a cosine function to simulate the distribution of trapping-desorption. Measurements were performed with a beam energy of 100 meV (pure methane) with an incident angle of 65°. The black arrow and line indicate the incident angle and the specular angle, respectively.

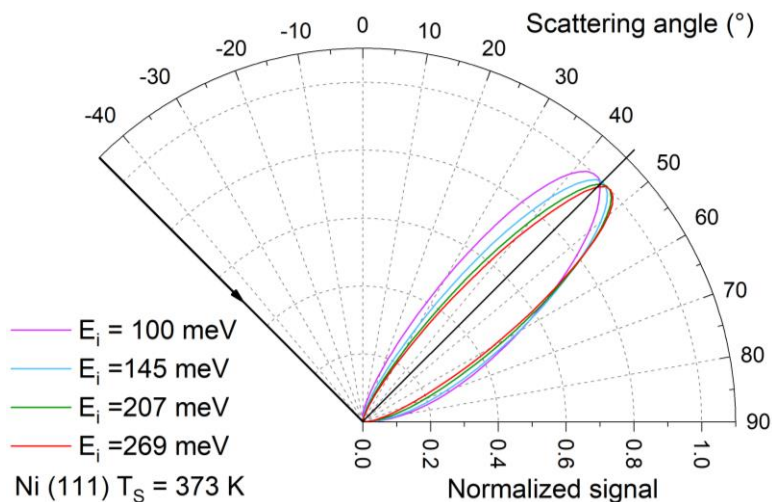


Figure 4.9 Angular distributions of scattered CH₄ from a 373 K Ni(111) surface with E_i ranging from 100 meV to 269 meV. The black arrow and line indicate the incident angle (45°) and the specular angle, respectively.

The shape of the angular distribution enables us to distinguish scattered products via trapping-desorption or direct scattering. Going back to Figure 4.8, the measured angular distributions differ significantly from a cosine distribution (dashed curve) even for low incident energy of 100 meV with a grazing incident angle of 65°. To eliminate the possibility of missing signals of trapping-desorbed products due to their slower velocities which may produce phase-shifted signals from

that of direct scattered products in lock-in detection, I monitor the lock-in R signals that are phase-independent. If there was a significant amount of scattered products via trapping-desorption, we should measure its signals near the surface normal where the cosine function peaks. This unambiguously tells that there is no measurable amount of trapping-desorbed product in the scattering conditions used. In the rest of our scattering conditions, we use faster molecular beams with smaller incident angles, i.e. higher normal kinetic energy, which makes trapping-desorption even less likely to happen.

Effect of T_S on E_{rot} in the scattering of CH_4 from Ni(111)

So far I have discussed the effect of T_S on the scattered angular distributions of CH_4 . The trend of these observations can be qualitatively predicted by the hard-cube model [63,97,98]. However, these models do not take into account rotational degrees of freedom of gas molecules. Surface thermal motion can excite molecular rotation via at least two mechanisms. Firstly, the up-moving surface atoms can collide with the incoming molecule and apply torque to the molecule. CH_4 , although being a spherical top molecule, the exact structure is not a sphere. The 4 C-H bonds can serve as lever arms and receive torque when the CH_4 collides with the surface and hits one of the hydrogen atoms. Consider a gas molecule propagating toward the surface with an amount of normal kinetic energy E_{\perp} , when it hits an up-moving surface atom, the available kinetic energy normal to the surface that can be coupled to rotational energy will be more than E_{\perp} with an extra amount of kinetic energy added up by the surface atom. Secondly, as surface temperature increases, the amplitude of surface motion also enhances, resulting in a stronger thermally induced corrugation. Surface corrugation introduces the role of tangential forces at the microscopic level that facilitates the conversion of E_{\parallel} to E_{rot} . The effects introduced by these two mechanisms should become stronger as increasing surface temperature. Therefore we expect to observe greater rotational excitation as the surface temperature elevates.

To test this picture, I measured the rotational energy of scattered CH_4 as a function of T_S , as shown in Figure 4.10. Here, scattering experiments were carried out with an incident beam of $E_i = 130$ meV, at two distinct incident angles $\theta_i = 30^\circ$ and 65° , corresponding to $E_{\perp} = 97.5$ and 22.5 meV, respectively. The error bars of the data points are expected to be similar to the data shown in Figures 4.4 and 4.5. In both sets of experiments, we observe an increase in $\langle E_{\text{rot}} \rangle_{\text{eff}}$ as T_S raised from 373 to 873 K. We observe the efficiency $d\langle E_{\text{rot}} \rangle_{\text{eff}}/d T_S$ to be higher for the grazing incident condition of $\theta_i = 65^\circ$. This can be understood by the picture discussed above reported by Goodman and Logan [97,98]. When the molecule approaches the surface with relatively low velocity normal to the surface, it is more likely to meet surface atoms with upward motions. These surface atoms hit the gas phase molecule, and not only add some amount of kinetic energy, but also rotational energy to the scattered molecule. The amount of energy transferred by the surface atoms depends on T_S . Assuming a linear response of $\langle E_{\text{rot}} \rangle_{\text{eff}}$ on T_S in the measured temperature range, I calculated the slopes for both angles, namely the efficiencies $d\langle E_{\text{rot}} \rangle_{\text{eff}}/d(k_B T_S)$ that are 0.10 and 0.15 for $\theta_i = 30^\circ$ and $\theta_i = 65^\circ$, respectively. For convenience, I define a new coefficient $\gamma = d\langle E_{\text{rot}} \rangle_{\text{eff}}/d(k_B T_S)$, representing the $k_B T_S \rightarrow \text{R}$ conversion efficiency.

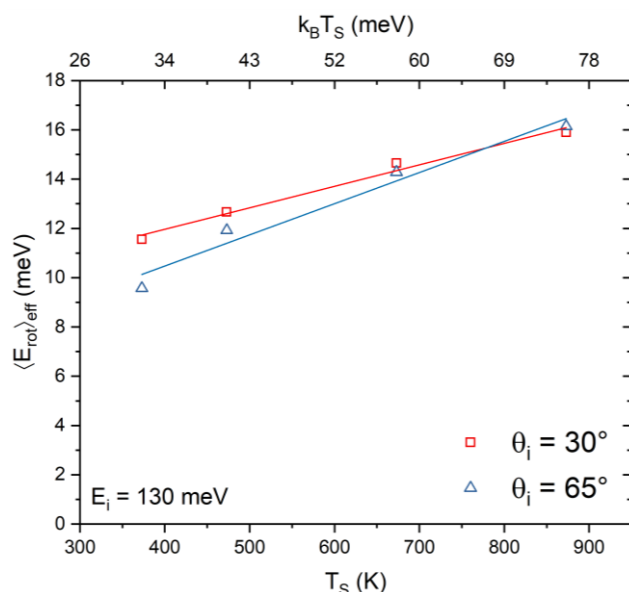


Figure 4.10 Effective rotational energy of scattered CH_4 from Ni(111) as a function of T_s for $E_i = 130$ meV. Measurements are performed at two different scattering geometries ($\theta_i = 30^\circ$, $\theta_f = 35^\circ$) and ($\theta_i = 65^\circ$, $\theta_f = 70^\circ$). Solid lines are linear fit to the data points. The slopes of the linear fit give the $k_B T_s \rightarrow R$ conversion efficiency $d\langle E_{\text{rot}} \rangle_{\text{eff}}/d(k_B T_s)$ which is calculated to be 0.10 and 0.15 for $\theta_i = 30^\circ$ and $\theta_i = 65^\circ$, respectively.

I observed a higher γ at a relatively grazing incidence, i.e. slower velocity component normal to the surface, and it is interpreted as a higher probability of colliding with up-moving surface atoms. The T_s factor γ is therefore dependent on molecular velocity normal to the surface u_{n0} . To quantitatively determine the variation of γ as a function of u_{n0} , I deduced γ values with 3 different incident velocities normal to the surface, from 524 to 1458 m/s, as shown in Figure 4.11. We see that γ reduces linearly as u_{n0} increases in the measured u_{n0} range. If we treat the surface thermal motion as a harmonic oscillator and given the mass of the Ni atom = 58 amu and the thermal energy = 58 meV for a 673 K surface, I calculate the maximum velocity of Ni atoms to be 447 m/s which is comparable to the slowest u_{n0} used in my measurements. According to eq 4.4, the incoming CH_4 molecules with $u_{n0} = 447$ m/s collide mostly on up-moving Ni atoms.

Our results clearly show that the surface thermal motions can excite molecular rotation, with its efficiency depending on the relative motion of the surface atoms and the gas phase molecules. Note that the rotational excitation due to thermally induced corrugation can not be ruled out.

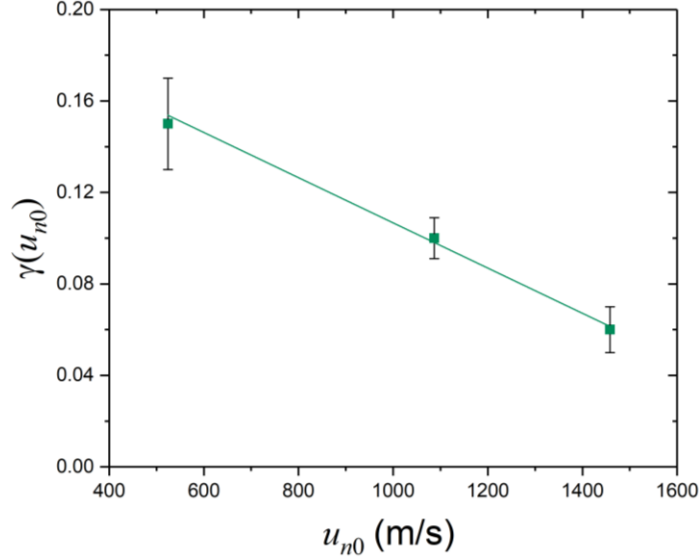


Figure 4.11 T_S efficiency coefficient γ as a function of normal incident velocity u_{n0} . The γ values are calculated from the data presented in Figure 4.10, which provide a range of E_{\perp} from 22.5 meV to 177 meV. The solid line is the linear fit of the data points.

Analyzing the contributions of rotational energy

So far, we have studied the contributions of E_{\perp} , E_{\parallel} , and T_S on the rotational energy of scattered CH_4 . Assuming the rotational energy is comprised of these factors, thus I decompose the rotational energy into the following form

$$\langle E_{rot} \rangle_{eff} = \alpha E_{\perp} + \beta E_{\parallel} + \gamma(u_{n0})k_B T_S \quad (4.5)$$

where $\alpha = \frac{d\langle E_{rot} \rangle}{dE_{\perp}}$, $\beta = \frac{d\langle E_{rot} \rangle}{dE_{\parallel}}$, and $\gamma(u_{n0}) = \frac{d\langle E_{rot} \rangle_{eff}}{d(k_B T_S)}$ that are determined experimentally in this work. One more contribution that I haven't addressed so far is the effect of the physisorption well experienced by the incident CH_4 . The physisorption well will accelerate the incident molecules toward the surface and thus will add an amount of normal kinetic energy E_{PW} to the incident molecules. Taking it into account, then eq 4.5 becomes

$$\langle E_{rot} \rangle_{eff} = \alpha(E_{\perp} + E_{PW}) + \beta E_{\parallel} + \gamma k_B T_S \quad (4.6)$$

Concerning the depth of the physisorption well, I use the value of 124 meV measured by temperature-programmed desorption experiments (TPD) by Beckerle et. al. [96]. Now, we can test the reliability of this empirical model. To do so, I calculate $\langle E_{rot} \rangle_{eff}$ for the measurement with the scattering conditions ($E_i = 130$ meV, $\theta_i = 30^\circ$, $T_S = 673$ K). The scattering conditions result in $E_{\perp} = 97.5$ meV and $E_{\parallel} = 32.5$ meV. By inserting these values into eq 4.6, then I calculate the rotational energy

$$\begin{aligned} \langle E_{rot} \rangle_{eff} &= 0.034 \times (97.5 \text{ meV} + 124 \text{ meV}) + 0.021 \times 32.5 \text{ meV} + 0.1 \times 58 \text{ meV} \\ &= 14.0 \text{ meV} \end{aligned} \quad (4.7)$$

which is in very good agreement with the experimental value of 14.7 meV. The calculation accounts for over 95% of the average rotational energy of scattered CH₄. The contributions of each factor are summarized in the bottom panel of Figure 4.12. There, we see the factor which contributes the most to the rotational energy of the scattered product is the surface thermal energy $k_B T_S$. The second most factor is the physisorption well depth. These two factors make a total contribution of up to 71% of the rotational energy. The portion of rotational energy really comes from the incident beam energy E_i is only 29%, in the scattering conditions ($E_i = 130$ meV, $\theta_i = 30^\circ$, $T_S = 673$ K).

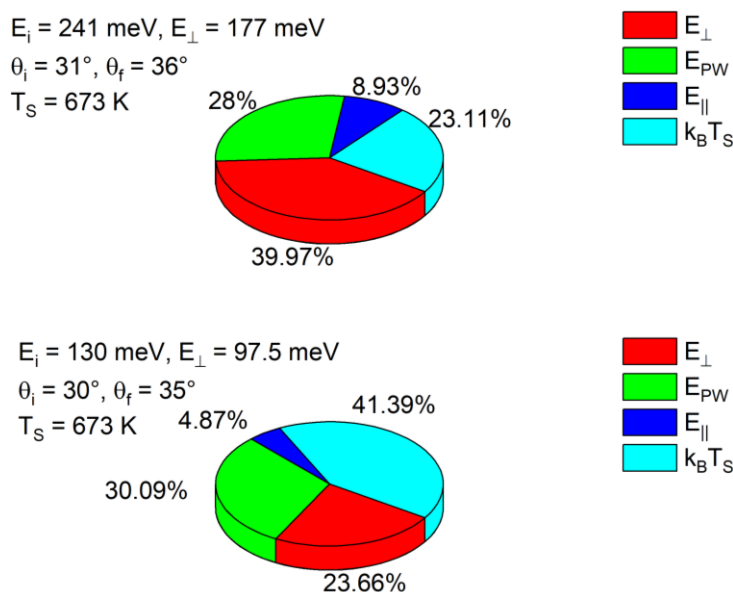


Figure 4.12 Compositions of $\langle E_{rot} \rangle_{eff}$ by the four factors that can contribute to the rotational energy of the scattered CH₄. Top panel: $\langle E_{rot} \rangle_{eff}$ composition for the scattering conditions of ($E_i = 241$ meV, $\theta_i = 31^\circ$, $\theta_f = 36^\circ$, $T_S = 673$ K). Bottom panel: $\langle E_{rot} \rangle_{eff}$ composition for the scattering conditions of ($E_i = 130$ meV, $\theta_i = 30^\circ$, $\theta_f = 35^\circ$, $T_S = 673$ K).

Next, I analyze the rotational energy of the scattering conditions of $E_i = 241$ meV, $\theta_i = 31^\circ$, giving rise to $E_{\perp} = 177$ meV and $u_{n0} = 1458$ m/s with the corresponding $\gamma(u_{n0}) = 0.06$. Using the approach of eq 4.6, I calculate $\langle E_{rot} \rangle_{eff} = 15.1$ meV, reproducing 82% of the experimental value (18.3 meV). This departure is probably due to the reliability of the β factor, namely $\frac{d\langle E_{rot} \rangle}{dE_{\parallel}}$. The parallel component of incident kinetic energy can be converted to the final rotational energy by surface corrugation. On a corrugated surface, the momentum component parallel to the bulk surface is not necessarily also parallel to the *local, microscopic* structure at the molecule/surface impact point. In this case, part of the momentum component parallel to the bulk surface then becomes the normal component on the *local, microscopic* surface which can be converted to the torque of the molecule. The degree of corrugation the incident molecules experience depends on how far they can penetrate into the surface. The deeper they can penetrate, the more structure of

the surface they can feel. Moreover, as T_S increases, stronger surface thermal motion gives rise to a more corrugated surface. Therefore it is reasonable to suspect that the β factor is dependent on both E_{\perp} and T_S . The β value I adapt here is derived by the scattering experiments performed at the conditions of $E_{\perp} = 65$ meV and $T_S = 673$ K. The reason why the empirical formula gives a lower calculated E_{rot} than the experimental value is very likely because the β value deduced at a lower E_{\perp} underestimates the conversion efficiency in the case where a higher $E_{\perp} = 177$ meV is applied. Determining the response of β with respect to E_{\perp} and T_S is needed in the future for improving the accuracy of the empirical formula. The composition of the calculated $\langle E_{\text{rot}} \rangle_{\text{eff}}$ is shown in the top panel of Figure 4.12. Under these scattering conditions, instead of the surface thermal energy $k_B T_S$, it is E_{\perp} that contributes the most to the rotational energy, and following is the physisorption well. The contribution of surface thermal energy reduces to 24% when a higher E_{\perp} is applied.

Now we should go back to answer the question about what provides the scattering CH_4 a surprisingly high degree of rotational excitation? The answer depends on the scattering conditions. In the conditions of low E_{\perp} , these are actually the surface thermal energy and the physisorption well. At low E_i , the surface thermal motion can excite the molecular rotation more efficiently and dominate the contribution among others. Whereas for high E_{\perp} , the surface thermal motions don't excite molecular rotation efficiently. In this case, the main contributions to the rotational energy are E_{\perp} and the additional energy added by the physisorption well.

4.4 Discussion

T \rightarrow R conversion efficiency

In the present work on CH_4 scattering from Ni(111), the rotational excitation of the scattered molecules has been investigated in detail. I found that both the normal and the parallel components of the incident kinetic energy can excite molecular rotation, with the normal component E_{\perp} showing higher T \rightarrow R conversion efficiency. The conversion efficiencies for both components $d\langle E_{\text{rot}} \rangle_{\text{eff}}/dE_{\perp}$ and $d\langle E_{\text{rot}} \rangle_{\text{eff}}/dE_{\parallel}$ are estimated to be 0.034 and 0.021 on a Ni(111) surface at $T_S = 673$ K, respectively. Compared to the system of formaldehyde scattering from Au(111) reported by G. B. Park et. al., where a very high conversion efficiency $d\langle E_{\text{rot}} \rangle/dE_i = 0.24$ was discovered [37], the conversion efficiency of CH_4 on Ni(111) is relatively low. I suspect the T \rightarrow R conversion efficiency is strongly correlated to the molecular geometry. Imagine bouncing a basketball and an American football from a flat ground with similar incident energies, it is intuitive to think of having higher imparted angular momentum for the football than the basketball. For football, due to its elliptical shape, when it collides on the ground, besides perfect side-on or end-on orientation, the force applied to its body is not directed to its center of mass but off a distance, giving rise to torque and spinning its body. Whereas on the basketball, the force applied by a collision directs to its center of mass, and therefore the only way to apply torque is by the friction of the ground. However, this friction is not presented on the microscopic level. Formaldehyde, as an asymmetric top molecule, compared to CH_4 , a spherical top molecule, is more facile to couple E_{\perp} into E_{rot} . For CH_4 , the 4 hydrogen atoms make its structure depart from a sphere such that it is still possible to

apply torque. Comparing molecules with other geometry, a high $T \rightarrow R$ conversion efficiency was also observed in the scattering of some linear molecules. Hines et. al. measured a very high conversion efficiency of up to 75% in the scattering of CO from Ni(111) [33]. Lykke et. al. observed an efficiency of 0.288 in the scattering of N_2 from Au(111). In the scattering of C_2H_2 from LiF(100), Miller et. al. measured an efficiency of 0.20 at low E_{\perp} ($23 < E_{\perp} < 65$ meV).

Effects of surface corrugation

In this work, I observed that not only E_{\perp} but also E_{\parallel} can excite molecular rotation via direct scattering from Ni(111). This indicates the Ni(111) surface structure sampled by CH_4 molecules must be corrugated. On a corrugated surface, the *local* surface normal at the molecule/surface impact point does not always lie parallel to the macroscopic surface normal. The momentum parallel to the macroscopic surface on this impact point can then give a momentum component normal to the *local* surface and be converted to molecular rotation. This may be surprising at the first glance because a close-packed (111) metal surface is normally considered a quite flat landscape due to the delocalized outer electrons [99]. However, several studies have shown the surface roughness of metal (111) surfaces can play an important role in the scattering dynamics. Hines, et. al. also observed total energy scaling in the scattering of CO from Ni(111) surface. Simply taking E_{\perp} into account could not explain the highest J -level they observed, and thus a total energy scaling is concluded. Furthermore, Kummel et. al. found that the angular momentum orientation (clockwise versus counterclockwise rotation) is influenced by the surface temperature in the system of N_2 scattering from Ag(111) [100]. They observed that as the surface temperature increased from 90 K to 540 K, the angular momentum orientation decreased drastically. Their stochastic trajectory calculations showed that the reduced orientation was caused by an averaging over the instantaneous positions and the momenta of surface atoms. Kondo et. al. studied CH_4 scattering from Pt(111) and measured the angular distribution of the scattered CH_4 by a mass spectrometer [99]. They observed small but non-negligible differences in the angular distributions of scattered CH_4 along two different azimuthal directions $[\bar{1}01]$ and $[\bar{2}11]$. If the surface is completely flat sampled by CH_4 molecules, the molecules should not show different scattering patterns for different scattering orientations. The fact that CH_4 scattering shows different angular distributions strongly indicates that CH_4 molecules do sense the surface corrugation. These results demonstrate the effects of surface corrugation are not negligible even on the close packed (111) surfaces.

Surface corrugation can be characterized by atomic beam diffractions [101]. On close-packed fcc(111) metal surfaces, normally weak diffraction peaks are observed in He diffraction spectra, indicating weak corrugation amplitudes. However, it has been found that different atoms or molecules can sample different degrees of corrugations [94,99]. By analyzing the intensities of the diffraction peaks generated by He and CH_4 , Taleb et. al. estimated that the corrugation potential of Ni(111) sampled by CH_4 is at most 10-fold stronger than that sampled by He [94].

Propensity of scattered CH₄ rotation

Going back to the rotational population of CH₄ scattered from Ni(111) shown in Figures 4.4 and 4.5, the most populated J -level is either $J = 0$ or $J = 3$, close to the initially prepared state $J = 0$. In Figure 4.4, we see a decrease in $J = 0$ population as E_{\perp} increases. This is due to an increase in rotational excitation for higher E_{\perp} and diluting the initially prepared $J = 0$ to higher J -levels. This trend is not clear in Figure 4.5 where I increase E_{\parallel} because the T \rightarrow R conversion efficiency of E_{\parallel} is weaker. In both cases, we observe a difference in the population of different sublevels in $J = 6$. The population of the sublevel with rotational symmetry A1 is always higher than that of A2 by a factor of 1.5. The energies of these two levels are 219.9451 and 219.9197 cm⁻¹, for A1 and A2 levels, respectively, according to the HITRAN database [70,75]. The energy difference between the two levels is therefore only 0.0254 cm⁻¹ which is insufficient to account for the difference in population.

The nature of the rotational sublevels can be considered as different K levels as in symmetric top molecules. For spherical top molecules, since the symmetric axis is equivalent no matter what reference axis is chosen, these sublevels should be degenerate. However, due to the effects of centrifugal distortion and anharmonicity, their energy levels split a few hundredths wavenumber (called cluster splitting) and therefore can be resolved by our TOPO laser [102]. The rotational quantum number K is the projection of total angular momentum J on the symmetric axis. If a rotational distribution preferentially populates in a specific K value, it means the molecule tends to spin in a specific way about the symmetric axis. For CH₄, understanding the spinning features of the A1 and A2 rotational levels of $J = 6$ requires a detailed analysis of rotational wave functions, which has not yet been accomplished in my Ph.D. work. Despite this, the inequivalent populations in the A1 and A2 rotational levels of $J = 6$ still indicates a spinning propensity of CH₄ along a specific axis after directly scattering from Ni(111). The propensity of rotation along a specific axis in rotational inelastic gas/surface scatterings was also observed in the systems of NH₃ scattering from Au(111) [36] and formaldehyde scattering from Au(111) [37]. In the scattering of NH₃ from Au(111), Kay et. al. found that the scattered NH₃ had a strong propensity of populating in low K . If $K = J$, the NH₃ molecule spins along the symmetric axis. The propensity for low K means the molecule is tumbling normal to the symmetric axis, instead of spinning along the symmetric axis. This dynamical feature is similar to what we see for CH₄ scattering from Ni(111). In the case of formaldehyde scattering from Au(111), C. B. Park et. al. found that the scattered formaldehyde tends to spin along the a-axis (CO bond axis), preferentially rotating in the twirling motion instead of tumbling or cartwheeling [37].

Effects of T_S on E_{rot}

Our results show a T_S -dependent feature of rotational energy in the scattered CH₄. The T_S efficiency coefficient γ depends on the normal component of incident velocity within the measured velocity range. The measured γ values range from 0.06 to 0.15 as u_{n0} increases from 524 to 1458 m/s. This value is far below unity, which is consistent with direct scattering processes. However, even when the scattering is direct, the scattered rotational energy can still be dependent on T_S due

to surface thermal motions and thermally induced corrugation. The effect of the surface thermal motions on E_{rot} can be qualitatively predicted by classical trajectory simulations using the Mathematica script provided by A. Kandratsenka, as documented in J. Werdecker's Ph.D. thesis [17]. However, in earlier studies of gas/surface scattering systems, under the conditions of direct scattering, the effect of T_S on E_{rot} is not obvious. In the system of NH_3 scattering from Au(111) with $E_{\perp} = 120$ meV, Kay et. al. found the scattered rotational distribution was insensitive to T_S [36]. For N_2 scattering from Ag(111), with $E_i > 0.1$ eV and $\theta_i = 30^\circ$, Sitz et. al. found no change in the scattered rotational temperature T_{rot} as T_S increased from 90 to 700 K [103]. In the case of NO scattering from Ag(111), Kleyn et. al. concluded a weak T_S dependent of E_{rot} (within 1 standard deviation) in the T_S ranged from 590 to 780 K with $E_{\perp} > 0.1$ eV [27]. These scattering experiments were carried out mostly on Au(111) and Ag(111) surfaces, where the surface atoms have higher mass compared to Ni atoms. At the same T_S , the vibrational frequency, and the velocity of the surface atoms are slower for heavier species. Consider the picture I have discussed in this chapter, that is, exciting molecular rotation by surface thermal motions, whose excitation efficiency depends on the relative velocity between the gas phase molecules and the surface atoms, it is not surprising that on heavier surface species such as Au and Ag, E_{rot} doesn't show obvious change with respect to T_S .

4.5 Conclusion

In this chapter, I presented the state-to-state study of CH_4 rotational inelastic scattering from Ni(111). The results show that not only the normal incident kinetic energy E_{\perp} is important for the rotational excitation but also the parallel component E_{\parallel} can also be converted to rotational energy in a direct scattering process due to surface corrugation. Besides conversion from incident kinetic energy, the surface thermal motion can also excite molecular rotation which contributes a significant portion of rotational energy in the scattered products. The empirical formula provided in this work taking into account the contributions of E_{\perp} , E_{\parallel} , physisorption well, and T_S , can resolve more than 80% of the measured rotational energy in the scattered CH_4 . The remaining fraction can be attributed to the fact that the E_{\parallel} conversion factor β is correlated to E_{\perp} and T_S which is not yet been resolved in this work. Our results demonstrate that the energy transfer that happens during the gas/surface encounter can be properly unraveled by the capabilities of the BILT machine. The rotatory bolometer detector enables independent variation of the incident and scattering angles. In combination with a variation of CH_4/He seed ratio of the gas mixtures, we can study the effects of E_{\perp} and E_{\parallel} on rotational excitation separately. In combination with a narrow band, tunable, CW-IR OPO, we can selectively excite rotational sublevels and discovered axis-specific rotation in the scattered products. The BILT technique is generally applicable to any molecule possessing IR-active vibrational modes with rotational state-resolved spectra. Besides the scattering of CH_4 from Ni(111), other molecule/surface systems can also be studied in detail by this technique.

Chapter 5 Vibrationally inelastic scattering

5.1 Introduction

In this chapter, I describe the state resolved measurements on vibrational energy transfer during CH₄ scattering from Ni(111) and graphene-covered Ni(111). This project was started by Van Reijzen and Werdecker, with the first results reported in Van Reijzen's thesis [16]. In the later stage of Werdecker's Ph.D. work, I participated in this project and performed experiments on CH₄ scattering from Gr-Ni(111).

Dissociative chemisorption of CH₄ on Ni is known as the rate-determining step of the steam reforming reaction for steam reforming of methane for the production of H₂ on an industrial scale and therefore has been the subject of many experimental and theoretical studies in the past decades [3,20]. State-resolved reactivity measurements show that CH₄ chemisorption is highly vibrational mode-specific [24]. By preparing the incident CH₄ in specific rovibrational quantum states and measuring the dissociation probability, it was observed that excitation of the symmetric C-H stretching normal mode ν_1 increases the CH₄ reactivity by up to an order of magnitude more than excitation of the antisymmetric C-H stretch ν_3 mode, even though the two modes are nearly isoenergetic (ν_1 2914 vs ν_3 3020 cm⁻¹) [102].

Excitation by a single-mode IR laser prepares a specific eigenstate of the incident molecules which has no time dependence in the molecular beam under collision-free conditions. However, once the molecule is sufficiently close to the target surface the interactions between the incident molecules and the solid surface can no longer be neglected and the initially prepared eigenstate of the isolated molecules is no longer an eigenstate of the combined molecule/surface system and will therefore evolve with time [104]. As a consequence the initially prepared vibrational state will couple with other vibrational states, resulting in internal vibrational redistribution (IVR), due to the molecule/surface interaction. The fact that the CH₄ chemisorption shows a strong mode-specificity indicates that the IVR during the approach to the surface is not complete before the dissociation occurs and the reacting molecule preserves some memory of its initially prepared state. If the redistribution were complete, the initial vibrational energy would be randomized over all energetically accessible states and the reactivity could be calculated from statistical rate theories such as RRKM and would therefore depend on the initial internal energy but not on the initially prepared state. By state-resolved detection of the scattered molecules, we can observe the result of this surface-induced IVR and obtain information on the molecule-surface interaction potential.

The results described in this chapter can be divided into two parts. First, I present experimental results for CH₄ scattering from clean Ni(111) and Ni(111) covered by a single layer of graphene (Gr-Ni(111)). A comparison of the tagging spectra with a spectral range covering two hot band transitions $\nu_1 \rightarrow \nu_1 + \nu_3$ and $\nu_3 \rightarrow 2\nu_3$ clearly demonstrates the dramatic difference in the vibrational energy redistribution between the two surfaces. These measurements were performed in the initial setup used for testing the BILT detection. I will also describe the results of quantum dynamics calculations performed by Bret Jackson which were performed in order to help interpret our experimental results. The combined results have been published in *Physical Review*

Research [105] and were presented at the 29th Edition of the *International Symposium on Molecular Beams in 2021*. In the second part, I describe how I used the new BILT machine to further investigate the properties of this vibrational energy redistribution by applying higher normal incident kinetic energy and performing measurements at lower surface temperatures. This study is still ongoing in the lab currently. Here, I present some preliminary results in comparison with theoretical calculations.

5.2 Experimental

The first results I present in this chapter were performed in the testing setup (our “old machine”). A detailed description of this setup can be found in Van Reijzen and Werdecker’s theses [16,17]. The setup was modified by adding a bolometer detector to an existing port of a molecular beam-surface science UHV apparatus. Due to this fact, the detection position is fixed at 135° relative to the incident molecular beam direction and all experiments reported here were measured at the scattering geometry $\theta_i = 65^\circ$, $\theta_f = 70^\circ$.

The incident CH₄ molecules are state-prepared in v_3 , $J = 1$ by infrared pumping using an Argos CW-IR OPO via rapid adiabatic passage with excitation efficiency of > 95%. After scattering from a clean Ni(111) or Gr-Ni(111) surface, the second OPO excites the scattered CH₄ via the combination overtone bands $v_1 \rightarrow v_1 + v_3$ and $v_3 \rightarrow 2v_3$ in order to detect molecules scattered in v_1 and v_3 vibrational states, respectively. To interrogate the quantum state distribution of scattered CH₄, I tune the laser frequency to the target transition and record the bolometer signal in laser amplitude-modulation mode. The laser frequency was optimized by scanning the transfer cavity and optimizing the bolometer signal to the peak of the absorption profile. In the old machine, scattering molecules are laser-excited via the rapid adiabatic passage because the narrower residual Doppler broadening can be fully covered by the total frequency sweep generated by an $f = 254$ mm cylindrical lens, as discussed in chapter 3. For transitions with a strong enough Einstein coefficient A_{12} , the bolometer signal at the highest laser power (> 1 W) is directly proportional to the population of the corresponding lower rovibrational level. Whereas for transitions with weaker transition dipole moment, especially for $v_1 \rightarrow v_1 + v_3$, measurements of fluence curves are needed followed by a fit of the Landau-Zener formula to derive the asymptote value which is proportional to the state population. BILT spectra were measured by performing tagging experiments in frequency-modulation scanning mode. In this case, the laser power stays constant, but the laser frequency is modulated by adding a sine wave signal from the lock-in amplifier which serves as a master oscillator. This sine wave signal is superimposed with the linear ramp voltage controlled by the transfer cavity VI by a home-built summing amplifier and then sent to the piezoelectric element of the seed laser for frequency scanning. The configuration of frequency modulation scanning can be found in Werdecker’s thesis [17], so I will not go into detail in this chapter.

The graphene-covered Ni(111) surface is prepared by chemical vapor deposition following the strategy in ref [106]. It is performed by dosing 5×10^{-7} mbar of ethylene on the Ni(111) surface at $T_s = 873$ K. The status of graphene formation can be monitored by the specular peak signal of He

scattering measured by the bolometer detector. The preparation normally takes about 50 minutes. Afterward, the structure of the graphene surface is characterized by LEED and AES, as documented in Van Reijzen's thesis [16].

5.3 Vibrational relaxation of CH₄ (ν_3 , $J = 1$) during scattering from Ni(111) and Gr-Ni(111)

To study the vibrational state distribution of CH₄ following a collision with clean and graphene-covered Ni(111) surface, we prepared the incident CH₄ molecules with one quantum of ν_3 antisymmetric stretch vibrational mode in $J = 1$ with incident kinetic energy $E_i = 100$ meV. After scattering from a clean Ni(111) or a Gr-Ni(111) surface, the quantum state distribution of the scattered CH₄ is measured by the BILT technique.

The results of vibrationally inelastic scattering of CH₄ from clean Ni(111) have been reported in Werdecker's thesis, readers are referred to his thesis for more detail [17]. Here, I summarize the main observations. After scattering from a clean Ni(111) surface, we observed "surface-induced" vibrational energy redistribution from the initially prepared ν_3 antisymmetric stretch mode to ν_1 symmetric stretch mode. Going into more detail, the branching ratio, defined as the total signal of rotational lines in ν_1 divided by the total signal of rotational lines in ν_3 was found to be ≈ 0.4 . This branching ratio appears to be insensitive to incident kinetic energy ranging from 100 to 370 meV at an incident angle $\theta_i = 65^\circ$. When an $E_i = 227$ meV of incident CH₄ beam is used, the rotational temperature was measured to be 178 ± 17 and 162 ± 11 K for the ν_1 and the ν_3 channel, respectively. The rotational energy of the CH₄ scattered via the ν_1 channel is about 40 cm^{-1} higher than that of ν_3 throughout all incident kinetic energy used, which accounts for nearly 40% of the energy difference between the two vibrational states (103 cm^{-1}).

As documented in Van Reijzen's thesis, he attempted to find vibrational energy relaxation from ν_3 (3020 cm^{-1}) not only to ν_1 (2914 cm^{-1}) but also to other vibrational states such as ν_2 (1524 cm^{-1}), ν_4 (1306 cm^{-1}), $2\nu_2$ (3072 cm^{-1}), $2\nu_4$ (2600 cm^{-1}), and $\nu_2 + \nu_4$ (2823 cm^{-1}) [16]. Results show that only very weak signals were observed for 3 rotational lines of $2\nu_2$ states, corresponding to 2.4% of the total scattered flux, and no measurable amount of signal was found for other vibrational states. This is consistent with the expectation that the molecule/surface vibrational energy transfer depends strongly on the energy gap. Any mismatch between the vibrational energy of the incident and scattered molecule has to be transferred to other degrees of freedom of the molecule/surface system, such as translation and rotation of the scattered molecule, as well as phonons and electron-hole pairs solid. As we have seen in the rotational energy of the CH₄ that scattered into the ν_1 and the ν_3 state, the higher rotational energy of the ν_1 state reflects 40% of the excess energy when the CH₄ redistributes from ν_3 to ν_1 . The low ratio for the $2\nu_2$ state can be due to its higher energy level than the ν_3 state that requires conversion of energy from other degrees of freedom. Moreover, conversion from the antisymmetric stretch mode to bending mode would require more distortions to the molecule than to symmetric stretch mode, and eventually make $\nu_3 \rightarrow 2\nu_2$ less likely to happen.

On the other hand, we found that by covering the clean Ni(111) surface with a graphene layer, the surface-induced vibrational energy redistribution $\nu_3 \rightarrow \nu_1$ was no longer observed. To demonstrate this, we performed frequency modulation (FM) scans over a spectral range covering transitions of both ν_1 and ν_3 hot bands. Figure 5.1 shows the measured FM spectra measured on both clean Ni(111) (red) and Gr-Ni(111) (black). By comparing these two measured spectra, it is clear that all lines corresponding to ν_1 hot band transitions are missing for Gr-Ni(111), indicating the $\nu_3 \rightarrow \nu_1$ redistribution is completely absent when a single layer of graphene covers the Ni(111) surface.

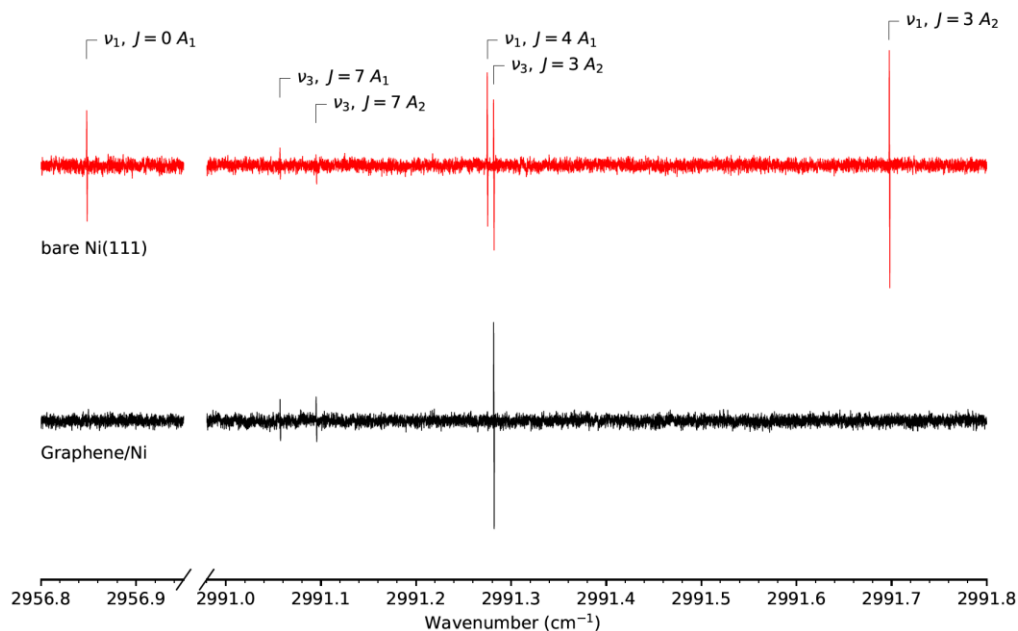


Figure 5.1 FM tagging spectra measured for CH₄ scattering from clean Ni(111) and graphene covered Ni(111) in a spectral range covering both ν_1 and ν_3 hot band transitions. Note the complete absence of any tagging signal for transitions originating from ν_1 . The figure is taken from ref [105].

As I have discussed earlier, we state-prepared the incident beam with a single-mode CW-IR laser which excites the incident molecules to a static eigenstate. Vibrational redistribution happens when the molecule/surface interactions start to cause a perturbation to the Hamiltonian of the isolated molecule. The fact that the vibrational redistribution/relaxation can happen on the clean Ni(111) surface but not on the Gr-Ni(111) surface unambiguously tells that the interaction potentials sampled by CH₄ on these two surfaces are completely different. Compared to clean Ni(111), the graphene-covered surface is inert and does not promote methane dissociation. Therefore the observed vibrational relaxation could be the signature of a catalytically active surface with a low reaction barrier such that the incident molecules can approach the transition state and experience a structural distortion. In the next section, I will show how this hypothesis can be confirmed by theory.

5.4 Rotational excitation of CH₄ (v_3 , $J = 1$) scattered from Ni(111) and Gr-Ni(111)

Using the BILT technique, we measured the rotational distribution of vibrationally elastic scattered CH₄(v_3 , $J = 1$) from Gr-Ni(111), as shown on the right in Figure 5.2, and compare it with the distribution measured for scattering from clean Ni(111) shown on the left. For clean Ni(111), the rotational population peaks at the initially prepared $J = 1$, whereas for Gr-Ni(111), the initially prepared $J = 1$ is greatly diluted and the highest population belongs to $J = 3$. Furthermore, the populations at high J are higher for scattering from Gr-Ni(111).

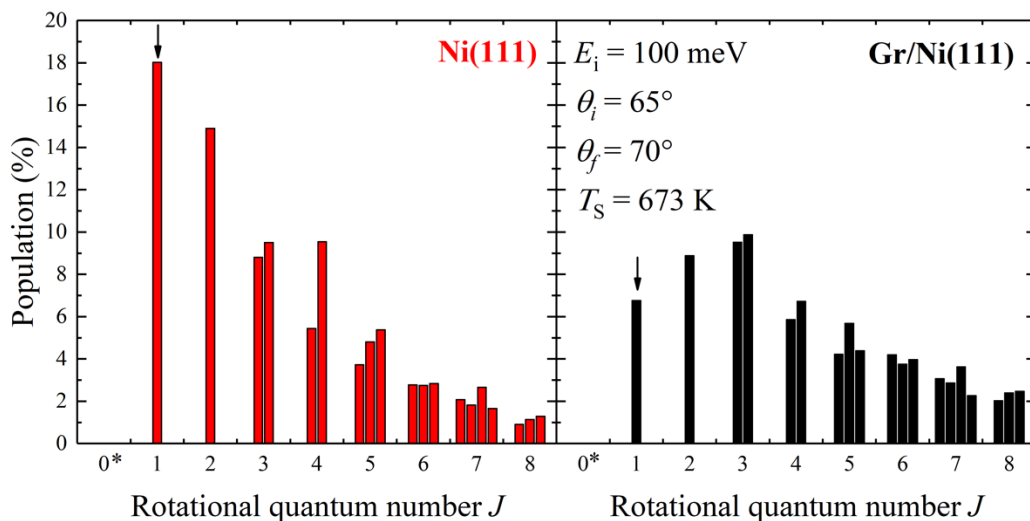


Figure 5.2 Rotational populations of the vibrationally elastic scattered CH₄ from clean Ni(111) (left) and Gr-Ni(111) (right). The black arrow indicates the initially prepared rotational state in the incident beam. *Note that the level $J = 0$ does not exist for *meta*-CH₄ due to symmetry restriction.

To quantitatively compare the extent of rotational excitation on both systems, I perform the Boltzmann fit of the data in Figure 5.2 but ignore the lowest two J levels as they are departing from Boltzmann behavior which is expected for a direct scattering process. Figure 5.3 presents the resulting Boltzmann plots for both systems. There, we observed a higher rotational temperature of 208 K for the scattering from Gr-Ni(111) surface than that from clean Ni(111) of 153 K. The greater rotational excitation on Gr-Ni(111) is very likely due to the fact that graphene-covered Ni(111) surface is more corrugated and thus facilitates the conversion of parallel momentum of the incident molecule to the molecular rotation [106]. In both cases, the measured rotational temperatures are far below the surface temperature of 673 K, indicating a direct scattering mechanism instead of trapping-desorption. Typically our tagging experiments for v_3 rotational populations on clean Ni(111) measure up to $J = 8$ due to the sensitivity of the setup. We therefore also measured rotational lines up to $J = 8$ for the scattering from Gr-Ni(111). However, as one can find from Figure 5.2, the hotter rotational population for the Gr-Ni(111) system warns us that there may still have a measurable amount of population above $J = 8$. Thus, I performed a linear fit on

the measured data points and extrapolated the expected signals up to $J = 10$. The expected signals above $J = 10$ are lower than 0.2 mV, the minimum measurable signal of the setup. For the Boltzmann plot of the Gr-Ni(111) system, the fitting includes the calculated populations for $J = 9$ and $J = 10$.

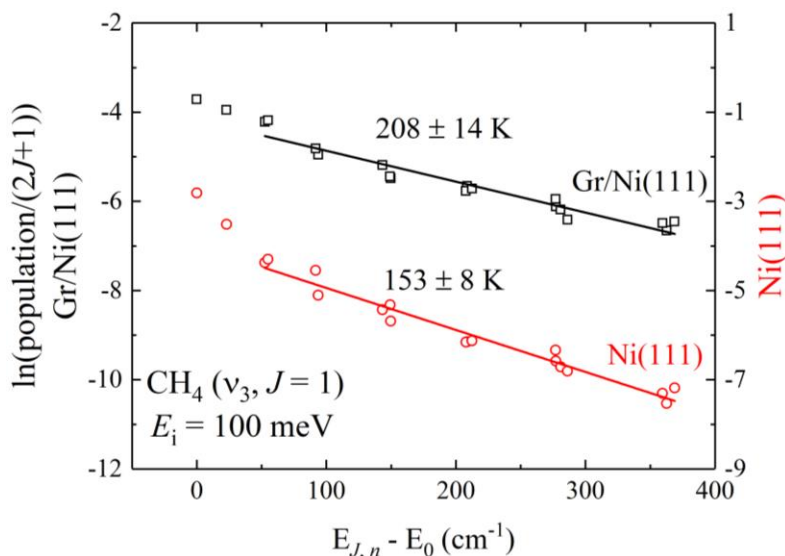


Figure 5.3 Boltzmann plots of the rotational populations shown in Figure 5.2 for scattering from Ni(111) (red) and Gr-Ni(111) (black). Note that the linear fits are performed without taking into account the lowest $2J$ levels as they depart from the line. The rotational temperatures of the two systems are derived by slopes of the linear fits, giving rise to $T_{\text{rot}} = 208 \pm 14 \text{ K}$ and $153 \pm 8 \text{ K}$ for the scattering from clean Gr-Ni(111) and clean Ni(111), respectively.

5.5 Theoretical predictions for state-to-state methane scattering

To understand the dramatic difference in vibrational energy redistribution between the clean Ni and Gr-Ni(11) systems, Prof. Bret Jackson at the University of Massachusetts performed quantum dynamics calculations for CH_4 scattering from Ni(111) using an approximate PES based upon reaction path Hamiltonian [107]. Previously this method was applied by Jackson and coworkers to explain the vibrational mode specificity observed in state resolved measurements of methane surface reactivity on different Ni and Pt surfaces [108–111]. Readers interested in the detail of the calculations are referred to the supplementary materials of our publication of this work in *Physical Review Research* [105].

The Ni(111) surface in the calculations is modeled as a 4 layers 2×2 surface unit cell, as shown in the right inset of Figure 5.4. The calculations consider collisions at 16 sites on the unit cell, resulting in 4 distinct impact sites, these are the top site (top), the half-bridge site (hb), the bridge site (br), and the near-hollow site (nh). The calculated probabilities of vibrational energy redistribution ν_3 to ν_1 for four different impact sites are illustrated in Figure 5.4. Results show that the probability of $\nu_3 \rightarrow \nu_1$ depends strongly on the impact site. The strongest vibrational energy

redistribution appears to be on the top site, and the probability decreases as we go from the top site to the bridge site, and finally to the near-hollow site. It has been shown that the barrier of CH₄ dissociative chemisorption is the lowest on the top site, and increases as one moves to the bridge site [7,112]. It is therefore suggested that the probability of $v_3 \rightarrow v_1$ redistribution reflects the catalytic activity of surface atoms. To estimate the effect of surface temperature, the calculations were performed on the condition where the Ni atom closest to the incoming CH₄ is puckered up by 0.1 Å, roughly the vibrational amplitude of surface atoms at 300 K. We found the probability of the $v_3 \rightarrow v_1$ redistribution on the half-bridge site with this displacement is higher, as shown in the surface “hb-Q” in the left inset of Figure 5.4. It has been found that the lattice displacement can reduce the barriers of CH₄ dissociative chemisorption of Ni(111) as the reactivity increases as T_s elevates [113].

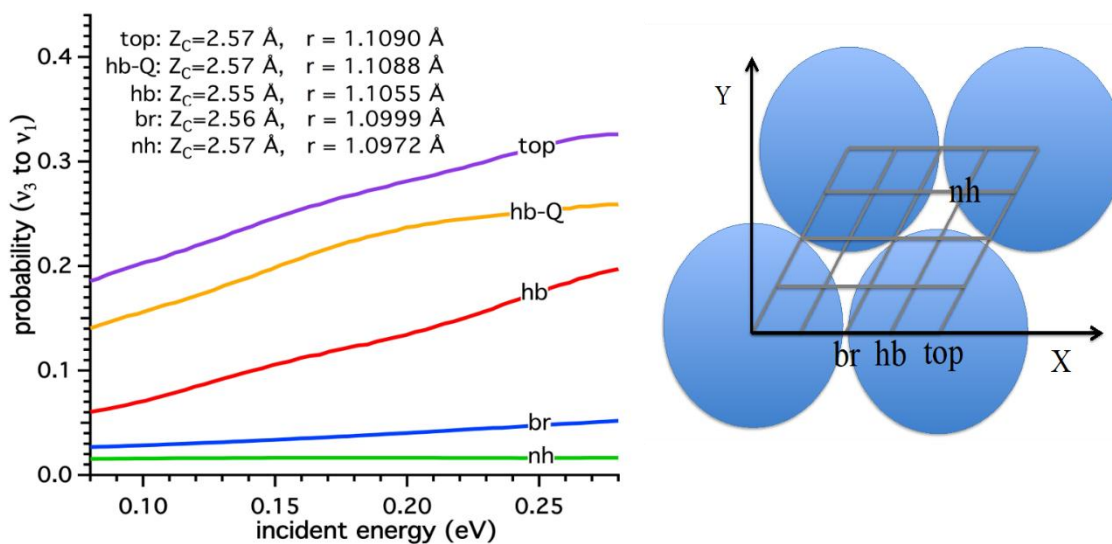


Figure 5.4 Left: the calculated probability of the $v_3 \rightarrow v_1$ redistribution of CH₄ scattered from clean Ni(111) on different impact sites. Z_C is the distance of the carbon atom above the surface when the total energy $V_0 = 0.2$ eV, and r is the C-H bond length closest to the surface at a given Z_C . Right: the model of the 2×2 unit cell with the definition of the 4 distinct impact sites, the top site, the half-bridge site (hb), the bridge site (br), and the half-bridge site (hb). The figure is taken from ref [105].

Also shown in Figure 5.4 is the length of the C-H bond closest to the surface at the classical turning point Z_C defined as the carbon to surface distance when the total energy $V_0 = 0.2$ eV, a value that resembles the collision energy. We find the C-H bond elongates more as it approaches a more reactive impact site. This C-H elongation is essentially the motion along the reaction coordinate of CH₄ dissociative chemisorption. Even though the incident energy of our scattering experiments is way below the activation energy of 1 eV, it is found that the C-H bond elongates earlier as it approaches an impact site with a lower barrier. Consider the difference between the v_1

symmetric stretch and the ν_3 antisymmetric stretch mode is simply the phase of the 4 identical C-H vibrations, the C-H bond elongation can then facilitate the coupling of the two vibrational modes. After averaging the $\nu_3 \rightarrow \nu_1$ probability over all surface impact sites, the $\nu_3 \rightarrow \nu_1$ probability on Ni(111) is found to be 10% at an incident energy of 0.2 eV. This probability increases by a factor of 2 or 3 if the lattice displacement is introduced in the model to represent an elevated T_S as our experimental conditions. The calculations are performed again on a Gr-Ni(111) surface and it turns out the probability of $\nu_3 \rightarrow \nu_1$ redistribution reduces to only 1.5% even on the most reactive top site, agreeing very well with our experimental observations.

The theoretical calculations provide an insight into our surface-induced vibrational energy redistribution. The results reveal that the probability of the $\nu_3 \rightarrow \nu_1$ redistribution is strongly related to the reactivity of the surface impact sites. This picture is clear because the $\nu_3 \rightarrow \nu_1$ redistribution is completely turned off if the clean Ni(111) is covered by a graphene layer which is known as a catalytically inert surface. Our results then suggest the extent of the surface-induced vibrational energy redistribution can serve as a probe of catalytic activity on surfaces.

5.6 T_S -dependent $\nu_3 \rightarrow \nu_1$ redistribution

The theoretical model discussed above suggests that the $\nu_3 \rightarrow \nu_1$ efficiency is dependent on the surface temperature T_S . This hypothesis was not possible to be tested in the old machine due to the limited T_S as discussed before. After the construction of the BILT machine, I performed CH₄ scattering experiments over a wide range of T_S from 96 -673 K. As a quick test, I decided to simply scan only one rotational line of each vibrational state ν_3 and ν_1 , and recorded the absorption profile as a function of T_S .

The rotational line scanings were performed in the frequency modulation mode. The incident CH₄ is state-prepared in ν_3 $J = 1$ with $E_i = 241$ meV at $\theta_i = 65^\circ$, $\theta_f = 70^\circ$. Since the measurements were done before acquiring the TOPO system, the Argos OPO-II system was used as the tagging laser using excitation via RAP. As I have described in chapter 3, the focusing conditions did not allow us to cover all the Doppler velocity classes in the scattered molecules, but RAP still enabled us to excite a higher portion of molecules and therefore higher signals. Figure 5.5 shows examples of FM scan BILT spectra for the Q(3) A2 transitions of both the ν_3 and the ν_1 channel of scattered CH₄ from a 373 K Ni(111) surface. Later the peak height was extracted by fitting the experimental spectra with the first derivative of a Gaussian function and taking the peak-to-peak value from the fitting function. I then measured the Q(3) A2 line scan for several T_S values, from 96 K to 673 K. The ratio of the ν_1 and ν_3 Q(3) A2 peak heights are plotted as a function of T_S , as shown in Figure 5.6. The statistical error is estimated to be 0.015 mV, determined by the student's t method on a line scan of 3 repetitions. The error propagates to the peak ratio is then estimated to be 0.06. There, we see the peak ratio ν_1/ν_3 reduces from 1.20 to 1.05 as T_S increases from 96 to 673 K, indicating a weak dependence on T_S . This observation may disagree with the theoretical calculations. However, the ratio is determined simply by one rotational line in each vibrational state. We could conclude the $\nu_3 \rightarrow \nu_1$ probability is insensitive to T_S only if the rotational distributions of the two rotational states react similarly with respect to T_S .

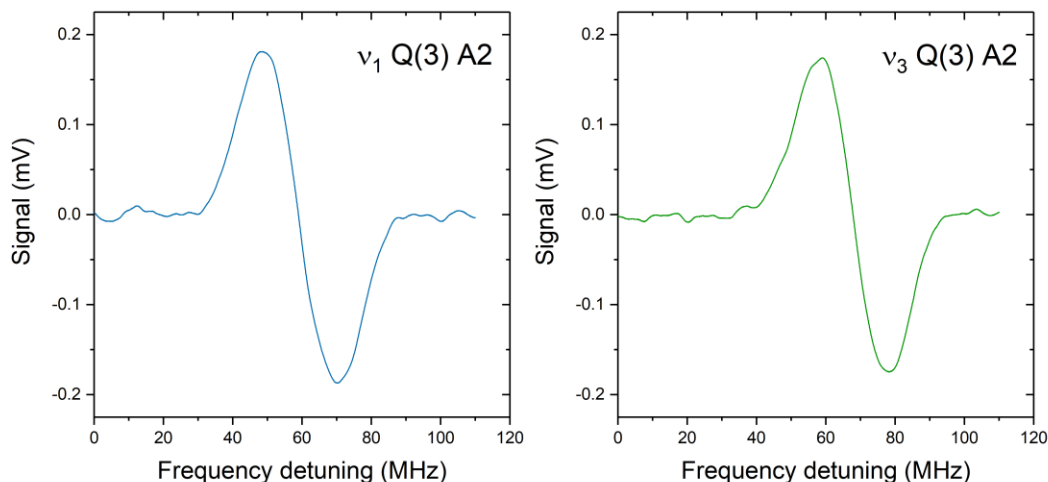


Figure 5.5 FM scanned BILT spectra of the Q(3) A2 transitions for both the ν_1 (left) and the ν_3 channel in the scattered CH_4 from a 373 K Ni(111) surface. The incident CH_4 is state-prepared in ν_3 $J = 1$ and $E_i = 241$ meV. Scattering experiments were carried out in the geometry of $\theta_i = 65^\circ$, $\theta_f = 70^\circ$. The modulation frequency is set to 210 Hz with RMS amplitude = 30 mV. The laser power is 72 and 52 mW for the ν_1 and the ν_3 lines, respectively.

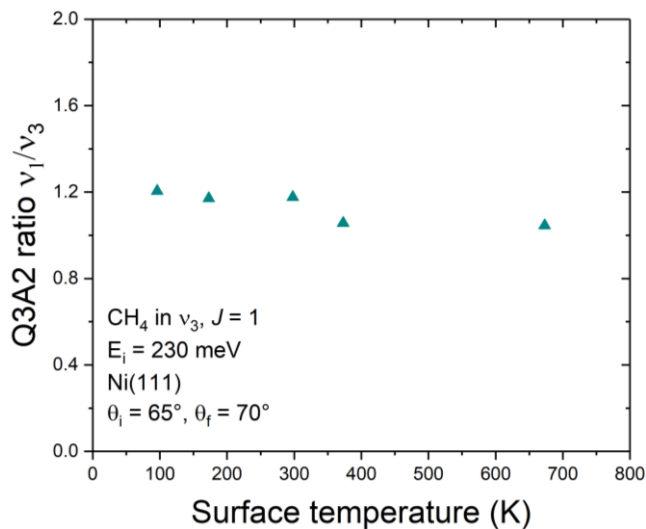


Figure 5.6 peak height ratio of the ν_1 and the ν_3 Q(3) A2 lines as a function of T_s .

To draw a reliable conclusion about the T_s -dependent $\nu_3 \rightarrow \nu_1$ efficiency, we would need to record all the accessible rotational lines for both vibrational states and calculate the branching ratio using the total signal taking into account all measured rotational lines. Unfortunately, I encountered a problem with bolometer stability due to the degradation of the adhesive which glues

the diamond absorber and the bolometer elements. The adhesive plays an important role as it conducts the thermal energy from the absorber to the bolometer. The degraded adhesive then reduced the thermal conductivity and caused instability of the bolometric measurements. Therefore within the available time of my Ph.D. work, the measurements of recording all the rotational lines as a function of T_S and E_i were not accomplished. This project is still ongoing in the lab. Now, with the program-controlled TOPO system, we expect to finish the rotational line scans more efficiently than using the manually tuning Argos system.

In the BILT machine, the broader residual Doppler broadening caused by the reduced sample-to-bolometer distance can not be fully covered by the total frequency sweep provided by the focusing conditions, instead of using RAP, we decided to frequency broaden the laser linewidth and saturate the transitions for the scattered molecules. In chapter 3, I have shown that this method can saturate most of the ν_3 fundamental transitions of scattered CH_4 . However, for the ν_1 hot band and part of the ν_3 hot band transitions which have relatively low Einstein coefficients ($9\text{-}18\text{ s}^{-1}$), it is important to confirm that we can also saturate these transitions with the available laser power. If saturations are not achieved for all the transitions, partial saturation will introduce an error in determining the ν_1/ν_3 branching ratio. Since ν_1 hot band transitions have on average lower Einstein coefficients, partial saturation will then underestimate the ν_1/ν_3 branching ratio. Future users should make sure the measured transitions are saturated to eliminate this error.

Chapter 6 Summary and outlook

6.1 Summary

This thesis describes my work on state-to-state surface scattering of CH₄ using the bolometric infrared laser tagging technique (BILT) with a newly designed apparatus. The design and construction comprise the main part of my Ph.D. work, therefore a high portion of this thesis is dedicated to describing the design and the functions of the machine accompanied by the results of testing the apparatus and methods.

In chapter 2, I started by introducing the idea of BILT detection and giving an overview of the molecular beam-surface scattering machine (BILT machine). The apparatus consists of a source chamber, two sequential differential pumping stages, and the UHV chamber where the surface scattering and detection take place. As a general UHV surface science apparatus, the BILT machine is equipped with a temperature-controlled sample mount, an ion sputter gun, a LEED, and an Auger spectrometer for surface preparations and characterizations.

The most distinctive feature of the BILT machine is the rotatable lid where a liquid helium-cooled cryogenic bolometer detector is installed. This enables the rotation of the bolometer detector for independent control of incidence and scattering angle. In order to keep the scattering chamber under UHV conditions during detector rotation, the top hub features two differential pumping stages separated by three spring-loaded PTFE O-rings. The performance of the rotary seal has been tested and the pressure rise due to lid rotation in the UHV stage was found to be less than 1×10^{-10} mbar during rotation of the detector.

Unlike the other machines in our lab, the BILT machine contains a molecular beam source with a simpler nozzle design consisting of a 6 mm diameter tube held on both ends by two copper clamps with a 60 μm pinhole laser-drilled in the middle. This design, developed by Daniel Auerbach, is easier to manufacture than previous designs used in our group as it requires no welding and therefore can be used to make nozzle tubes from a range of different metals. For example, we have found that the nozzles made from stainless steel have a tendency to produce CO when used with methane as a seed gas due to the catalytical activity of nickel contained in the stainless steel. Using a different, less reactive metal such as gold is expected to avoid this problem. The velocity distributions of the molecular beams generated by this new nozzle have been characterized by the time-of-flight (TOF) method using a quadrupole mass spectrometer equipped with a cross-beam ionizer. The calibrations of the TOF method are documented in this chapter. With the calibrated TOF, the measured velocity of a He beam is consistent with the theoretical value with a narrow velocity distribution (translational temperature = 2.5 K).

The process of surface cleaning using Ar ion sputtering and followed by annealing is described. The performance of the cleaning process has been confirmed by the AES and LEED analysis of the Ni(111) sample. Temperature regulation of the surface sample is accomplished by e-beam heating controlled by a power supply with a built-in PID. During heating the sample, the entire sample mount is liquid nitrogen-cooled to prevent undesired outgassing coming from a hot surface

surrounding the hot filament. To move the sample to the desired position for measuring LEED, AES, and surface scattering, the sample mount is connected to a 4-axis manipulator (X, Y, Z, and θ).

A major portion of chapter 2 describes the design and performance of the bolometer detector and some of the problems we encountered during its use. Unlike the standard V1 version of the bolometer offered by IRLabs, the design of the V2 bolometer was specifically adapted for use in the BILT machine. However, the first test of the bolometer turned out to be disappointing because the measured helium atom scattering signal was more than 10-fold weaker than the V1 bolometer used in the test setup. Load curve measurements for several conditions showed that the low sensitivity was due to a higher thermal heat load on the bolometer due to background infrared radiation from the room temperature apparatus. This problem was solved by restricting the field of view of the bolometer by adding a cooled extension aperture. The modified bolometer then showed sufficient sensitivity to detect scattered CH₄. After installing the V2 bolometer in the BILT machine, we observed a scattered CH₄ signal 20-fold stronger compared to the V2 bolometer in the old machine due to the reduced sample-to-bolometer distance and a stronger molecular beam flux.

In September 2020, our group acquired a new, widely tunable CW-IR laser system (Toptica TOPO system) which features computer-controlled frequency tuning which makes it well suited as a tagging laser. Due to the contributions of the postdoctoral researcher Dr. Christopher Reilly, the TOPO system is now able to automatically find tagging transitions from a list of transitions and rapidly record the corresponding tagging signals under computer control. This replaces the manual tagging experiments using our Argos OPO systems which were very time-consuming. The TOPO can be frequency stabilized by locking it to a Fabry-Pérot interferometer (FPI) as well as to a transfer cavity. The frequency tuning algorithm and the configuration of the FPI stabilization are described in chapter 2. The performance of FPI has been proved to be reliable as it greatly increases the S/N ratio of the recorded absorption profiles.

Although we expected to obtain a great enhancement of the laser tagging signals by the much-reduced sample-to-bolometer distance in the BILT machine, the observed tagging signal is only a factor of 2 stronger for the R(0) ν_3 fundamental transitions compared to tagging in the old machine. Furthermore, the measured fluence curves for the ν_3 fundamental transitions were far from saturated. In this case, the tagging signals at the highest laser power could not be extracted as populations of the corresponding states. This departure from our expectation is due to the broader residual Doppler broadening that can not be fully covered by the available total frequency sweep in our focusing conditions. Chapter 3 is therefore dedicated to elucidating this problem. I started with the theory of the rapid adiabatic passage which allows nearly complete population inversion. With the provided theory, the calculated total frequency sweep with our focusing conditions ($f = 254$ mm cylindrical lens) is found to be insufficient to cover the full residual Doppler width of the tagging transitions. To create a broad enough frequency sweep, I found that it required a cylindrical lens with $f < 50$ mm. However, with this lens, the adiabatic condition won't be satisfied, meaning the RAP process won't be successful.

As an alternative, instead of seeking a full population inversion by RAP, I decided to frequency-broaden the laser such that the broadened laser linewidth could cover all the Doppler velocity classes of the scattered molecules and reach 50% of excitation probability. This is realized by adding a white noise from a function generator to the DFB seed laser which provides up to GHz of bandwidth using the diode current modulation mode. With the frequency-broadened laser, I recorded the fluence curves of several ν_3 fundamental transitions and observed asymptotes of the curves. The tagging signals at the highest laser power can then be treated as state populations. This method was adapted to record rotational lines of scattered CH_4 at a wide variety of scattering conditions to study the rotational inelastic scattering of CH_4 from Ni(111).

In chapter 4, I presented the results of rotational inelastic scattering measurements of CH_4 from Ni(111). I studied the effects of the parallel E_{\parallel} and normal component E_{\perp} of the incident kinetic energy, and surface temperature T_S on the final rotational energy of scattered CH_4 . The independent variation of E_{\parallel} and E_{\perp} was accomplished by selecting a proper gas mixture and incident angle such that E_{\perp} or E_{\parallel} can be varied by keeping the other constant. Results showed that both components could excite molecular rotation but a higher efficiency was observed for the normal component. The conversion efficiency is found to be $d\langle E_{\text{rot}} \rangle_{\text{eff}}/dE_{\perp} = 0.034$ and $d\langle E_{\text{rot}} \rangle_{\text{eff}}/dE_{\parallel} = 0.021$ for the normal and the parallel component, respectively. The fact that the parallel component of the incident kinetic energy can couple to rotational energy indicates that the surface corrugation has an effect on the rotational energy of the scattered CH_4 molecules. I cited several surface scattering studies that also suggested that surface corrugation did affect the scattering patterns such as final rotational energy, angular distributions, and preference of rotational orientations even on (111) metal surfaces.

Effects of T_S on rotational excitation were investigated by measuring the rotational state populations as a function of T_S . I found the final rotational energy increased as a function of T_S , but the slope $d\langle E_{\text{rot}} \rangle_{\text{eff}}/d(k_B T_S)$ was dependent on the incident angle at a given incident kinetic energy E_i . Further studying showed that the efficiency of rotational excitation increased linearly with decreasing velocity component normal to the surface. The observations are interpreted as a higher probability for the slow incoming molecules to collide with fast up-moving surface atoms on a hot surface, an idea supported by Logan and Goodman's model [97,98]. I provided an empirical formula taking into account the contribution of the E_{\perp} , E_{\parallel} , and T_S , that could resolve more than 80% of the contribution to rotational excitation. By analyzing the components of the final rotational energy, I found a high portion (> 70%) of rotational energy was provided by surface thermal motion and physisorption well when a slow incident beam ($E_i = 130$ meV) was used. If a fast incident beam was used ($E_i = 241$ meV), then the contribution from E_i dominates over others. In this work, I demonstrated that by the capabilities of the BILT, the mechanism of rotational excitation could be studied in much more detail than possible in the previous testing setup.

Besides rotationally inelastic scattering of CH_4 , in Chapter 5, I reported the results of vibrationally inelastic state-to-state scattering of $\text{CH}_4(\nu_3, J = 1)$ from Ni(111) and Gr-Ni(111). By comparing state-resolved tagging spectra of CH_4 scattering from clean Ni(111) and Gr-Ni(111), we discovered that the surface-induced vibrational energy redistribution from the initially prepared ν_3 state to the ν_1 state completely disappeared when the clean Ni(111) was covered by a single

layer of graphene. The rotational distribution of CH₄ scattered from Gr-Ni(111) is found to be hotter than scattering from clean Ni(111) which is ascribed to the increased corrugation of the graphene adlayer. Theoretical calculations based upon reaction path Hamiltonian suggest that the probability of the surface-induced $\nu_3 \rightarrow \nu_1$ redistribution is correlated to the catalytic activity of the impact sites [47]. The calculations show that as the CH₄ approaches the surface, the C-H bond closest to the surface elongates. This elongation distorts the CH₄ molecule and induces coupling between the ν_1 symmetric C-H stretch mode and the ν_3 antisymmetric C-H stretch mode, as these two modes simply differ by the phase of the four C-H bond stretches. The extent of this elongation is found to be greatest when the incoming CH₄ collides with the reactive impact site.

The calculations also predict that the probability of $\nu_3 \rightarrow \nu_1$ redistribution is sensitive to the lattice displacement in the vertical direction. Therefore we expect to see a T_S -dependence in the $\nu_3 \rightarrow \nu_1$ redistribution efficiency. To verify this prediction, I performed T_S -dependent scattering experiments in the BILT machine. As a quick test, I only measured one line Q(3) A2 for each vibrational state which probes the $J = 3$ population. By monitoring the ratio of the bolometer signal for the two tagging lines I expected to detect any change of $\nu_3 \rightarrow \nu_1$ redistribution efficiency as a function of T_S . The ratio showed less than 10% change as T_S increased from 96 K to 673 K. However, we can not yet conclude the $\nu_3 \rightarrow \nu_1$ redistribution is insensitive to T_S because only one line in each vibrational state was measured. If the rotational excitations of the two vibrational states react similarly to T_S , the ratio of the two rotational lines can serve as a good representative of the $\nu_3 \rightarrow \nu_1$ redistribution efficiency. However, this assumption has not yet been verified. Hence, determining the branching ratio of the two vibrational channels on different T_S still requires measuring all the available rotational lines and comparing the ratio by their total signals.

Finally, in my Ph.D. work, I have finished the construction of the BILT machine and demonstrated its capabilities by studying the rotational inelastic scattering of CH₄ from Ni(111). The puzzle left by the previous work, namely the surprisingly high degree of rotational excitation of scattered CH₄ with low E_i , has been solved in this work. It is due to a high contribution of surface thermal motion and by an acceleration of the CH₄ molecules when they drop into the physisorption well. The BILT machine enables us to perform experiments with a wide variety of scattering geometry and a broader surface temperature that were not available in the old machine. The ongoing work in the lab is focused on discovering the nature of the surface-induced vibrational energy redistribution of CH₄ on Ni(111). I present in this thesis some preliminary results but more work is needed to draw a convincing conclusion. Incorporating our computer-controlled TOPO system, the scattering experiments can now be performed more efficiently than with the Argos systems. The BILT technique I described here is generally applicable to any molecule possessing IR-active vibrational modes with rotational state-resolved spectra. With this setup, I expect to have more surface scattering dynamics unraveled by future users.

6.2 Future experiments

Vibrational energy redistribution

As I have shown in chapter 5, starting from the Ph.D. work of Van Reijzen, our group studied state-to-state CH₄ surface scattering from Ni(111) and discovered surface-induced vibrational energy redistribution in a direct collision manner. The BILT technique opened up the possibility to study the coupling of vibrational modes of polyatomic molecules in the presence of the molecule-surface potential which is still an unknown field to surface scientists. The theory I discussed in chapter 5 pointed out that the efficiency of the vibrational energy redistribution is an indication of the catalytic activity of the surface impact sites. The observed C-H bond elongation when the CH₄ molecule approaches the surface facilitates coupling of the two vibrational modes. To test this theory, more investigations of vibrationally excited CH₄ scattering from surfaces with various catalytic activities are needed.

The barrier of CH₄ dissociation has been found to be ≈ 28 kJ/mol higher on Ni(111) compared to Pt(111) [114]. However, by exciting the incident CH₄ to $2\nu_3$ vibrational state, the reactivity on Ni(111) increases 2 order of magnitude more than on Pt(111), suggesting different transition state geometries on two distinct surfaces. This observation indicates that the vibrational energy is less efficient for CH₄ to overcome the barrier on Pt(111). According to the theoretical picture provided in chapter 5, we would then expect the incident CH₄ to experience weaker C-H bond elongation and therefore weaker surface-induced vibrational energy redistribution on Pt(111). This hypothesis can be tested by measuring the state distribution of vibrationally excited CH₄ scattered from Pt(111) and deducing the branching ratio ν_1/ν_3 . If a lower branching ratio is observed, it can strongly approve the validity of the theoretical picture. Furthermore, state-to-state surface scattering can serve as a probe of not only the surface reactivity but also the geometry of the transition state. Our results obtained so far only measured a branching ratio ν_1/ν_3 of 0.4 on clean Ni(111) and 0 on Gr-Ni(111), therefore more data on different surfaces is highly desired.

In the Ph.D. thesis of Van Reijzen, he reported that besides vibrational energy redistribution from the initially prepared ν_3 mode to the ν_1 mode, he also observed a small portion $\approx 2\%$ of CH₄ redistributed to the $2\nu_2$ mode. He suggested that the higher probability of $\nu_3 \rightarrow \nu_1$ redistribution is likely due to the small energy mismatch between the two modes. According to this observation, I would expect the surface-induced vibrational energy redistribution can also be observed in the scattering of NH₃ on catalytically active surfaces. Similar to CH₄, NH₃ also possesses a symmetric stretch mode (3534 cm^{-1}) and an antisymmetric stretch mode (3464 cm^{-1}) with an energy difference of 40 cm^{-1} . These vibrational frequencies are accessible by our Argos and TOPO lasers.

State-to-state surface scattering of CO₂

Besides studying the state-to-state surface scattering of NH₃ and other polyatomic molecules, it is probably more desirable to study the surface scattering of CO₂ because a rovibrational state-resolved scattering study of CO₂ from a metal surface has not yet been reported due to the lack of

a proper detection method in the past. Although Perkins and Nesbitt have reported a series of state-resolved studies of CO₂ surface scattering [42,43,115–117], these works are concerned only with liquid surfaces due to the limitation of their vacuum conditions. With the capabilities of the BILT machine, we can explore the scattering dynamics of CO₂ on solid metal surfaces.

Since the studies of state-resolved CO₂ scattering on solid metal surfaces are not available in the literature, there are of course plenty of topics one can explore with CO₂. Here, I simply propose some topics based on my personal interest, and hopefully, these can inspire readers with more possibilities. Unlike CH₄ which possesses vibrational modes with relatively high frequency, the highest frequency of CO₂ only takes 2349 cm⁻¹, corresponding to ≈ 290 meV. The energy can be accessed by seeding CO₂ in helium with low concentration, which enables us to study translational to vibrational energy conversion (T \rightarrow V). Given an amount of incident kinetic energy, we can study vibrational excitations of CO₂, and interrogate which mode can be excited and the branching ratio. Besides T \rightarrow V conversion, one can possibly observe vibrational excitations via coupling with electron-hole pairs (EHPs), i.e. via the electronically non-adiabatic process. In this case, one would observe increasing excitation probability as T_S increases, as observed in the system of NO scattering from Ag(111) [118]. Using a linearly polarized light, one can also align the angular momentum of CO₂ to collide with the surface in the helicopter mode or the cartwheel mode, I expect the resulting rotational and vibrational excitations could be very different. It has been shown that the vibration excitations of NO and CO via EHPs occur by receiving an electron from surfaces and followed by the formation of a transient anion [119,120]. According to the molecular orbital diagram of CO₂, the lowest unoccupied molecular orbital (LUMO) is localized toward the carbon atom, which makes the central carbon atom more likely to receive an electron. If vibrational excitation of CO₂ via coupling with EHPs can happen, I expect a higher excitation probability would be observed when the incident CO₂ is aligned in the helicopter mode since the carbon atom is exposed to the surface in this geometry.

Practically, with the available output laser frequency of our laser systems, we can excite the scattered CO₂ by adding a quantum of ν_3 (≈ 2300 cm⁻¹) which can be provided by the Argos D-module OPO. Since CO₂ has a low rotational constant (≈ 0.4 cm⁻¹), it can be easily excited to high J . To increase the performance of the measurements, it is worth automating the frequency tuning of the Argos system. Alternatively, excitation can also be performed via overtone transitions such as $\nu_1 + \nu_3$ and $2\nu_2 + \nu_3$ at ≈ 3500 - 3700 cm⁻¹ that is available by the TOPO system which has already the capability of performing programmed scans. Although the Einstein coefficients of the overtone transitions are lower (< 10 s⁻¹), the TOPO laser at this frequency range can provide higher power ≈ 3 W. Furthermore, the BILT detection measures energy added by the power or frequency modulated laser to the scattered molecules, the energy dissipated to the bolometer by the overtone-excited molecules is therefore higher.

References

- [1] H. Liu, *Chinese J. Catal.* **35**, 1619 (2014).
- [2] J. Humphreys, R. Lan, and S. Tao, *Adv. Energy Sustain. Res.* **2**, 2000043 (2021).
- [3] J. H. Larsen and I. Chorkendorff, *Surf. Sci. Rep.* **35**, 163 (1999).
- [4] G. Füchsel, K. Cao, S. Er, E. W. F. Smeets, A. W. Kleyn, L. B. F. Juurlink, and G. J. Kroes, *J. Phys. Chem. Lett.* **9**, 170 (2018).
- [5] A. Lozano, X. J. Shen, R. Moiraghi, W. Dong, and H. F. Busnengo, *Surf. Sci.* **640**, 25 (2015).
- [6] X. J. Shen, A. Lozano, W. Dong, H. F. Busnengo, and X. H. Yan, *Phys. Rev. Lett.* **112**, 1 (2014).
- [7] H. Guo and B. Jackson, *J. Phys. Chem. C* **119**, 14769 (2015).
- [8] Q. Ran, D. Matsiev, A. M. Wodtke, and D. J. Auerbach, *Rev. Sci. Instrum.* **78**, 104104 (2007).
- [9] Q. Ran, D. Matsiev, D. J. Auerbach, and A. M. Wodtke, *Nucl. Instruments Methods Phys. Res. Sect. B Beam Interact. with Mater. Atoms* **258**, 1 (2007).
- [10] R. J. V. Wagner, N. Henning, B. C. Krüger, G. B. Park, J. Altschäffel, A. Kandratsenka, A. M. Wodtke, and T. Schäfer, *J. Phys. Chem. Lett.* **8**, 4887 (2017).
- [11] C. T. Rettner, F. Fabre, J. Kimman, and D. J. Auerbach, *Phys. Rev. Lett.* **55**, 1904 (1985).
- [12] Y. Huang, C. T. Rettner, D. J. Auerbach, and A. M. Wodtke, *Science* **290**, 111 (2000).
- [13] N. Bartels, B. C. Krüger, D. J. Auerbach, A. M. Wodtke, and T. Schäfer, *Angew. Chemie - Int. Ed.* **53**, 13690 (2014).
- [14] A. C. Wight and R. E. Miller, *J. Chem. Phys.* **109**, 1976 (1998).
- [15] A. C. Wight and R. E. Miller, *J. Chem. Phys.* **109**, 8626 (1998).
- [16] M. E. Van Reijzen, *State-to-State Scattering of Methane from Ni(111) and Gr/Ni(111)*, École polytechnique fédérale de Lausanne, 2016.
- [17] J. Werdecker, *Vibrationally and Rotationally Inelastic Scattering of Methane from Ni(111)*, École polytechnique fédérale de Lausanne, 2018.
- [18] J. Werdecker, M. E. Van Reijzen, B. J. Chen, and R. D. Beck, *Phys. Rev. Lett.* **120**, 53402 (2018).
- [19] S. S. Sung and R. Hoffmann, *J. Am. Chem. Soc.* **107**, 578 (1985).
- [20] H. Chadwick and R. D. Beck, *Chem. Soc. Rev.* **45**, 3576 (2016).
- [21] J. C. Polanyi, *Acc. Chem. Res.* **5**, 161 (1972).
- [22] L. B. F. Juurlink, P. R. Mc Cabe, R. R. Smith, C. L. Di Cologero, and A. L. Utz, *Phys.*

- Rev. Lett. **83**, 868 (1999).
- [23] R. R. Smith, D. R. Killelea, D. F. DelSesto, and A. L. Utz, *Science* **304**, 992 (2004).
- [24] P. Maroni, D. C. Papageorgopoulos, M. Sacchi, T. T. Dang, R. D. Beck, and T. R. Rizzo, *Phys. Rev. Lett.* **94**, 1 (2005).
- [25] F. Frenkel, J. Häger, W. Krieger, H. Walther, C. T. Campbell, G. Ertl, H. Kuipers, and J. Segner, *Phys. Rev. Lett.* **46**, 152 (1981).
- [26] A. W. Kleyn, A. C. Luntz, and D. J. Auerbach, *Surf. Sci.* **117**, 33 (1982).
- [27] A. W. Kleyn, A. C. Luntz, and D. J. Auerbach, *Phys. Rev. Lett.* **47**, 1169 (1981).
- [28] A. M. Wodtke, Y. Huang, and D. J. Auerbach, *J. Chem. Phys.* **118**, 8033 (2003).
- [29] J. Werdecker, P. R. Shirhatti, K. Golibrzuch, C. Bartels, A. M. Wodtke, and D. J. Harding, *J. Phys. Chem. C* **119**, 14722 (2015).
- [30] Q. Ran, D. Matsiev, D. J. Auerbach, and A. M. Wodtke, *Phys. Rev. Lett.* **98**, 1 (2007).
- [31] J. Geweke, P. R. Shirhatti, I. Rahinov, C. Bartels, and A. M. Wodtke, *J. Chem. Phys.* **145**, 054709 (2016).
- [32] P. R. Shirhatti, J. Werdecker, K. Golibrzuch, A. M. Wodtke, and C. Bartels, *J. Chem. Phys.* **141**, 124704 (2014).
- [33] M. A. Hines and R. N. Zare, *J. Chem. Phys.* **98**, 9134 (1993).
- [34] G. O. Sitz, A. C. Kummel, and R. N. Zare, *J. Chem. Phys.* **89**, 2558 (1988).
- [35] G. O. Sitz, A. C. Kummel, R. N. Zare, and J. C. Tully, *J. Chem. Phys.* **89**, 2572 (1988).
- [36] B. D. Kay, T. D. Raymond, and M. E. Coltrin, *Phys. Rev. B* **36**, 6695 (1987).
- [37] G. B. Park, B. C. Krüger, S. Meyer, A. Kandratsenka, A. M. Wodtke, and T. Schäfer, *Phys. Chem. Chem. Phys.* **19**, 19904 (2017).
- [38] B. C. Krüger, G. B. Park, S. Meyer, R. J. V. Wagner, A. M. Wodtke, and T. Schäfer, *Phys. Chem. Chem. Phys.* **19**, 19896 (2017).
- [39] K. Golibrzuch, J. H. Baraban, P. R. Shirhatti, J. Werdecker, C. Bartels, and A. M. Wodtke, *Zeitschrift Fur Phys. Chemie* **229**, 1929 (2015).
- [40] B. D. Kay, T. D. Raymond, and M. E. Coltrin, *Phys. Rev. Lett.* **59**, 2792 (1987).
- [41] B. C. Krüger, G. B. Park, S. Meyer, R. J. V. Wagner, A. M. Wodtke, and T. Schäfer, *Phys. Chem. Chem. Phys.* **19**, 19896 (2017).
- [42] B. G. Perkins and D. J. Nesbitt, *J. Phys. Chem. B* **110**, 17126 (2006).
- [43] B. G. Perkins and D. J. Nesbitt, *Proc. Natl. Acad. Sci. U. S. A.* **105**, 12684 (2008).
- [44] S. Picaud, P. Hoang, C. Girardet, A. Glebov, R. Miller, and J. Toennies, *Phys. Rev. B - Condens. Matter Mater. Phys.* **57**, 10090 (1998).

- [45] A. Glebov, R. E. Miller, and J. P. Toennies, *J. Chem. Phys.* **106**, 6499 (1997).
- [46] T. W. Francisco, N. Camillone, and R. E. Miller, *Phys. Rev. Lett.* **77**, 1402 (1996).
- [47] J. Werdecker, B. J. Chen, M. E. Van Reijzen, A. Farjamnia, B. Jackson, and R. D. Beck, *Phys. Rev. Res.* **2**, 43251 (2020).
- [48] L. Chen, *Vibrationally Bond-Selective Chemisorption of Reflection Absorption Infrared Spectroscopy*, École polytechnique fédérale de Lausanne, 2012.
- [49] B. L. Yoder, *Steric Effects in the Chemisorption of Vibrationally Excited Methane on Nickel*, École polytechnique fédérale de Lausanne, 2010.
- [50] D. J. Auerbach and C. T. Rettner, *Rev. Sci. Instrum.* **63**, 3939 (1992).
- [51] S. Wright and R. R. A. Syms, *J. Micromechanics Microengineering* **31**, 045010 (2021).
- [52] R. Campargue, *J. Phys. Chem.* **88**, 4466 (1984).
- [53] G. Scoles, *Atomic and Molecular Beam Methods Volume 1* (1988).
- [54] P. Maroni, *Bond- and Mode-Specific Reactivity of Methane on Ni(100)*, École polytechnique fédérale de Lausanne, 2005.
- [55] Parker, *PTFE Seals Design Guide* (2015).
- [56] Advanced Glass Industries, *Pressure Window Design*.
- [57] Parker Hannifin Corporation, *Parker O-Ring Handbook* (2021).
- [58] H. Chadwick, P. M. Hundt, M. E. van Reijzen, B. L. Yoder, and R. D. Beck, *J. Chem. Phys.* **140**, 034321 (2014).
- [59] G. E. McGuire, *Auger Electron Spectroscopy Reference Manual*, 1st ed. (Springer, New York, 1979).
- [60] F. J. Low, *J. Opt. Soc. Am.* **51**, 1300 (1961).
- [61] M. Cavallini, G. Gallina, and G. Scoles, *Zeitschrift Für Naturforsch. A* **22**, 413 (1967).
- [62] R. Schinke and R. B. Gerber, *J. Chem. Phys.* **82**, 1567 (1985).
- [63] E. K. Grimmlmann, J. C. Tully, and M. J. Cardillo, *J. Chem. Phys.* **72**, 1039 (1980).
- [64] W. G. Mallard and P. J. Linstrom, *NIST Chemistry WebBook, NIST Standard Reference Database Number 69* (2021).
- [65] W. Kress and F. W. de Wette, *Springer Series in Surface Sciences, Vol. 21: Surface Phonons* (Springer-Verlag, Berlin Heidelberg, 1991).
- [66] R. Boyd, *Nonlinear Optics*, 3rd ed. (Elsevier, 2008).
- [67] J. P. C. Kroon, H. A. J. Senhorst, H. C. W. Beijerinck, B. J. Verhaar, and N. F. Verster, *Phys. Rev. A* **31**, 3724 (1985).
- [68] C. Zener, *Proc. Roy. Soc. A* **33**, 696 (1932).

- [69] H. Chadwick, P. M. Hundt, M. E. van Reijzen, B. L. Yoder, and R. D. Beck, *J. Chem. Phys.* **140**, 034321 (2014).
- [70] L. R. Brown, D. C. Benner, J. P. Champion, V. M. Devi, L. Fejard, R. R. Gamache, T. Gabard, J. C. Hilico, B. Lavorel, M. Loete, G. C. Mellau, A. Nikitin, A. S. Pine, A. Predoi-Cross, C. P. Rinsland, O. Robert, R. L. Sams, M. A. H. Smith, S. A. Tashkun, and V. G. Tyuterev, *J. Quant. Spectrosc. Radiat. Transf.* **82**, 219 (2003).
- [71] F. A. Cotton, *Chemical Applications of Group Theory*, 3rd ed. (Wiley-Interscience, 1990).
- [72] D. Harris and M. Bertolucci, *Symmetry and Spectroscopy an Introduction to Vibrational and Electronic Spectroscopy*, 1st ed. (Dover, Mineola, 1989).
- [73] J. Niederer, *The Infrared Spectrum of Methane*, ETH Zürich, 2012.
- [74] E. B. Wilson, J. C. Decius, and P. C. Cross, *Molecular Vibrations the Theory of Infrared and Raman Vibrational Spectra*, Revised (Dover Publications, 1980).
- [75] L. S. Rothman, D. Jacquemart, A. Barbe, D. C. Benner, M. Birk, L. R. Brown, M. R. Carleer, C. Chackerian, K. Chance, L. H. Coudert, V. Dana, V. M. Devi, J. M. Flaud, R. R. Gamache, A. Goldman, J. M. Hartmann, K. W. Jucks, A. G. Maki, J. Y. Mandin, S. T. Massie, J. Orphal, A. Perrin, C. P. Rinsland, M. A. H. Smith, J. Tennyson, R. N. Tolchenov, R. A. Toth, J. Vander Auwera, P. Varanasi, and G. Wagner, *J. Quant. Spectrosc. Radiat. Transf.* **96**, 139 (2005).
- [76] I. E. Gordon, L. S. Rothman, C. Hill, R. V Kochanov, Y. Tan, P. F. Bernath, M. Birk, V. Boudon, A. Campargue, K. V Chance, B. J. Drouin, J.-M. Flaud, R. R. Gamache, J. T. Hodges, D. Jacquemart, V. I. Perevalov, A. Perrin, K. P. Shine, M.-A. H. Smith, J. Tennyson, G. C. Toon, H. Tran, V. G. Tyuterev, A. Barbe, A. G. Császár, V. M. Devi, T. Furtenbacher, J. J. Harrison, J.-M. Hartmann, A. Jolly, T. J. Johnson, T. Karman, I. Kleiner, A. A. Kyuberis, J. Loos, O. M. Lyulin, S. T. Massie, S. N. Mikhailenko, N. Moazzen-Ahmadi, H. S. P. Müller, O. V Naumenko, A. V Nikitin, O. L. Polyansky, M. Rey, M. Rotger, S. W. Sharpe, K. Sung, E. Starikova, S. A. Tashkun, J. Vander Auwera, G. Wagner, J. Wilzewski, P. Wcisło, S. Yu, and E. J. Zak, *J. Quant. Spectrosc. Radiat. Transf. J. Quant. Spectrosc. Radiat. Transf.* **203**, 3 (2017).
- [77] C. Richard, V. Boudon, and M. Rotger, *J. Quant. Spectrosc. Radiat. Transf.* **251**, 107096 (2020).
- [78] B. Amyay, A. Gardez, R. Georges, L. Biennier, J. Vander Auwera, C. Richard, and V. Boudon, *J. Chem. Phys.* **148**, 134306 (2018).
- [79] J. Thiévin, R. Georges, S. Carles, A. Benidar, B. Rowe, and J. P. Champion, *J. Quant. Spectrosc. Radiat. Transf.* **109**, 2027 (2008).
- [80] E. Bright Wilson, *J. Chem. Phys.* **3**, 276 (1935).
- [81] G. Herzberg, *Molecular Spectra and Molecular Structure Volume II Infrared and Raman Spectra of Polyatomic Molecules*, Reprint (Krieger, Florida, 1991).
- [82] C. di Lauro, *Rotational Structure in Molecular Infrared Spectra*, 1st ed. (Elsevier, San

- Diego, 2013).
- [83] G. Brusdeylins, R. B. Doak, and J. P. Toennies, *Phys. Rev. B* **27**, 3662 (1983).
 - [84] G. Brusdeylins, R. B. Doak, and J. P. Toennies, *Phys. Rev. Lett.* **46**, 437 (1981).
 - [85] N. Garcia, *Phys. Rev. Lett.* **37**, 912 (1976).
 - [86] A. W. Kleyn and T. C. M. Horn, *Phys. Rep.* **199**, 191 (1991).
 - [87] B. Jackson and S. Nave, *J. Chem. Phys.* **138**, 174705 (2013).
 - [88] I. Iftimia and J. R. Manson, *Phys. Rev. Lett.* **87**, 932011 (2001).
 - [89] H. Ambaye and J. R. Manson, *J. Chem. Phys.* **125**, 1 (2006).
 - [90] K. R. Lykke and B. D. Kay, *J. Phys. Condens. Matter* **3**, S65 (1991).
 - [91] K. R. Lykke and B. D. Kay, *J. Chem. Phys.* **92**, 2614 (1990).
 - [92] K. Golibrzuch, A. Kandratsenka, I. Rahinov, R. Cooper, D. J. Auerbach, A. M. Wodtke, and C. Bartels, *J. Phys. Chem. A* **117**, 7091 (2013).
 - [93] N. Bartels, K. Golibrzuch, C. Bartels, L. Chen, D. J. Auerbach, A. M. Wodtke, and T. Schafer, *Proc. Natl. Acad. Sci.* **110**, 17738 (2013).
 - [94] A. Al Taleb and D. Farías, *Phys. Chem. Chem. Phys.* **19**, 21267 (2017).
 - [95] A. Al Taleb, R. Miranda, and D. Farías, *Phys. Chem. Chem. Phys.* **23**, 7830 (2021).
 - [96] J. D. Beckerle, A. D. Johnson, Q. Y. Yang, and S. T. Ceyer, *J. Chem. Phys.* **91**, 5756 (1989).
 - [97] R. M. Logan and R. E. Stickney, *J. Chem. Phys.* **44**, 195 (1966).
 - [98] F. O. Goodman, *J. Phys. Chem. Solids* **26**, 85 (1965).
 - [99] T. Kondo, A. Al Taleb, G. Anemone, and D. Farías, *J. Chem. Phys.* **149**, 084703 (2018).
 - [100] A. C. Kummel, G. O. Sitz, R. N. Zare, and J. C. Tully, *J. Chem. Phys.* **91**, 5793 (1989).
 - [101] D. F. and K.-H. Rieder, *Reports Progress Phys.* **61**, 1575 (1998).
 - [102] P. F. Bernath, *Spectra of Atoms and Molecules*, 3rd ed. (Oxford university press, New York, 2016).
 - [103] G. O. Sitz, A. C. Kummel, and R. N. Zare, *J. Chem. Phys.* **89**, 2558 (1988).
 - [104] D. J. Nesbitt and R. W. Field, *J. Phys. Chem.* **100**, 12735 (1996).
 - [105] J. Werdecker, B. J. Chen, M. E. Van Reijzen, A. Farjamnia, B. Jackson, and R. D. Beck, *Phys. Rev. Res.* **2**, 43251 (2020).
 - [106] A. Tamtögl, E. Bahn, J. Zhu, P. Fouquet, J. Ellis, and W. Allison, *J. Phys. Chem. C* **119**, 25983 (2015).
 - [107] W. H. Miller, N. C. Handy, and J. E. Adams, *J. Chem. Phys.* **72**, 99 (1980).

- [108] S. Nave, A. K. Tiwari, and B. Jackson, *J. Phys. Chem. A* **118**, 9615 (2014).
- [109] H. Guo and B. Jackson, *J. Chem. Phys.* **144**, 184709 (2016).
- [110] H. Chadwick, H. Guo, A. Gutiérrez-González, J. P. Menzel, B. Jackson, and R. D. Beck, *J. Chem. Phys.* **148**, 014701 (2018).
- [111] B. Jackson, F. Nattino, and G. J. Kroes, *J. Chem. Phys.* **141**, 054102 (2014).
- [112] S. Nave, A. K. Tiwari, and B. Jackson, *J. Chem. Phys.* **132**, 054705 (2010).
- [113] D. R. Killelea, V. L. Campbell, N. S. Shuman, R. R. Smith, and A. L. Utz, *J. Phys. Chem. C* **113**, 20618 (2009).
- [114] R. Bisson, M. Sacchi, T. T. Dang, B. Yoder, P. Maroni, and R. D. Beck, *J. Phys. Chem. A* **111**, 12679 (2007).
- [115] B. G. Perkins and D. J. Nesbitt, *J. Phys. Chem. A* **111**, 7420 (2007).
- [116] B. G. Perkins and D. J. Nesbitt, *J. Phys. Chem. B* **112**, 507 (2008).
- [117] B. G. Perkins and D. J. Nesbitt, *Phys. Chem. Chem. Phys.* **12**, 14294 (2010).
- [118] A. M. Wodtke, J. C. Tully, and D. J. Auerbach, *Int. Rev. Phys. Chem.* **23**, 513 (2004).
- [119] S. Li and H. Guo, *J. Chem. Phys.* **117**, 4499 (2002).
- [120] N. Shenvi, S. Roy, and J. C. Tully, *J. Chem. Phys.* **130**, 174107 (2009).

List of Figures

- Figure 1.1 A plot of potential energy as a function of molecule-surface distance which illustrates the concepts of chemisorption and physisorption. The dashed line indicates the level of zero potential energy. See text for the concept. 3
- Figure 1.2 Potential energy surfaces of the reaction $A + BC \rightarrow AB + C$. Left panels show PES with an early barrier, i.e. the saddle point is located in the entrance valley, whereas the right panels present the late barrier type of PES. Top panels show the case of reagents entering the valley with only translational energy-yielding a vibrationally excited AB product. On the other hand, the bottom panels illustrate the cases where BC reagent is vibrationally excited leading to translation energy release. The red lines are the trajectories moving from right to left on the underlying PES. The figure is adapted from ref [20]. 5
- Figure 2.1 Schematic diagram of state-to-state gas/surface scattering experiments. The P1/P2, the P2/P3, and the P3/P4 walls separate the four differential pumping stages. 14
- Figure 2.2 3D model of the BILT machine (Solidworks). The front wall of the model is transparent in order to show the internal components of the apparatus. See text for the functions of all the components. Pumps, cables, and pressure sensors are not shown in this model. 15
- Figure 2.3 (a) 3D model of the source chamber. For visibility, some parts of the chamber are made transparent. (b) Exploded view of the source chamber assembly. The entire assembly consists of the source chamber, the top cover plate, the P1 extension, and the skimmer mounting plate. The junctions between these parts are sealed by Viton O-rings. 18
- Figure 2.4 (a) Design of the expansion nozzle. Round tube with 1/4" OD and 0.4 mm wall thickness 0.4 mm which is reduced to 0.2 mm near the center. (b) Photo of the hot nozzle with $T_n=1200$ K. Only the central part with reduced thickness and thus higher resistance is glowing while the ends are clamped by water-cooled copper blocks. 19
- Figure 2.5 (a) 3D model of the nozzle and its holder. The top and the bottom brass blocks are made transparent to illustrate the O-ring sealed configuration inside. (b) Exploded view of the 3D model. Four nylon washers sit between the top copper block and the connecting bridge for electrical insulation. (c) the real object of the nozzle assembly. Two thermocouples are used, one is spot-welded to the side of the nozzle for measuring the nozzle temperature, and the other one attaches to the top brass block. Different than the 3D model, on the bottom copper block, the copper tubes are brazed from the back instead of from the side. We made this modification because the copper tubes interfered with the chopper motor in the original design. 20
- Figure 2.6 (a) 3D model of the nozzle tube mounting. For visibility, some parts of the source manipulator are removed in this model. On the base plate, there are four 1/4" Swagelok to 1/4" NPT nylon tube fittings (Swagelok, NY-400-1-4 BT) used as feedthroughs for the 1/4" copper water cooling tubes. A 1/8" Swagelok to 1/4" NPT nylon tube fitting is used for the 1/8" copper tube which delivers gas from a source manifold. (b) A photo of the fittings on the base plate. 21

Figure 2.7 Heating power vs. nozzle temperatures from 300 to 1200 K. See text for the detail of the nozzle heating setup.	21
Figure 2.8 (a) 3D model of the source manipulator and the top cover plate of the source chamber in exploded view. (b) 3D model of the Z-drive mechanism. (c) Exploded view of the 3D model. the bearing housing attaches to the top cover plate and holds an M8 threaded rod by two nuts. Two thrust bearings (AST, F8-16M) located between the nut and the bearing house allow for rotation of the threaded rod which drives the Z-drive block and the source manipulator.	22
Figure 2.9 (a) 3D model of the source manipulator. To illustrate the detail near the bearings, some parts are made transparent. Two linear bearings are located in each leg of the Y-motion support. Two Y-motion rods from the top plate inserted into the bearings align the Y-motion. (b) Exploded view of the 3D model. The top plate accommodates two bearings (AST, 636H), one constrains the motion of the support rod, and the other constrains the Y-motion screw.	23
Figure 2.10 (a) Back of the skimmer mounting plate where the chopper disk and the optocoupler are located. The optocoupler is glued on a 25 x 20 mm rectangular plate which is bolted to the skimmer mounting plate. (b) Section view of the chopper disk and the hub assembly. The chopper hub has both sides threaded. On the outer side, the chopper disk is attached. The inner side connects to the motor shaft and the inner nut fixes the hub on the shaft. (c) 3D model of the chopper hub. Four slots are cut into the threaded tube for symmetric mounting of the hub with the chopper disk in order to prevent vibrations due to imbalance during fast rotation.	25
Figure 2.11 (a) Front side of the skimmer mounting plate where the chopper motor attaches and is fixed by four M3 screws coming from the other side. Near the corner, there is a 5 pin electrical feedthrough for delivery of power needed and signal output of the optocoupler. (b) Electrical connections of the optocoupler and the chopper motor on the vacuum side of the feedthroughs.	26
Figure 2.12 Left: structure of a supersonic jet expansion adapted from Ref [51]. M is the Mach number. Right: images of supersonic expansion of He obtained by electron beam induced fluorescence. Images are taken from Ref [52].	27
Figure 2.13 (a) TOF trace of CH_4 for a 3% CH_4 in He mixture and $T_n = 300$ K nozzle which corresponds to an average velocity of 1700 m/sec and average kinetic energy of 23 kJ/mol. The blue trace shows a weak tail since it was measured without an aperture limiting the molecular beam size. Placing a 1 mm aperture in front of the QMS ionizer removes the tail as shown in the red trace. (b) TOF measurements with the same gas mixture but with different limiting apertures.	29
Figure 2.14 TOFs of a He atom beam measured at +8000, +10000, +12000, and +14000 rpm and the opposite direction. +/- denotes different spinning directions. Measurements were carried out using 2 bar of nozzle pressure and a room temperature nozzle.	31
Figure 2.15 (a) TOF of a He atom beam measured at different field axis voltages ranging from 6 to 15 V. (b) Using the same set of data as (a), but replace the field axis voltage U by the effective voltage U_{eff} with 4.9 V of correction voltage U_{corr} . The slopes provides the ion flight distance of 0.155 m.	33

Figure 2.16 Measured velocities of helium atom beams as a function of nozzle temperature T_n and their corresponding theoretical velocities calculated by eq 2.3.	35
Figure 2.17 (a) 3D model of the scattering chamber without attached source chamber.	36
Figure 2.18 (a) Exploded view of the top hub and the rotating platform. Between them, three spring-loaded O-rings and two differentially pumped stages protect the UHV condition from leaking during the rotation of the platform. (b) Section view of the rotary seal. See text for the working principle.	38
Figure 2.19 (a) Photo of the NAA type spring-loaded O-ring installed in the top hub. (b) Cross-section of the NAA type profile. The spring-loaded O-ring consists of a jacket and an energizer (spring), that are made out of PTFE and stainless steel, respectively.	38
Figure 2.20 (a) Structure of the rotating platform which consists of a support ring and a base. The two pieces are bolted together by 11 M8 screws. (b) Section view of the chamber. The labels indicate the distance from the CF160 flange to the scattering plane and from the CF160 flange of the bolometer to the bolometer detector.	39
Figure 2.21 (a) 3D model of the tagging and Doppler flange. The red arrows highlight the path of the incident and the reflected laser beam. The port of the reflected laser tilts 12° about the incident port for the velocity resolution of the Doppler velocimetry. (b) Section view of the CF40 differentially pumped window as an access of the tagging laser. See the text for more detail.	40
Figure 2.22 Left: Chain drive mechanism of the rotating platform. Right: Stepper motor and the 25x reduction gear installed below the bearing house. Between the bearing house and the reduction gear, there is a homemade adaptor flange.	41
Figure 2.23 (a) 3D model of the bearing housing with the 11 teeth sprocket gear. Two M8 screws on the mobile plate allow for adjustment of the tension of the chain. (b) Exploded view of the bearing housing attachment which is composed of a base plate, a mobile plate assembly, and the sprocket gear. (c) Exploded view of the bearing house. It accommodates two bearings which constrain the motion of the gear shaft.	42
Figure 2.24 RGA spectra UHV chamber measured with and without the bolometer. Both spectra were measured after a week of bakeout. On the panel, I highlight the partial pressure of water ($m/z = 18$) and CO_2 ($m/z = 44$).	43
Figure 2.25 RGA spectra of the UHV chamber measured before and after cooling down the bolometer. The conditions “cooled down” mean the bolometer is at its operation conditions where the LN_2 dewar and LHe dewars are thermalized with LN_2 and LHe, respectively. After cooling down the bolometer, the partial pressure at $m/z = 44$ and the corresponding fragmentations at $m/z = 12, 16,$ and 28 reduced drastically.	44
Figure 2.26 Pressure traces of the 1 st , 2 nd differentially pumped stages of the rotary seal, and the UHV stage. The dashed line highlights the timing (hh: mm) when the rotatory lid starts moving.	45
Figure 2.27 Section view of the BILT machine which highlights the nozzle-to-skimmer distance, the distance between collimators, and the collimator-to-rotational axis distance.	46
Figure 2.28 Left: front side of the pyroelectric detector. The detector has a square sensor area with an edge length of 3.5 mm. Right: Back of the detector. The leads of the detector connect to Kapton insulated wires via crimp connectors. The crimp connectors are covered by Teflon	

tubes to prevent a short circuit. In the end, a 9-pin subminiature type-C plug collects these three wires and connects to a CF16 9-pin subminiature type-C electrical feedthrough.	48
Figure 2.29 Pinout of the cable connecting the feedthrough of the pyroelectric detector to the home build amplifier. Left: 9-pin subminiature type-C female plug. Right: 4 pin LEMO male plug.	48
Figure 2.30 Left: Lock-in detected pyroelectric signal of the CH ₄ R(0) v ₃ fundamental transition with E _i = 100 meV. The signals are recorded 100 samples for molecular beam on, and another 100 samples for beam off to subtract the background value. Right: Fluence curve of the R(0) v ₃ fundamental R(0) transition of the incident CH ₄ beam with E _i = 100 meV. In both measurements, laser excitations are performed by Rapid adiabatic passage with a 25.4 cm cylindrical lens. The IR laser (Argos OPO I) was locked by the lamb-dip technique.....	49
Figure 2.31 3D model of the sample mount as well as the manipulator. To illustrate the structure of the connections, the bellow of the manipulator is not shown.....	50
Figure 2.32 (a) 3D model of the sample mount. The copper block acts as a base where the rest of the parts attach. The block is mounted on a cryogenic break connecting to the sample rotation platform. Two other cryogenic breaks are brazed to the back of the block for liquid nitrogen cooling. (b) Exploded view of the sample mount. The copper block has a central opening to accommodate the heating filament. The sample is mounted on the front and centered at the opening.....	51
Figure 2.33 (a) Section view of the sample mount which shows the configuration of the surface heating. (b) 3D model of the filament and filament support assembly. The two ends of the filaments are fixed on the ends of the Ta rod by M1.2 screws. These two rods are then sandwiched by ceramic bushes and a pair of stainless steel clamps.....	52
Figure 2.34 (a) 3D model of the sample rotation platform. The platform has a rectangular bearing housing as the main body. Inside, it holds a rotating tube with two bearings. On the top of the tube, a Z-slide, where the sample mount sits, is fixed on a collar. This Z-slide provides a translational motion for aligning the sample to the sample rotation axis. (b) Exploded view of the sample rotation platform. On the gear housing, there is a pair of bevel gears with a gear ratio of 0.5. Together with the pair of spur gears with the gear ratio of 14/144, the entire gear set provides a reduction ratio of 21.....	53
Figure 2.35 (a) Design of the connections between the sample rotation platform and the stainless steel tube. Please note that the bellows for transferring liquid nitrogen and the copper wires for delivering electricity are not shown in this model. (b) A 3D model which illustrates the connections between the stainless tube and the CF100 base flange.	53
Figure 2.36 Arrangement of the feedthroughs installed on the CF100 base flange that couples the sample mount to the manipulator.....	54
Figure 2.37 Left: Routing of the electrical wires and the liquid nitrogen bellows on the sample mount. Right: Connections from the flexible part to the stationary part.	55
Figure 2.38 Auger spectra measured before and after surface cleaning. The spectra were measured with the following conditions. SEM gain: 1300 V, emission current: 4.5 μA, step width: 1 V, modulation: 7 div, dE/E: 1 %, Lock-in sensitivity: 50 mV, and time constant: 300 ms.	57
Figure 2.39 Auger spectra of a clean Ni(111) surface with two different phase angles. The experimental parameters are set the same as the spectra in Figure 2.38.....	58

- Figure 2.40 LEED pattern of the Ni(111) surface measured after the surface cleaning procedure. The pattern was measured with 150 eV of beam energy, 2.55 A of filament current, and 3.5 kV of screen voltage. 58
- Figure 2.41 (a) 3D model of the bolometer detector in section view. (b) The front side of the bolometer pedestal. Inside the baffle, one can see the diamond absorber with Ag/Cr coating at the backside. Above the baffle, there is a doped silicone thermometer. (c) The backside of the pedestal. The bolometer element is installed inside the rectangular substrate. The cold module with the JFET is sitting near the bolometer substrate with a minimum wire length to prevent noise pick up. 60
- Figure 2.42 Left: The Si bolometer element bonded to the backside of the diamond absorber. Middle: Front side of the diamond absorber. The bolometer/diamond assembly is suspended by two copper wires on the copper substrate. Right: Front side of the bolometer substrate. One of the copper wires is glued to the substrate, and the other is held by a sapphire disk to prevent the signal short out but still provide a good thermal conductivity to the cryostat. .. 61
- Figure 2.43 Circuit diagram of the bolometer as well as the JFET. The figure is provided by Infrared Laboratories. 62
- Figure 2.44 DC load curves of different conditions measured by reading the voltage drop across the bolometer from the JFET when applying a bias voltage from 0-40 V to the bolometer circuit. (a) Original V2 bolometer without any modification on the cold shield (b) V2 bolometer with a 30 mm extension aperture attached to the cold shield. The “+” highlights the working point of the bolometer when using a 15 V bias battery. (c) Original V2 bolometer but with the 4 mm aperture blocked by aluminum tape. (d) Factory data of the V2 bolometer provided by IRLabs. Data was measured when the aperture was closed. (e) Original V1 bolometer with the aperture open. The measurement date is recorded in the bracket with the format (year-month-day)..... 63
- Figure 2.45 Load curves of the same set of data from Figure 2.44, but plotted in bolometer resistance versus power applied by the external power supply. 64
- Figure 2.46 Photos of the V1 bolometer system. Left: Complete assembly of the bolometer system with the LN₂ cold shield. Middle: Bolometer system with the LN₂ cold shield removed. Right: Bolometer system with both the LN₂ and LHe cold shields removed. 65
- Figure 2.47 Left: original structure of the LN₂ cold shield on the V2 bolometer. Middle: Modified cold shield with an adaptor flange and a 30 mm long extension aperture of 4 mm diameter. Right: section view of the modified cold shield. 66
- Figure 2.48 Lock-in signals of HAS experiments measured by the V2 bolometer in the old machine using different input settings “float” and “ground” in the lock-in amplifier. Experiments are performed with an RT helium atom beam with a nozzle pressure of 2 bar, then scattered from a 673 K Ni(111) surface at the geometry $\theta_i = \theta_f = 67.5^\circ$ 67
- Figure 2.49 Lock-in signals for methane scattering measured by the V2 bolometer in the old machine using different input settings “float” and “ground” of the lock-in amplifier. Experiments are performed with a pure CH₄ beam and RT nozzle using a nozzle pressure of 3 bar, then scattered from a 673 K Ni(111) surface at the geometry $\theta_i = 65^\circ$, $\theta_f = 70^\circ$. The signal of “Ground” (blue) is shifted down by 0.05 mV for better visibility. 67

Figure 2.50 HAS signals recorded at a range of V_{bias} from 1 to 20 V. The V_{bias} is provided by an external power supply. HAS was performed in the old machine with the scattering geometry $\theta_i = \theta_f = 67.5^\circ$, a room temperature nozzle, 2 bar of nozzle pressure, and 673 K of Ni(111) surface.....	68
Figure 2.51 Noise spectra of the V1 and the V2 bolometer measured by a 14-bit 48 kHz DAQ card (NI USB-6009) The waveforms are first filtered by a low-pass filter at a frequency cutoff of 2 kHz. Then the waveforms are converted to the frequency spectra by the fast Fourier transform and the power spectral density (PSD) is calculated by the build-in routine in LabVIEW.....	70
Figure 2.52 Angular distribution of scattered CH_4 from a 673 K Ni(111) surface. The incident beam is pure methane at $P_0 = 3$ bar, $\theta_i = 65^\circ$. The bolometer detector was rotated to detect scattering angles θ_f from 5° to 95° . The red dash line is a fit of the $\cos^n(\theta_f - \theta_M)$ function to the data.....	72
Figure 2.53 Angular distributions of helium atom scattering in three different incident angles ($\theta_i = 30, 45, \text{ and } 67.5^\circ$). The He beam is generated by 2 bar of nozzle pressure at room temperature. The Ni(111) sample was heated at 673 K. The bolometer preamplifier was set to gain 100X.....	74
Figure 2.54 Normalized angular distributions for scattered CH_4 and He from a Ni(111) surface at $T_S = 673$ K. The arrow indicates the incident angle of 30° . The methane beam was generated by 3 bar of nozzle pressure at $T_n = 600$ K. For the He beam, I used a nozzle pressure of 2 bar and $T_n = 300$ K.....	75
Figure 2.55 Scheme of the TOPO laser system. See the text for more detail.....	77
Figure 2.56 Results of a measured LUT, plotted as Idler power as a function of etalon-motor position.....	80
Figure 2.57 Left: extracted fringes from Figure 2.56. Right: LUT data plotted as Idler frequency as a function of etalon angle. The red curves are fitting with cubic spline functions.....	81
Figure 2.58 System setup of the laser stabilization and scanning mechanism by the Fabry-Pérot interferometer (FPI) and the LaseLock electronics.....	83
Figure 2.59 Illustration of the side-of-the fringe locking method for laser frequency stabilization (Left) and laser frequency scanning (Right). See text for the working principle.....	84
Figure 2.60 Absorption profiles of the R(0) A1 transition of the ν_3 fundamental of scattered CH_4 from a 673 K Ni(111) surface. The incident methane beam is generated by a 20% mixture in He at room temperature nozzle, providing 185 meV of kinetic energy. Scattering geometry is $\theta_i = 36^\circ$, $\theta_f = 41^\circ$. Bolometer amplifier gain is set to 1000.....	85
Figure 2.61 Doppler-broadened absorption profile with Lamb dip observed for the CH_4 R(0) ν_3 fundamental transition. Spectrum is taken from Ref [49].....	87
Figure 2.62 Transmission fringes of the IR and HeNe laser produced by our transfer cavity. The figure is adapted from Ref [17].....	89
Figure 3.1 Schematic of state-selective bolometric detection i.e. tagging experiments. See text for the working principle.....	91

Figure 3.2 Tagging signal of the CH ₄ ν_3 fundamental R(0) transition. Both the lock-in time constant and the dwell time were set to 300 ms. After 100 samples, the molecular beam was blocked by a beam flag to record the scattered light signal.....	92
Figure 3.3 Diagram that illustrates the concept of rapid adiabatic passage. See text for the concept. The figure is adapted from Ref [49]	95
Figure 3.4 (a) schematic diagram of the curved waveform created by a cylindrical lens. The black arrow indicates the propagation direction of the CH ₄ molecule. (b) Frequency detuning from the transition the molecule experiences as it travels from A to C. Figures are adapted from ref [17]	96
Figure 3.5 Fluence curves of the ν_3 R(0) fundamental transition for a 241 meV incident CH ₄ beam measured with/without a cylindrical lens. The amplifier gain of the pyroelectric detector was set to 10X. The incident beam was generated by expending a 3% CH ₄ mixture in He at 3 bar of nozzle pressure and room temperature nozzle.....	97
Figure 3.6 (a) Schematic of the correlation between the acceptance angle and the sample-to-bolometer distance. The acceptance angles θ_1 and θ_2 are calculated with the scattering geometry of $\theta_i = 65^\circ$, and $\theta_f = 70^\circ$ for the BILT and the old machine, respectively. (b) A diagram that shows the concept of broader residual Doppler shift for a wider acceptance angle. The solid arrows indicate the velocity vectors of scattered molecules with the largest angles α_1 and α_2 about the surface-to-bolometer axis that can be captured by the bolometers of the BILT and the old machine, respectively. Here, α is half of the acceptance angle. The dashed arrows are the velocity components projected on the laser propagation axis.....	98
Figure 3.7 Illustration for the scattering geometry of the BILT machine that shows the divergence of the incident molecular beam and its projection on the surface and the resulting acceptance angle of the bolometer. Scattering geometry in this figure is set to $\theta_i = 65^\circ$, $\theta_f = 70^\circ$	101
Figure 3.8 Lineshape measurements of the R(0) ν_3 fundamental transition for the BILT and the old machine with incident CH ₄ beam at $E_i = 100$ meV. The preamplifier gain was set to 1000. The scattering geometry of the old machine measurement was set to $\theta_i = 65^\circ$, $\theta_f = 70^\circ$. Whereas for the BILT machine is was $\theta_i = \theta_f = 45^\circ$. Note that the lineshape measurements were performed without the cylindrical lens. The solid curves are fittings using the Gaussian function.	103
Figure 3.9 Fluence curves of the ν_3 Q(3) A2 fundamental transition measured by the BILT and the old machine using the same scattering geometry of $\theta_i = 65^\circ$, $\theta_f = 70^\circ$ and the incident beam energy of 100 meV.....	104
Figure 3.10 Ratio of calculated squared Rabi frequency and frequency sweep rate for different focal lengths used for RAP excitation of the ν_3 R(0) fundamental transition with frequency 3028 cm ⁻¹ and transition dipole moment = $1.8 \cdot 10^{-31}$ Cm. The laser power is set to 1 W with 4 mm of the beam diameter. The velocities of the scattered molecules are set to 1000 m/s (left) and 1700 m/s (right).....	105
Figure 3.11 Absorption profiles for the ν_3 R(0) fundamental transition for CH ₄ scattered from a 673 K Ni(111) surface for tagging laser frequency modulation amplitude ranging from 0 to 150 mV applied to the AC-coupled input of the DFB seed laser. Experiments are performed with the scattering geometry of $\theta_i = 65^\circ$, $\theta_f = 70^\circ$ and $E_i = 241$ meV.	107

Figure 3.12 Characteristics extracted from the absorption profiles shown in Figure 3.11. Left: peak height (red data points) and peak area (green data points) of the absorption. Right: FWHM of the absorption profiles. All values are derived by fitting the experimental spectra with Gaussian functions and then extracting the corresponding fitting parameters.	108
Figure 3.13 Hönl-London factors calculated by the expressions in Table 3.3 for R branch (left) and Q branch (right) transitions.	110
Figure 3.14 Fluence curves of the ν_3 R(6) A2 and the R(9) A2 transitions of scattered CH ₄ measured the frequency-broadened laser. The frequency broadening was performed by adding 100 mV (RMS) of white noise to the DC-coupled input of the DFB seed laser. The scattering experiments were carried out at the geometry of $\theta_i = 65^\circ$, $\theta_f = 70^\circ$ with 241 meV of incident beam energy.	111
Figure 3.15 Normal vibrational modes of CH ₄ , their corresponding symmetry, and the vibrational frequencies. The vibrational frequencies are adapted from ref [73].	112
Figure 3.16 Energy levels of the first four polyads of CH ₄ , adapted from ref [16].	112
Figure 3.17 Allowed rotational levels of vibrational states with symmetry A_1 (left) and F_2 (right). Note that the F_2 vibrational state splits into three Coriolis stacks. The figure is adapted from ref [17].	115
Figure 4.1 Schematic of the two sets of experiments. Left: changing E_\perp at constant E_\parallel . Right: changing E_\parallel at constant E_\perp	122
Figure 4.2 Fluence curve measurements for interrogating the populations of the three incident molecular beams. The preamplifier of the pyroelectric detector was set to gain 10X. The insets show signals for R(3) A2 and R(4) A1 transitions on a smaller scale for visibility. Populations of the three beams are summarized in the bottom-right bar graph. The asterisk * labels non-existing J -levels due to Pauli-allowed symmetry restriction.	124
Figure 4.3 Tagging signals of an R-branch scan for scattering of CH ₄ from a 673 K Ni(111), with $E_i = 185$ meV at $\theta_i = 36^\circ$, and $\theta_f = 41^\circ$, corresponding to $E_\perp = 121$ meV and $E_\parallel = 64$ meV.	125
Figure 4.4 Rotational populations of scattered <i>meta</i> -CH ₄ from a 673 K Ni(111) surface with $E_\perp = 65, 121, \text{ and } 177$ meV at a constant E_\parallel of 65 meV. Error bars indicated an 80% confidence interval for repeated measurements based on student's t statistics.	126
Figure 4.5 Rotational populations of scattered <i>meta</i> -CH ₄ from a 673 K Ni(111) surface with $E_\parallel = 65, 121, \text{ and } 177$ meV at a constant E_\perp of 65 meV. Error bars indicated an 80% confidence interval for repeated measurements based on student's t statistics.	127
Figure 4.6 Effective rotational energy as a function of E_\perp (red) and E_\parallel (blue). Data points are derived from the results presented in Figures 4.4 and 4.5.	128
Figure 4.7 A picture of two particles collision reported by Goodman [98]. See text for the principle.	129
Figure 4.8 Angular distributions of CH ₄ scattering from Ni(111) with a surface temperature of 473 K (blue curve) and 673 K (red curve). The black dashed curve shows a cosine function to simulate the distribution of trapping-desorption. Measurements were performed with a beam	

energy of 100 meV (pure methane) with an incident angle of 65° . The black arrow and line indicate the incident angle and the specular angle, respectively.	131
Figure 4.9 Angular distributions of scattered CH_4 from a 373 K Ni(111) surface with E_i ranging from 100 meV to 269 meV. The black arrow and line indicate the incident angle (45°) and the specular angle, respectively.	131
Figure 4.10 Effective rotational energy of scattered CH_4 from Ni(111) as a function of T_S for $E_i = 130$ meV. Measurements are performed at two different scattering geometries ($\theta_i = 30^\circ$, $\theta_f = 35^\circ$) and ($\theta_i = 65^\circ$, $\theta_f = 70^\circ$). Solid lines are linear fit to the data points. The slopes of the linear fit give the $k_B T_S \rightarrow R$ conversion efficiency $d\langle E_{\text{rot}} \rangle_{\text{eff}}/d(k_B T_S)$ which is calculated to be 0.10 and 0.15 for $\theta_i = 30^\circ$ and $\theta_i = 65^\circ$, respectively.....	133
Figure 4.11 T_S efficiency coefficient γ as a function of normal incident velocity u_{n0} . The γ values are calculated from the data presented in Figure 4.10, which provide a range of E_\perp from 22.5 meV to 177 meV. The solid line is the linear fit of the data points.	134
Figure 4.12 Compositions of $\langle E_{\text{rot}} \rangle_{\text{eff}}$ by the four factors that can contribute to the rotational energy of the scattered CH_4 . Top panel: $\langle E_{\text{rot}} \rangle_{\text{eff}}$ composition for the scattering conditions of ($E_i = 241$ meV, $\theta_i = 31^\circ$, $\theta_f = 36^\circ$, $T_S = 673$ K). Bottom panel: $\langle E_{\text{rot}} \rangle_{\text{eff}}$ composition for the scattering conditions of ($E_i = 130$ meV, $\theta_i = 30^\circ$, $\theta_f = 35^\circ$, $T_S = 673$ K).	135
Figure 5.1 FM tagging spectra measured for CH_4 scattering from clean Ni(111) and graphene covered Ni(111) in a spectral range covering both ν_1 and ν_3 hot band transitions. Note the complete absence of any tagging signal for transitions originating from ν_1 . The figure is taken from ref [105].....	143
Figure 5.2 Rotational populations of the vibrationally elastic scattered CH_4 from clean Ni(111) (left) and Gr-Ni(111) (right). The black arrow indicates the initially prepared rotational state in the incident beam. *Note that the level $J = 0$ does not exist for <i>meta</i> - CH_4 due to symmetry restriction.	144
Figure 5.3 Boltzmann plots of the rotational populations shown in Figure 5.2 for scattering from Ni(111) (red) and Gr-Ni(111) (black). Note that the linear fits are performed without taking into account the lowest 2 J levels as they depart from the line. The rotational temperatures of the two systems are derived by slopes of the linear fits, giving rise to $T_{\text{rot}} = 208 \pm 14$ K and 153 ± 8 K for the scattering from clean Gr-Ni(111) and clean Ni(111), respectively.....	145
Figure 5.4 Left: the calculated probability of the $\nu_3 \rightarrow \nu_1$ redistribution of CH_4 scattered from clean Ni(111) on different impact sites. Z_C is the distance of the carbon atom above the surface when the total energy $V_0 = 0.2$ eV, and r is the C-H bond length closest to the surface at a given Z_C . Right: the model of the 2×2 unit cell with the definition of the 4 distinct impact sites, the top site, the half-bridge site (hb), the bridge site (br), and the half-bridge site (hb). The figure is taken from ref [105].....	146
Figure 5.5 FM scanned BILT spectra of the Q(3) A2 transitions for both the ν_1 (left) and the ν_3 channel in the scattered CH_4 from a 373 K Ni(111) surface. The incident CH_4 is state-prepared in ν_3 $J = 1$ and $E_i = 241$ meV. Scattering experiments were carried out in the geometry of $\theta_i = 65^\circ$, $\theta_f = 70^\circ$. The modulation frequency is set to 210 Hz with RMS amplitude = 30 mV. The laser power is 72 and 52 mW for the ν_1 and the ν_3 lines, respectively.	148

Figure 5.6 peak height ratio of the ν_1 and the ν_3 Q(3) A2 lines as a function of T_s 148

List of Tables

Table 2.1 Measured chopper delay at +200 Hz for He, Ne, and Ar. The average value of 18.2 μs will be taken for calibrations.....	31
Table 2.2 Correction voltage and the corresponding ion flight distance calculated from TOF data of He, Ne, Ar^+ , and Ar^{2+}	33
Table 2.3 Measured velocities of He, Ne, and Ar beams in comparison with the theoretical values. The experiments were carried out using a room temperature nozzle $T_n = 296$ K. The average energies show a very similar value because the theoretical energy is $52R \approx 6.1$ kJ/mol. ..	34
Table 2.4 Velocity characteristics of the He atom beam generated by 4 bar of nozzle pressure with nozzle temperatures ranging from 289 to 1100 K. The theoretical velocities are derived by eq 2.3.....	35
Table 2.5 Turbo-molecular pumps installed on different pumping stages, their specifications, and the typical background pressures at every stage. *The pressure at the UHV stage drops to $1 \cdot 10^{-10}$ mbar when the bolometer dewar is cold.....	43
Table 2.6 Long axis length of the ellipse projected on the surface with θ_i used frequently.	46
Table 2.7 Lock-in signals of CH_4 and helium atom scatterings with different lock-in input setting and their corresponding noise levels and signal-to-noise ratios.	68
Table 2.8 Frequency response of the V2 bolometer deduced by HAS experiments measured at different modulation frequencies. The signals are derived by averaging 200 samples with a dwell time of 300 ms and a time constant of 300 ms.....	70
Table 2.9 Specifications of the TOPO laser output	78
Table 2.10 Tuning range and resolution of frequency tuning parameters.	79
Table 2.11 Specifications of the AC and DC ports on the DFB laser head for controlling current tuning mode.	84
Table 3.1 The collection of parameters needed to estimate the bolometer acceptance angles for the two machines. The dimensions of the old machine are derived by the value recorded in the Ph.D. thesis of Van Reijzen and Werdecker [16,17]. *The nozzle-to-aperture distance of the old machine is estimated from a Solidworks 3D model built by Van Reijzen. Note that in this model, the nozzle-to-skimmer distance is not included therefore I assume a value of 5 mm.	101
Table 3.2 Calculated total frequency sweep, residual Doppler broadening, and measured FWHM of the $R(0) \nu_3$ fundamental transition for the BILT and the old machine. For the total frequency sweep, I assume the velocity of the scattered CH_4 is 1000 m/s. The distances z between the $f = 254$ mm cylindrical lens and the surface-to-detector axis are taken into account for the calculations.	103
Table 3.3 Analytical expressions of Hönl-London factors for different branches of transitions using a linear polarized light.	109
Table 4.1 Incident kinetic energies and the corresponding scattering geometries for the experiments of varying E_{\perp}	122

Table 4.2 Beam energies and the corresponding scattering geometries for the experiments of varying E_{\parallel}	122
Table 4.3 Molecular beam energy characteristics of three different mixtures.	123
Table 4.4 Rotational state populations of the 3 incident beams and their corresponding rotational energies.	124

Acknowledgments

Once upon a time, my supervisor, Rainer, said that the period, while he was studying Ph.D., was the best moment in his life. When I heard this, I was quite sure this won't be my case at that moment. However, now, looking back on the journey over the past 5 years, I found what he said is so true, also to me. Looking back on my Ph.D. life over the past five years, I realized that I'm so lucky to be here to study Ph.D. and meet nice people from around the world. It is these great people I met that make my Ph.D. life rich and colorful.

First of all, I have to thank my supervisor, Prof. Rainer Beck, for accepting me into the Group of Gas-Surface Dynamics. The story happened at the conference *Stereodynamics 2016* when I was searching for a laboratory that allowed me to construct a new experimental setup. There I met Rainer who needed a Ph.D. student to build a new machine. I was truly lucky to meet Rainer and found a position I was dreaming of. I'm grateful to Rainer for always being enthusiastic and helpful in the lab and for guiding me in the right way of making progress. I would also like to thank Prof. Daniel Auerbach, the main designer of the BILT machine, for his great help and suggestions on the design and construction of the BILT machine. Without his participation, my work won't be as successful as it is. My appreciations also go to my jury members Prof. Ken Mckendrick, Dr. Tim Schäfer, and Dr. Andreas Osterwalder for evaluating my thesis, participating in the thesis defense, and providing your unique insights into my work.

Also, I have to thank all the former and current group members of the LCPM and the GGSD for the friendly atmosphere they brought and for the joyful conversations we had. Among them, first I have to thank Dr. Jörn Werdeker for teaching me the experimental skills that are utterly useful in my entire Ph.D. life. Also, your thesis is very well written where I could always find solutions I need in the problems I encountered. I would like to also thank Dr. Chiara Masellis for always being kind and friendly to me, and helping me when I had trouble with a rental problem.

Of course, I'm grateful to Dr. Ana Gutiérrez Gonzalez for all the joyful moments we experienced in the lab. I miss very much the period when you were still working in our group and the conversations about every little thing in our life. I wish our paths will cross again in the future. I also have to give big gratitude to Harmina Vejjayan for being a great colleague and buddy in the group. A relaxing conversation with you always neutralizes some stress and frustrations. I especially thank you for the help in bringing me a pair of crutches when my foot was badly broken. Otherwise, I even could not go to the hospital. I wish you also finish your Ph.D. successfully soon. For Iwona Świdarska, I enjoyed a lot the moments of our interactions. Your funny characteristics truly entertained me and brought so much joy to my life. I wish you live happily and nicely all the time.

I would like to thank my great buddy Milica Vasiljevic for sharing a lot of good times with me on some pleasant, sometimes risky hikes and gorgeous skiing slopes. Without your participation, my adventures won't have been that much fun. I wish we can still find some time for more adventures. A great thank contributing to your coordination and help so that I can finally find Alice

who I have been searching for for a long time. Alice, grazie per essere così gentile e adorabile. Vorrei che potessimo incontrarci di nuovo e sviluppare un'amicizia più profonda.

A great appreciation of mine goes to Dr. Chris Reilly for your significant help in improving our experimental setup which makes our work a lot more efficient. Without your contribution, it would take me much more time to finish this thesis work. It is also joyful to work with you and learn some “practical” English from you. I will never forget the impressive hike we did that almost cost our life. I wish we can do it again, but, next time, with proper gear. Also for Patrick Floss, I enjoy the moments we spent together in mountains. You truly came back to Lausanne after two years of work in Göttingen. Together with Chris, I wish you can explore more with the BILT machine and bring our work to the next level.

I would like to give a big piece of my gratitude to Dr. Silvia Tanteri for expanding the diversity of my life. I'm very grateful to you for teaching me all kinds of desserts and Italian recipes that greatly enrich my cooking knowledge. Besides this, I'm glad that you always take my jokes making me feel so pleasant to chat with you all the time. I enjoy very much the moment when we were having delightful conversations together with Bruno Credidio, Sean Gordon, and Nikolaos Gkogkoglou. I wish this can still happen regularly in the future. I want to give a special appreciation to Andrew Clark for sharing his experiences with constructing a machine. It is nice to have you there to talk about the feeling of building a setup.

Comme mon travail comportait beaucoup de construction et de développement, j'ai vraiment très apprécié l'aide de nos ateliers mécanique et électronique. Je dois surtout remercier le responsable de l'atelier, André Fattet, pour la gestion de mes demandes de travaux, son écoute et ces conseils avisés. Je remercie également Roger Mottier et Yves Morier pour avoir travaillé sur mes projets et pour avoir aussi partagé volontiers avec moi des informations utiles sur le ski et la randonnée en montagne. Je tiens à remercier vivement Benjamin Le Geyt pour son aide et sa réactivité. Enfin, la plus grande partie de ma gratitude va à mon bon ami Guillaume Francey. Je te suis très reconnaissant d'avoir été si efficace pour m'aider dans tous les travaux que j'ai demandés. De plus, tu es toujours patient et tu m'aides à améliorer mon français. Et bien sûr, ce que j'aime le plus, c'est de faire des randonnées et du ski avec toi et, en même temps, d'apprendre quelques cultures suisses.

Outre nos ateliers, je tiens également à remercier Jacques Gremaud et son équipe, Loïc Nyffenegger et Roxane Moinat de notre magasin de chimie. Merci à eux pour la bonne gestion du magasin afin que nous puissions toujours trouver les articles dont nous avons besoin avec une grande commodité. De plus, vous me fournissez également une plateforme pour pratiquer le français. Je remercie tout particulièrement Roxane d'avoir été si gentille lorsque mon pied était cassé et que je ne pouvais pas marcher correctement. Je vous souhaite à tous de travailler dans la joie et la bonne humeur.

I should also thank our lovely secretary Angeles Alarcon for always being nice and friendly to us. It is because of your help in all the paperwork that makes our life much easier. Especially when I had trouble understanding French documents. It is always pleasant to practice French with you. Talking about French learning, I have to thank my tandem partner Heidi Francelet for improving

a lot my French. It was a great pleasure for me to teach someone Chinese which I never expected before.

I would love to appreciate my Siberian outdoor team members Anastasia Komarova, Kristina Makasheva, and Irina Diukova for sharing delightful moments with me during some breathtaking hikes and skiing. Especially I have to give magnificent gratitude to Ira for introducing me to this Siberian group, and more importantly, for your kindness in helping me with grocery shopping when I was living with crutches. It was the light in the worse moment of my Pd.D. life. I wish we will have more nice hikes and fast slopes.

Near the end of this page, I want to thank my mountain partner Fiona Köster for spending some time with me no matter in summer or winter in mountains. I'm grateful to you for always being willing to be with me in hiking and skiing even though sometimes I was really pushed to my limit and almost destroyed. However, thanks to your hardcore training, my snowboarding level improved dramatically this winter. I wish you live happily and stay healthy for more upcoming adventures.

Finally, I would like to thank my parents for believing my decision of studying Ph.D. on the other side of the world. I'm sorry that I always like some activities coming with a risk that makes you worry a lot about me. However, I believe that "what doesn't kill you makes you stronger". Although this departs from what you expect of me, I would still like to continue in this way. I hope you understand and support me. My best wishes to you.

Lausanne, 16th April 2022

Curriculum Vitae

Avenue des Bergières 59
1004 Lausanne
Switzerland
Mail: bjchen173@me.com
Nationality: Taiwanese



Bo-Jung Chen

❖ Education

2017-2022 Swiss Federal Institute of Technology, Lausanne (EPFL), Switzerland

Ph.D. in physical chemistry

Supervisor: Prof. Rainer Beck

Thesis title: *Rotationally inelastic scattering of CH₄ from Ni(111) using bolometric infrared laser tagging*

2012-2014 National Taiwan University, Taipei, Taiwan

Master's degree in chemistry

2008-2012 National University of Kaohsiung, Kaohsiung, Taiwan

Bachelor's degree in applied chemistry

❖ Publications

[1] Jörn. Werdecker, Bo-Jung Chen, Maarten E. Van Reijzen, Azar Farjamnia, Bret. Jackson, and Rainer D. Beck, “*State-to-state methane-surface scattering as a probe of catalytic activity.*”, *Phys. Rev. Res.* 2020, 2, 43251.

[2] Jörn Werdecker, Maarten E. van Reijzen, Bo-Jung Chen, and Rainer D. Beck, “*Vibrational Energy Redistribution in a Gas-Surface Encounter: State-to-State Scattering of CH₄ from Ni(111).*”, *Phys. Rev. Lett.* 2018, 120, 053402.

[3] Ting-Kang Huang, Bo-Jung Chen, King-Chuen Lin*, Lin Lin, Bing-Jian Sun, and A. H. H. Chang, “*Cl₂ Elimination in 248 nm Photolysis of (COCl)₂ Probed with Cavity Ring-Down Absorption Spectroscopy.*”, *J. Phys. Chem. A*, 2017, 121, 2888-2895

[4] Bo-Jung Chen, Po-Yu Tsai, Ting-Kang Huang, Zhu-Hong Xia, King-Chuen Lin, Chuei-Jhih Chiou, Bing-Jian Sun, and A. H. H. Chang, “*Characterization of molecular channel in*

photodissociation of SOCl₂ at 248 nm: Cl₂ probing by cavity ring-down absorption spectroscopy.”, *Phys. Chem. Chem. Phys.*, 2015, 17, 7838-7847

❖ **Conference presentations**

Oral

2021 “*state-to-state methane-surface scattering with bolometer infrared laser tagging detection*” 29th Edition International Symposium of Molecular Beams.

Poster

2019 “*State-to-State Molecule/Surface Scattering Apparatus Using Bolometric Infrared Laser Tagging Technique*” Gordon Research Conference: Dynamics at Surfaces, New Port, United States.

2019 “*State-to-State Molecule/Surface Scattering Apparatus Using Bolometric Infrared Laser Tagging Technique*” SCS Fall Meeting 2019, Zurich, Switzerland.

2018 “*A Molecular Beam/Surface Science Apparatus with a Rotating Bolometer Detector for State-to-State Surface Scattering Experiments*” Stereodynamics 2018, Arosa, Switzerland.

❖ **Awards**

2019 Chemistry Travel Award

Provided by the Swiss Academy of Sciences (SCNAT) and the Swiss Chemical Society (SCS) for attending the *2019 Gordon Research Conference, Dynamics at Surfaces*.

❖ **Languages**

Chinese: Native

English: Fluent

French: Basic